Active Cancellation of Electromagnetic Emissions of Power Electronic Systems by Injecting Synthesized and Synchronized Signals

by

M.Sc. Andreas Bendicks

Dortmund, Germany, 6 July 2020

A Dissertation Submitted to the

Faculty of Electrical Engineering and Information Technology
of the TU Dortmund University

in Partial Fulfillment of the Requirements for the Degree of

Doctor of Engineering (Dr.-Ing.)

Supervisor:	Prof. Dr.-Ing Stephan Frei
External Examiner:	Prof. Dr.-Ing. Gerd Griepentrog
	(TU Darmstadt University)
Date of Disputation:	30 June 2020

Abstract

In this thesis, a new method is developed for the active cancellation of predictable EMI by injecting synthesized and synchronized signals. At first, a generic description is derived for the active cancellation of conducted EMI of arbitrary single- and multi-port electronic systems. From the mathematical description, important requirements for the overall system and the cancellation signals are found.

Analog active EMI filters as an established method for active EMI cancellation are discussed. These use analog circuitry to generate the cancellation signals from a measured quantity by a feedback or feedforward approach. It is shown that the performance of these structures is systematically limited by the amplifiers' gain-bandwidth products (that can also be interpreted as time constants) and the finite propagation speed of electrical signals.

Digital active EMI filters use digital signal processing hardware instead of analog amplifiers in the feedback or feedforward structures. By doing so, restricting gain-bandwidth products are avoided. However, the signal processing causes significant delay times that limit the performance of these systems.

Active cancellation methods and systems in the fields of power quality and acoustics are reviewed for their applicability to active EMI cancellation. The most promising approaches are applicable to periodic disturbances. These synthesize artificial cancellation signals and inject them in synchronicity with the disturbances. For quasi-periodic EMI, these systems can use the knowledge of the past for the future. Therefore, time constants and delay times can be compensated by shaping the cancellation signal and injecting it earlier than the EMI occurs. By doing so, the signal generation is no limiting factor for the achievable EMI reduction anymore. The remaining limitations are the capabilities of the digital hardware.

These methods are further abstracted to a new active cancellation technique that uses synthesized and synchronized cancellation signals. This method requires the EMI to be predictable so that the cancellation signals can be synthesized and injected at the right time. The predictability is given for quasi-periodic signals (since the past signals allow for an extrapolation into the future), but may also be given for non-periodic signals if there is sufficient knowledge on the upcoming events. Various possibilities for implementation are discussed.

The method is realized by an FPGA system with an ADC and a DAC, or a laboratory setup consisting of arbitrary waveform generators, an oscilloscope and a PC. The FPGA system is investigated and applied to one port of a DC-to-DC converter and a PFC. The laboratory setup is first applied to one and afterward to multiple ports of a DC-to-DC converter. After a system identification, the components are purposefully designed to fulfill specific EMI requirements. Measurement results demonstrate the high potential of the method with promising EMI reductions of up to 64 dB for 1 MHz and up to 47 dB for frequencies of up to 30 MHz.

Contents

List of Abbreviations

Abbreviation	Full meaning
AC	**a**lternating **c**urrent
ADC	**a**nalog-to-**d**igital **c**onverter
AEF	**a**ctive **E**MI **f**ilter
AN	**a**rtificial **n**etwork
ANC	**a**ctive **n**oise **c**ancellation
APF	**a**ctive **p**ower **f**ilter
AWG	**a**rbitrary **w**aveform **g**enerator
CM	**c**ommon **m**ode
CSCI	**c**urrent **s**ense **c**urrent **i**nject
CSVI	**c**urrent **s**ense **v**oltage **i**nject
DAC	**d**igital-to-**a**nalog **c**onverter
DC	**d**irect **c**urrent
DM	**d**ifferential **m**ode
DSP	**d**igital **s**ignal **p**rocessor
DUT	**d**evice **u**nder **t**est
EMC	**e**lectro**m**agnetic **c**ompatibility
EMI	**e**lectro**m**agnetic **i**nterference
FB	**f**eed**b**ack
FF	**f**eed**f**orward
FFT	**f**ast **F**ourier **t**ransform
FPGA	**f**ield **p**rogrammable **g**ate **a**rray
LISN	**l**ine **i**mpedance **s**tabilization **n**etwork
LMS	**l**east-**m**ean-**s**quare
NF	**n**oise **f**loor
OpAmp	**op**erational **amp**lifier
PC	**p**ersonal **c**omputer
PEF	**p**assive **E**MI **f**ilter
PFC	**p**ower **f**actor **c**orrection
PLL	**p**hase-**l**ocked **l**oop
PM	**p**hase **m**argin
PWM	**p**ulse-**w**idth **m**odulation
RMS	**r**oot **m**ean **s**quare
SMPS	**s**witched-**m**ode **p**ower **s**upply
SNR	**s**ignal-to-**n**oise **r**atio
VNA	**v**ector **n**etwork **a**nalyzer
vs	**v**er**s**us
VSCI	**v**oltage **s**ense **c**urrent **i**nject
VSVI	**v**oltage **s**ense **v**oltage **i**nject
w/o	**w**ith**o**ut

List of Mathematical Symbols

Variable	Meaning
C	capacitance value
f	spectral frequency
f_0	fundamental frequency
G	amplification
H	transfer function
$\boldsymbol{H}$	transfer matrix
I	frequency-domain current
i	time-domain current
$\vec{I}$	vector of frequency-domain currents
$\vec{i}$	vector of time-domain currents
k	order of harmonic
L	inductance value
P	amount of ports
p	number of port
S	scattering parameter
$\boldsymbol{S}$	scattering matrix
SNR	**s**ignal-to-**n**oise **r**atio
T	period
t	time
t_d	propagation delay time
V	frequency-domain voltage
v	time-domain voltage
$\vec{V}$	vector of frequency-domain voltages
$\vec{v}$	vector of time-domain voltages
X	arbitrary frequency-domain signal
x	arbitrary time-domain signal
$\vec{X}$	vector of arbitrary frequency-domain signals
$\vec{x}$	vector of arbitrary time-domain signals
Y	admittance
$\boldsymbol{Y}$	admittance matrix
Z	impedance
$\boldsymbol{Z}$	impedance matrix

Subscript	Meaning
anti	reference to anti-EMI source
coup	**coup**ling
dB	Quantity in dB
dec	**dec**oupling
det	**det**ermined
dev	**dev**iation
EMI	reference to EMI source
inj	**inj**ecting
meas	**meas**urement
res	**res**idual signal
sense	reference to sensor
victim	reference to EMI victim

Superscript	Meaning
@sensor	signal at sensor ports
$\rightarrow$ sensor	propagation to sensor ports
@victim	signal at victim ports
$\rightarrow$ victim	propagation to victim ports
@victim*	signal at EMI victims
$\rightarrow$ victim*	propagation to EMI victims

Symbol	Meaning
$\angle$	angle of a complex number
Δ	difference (relative or absolute)

List of Figures

List of Tables

1 Introduction

Power electronic systems tend to be considerable sources of **e**lectro**m**agnetic **i**nterferences (EMI) due to the high-frequency switching of potentially high currents and voltages. To comply with international standards (e.g. CISPR 25 in automotive [4]), the EMI is commonly reduced by the application of passive filters or shields. However, these elements are often bulky, heavy and costly. To resolve this issue, active EMI cancellation techniques can be applied that aim at a destructive interference between noise and anti-noise [5]. This strategy is already well established in, e.g., acoustics [3].

In **e**lectro**m**agnetic **c**ompatibility (EMC), active EMI filters have been developed in, e.g., [1,6–8] since 1970. These systems use analog circuitry in a feedback or feedforward structure to generate the cancellation signals from a measured quantity. As analyzed later in this work, this approach is limited by the gain-bandwidth products of the amplifiers (that are directly linked to time constants) and the finite propagation speed of signals.

To resolve the issues of limited gain-bandwidth products, digital active EMI filters have been proposed in, e.g., [9–11] in 2013. These systems still use feedback or feedforward approaches to generate the cancellation signals from a measured quantity. Since the digital signal processing introduces small but significant delay times, the performance of this method is also limited.

There are also active cancellation techniques in other disciplines. E.g., for the improvement of power quality in grid applications, active power filters have been developed. Analog realizations have been proposed in [12] in 1971, at a very similar time as active EMI filters. Since the considered frequencies are much lower, digital hardware was already available at reasonable costs in 1999 [13]. So, the level of maturity for digital realizations is much higher in these systems. In this work, the methods of active power filters are evaluated for the application to active EMI cancellation. Promising methods are identified and transferred.

Another interesting field of application is active noise cancellation in acoustics. Active cancellation of sound has been patented much earlier, in 1936 [5]. Digital systems could already be realized at low costs in the 1980s [14]. So, this field of application has even a higher level of maturity than active power filters. Also for this discipline, different methods are evaluated for the application to EMC. Since the physical domains are different, the possibilities and limitations are not the same. However, there are still interesting methods that can be transferred to active EMI cancellation.

All of these insights are used to derive a new active EMI cancellation strategy that uses synthesized and synchronized signals. For predictable EMI, this strategy can compensate time constants and delay times by shaping the cancellation signals and injecting them before the EMI occurs. By doing so, the performance of the active EMI cancellation can be significantly improved in comparison to the conventional feedback or feedforward approach.

This work starts with some required basics on power electronic systems and EMC. Afterward, a generic description for single- and multi-port active EMI cancellation systems is derived that will be used throughout this work. From this description, important requirements for the cancellation systems and cancellation signals can be derived.

Next, different active cancellation techniques are evaluated. First, (analog) active EMI filters are summarized and analyzed. The potentials and physical limitations are systematically identified. Published experimental results are summed up. Digital variants are motivated and discussed. Also here, the limiting factors are elaborated and experimental results are summarized. Afterward, active cancellation techniques in power quality and acoustics are discussed and evaluated. Promising approaches are transferred to the application in active EMI cancellation and analyzed in regard to their potentials and limitations.

From all of these insights, a new active EMI cancellation technique is derived that injects artificially synthesized cancellation signals in synchronicity with the EMI. Important requirements and possible variants for implementation are discussed. During the work on this thesis, numerous experimental results have been generated and published. These show a high potential for the proposed method and are briefly summarized.

One realization of the proposed method uses a programmable FPGA (**f**ield **p**rogrammable **g**ate **a**rray) system. Systematic investigations on the performance of this active EMI cancellation system are summed up in this work. Demonstrator results for DC-to-DC converters and a power factor correction are presented and discussed.

In all publications until now (e.g. [15–17, author]), the active EMI cancellation systems using the proposed method have basically been designed by trial and error. In this work, the active cancellation system for a DC-to-DC converter will be systematically designed after an identification process. At first, this is done for one port of the converter in a typical automotive test setup according to the EMC standard CISPR 25 [4]. In this prototype setup, the active EMI cancellation system is realized by an arbitrary waveform generator, an oscilloscope and a PC. The performance is shown by standard measurements.

Afterward, the method is applied to all four ports of an isolated DC-to-DC converter in a similar test setup. To do so, the system identification is extended. The additional aspects for the design of multi-port cancellation systems are discussed and respected. For this multi-port application, the prior used active EMI cancellation system is extended. Also here, the performance of the system is demonstrated by standard measurements.

This work is closed by a conclusion of all the new insights and a short summary of the achieved results.

2 Fundamentals of Electromagnetic Emissions of Power Electronic Systems

In this chapter, the fundamentals relevant for this work are presented. These comprise some basics on power electronic systems and **e**lectro**m**agnetic **c**ompatibility (EMC). Spectra of quasi-periodic signals are discussed for later use. The propagation of electromagnetic emissions is briefly described. Afterward, passive EMI filters are discussed as conventional method for disturbance reduction. From this description, the motivation for this work is derived.

2.1 Power Electronic Systems

Many electronic systems need some form of electrical energy conversion to operate. These processes must be very efficient due to numerous reasons; from a technical point of view, power losses cause heat that must be dissipated from the electrical system. A sufficient cooling can be a significant challenge in small, light and cheap systems. From a financial point of view, wasted energy means additional operational costs. From an ecological point of view, energy must be used efficiently to reduce the environmental burden since all saved energy reduces the necessary power generation. [18, pp. 3-4]

Fundamentally, the energy conversion could be done by linear electronics with semiconductors operating in their linear (or active) region. Nevertheless, this form of energy conversion shows a very low efficiency. In power electronic systems, the semiconductors are basically used as switches that are rapidly turned on and off. In the on and off states, the power losses are usually significantly reduced in comparison to linear electronics. During the transition, the semiconductor goes quickly through its linear (or active) region. This causes switching power losses, but the total power losses in power electronic systems are usually still much lower than in linear electronics. On the downside, the high-frequency switching of the power transistors may cause high levels of electromagnetic disturbances that are discussed later. [18, pp. 4-7]

There are many important applications and topologies for power electronic systems. Some important are DC-to-DC converters, inverters and rectifiers. The latter two are often used for, e.g., motor or grid applications.

2.2 Electromagnetic Compatibility (EMC)

The field of EMC deals with the possible interference between electronic systems. This is a critical aspect since all electronic systems can be sources of intentional or unintentional electromagnetic signals that can interfere with susceptible electronic systems.

Unintentional electromagnetic signals (disturbances, **e**lectro**m**agnetic **i**nterferences

(EMI)) often occur as byproduct of the operation of electronic systems. For, e.g., DC-to-DC converters, the intentional input and output signals are DC. For rectifiers in grid applications, the intentional signals are usually sine waves with frequencies of 50 or 60 Hz at the input and DC at the output. For inverters in grid applications, the intentional signals at the input and output are swapped in comparison to the rectifier. Inverters for motor applications generate variable output frequencies (e.g. up to 200 Hz) to adjust the rotational speed of the rotor. The high-frequency switching of the power transistors can lead to unintentional EMI that superposes the intentional DC or low-frequency signals. Since power electronic systems often convert large currents and voltages, they tend to be considerable EMI sources.

All electronic systems are to some degree susceptible to EMI. Typical very susceptible systems are AM or FM broadcast receivers since the intentional radio signals can have a very low level at the receiver's antenna. Therefore, the signal can easily be corrupted by EMI. To avoid disturbances in electrical systems, there are three fundamental possibilities [19, pp. 1-2]:

1. Reducing the unintentional emission of the EMI source.

2. Weakening the coupling path between EMI source and EMI victim.

3. Making the EMI victim less susceptible.

In this thesis, the first measure is investigated.

2.3 Spectra of Periodic and Quasi-Periodic Signals

Since many power electronic systems in a stationary operating mode generate periodic or quasi-periodic disturbances, these signals are very important for this thesis. These signals have a period of T, and repeat themselves with their fundamental frequency $f_0 = 1/T$. Due to the periodicity, the signal can be described by harmonic sine waves according to the Fourier series. The complex-exponential form for the generic periodic function $x(t)$ is depicted in (2.1). The complex Fourier coefficients $X(kf_0) \in \mathbb{C}$ can be calculated by (2.2).

$$x(t) = \sum_{k=-\infty}^{\infty} X(kf_0) e^{j \cdot 2\pi \cdot kf_0 \cdot t} \tag{2.1}$$

$$X(kf_0) = \frac{1}{T} \cdot \int_{t_0}^{t_0+T} x(t) \cdot e^{j \cdot 2\pi \cdot kf_0 \cdot t} dt \tag{2.2}$$

There are complex amplitudes for all harmonics $k \in \mathbb{Z} \setminus \{0\}$ corresponding to the spectral frequencies kf_0. $X(0) \in \mathbb{R}$ is the DC component. Since there are complex amplitudes for positive and negative frequencies, it is often referred to as *two-sided mathematical spectrum*. [19, pp. 95-96]

To find the *one-sided physical spectrum* with positive frequencies only, the sum of (2.1) can be separated to (2.3) and rewritten to (2.4):

$$x(t) = X(0) + \sum_{k=1}^{\infty} X(kf_0)e^{j\cdot 2\pi\cdot kf_0\cdot t} + \sum_{k=-1}^{-\infty} X(kf_0)e^{j\cdot 2\pi\cdot kf_0\cdot t} \tag{2.3}$$

$$\Rightarrow\ x(t) = X(0) + \sum_{k=1}^{\infty} X(kf_0)e^{j\cdot 2\pi\cdot kf_0\cdot t} + \sum_{k=1}^{\infty} X(-kf_0)e^{-j\cdot 2\pi\cdot kf_0\cdot t} \tag{2.4}$$

(2.5) follows for $X(-kf_0)$ from (2.2):

$$X(-kf_0) = \frac{1}{T}\cdot\int_{t_0}^{t_0+T} x(t)\cdot e^{-j\cdot 2\pi\cdot kf_0\cdot t}dt = X(kf_0)^* \tag{2.5}$$

By inserting (2.5) into (2.4) and splitting $X(kf_0)$ into amplitude $|X(kf_0)|$ and phase $\angle X(kf_0)$, (2.6) follows:

$$\Rightarrow\ x(t) = X(0) + \sum_{k=1}^{\infty} |X(kf_0)|\, e^{j(2\pi\cdot kf_0\cdot t+\angle X(kf_0))} + \sum_{k=1}^{\infty} |X(kf_0)|\, e^{-j(2\pi\cdot kf_0\cdot t+\angle X(kf_0))} \tag{2.6}$$

By applying Euler's identity according to (2.7), (2.8) results:

$$\cos(\theta) = \frac{e^{j\theta}+e^{-j\theta}}{2} \tag{2.7}$$

$$\Rightarrow\ x(t) = X(0) + \sum_{k=1}^{\infty} 2\,|X(kf_0)|\cos(2\pi\cdot kf_0\cdot t+\angle X(kf_0)) \tag{2.8}$$

So, the amplitudes of the one-sided physical spectrum $(k \geq 1)$ can be found by doubling the corresponding absolute values of the two-sided mathematical spectrum. The phases of the two-sided mathematical spectrum are directly valid for the one-sided physical spectrum. Note that the DC component $X(0)$ is not doubled for the one-sided physical spectrum. [19, pp. 96-97]

In reality, there are no truly periodic signals since this would imply that the signal repeats itself since the begin of time into all of eternity. Hence, *quasi-periodic* signals are a very important class in practical applications. If a signal repeats itself over a sufficient time, it can be considered to be quasi-periodic and the Fourier series delivers a proper representation. If the signal does not repeat itself over a sufficient time, the Fourier series is not applicable anymore. Such *non-periodic* signals can still be transferred to the frequency domain by applying the Fourier transform. Since there is no periodicity, the signal is represented by a continuous spectrum (in difference to the discrete spectrum for quasi-periodic signals). [19, p. 148]

2.4 Propagation of Electromagnetic Emissions

In this section, the propagation of electromagnetic emissions is discussed. This includes the coupling (conducted or radiated) and the mode (common or differential).

2.4.1 Conducted and Radiated Emissions

Fundamentally, the propagation of emissions can be divided in conducted and radiated. Conducted emissions propagate via conductive structures like wires or metal housings from the EMI source (e.g. power electronic systems) to the EMI victim (e.g. broadcast receivers). To reduce these emissions, EMI filters can be applied (Section 2.5). High-frequency disturbances inside the device and on the wires can also cause radiated emissions. To avoid radiation from the device itself, a shielding enclosure can be applied. To avoid radiation from the wires, the conducted emissions must be reduced. [19, pp. 5-7]

2.4.2 Common Mode vs. Differential Mode

Conducted emissions can be separated in **c**ommon **m**ode (CM) and **d**ifferential **m**ode (DM). In Figure 2.1, a two-wire system is considered. These two wires are isolated from ground and conduct the operating currents. The DM disturbances flow through one wire to the EMI victim and through the other wire back to the EMI source. The CM disturbances flow through the ground plane to the EMI victim and through both wires back to the EMI source. [19, pp. 381-382]

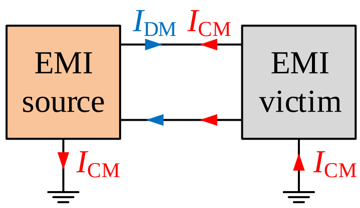

Figure 2.1: Differential-mode and common-mode disturbances

2.5 Passive Filters as Conventional Solution for Conducted EMI Reduction

A common method to reduce the conducted EMI of electronic systems is to apply passive filters between EMI source (e.g. power electronic system) and EMI victim according to Figure 2.2 [19, pp. 385-388]. For the sake of simplicity, it is assumed that there is only one current conducting line with the ground plane as return conductor. Therefore, there are only differential-mode disturbances and the passive EMI filter requires only two ports (however, there are also filters with more ports for more complex systems [19, pp. 388-390]). On the one side, there are the disturbances V_{EMI} of the EMI source and, on the other side, there are the **res**idual disturbances V_{res}. In power electronics, the actually desired signal is often either DC or a very low frequency (e.g. of up to 200 Hz). Switching frequencies are often in the range of tens to hundreds of kHz. Therefore, the passive EMI filter must usually have a low-pass characteristic for these systems.

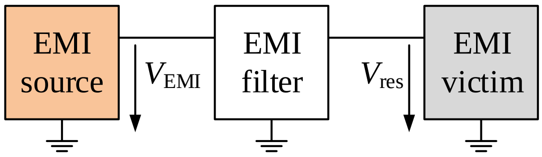

Figure 2.2: Generic passive EMI filter

In most practical applications, passive EMI filters are designed and integrated into the device. The disturbances are diverted from the EMI victim by adding paths with low or high impedances. These paths are created by reactive elements, namely capacitors and inductors. Resistors would lead to significant additional power losses and are usually no viable solution. One common topology is the so called π-filter that is exemplary depicted in Figure 2.3 [19, p. 388-390]. In this structure, there are basically two relevant current dividers. In the first, the disturbing current is split between the left capacitance (low high-frequency impedance) and the inductance (high high-frequency impedance). Hence, most of the current flows through the capacitance back to the EMI source. The remaining current of the inductance is divided by the impedances of the right capacitance and the EMI victim. Ideally, also most of this current flows through the capacitance back to the source. Therefore, the disturbing current at the EMI victim is significantly reduced.

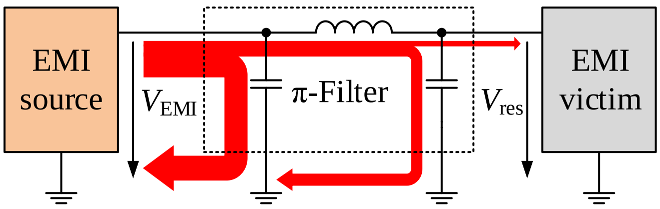

Figure 2.3: Exemplary passive π-filter

As stated before, this π-filter is only an example for passive EMI filters. Usually, the topology is selected in regard to the specific application. In many cases, one filter stage is not enough to achieve the necessary EMI attenuation. To resolve this issue, it is not uncommon that, e.g., two π-filters are installed in series. The here shown π-filter dampens only differential-mode emissions. If there are also common-mode emissions (e.g. isolated two-wire or three-wire systems), a passive filter with more ports must be applied (e.g. [19, pp. 388-390]). So, passive EMI filters can become quite complex due to the necessity of numerous reactive components.

Since the capacitors must withstand the operating voltages without breakdown and the inductors must conduct the operating currents without saturation effects or overheating, these elements tend to considerable sizes. Capacitances against ground are often limited by legal regulations due to safety reasons [19, p. 390]. Thus, it is often necessary to introduce inductors with relatively high inductance values to achieve a required attenuation.

In many cases, passive EMI filters become quite large and take up much of the overall volume of the power electronic system. There are potentially high volume, weight and cost savings if the passive filtering effort can be reduced. This is the main motivation for the investigation of active EMI cancellation techniques.

3 Generic Description for Active EMI Cancellation Systems

In this chapter, a generic description for active EMI cancellation systems is derived that will be used throughout this thesis. While passive EMI filters use reactive components to attenuate the EMI, active cancellation systems aim at a destructive interference between the disturbances and an injected signal. This cancellation signal can be generated and injected by analog and/or digital circuitry. At first, a generic description for single-port cancellation systems is developed. Ideal cancellation signals are determined and the effects of deviations in amplitude, phase and frequency are investigated. Afterward, the description is extended for multi-port systems.

3.1 Single-Port Active EMI Cancellation Systems

In this section, a generic topology for single-port cancellation systems is introduced. At first, arbitrary disturbing and disturbed electric subsystems are defined that are coupled via one interface port. The subsystems are simplified in regard to their interface port and the active cancellation subsystem is applied in between. The signal propagation of EMI and anti-EMI is described mathematically. To do so, a nodal analysis is done for the complete system. A similar systems-theoretical approach using network theory has also been proposed in [20]. Transfer functions are introduced for a convenient representation of the relevant coupling paths. From this description, the ideal cancellation signals are determined. Effects of the coupling and decoupling circuits are discussed. The influence of amplitude, phase and frequency deviations between EMI and anti-EMI are analyzed.

3.1.1 Generic Topology

In this section, a generic description for systems with multiple EMI sources, multiple EMI victims and one coupling interface port is derived. Here, it is assumed that all elements behave predominantly linear. Thus, the analysis can be simplified by descriptions in frequency domain. Furthermore, the superposition principle is applicable to EMI and anti-EMI.

a) Disturbing and Disturbed Subsystem

In Figure 3.1, a generic system is shown that consists of a disturbing and a disturbed subsystem. It is assumed that these systems meet at one interface port. The disturbing subsystem contains M EMI sources. These are depicted by Thévenin equivalents with $V_{\mathrm{EMI*,m}}(f)$ and $Z_{\mathrm{EMI*,m}}(f)$ ($m = 1, 2, \ldots, M$). These equivalents are **coup**led to each other and to the interface port by an $(M+1) \times (M+1)$ impedance matrix $\mathbf{Z}_{\mathrm{coup,s}}(f)$ (subscript 's' for **s**ource). The disturbed subsystem contains N EMI victims that are represented by the impedances $Z_{\mathrm{victim*,n}}(f)$ ($n = 1, 2, \ldots, N$). These elements are **coup**led to each other and to the interface port by an $(N+1)\times(N+1)$ impedance matrix $\mathbf{Z}_{\mathrm{coup,v}}(f)$ (subscript 'v' for **v**ictim). The disturbances are defined as voltage drops $V_{\mathrm{EMI}}^{@\mathrm{victim}^*,\mathrm{n}}(f)$ over the victim impedances $Z_{\mathrm{victim}^*,\mathrm{n}}(f)$. For a successful cancellation, all disturbances $V_{\mathrm{EMI}}^{@\mathrm{victim}^*,\mathrm{n}}(f)$ must be suppressed. This can be achieved by cancelling the voltage at the coupling interface port $V_{\mathrm{EMI}}^{@\mathrm{victim}}(f)$ since all disturbances $V_{\mathrm{EMI}}^{@\mathrm{victim}^*,\mathrm{n}}(f)$ can be traced back to it.

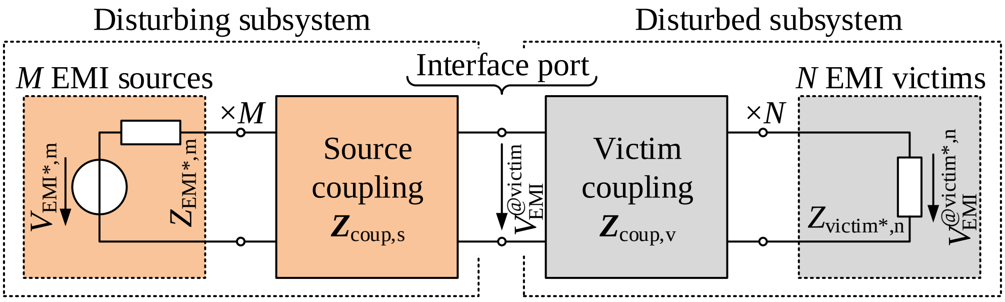

Figure 3.1: Disturbing and disturbed subsystems for one interface port

The disturbing and the disturbed subsystem can be simplified in regard to the interface port using equivalent sources and impedances. The resulting system is depicted in Figure 3.2. The source can be represented by a Thévenin equivalent with $V_{\mathrm{EMI}}(f)$ and $Z_{\mathrm{EMI}}(f)$. The victim is represented by an equivalent impedance $Z_{\mathrm{victim}}(f)$. The actual amount of sources M and victims N is irrelevant since the voltage at the coupling interface port $V_{\mathrm{EMI}}^{@\mathrm{victim}}(f)$ is responsible for all disturbances in the disturbed subsystem. The lower terminal of the interface port is defined as reference ground.

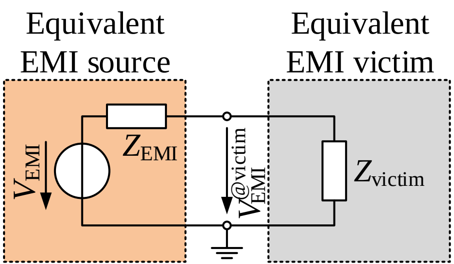

Figure 3.2: Equivalent disturbing and disturbed subsystems for one interface port

b) Introduction of the Cancelling Subsystem

For active EMI cancellation, an injecting circuit and an additional source for the cancellation signal must be introduced. In general, it is no trivial task to find the right position and coupling for the injector. Here, a straight-forward solution is proposed in which the injector is placed at the interface port between the disturbing and disturbed subsystem. The resulting system is depicted in Figure 3.3.

The cancellation source is given as an Thévenin equivalent with $V_{\mathrm{anti}}(f)$ and $Z_{\mathrm{anti}}(f)$. In practical realizations, this could also be a current source. The **inj**ecting circuit can be repre-

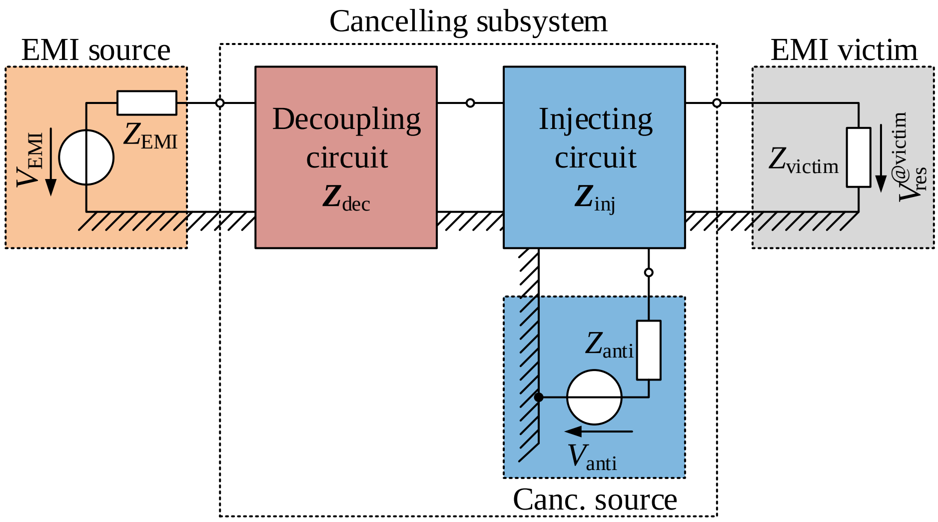

Figure 3.3: Generic topology for single-port active EMI cancellation systems

sented by an arbitrary 3×3 impedance matrix $\mathbf{Z}_{inj}(f)$. As discussed later in Section 4.4.2, typical injecting circuits use capacitors or high-frequency transformers. The coupling between cancellation source and EMI victim should be strong to avoid unnecessarily large cancellation signals. Both EMI and anti-EMI propagate through the overall system and superpose each other. Ideally, there should be a destructive interference at the EMI victim leading to a suppressed, **res**idual EMI $V_{res}^{@victim}(f)$.

Depending on the injecting circuit, the equivalent impedance of the EMI source $Z_{EMI}(f)$ may divert the injected signal away from the actual EMI victim. This is problematic since the cancellation source would need to inject unnecessarily large signals to fulfill the requirements at the EMI victim. To avoid this issue, a decoupling circuit can be used to weaken the coupling to the EMI source. This **dec**oupling circuit can be described by a 2×2 impedance matrix $\mathbf{Z}_{dec}(f)$. It can be realized by using capacitors or inductors (Section 4.4.2).

3.1.2 Mathematical Description and Calculation of the Required Cancellation Signal

In this section, the generic system of Figure 3.3 is described mathematically in regard to the relevant EMI and anti-EMI. The goal is to find a convenient description to calculate the required cancellation signals. At first, a nodal analysis is conducted. Afterward, transfer functions are introduced to simplify the description. Using this description, the ideal cancellation signals are determined. Furthermore, effects of the coupling and decoupling are further discussed.

a) Nodal Analysis

In the following, the system depicted in Figure 3.3 is described by using a nodal analysis. All elements are represented by their admittances $Y(f)$ for convenience. The Thévenin voltage sources are replaced by equivalent Norton current sources. By doing so, the number of nodes is reduced by two. Furthermore, the current sources require no additional rows or columns in the total admittance matrix. The resulting system is depicted in Figure 3.4.

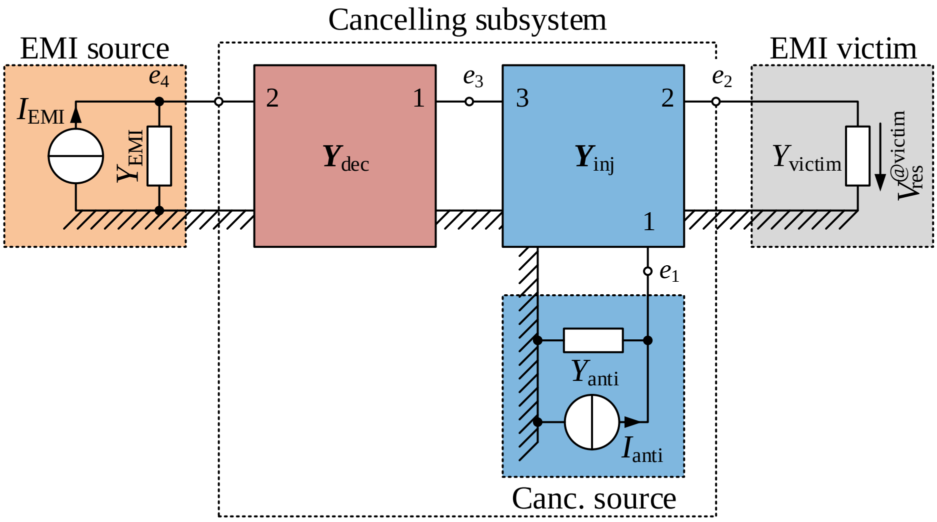

Figure 3.4: Generic topology for single-port active EMI cancellation systems with equivalent current sources for the nodal analysis

The new currents $I_{\mathrm{EMI}}(f)$ and $I_{\mathrm{anti}}(f)$ are defined by (3.1) and (3.2), respectively:

$$I_{\mathrm{EMI}}(f) = Y_{\mathrm{EMI}}(f) \cdot V_{\mathrm{EMI}}(f) \tag{3.1}$$

$$I_{\mathrm{anti}}(f) = Y_{\mathrm{anti}}(f) \cdot V_{\mathrm{anti}}(f) \tag{3.2}$$

By applying the nodal analysis, the description according to (3.3) and (3.4) follows:

$$\boldsymbol{Y}_{\mathrm{total}}(f) \cdot \begin{pmatrix} e_1(f) \\ e_2(f) \\ e_3(f) \\ e_4(f) \end{pmatrix} = \begin{pmatrix} I_{\mathrm{anti}}(f) \\ 0 \\ 0 \\ I_{\mathrm{EMI}}(f) \end{pmatrix} \quad \text{with} \tag{3.3}$$

$$\boldsymbol{Y}_{\mathrm{total}} = \begin{bmatrix} Y_{\mathrm{inj},1,1} + Y_{\mathrm{anti}} & Y_{\mathrm{inj},1,2} & Y_{\mathrm{inj},1,3} & 0 \\ Y_{\mathrm{inj},2,1} & Y_{\mathrm{inj},2,2} + Y_{\mathrm{victim}} & Y_{\mathrm{inj},2,3} & 0 \\ Y_{\mathrm{inj},3,1} & Y_{\mathrm{inj},3,2} & Y_{\mathrm{inj},3,3} + Y_{\mathrm{dec},1,1} & Y_{\mathrm{dec},1,2} \\ 0 & 0 & Y_{\mathrm{dec},2,1} & Y_{\mathrm{dec},2,2} + Y_{\mathrm{EMI}} \end{bmatrix} \tag{3.4}$$

In the next step, the currents $I_{\mathrm{EMI}}(f)$ and $I_{\mathrm{anti}}(f)$ of (3.1) and (3.2) are inserted again. Furthermore, the potential $e_2(f)$ is replaced by the residual voltage $V_{\mathrm{res}}^{@\mathrm{victim}}(f)$. The result is given in (3.5):

$$\overset{(3.3)}{\Rightarrow} \boldsymbol{Y}_{\text{total}}(f) \cdot \begin{pmatrix} e_1(f) \\ V_{\text{res}}^{@\text{victim}}(f) \\ e_3(f) \\ e_4(f) \end{pmatrix} = \begin{pmatrix} Y_{\text{anti}}(f) \cdot V_{\text{anti}}(f) \\ 0 \\ 0 \\ Y_{\text{EMI}}(f) \cdot V_{\text{EMI}}(f) \end{pmatrix} \tag{3.5}$$

For an ideal EMI cancellation, the voltage at the EMI victim $V_{\text{res}}^{@\text{victim}}(f)$ equals 0. Assuming that $\boldsymbol{Y}_{\text{total}}(f)$, $Y_{\text{EMI}}(f)$, $V_{\text{EMI}}(f)$ and $Y_{\text{anti}}(f)$ are known, the necessary cancellation signal $V_{\text{anti}}(f)$ can be calculated. However, there is no simple solution for the description of (3.5). In this case, transfer functions can be used to find a reduced and simplified relationship.

b) Introduction of the Relevant Transfer Functions

In the following, transfer functions are introduced for the relevant coupling paths. To do so, (3.5) is solved to (3.6):

$$\overset{(3.5)}{\Rightarrow} \begin{pmatrix} e_1(f) \\ V_{\text{res}}^{@\text{victim}}(f) \\ e_3(f) \\ e_4(f) \end{pmatrix} = \boldsymbol{Y}_{\text{total}}^{-1}(f) \cdot \begin{pmatrix} Y_{\text{anti}}(f) \cdot V_{\text{anti}}(f) \\ 0 \\ 0 \\ Y_{\text{EMI}}(f) \cdot V_{\text{EMI}}(f) \end{pmatrix} \tag{3.6}$$

Considering (3.6), it can be found that the residual voltage $V_{\text{res}}^{@\text{victim}}(f)$ depends on the EMI $V_{\text{EMI}}(f)$ and anti-EMI $V_{\text{anti}}(f)$. The coupling is described by the admittances of the system. For a simplified description, the following two transfer functions can be derived from (3.6):

- $H_{\text{anti}}^{\rightarrow\text{victim}}(f)$: Propagation of the anti-EMI signal to the victim port
- $H_{\text{EMI}}^{\rightarrow\text{victim}}(f)$: Propagation of the EMI signal to the victim port

The residual EMI $V_{\text{res}}^{@\text{victim}}(f)$ of (3.6) can be rearranged to (3.7) by using the introduced transfer functions. For the sake of transparency, the transfer functions are visualized in Figure 3.5.

$$\overset{(3.6)}{\Rightarrow} V_{\text{res}}^{@\text{victim}}(f) = \underbrace{H_{\text{EMI}}^{\rightarrow\text{victim}}(f) \cdot V_{\text{EMI}}(f)}_{=V_{\text{EMI}}^{@\text{victim}}(f)} + \underbrace{H_{\text{anti}}^{\rightarrow\text{victim}}(f) \cdot V_{\text{anti}}(f)}_{=V_{\text{anti}}^{@\text{victim}}(f)} \tag{3.7}$$

c) Calculation of the Required Cancellation Signal

As stated before, the residual EMI $V_{\text{res}}^{@\text{victim}}(f)$ must equal 0 for an ideal active EMI cancellation. This requirement is stated in (3.8):

$$V_{\text{res}}^{@\text{victim}}(f) \overset{!}{=} 0 \tag{3.8}$$

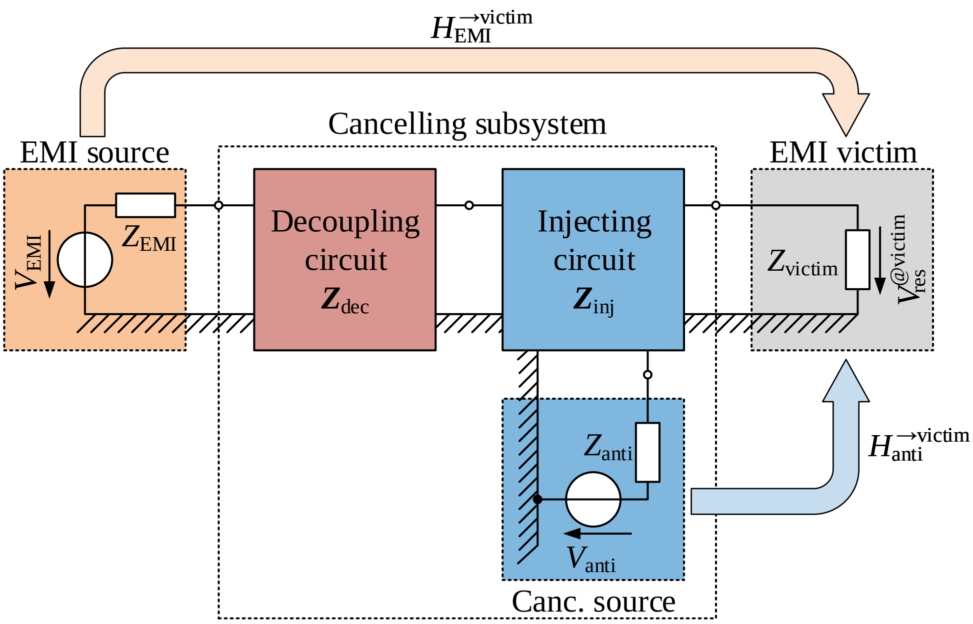

Figure 3.5: Generic topology for single-port active EMI cancellation systems with relevant transfer functions

Using this requirement and (3.7), the ideal cancellation signal $V_{\text{anti}}(f)$ can directly be calculated by (3.9):

$$\overset{(3.7)}{\Rightarrow} V_{\text{anti}}(f) = -\frac{H_{\text{EMI}}^{\rightarrow\text{victim}}(f)}{H_{\text{anti}}^{\rightarrow\text{victim}}(f)} \cdot V_{\text{EMI}}(f) \tag{3.9}$$

Due to the transfer functions, the calculation is widely simplified. Furthermore, the transfer functions enable some interpretations. In general, the cancellation signal $V_{\text{anti}}(f)$ should be as small as possible for an efficient cancellation system. This means that the coupling of the cancellation source to the EMI victim $H_{\text{anti}}^{\rightarrow\text{victim}}(f)$ should be as strong as possible. This can generally be achieved by using large coupling and decoupling elements.

The transfer function $H_{\text{EMI}}^{\rightarrow\text{victim}}(f)$ describes the coupling of the EMI source to the EMI victim. This coupling should be weak to reduce the EMI at the victim $V_{\text{EMI}}^{@\text{victim}}(f)$ that must be cancelled out. The injecting and decoupling circuits introduce some passive attenuation reducing the EMI source's coupling. Although this is not the main purpose of these circuits, it is a positive side effect.

3.1.3 Precision Requirements for the Cancellation Signals

In this section, the requirements for the cancellation signals are discussed to illustrate the necessary precision for a specific EMI reduction. The cancellation signal can deviate in amplitude, phase and frequency. The influence of these deviations on the achievable EMI reduction is analyzed in the following.

a) Amplitude and Phase

The ideal cancellation signal has already been derived by (3.9). Here, it is assumed that the cancellation signal deviates relatively by $a_{\text{dev}} \in \mathbb{R}$ in amplitude and absolutely by $\varphi_{\text{dev}} \in \mathbb{R}$ in phase from the ideal signal. So, (3.10) follows by combining (3.7) and (3.9), and inserting the assumed deviation:

$$V_{\text{res}}^{@\text{victim}}(f) = H_{\text{EMI}}^{\rightarrow\text{victim}}(f) \cdot V_{\text{EMI}}(f) - (1 + a_{\text{dev}}) \cdot e^{j\varphi_{\text{dev}}} \cdot H_{\text{EMI}}^{\rightarrow\text{victim}}(f) \cdot V_{\text{EMI}}(f) \tag{3.10}$$

The achievable active EMI reduction $\Delta V_{\text{dB}}^{@\text{victim}}(f)$ (in dB) can be calculated by setting the EMI at the victim without active cancellation $V_{\text{EMI}}^{@\text{victim}}(f)$ in relation to the residual EMI with active cancellation $V_{\text{res}}^{@\text{victim}}(f)$ according to (3.11):

$$\Delta V_{\text{dB}}^{@\text{victim}}(f) = 20\ \text{dB} \cdot \log_{10} \left| \frac{V_{\text{EMI}}^{@\text{victim}}(f)}{V_{\text{res}}^{@\text{victim}}(f)} \right| \tag{3.11}$$

Note that this value only represents the active cancellation performance of the system. The additional passive attenuation of the injecting and decoupling circuits comes on top. After some solving, (3.12) and (3.13) follow for the active EMI reduction $\Delta V_{\text{dB}}^{@\text{victim}}(f)$. This value is independent from the frequency f.

$$\Rightarrow \Delta V_{\text{dB}}^{@\text{victim}} = 20\ \text{dB} \cdot \log_{10} \left| \frac{1}{1 - (1 + a_{\text{dev}}) \cdot e^{j\varphi_{\text{dev}}}} \right| \tag{3.12}$$

$$= -10\ \text{dB} \cdot \log_{10} \left(a_{\text{dev}}^2 + 4 \cdot (1 + a_{\text{dev}}) \cdot \sin^2\left(\frac{\varphi_{\text{dev}}}{2}\right) \right) \tag{3.13}$$

In Figure 3.6, the achievable EMI reduction is depicted in regard to different relative amplitude deviations a_{dev} and absolute phase deviations φ_{dev}. Here, only positive amplitude deviations are depicted. The negative amplitude deviations cause basically the same EMI reduction in the considered parameter range.

If there are no amplitude or phase deviations, the anti-EMI matches exactly with the EMI. Therefore, the achievable EMI reduction is infinite. In practical realizations, there will always be some deviation. It can be found that small deviations degrade the cancellation performance significantly. Amplitude deviations of 1% and phase deviations of 0.5° will lead to an EMI reduction of 40 dB. To achieve an EMI reduction of, e.g., 60 dB, the amplitude and phase deviations must be below 0.1% and 0.05°, respectively. So, extremely precise cancellation signals are necessary for convincing results. This leads to very high requirements for the cancellation signal generation.

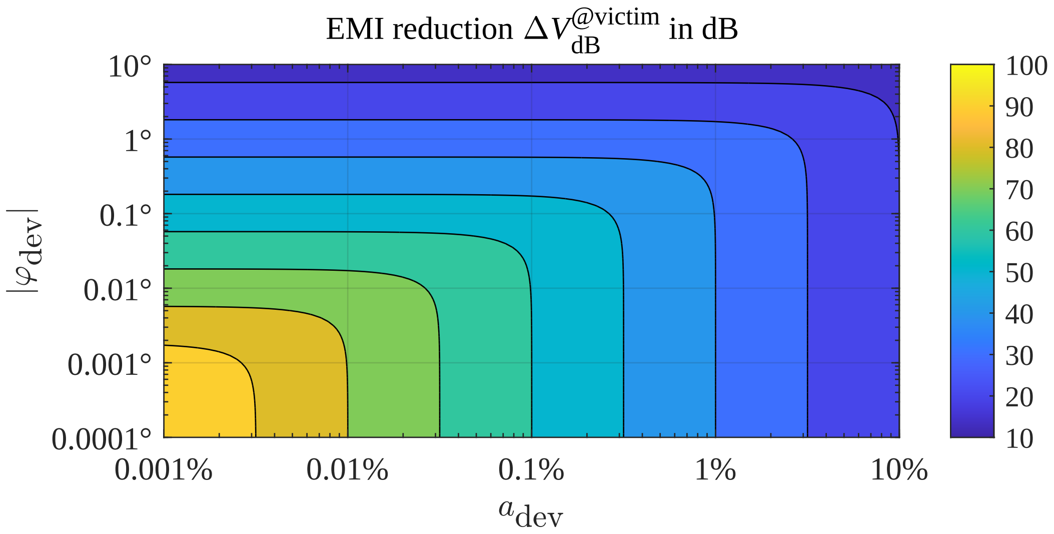

Figure 3.6: Achievable active EMI reduction for different amplitude and phase deviations

b) Frequency

Frequency deviations can be a severe issue for active cancellation systems [21, co-author]. In this section, the resulting limitations are analyzed. To do so, the voltages are described in time domain. For the sake of simplicity, the signals are considered at the victim. By doing so, the transfer functions can be neglected. The disturbance signal $v_{\mathrm{EMI}}^{@\mathrm{victim}}(t,f)$ is defined by (3.14) with $A \in \mathbb{R}^+ \setminus \{0\}$ and $\varphi \in \mathbb{R}$:

$$v_{\mathrm{EMI}}^{@\mathrm{victim}}(t,f) = A \cdot e^{j2\pi f \cdot t + j\varphi} \tag{3.14}$$

The amplitude of the cancellation signal must be the inverse of the disturbance and the phase must be the same. It is assumed that there is a frequency deviation f_{dev} in the cancellation signal. The signals (3.15)-(3.17) result:

$$v_{\mathrm{anti}}^{@\mathrm{victim}}(t,f) = -A \cdot e^{j2\pi(f+f_{\mathrm{dev}})\cdot t + j\varphi} \tag{3.15}$$

$$v_{\mathrm{res}}^{@\mathrm{victim}}(t,f) = v_{\mathrm{EMI}}^{@\mathrm{victim}}(t,f) + v_{\mathrm{anti}}^{@\mathrm{victim}}(t,f) \tag{3.16}$$

$$\Rightarrow \; v_{\mathrm{res}}^{@\mathrm{victim}}(t,f) = A \cdot e^{j2\pi f \cdot t + j\varphi} - A \cdot e^{j2\pi(f+f_{\mathrm{dev}})\cdot t + j\varphi} \tag{3.17}$$

Due to the frequency deviation, EMI and anti-EMI may be in phase at first, but drift apart over time. To find the momentary EMI reduction $\Delta v_{\mathrm{dB}}^{@\mathrm{victim}}(t,f)$, (3.18) is introduced:

$$\Delta v_{\mathrm{dB}}^{@\mathrm{victim}}(t,f) = 20\ \mathrm{dB} \cdot \log_{10} \left| \frac{v_{\mathrm{EMI}}^{@\mathrm{victim}}(t,f)}{v_{\mathrm{res}}^{@\mathrm{victim}}(t,f)} \right| \tag{3.18}$$

The absolute values of the signals $v_{\text{EMI}}^{\text{@victim}}(t,f)$ and $v_{\text{res}}^{\text{@victim}}(t,f)$ are calculated by (3.19)-(3.25):

$$\left|v_{\text{EMI}}^{\text{@victim}}(t,f)\right| = \left|A \cdot e^{j2\pi f \cdot t + j\varphi}\right| \tag{3.19}$$

$$= |A| \cdot \underbrace{\left|e^{j2\pi f \cdot t + j\varphi}\right|}_{=1} \tag{3.20}$$

$$= A \tag{3.21}$$

$$\left|v_{\text{res}}^{\text{@victim}}(t,f)\right| = \left|A \cdot e^{j2\pi f \cdot t + j\varphi} - A \cdot e^{j2\pi (f + f_{\text{dev}}) \cdot t + j\varphi}\right| \tag{3.22}$$

$$= |A| \cdot \underbrace{\left|e^{j2\pi f \cdot t + j\varphi}\right|}_{=1} \cdot \left|1 - e^{j2\pi f_{\text{dev}} \cdot t}\right| \tag{3.23}$$

$$= A \cdot \left|1 - e^{j2\pi f_{\text{dev}} \cdot t}\right| \tag{3.24}$$

$$= A \cdot \sqrt{2 - 2 \cdot \cos\left(2\pi f_{\text{dev}} \cdot t\right)} \tag{3.25}$$

After inserting and some more solving, (3.26) follows:

$$\overset{(3.18)}{\Rightarrow} \Delta v_{\text{dB}}^{\text{@victim}}(t) = -10\ \text{dB} \cdot \log_{10}\left(2 - 2 \cdot \cos\left(2\pi f_{\text{dev}} \cdot t\right)\right) \tag{3.26}$$

Interestingly, the momentary EMI reduction is independent from the actual frequency f of the EMI. However, there is a dependency on time that is discussed in the following. In Figure 3.7, the momentary EMI reduction is depicted for different frequency deviations f_{dev}.

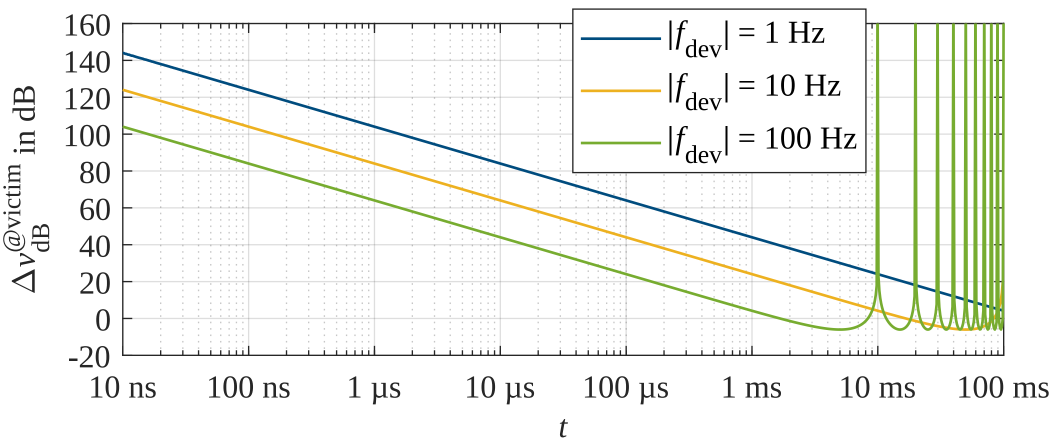

Figure 3.7: Momentary active EMI reduction for different frequency deviations

Assuming that the signals are perfectly in phase for $t = 0$ s, there is theoretically an infinite EMI reduction. Since the anti-EMI drifts apart from the EMI due to the frequency deviation, the momentary EMI reduction declines. It can be found that the momentary EMI reduction increases again at the time 10 ms (and multiples) for a frequency deviation of 100 Hz. At theses times, the cancellation signal is shifted so far that it matches with the disturbances again.

Assuming that a EMI reduction of at least 60 dB should be maintained, it can be found that this value is reached after approximately 1.59 µs for 100 Hz, 15.9 µs for 10 Hz and 159 µs for 1 Hz. So, after very short times, the phase difference between EMI and anti-EMI is too large for the requirement. Since frequency deviations can be a severe issue for active cancellation systems due to the resulting phase shifts, they must be avoided or dealt with in the cancellation method.

3.2 Extension for Multi-Port Active EMI Cancellation Systems

Previously, it has been assumed that the disturbing and disturbed subsystems are connected by only one port. However, in many practical systems, the disturbing and disturbed subsystems are coupled by numerous ports (e.g. due to multiple supply lines of a power electronic system). To account for such systems, the description for a single-port active EMI cancellation system is extended for the multi-port case.

3.2.1 Extended Generic Topology

Assuming P coupling interface ports, the system can be described according to Figure 3.8. In this multi-port case, there are P voltages $V_{\mathrm{EMI}}^{@\mathrm{victim,p}}(f)$ with $p = 1, 2, \ldots, P$ that must be cancelled out.

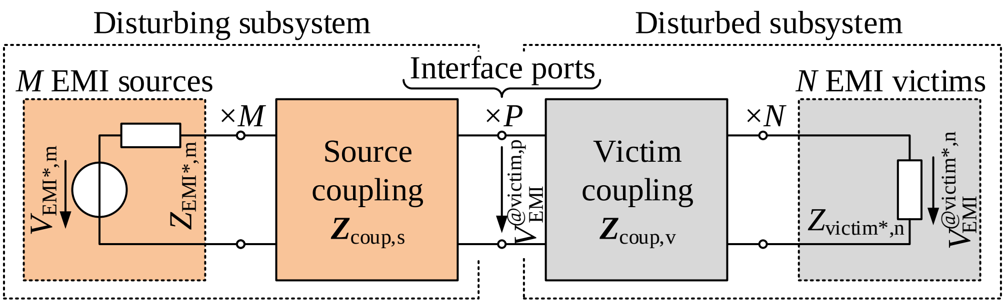

Figure 3.8: Disturbing and disturbed subsystems for P interface ports

Also this system can be simplified in regard to the P coupling interface ports (Figure 3.9). The EMI victim is replaced by a $P \times P$ impedance matrix $\mathbf{Z}_{\mathrm{victim}}(f)$ that describes the coupling between all P ports. The EMI source is replaced by an equivalent $P \times P$ impedance matrix $\mathbf{Z}_{\mathrm{EMI}}(f)$ and P voltage sources $V_{\mathrm{EMI,p}}(f)$. Note that all EMI sources $V_{\mathrm{EMI,p}}(f)$ can potentially be coupled to each other due to the equivalent source impedance $\mathbf{Z}_{\mathrm{EMI}}(f)$. The description of the EMI source is basically a multi-port Thévenin equivalent. All ports are referred to ground.

Also for this multi-port case, the cancellation subsystem can be placed at the interface ports between EMI source and EMI victim (Figure 3.10). Since there are P interface ports, P cancelling sources with $V_{\mathrm{anti,p}}(f)$ and $Z_{\mathrm{anti,p}}(f)$ are applied. The decoupling circuit can be described by a $2P \times 2P$ impedance matrix $\boldsymbol{Z}_{\mathrm{dec}}(f)$. The injecting circuit can be described by a $3P \times 3P$ impedance matrix $\boldsymbol{Z}_{\mathrm{inj}}(f)$. The injecting circuit must be designed in such way that the cancelling subsystem can "reach" all of the EMI victim's interface ports with at least one cancellation source.

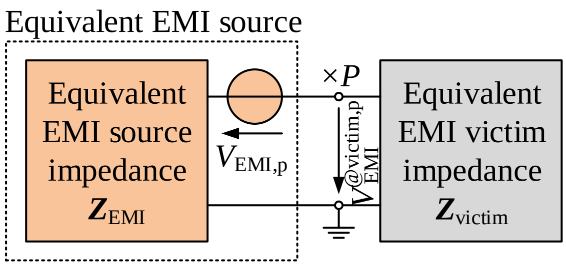

Figure 3.9: Equivalent disturbing and disturbed subsystems for P interface ports

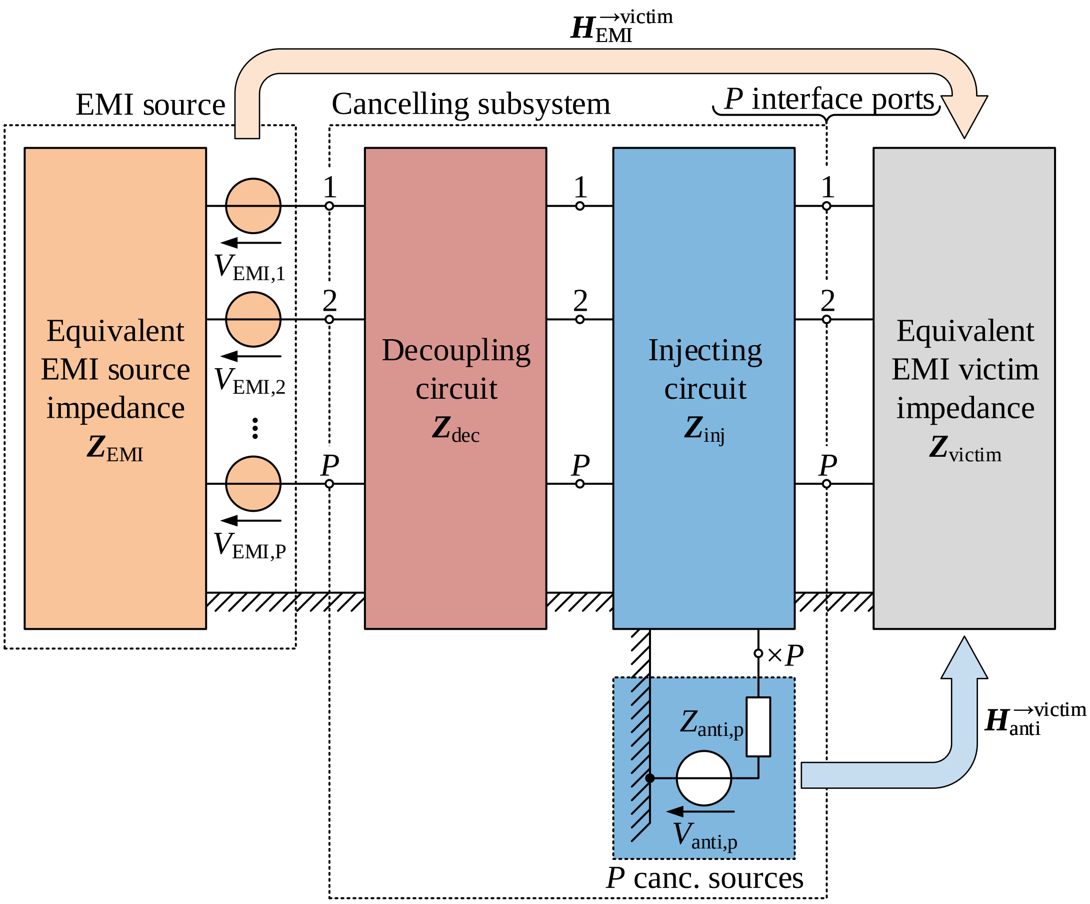

Figure 3.10: Generic topology for multi-port active EMI cancellation systems with relevant transfer matrices

The transfer function $H_{\mathrm{EMI}}^{\rightarrow\mathrm{victim}}(f)$ of the single-port description can be extended to a $P \times P$ transfer matrix $\boldsymbol{H}_{\mathrm{EMI}}^{\rightarrow\mathrm{victim}}(f)$ that describes the coupling of each EMI source to each port of the EMI victim. The transfer function $H_{\mathrm{anti}}^{\rightarrow\mathrm{victim}}(f)$ is extended to a $P \times P$ transfer matrix $\boldsymbol{H}_{\mathrm{anti}}^{\rightarrow\mathrm{victim}}(f)$ that describes the coupling of each cancellation source to each port of the EMI victim. This description enables a convenient calculation of the required signals as shown in the next section.

3.2.2 Extended Mathematical Description and Calculation of the Required Cancellation Signals

Finding the right cancellation signals is no trivial task since all P cancelling sources can be coupled to all P ports of the EMI victim. So, it would be possible that a cancelling source suppresses the EMI at one port, but worsen it at another. To resolve this issue, precise cancellation signals $V_{\mathrm{anti,p}}(f)$ are required that suppress all of the EMI signals at the victim's interface ports and compensate the effects of the other cancellation sources. These signals can be found by using the introduced transfer matrices. A similar description for a four-port system has been published and demonstrated in [17, author].

In analogy to (3.7), the residual EMI at the P interface ports $\vec{V}_{\mathrm{res}}^{\,@\mathrm{victim}}(f)$ can be calculated by (3.27). In this description, all voltages are summarized to respectively denoted vectors.

$$\overset{(3.7)}{\Rightarrow} \vec{V}_{\mathrm{res}}^{\,@\mathrm{victim}}(f) = \underbrace{\boldsymbol{H}_{\mathrm{EMI}}^{\rightarrow\mathrm{victim}}(f) \cdot \vec{V}_{\mathrm{EMI}}(f)}_{=\vec{V}_{\mathrm{EMI}}^{\,@\mathrm{victim}}(f)} + \underbrace{\boldsymbol{H}_{\mathrm{anti}}^{\rightarrow\mathrm{victim}}(f) \cdot \vec{V}_{\mathrm{anti}}(f)}_{=\vec{V}_{\mathrm{anti}}^{\,@\mathrm{victim}}(f)} \tag{3.27}$$

To suppress the EMI in the complete disturbed subsystem, the voltages at the interface ports $\vec{V}_{\mathrm{res}}^{\,@\mathrm{victim}}(f)$ must be cancelled out according to (3.28):

$$\vec{V}_{\mathrm{res}}^{\,@\mathrm{victim}}(f) \overset{!}{=} \vec{0} \tag{3.28}$$

By using this requirement and (3.27), the ideal cancellation signals $\vec{V}_{\mathrm{anti}}(f)$ result from (3.29):

$$\overset{(3.27)}{\Rightarrow} \vec{V}_{\mathrm{anti}}(f) = -\boldsymbol{H}_{\mathrm{anti}}^{\rightarrow\mathrm{victim}^{-1}}(f) \cdot \boldsymbol{H}_{\mathrm{EMI}}^{\rightarrow\mathrm{victim}}(f) \cdot \vec{V}_{\mathrm{EMI}}(f) \tag{3.29}$$

For this solution, the transfer matrix $\boldsymbol{H}_{\mathrm{anti}}^{\rightarrow\mathrm{victim}}(f)$ must be invertible. So, all cancellation sources must be linearly independent. As long as the cancellation sources are not directly coupled, this requirement is fulfilled. However, also partial couplings between the cancellation sources can be problematic since they cause the sources to "work" against each other. As a consequence, the cancellation sources may have to inject unnecessarily large cancellation signals to fulfill the requirements at the EMI victim's ports. While couplings between the cancellation sources can never be completely eliminated, they should be minimized.

In general, the injecting and decoupling circuits should be designed in such way that the cancellation sources are as independent from each other as possible. One pragmatic solution for the injecting circuits is to couple each cancellation source p closely to the respective interface port p. In this case, the intended couplings $H_{\mathrm{anti,p}}^{\rightarrow\mathrm{victim,p}}(f)$ can be found on the main diagonal of the matrix $\boldsymbol{H}_{\mathrm{anti}}^{\rightarrow\mathrm{victim}}(f)$. For an ideal, direct coupling, these entries equal 1. The other entries of the matrix represent the unintended coupling of the cancellation source p to the other interface ports. These entries should ideally equal 0. The unintended coupling may result from, e.g., a parasitic coupling between the injecting circuits or the EMI source's equivalent impedance $\boldsymbol{Z}_{\mathrm{EMI}}(f)$. The parasitic coupling between the injecting circuits may be avoided by appropriate designs. The unintended coupling due to the EMI source's equivalent impedance can be mitigated by appropriate decoupling circuits. If all cancellation sources are ideally coupled to their respective ports and ideally decoupled from the others, the transfer matrix $\boldsymbol{H}_{\mathrm{anti}}^{\rightarrow\mathrm{victim}}(f)$ equals a $P \times P$ identity matrix according to (3.30):

$$\boldsymbol{H}_{\mathrm{anti}}^{\rightarrow\mathrm{victim}}(f) = \boldsymbol{I}_{\mathrm{P}} \tag{3.30}$$

3.3 Chapter Summary

In this section, a generic description for single- and multi-port active EMI cancellation systems has been developed. It has been shown that the number of required cancellation sources depends on the number of interface ports between the disturbing and disturbed subsystem. The actual number of EMI sources or EMI victims within these systems is irrelevant since all signals can be referred to these ports.

The single-port system has been mathematically described by using a nodal analysis. Transfer functions have been introduced for the relevant signal propagation paths. By doing so, the required cancellation signals can conveniently be calculated. Requirements of the decoupling and injecting circuits have been discussed. Furthermore, it has been shown that the cancellation signals must be generated very precisely. An amplitude deviation of 1% or a phase deviation of 0.5° will limit the achievable EMI reduction to 40 dB. To achieve a cancellation performance of 60 dB, amplitude and phase may only deviate by 0.1% and 0.05°, respectively. Frequency deviations must be avoided or dealt with in the cancellation strategy. Otherwise, EMI and anti-EMI will drift apart after very short times.

Last, the single-port description has been extended for the application to multi-port cancellation systems. In this case, one cancellation source is required for each interface port. Since all cancellation sources can potentially be coupled to all ports, the calculation of the right cancellation signals is no trivial task. The introduction of transfer matrices has shown to be a convenient approach to calculate the required signals.

From these general descriptions, the required cancellation signals can be calculated. To find ways to actually generate these signals, various approaches of different disciplines are analyzed in the following. At first, active EMI filters are discussed.

4 Analysis of Active EMI Filter (AEF) Approaches

Active **EMI f**ilters (AEFs) are an established method to actively suppress conducted disturbances. In this chapter, these systems will be analyzed in regard to possible topologies, systematic limitations, fundamental building blocks and results of the literature. AEFs are usually discussed for only one port and only one EMI mode (CM or DM) in the literature.

At first, the basics of AEFs are discussed with a short historic background. Afterward, the fundamental topologies are depicted and analyzed in regard to their systematic limitations. Then, building blocks are summarized that can also be used for the realization of other active EMI cancellation systems. To give an idea of the practical performance of AEFs, numerous demonstrator results are summarized and discussed. The chapter closes with a summary on the insights on AEFs.

4.1 Fundamentals

AEFs are installed on the lines between the EMI source and the EMI victim. This is the same placement as for passive EMI filters and also the same as for the generic active EMI cancellation system of Chapter 3. AEFs use a straight-forward method for signal generation: **F**eed**b**ack (FB) types sense the residual disturbances at the EMI victim, invert the signal, amplify it by the gain G and inject it back into the system at the EMI source (Figure 4.1, top). Due to the closed feedback loop, the residual disturbances at the EMI victim should be minimized. For **f**eed**f**orward (FF) types, the positioning of sensor and injector is swapped and there is no closed feedback loop (Figure 4.1, bottom). [2,22]

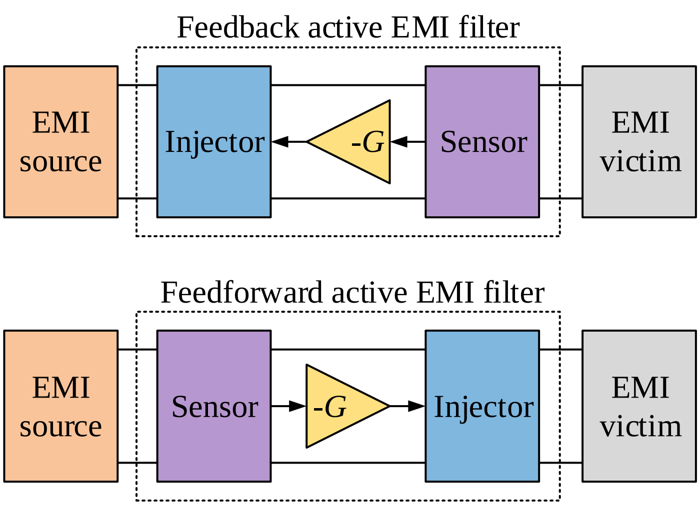

Figure 4.1: Feedback vs. feedforward active EMI filters

So, for the FB and FF signal generation approaches, a sensor and an amplifier must be added to the cancelling subsystem of Figure 3.3. Since AEFs are generally discussed without decoupling circuits in the literature, the respective block is removed. [2, 22]

4.2 Historic Background

AEFs have firstly been scientifically discussed in [1] in 1970. The application is a DC-to-DC converter for spacecrafts. To fulfill the integrity demands of the overall power system, filtering of the power electronic systems is very important. To achieve sufficient EMI attenuations by passive filters (e.g. Figure 4.2a), large capacitances are necessary. Interestingly, the size is not the only problem in this application. To achieve large capacitance values (in the range of microfarads), tantalum capacitors have usually been applied. However, these capacitors tend to fail under the harsh conditions of outer space. So, the usage of these capacitors is not only an issue of size but also of reliability in this application. To solve these problems, passive and active ripple filters (Figure 4.2b) are discussed in [1]. The proposed active ripple filter (Figure 4.2c) is fundamentally an FF AEF that is enhanced by an additional FB loop. It is shown that the capacitance values can be reduced by 98.8% in comparison to a conventional passive filter with the same EMI reduction. By applying this AEF, much less capacitance must be installed and, therefore, more reliable capacitors (e.g. ceramic) can be used. However, the efficiency of the power electronic system is slightly reduced due to the additional power consumption of the AEF. [1]

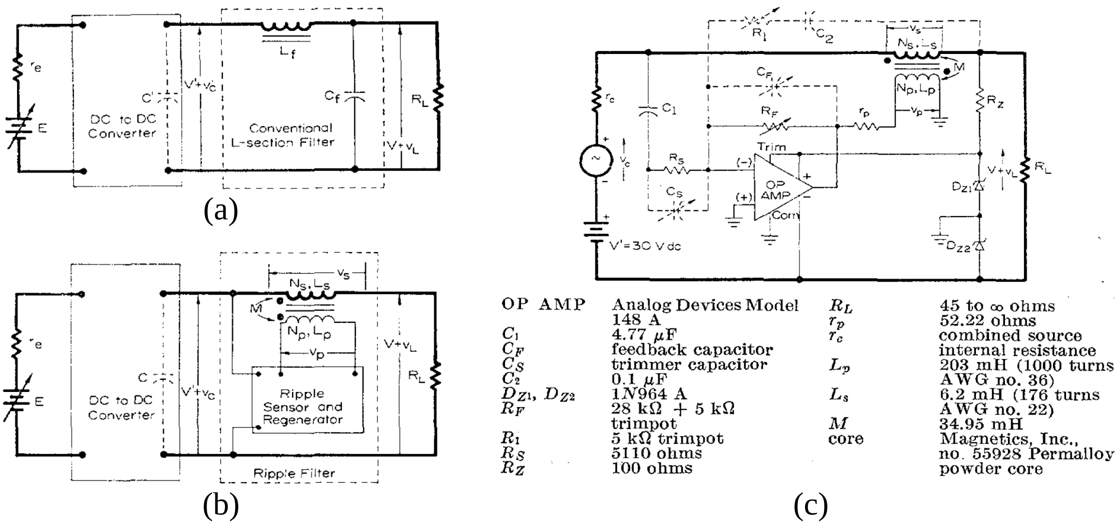

Figure 4.2: Original figures of [1]: (a) conventional passive filter, (b) concept for a “ripple filter”, (c) realized active circuit

The next scientific reports on AEFs came up in the 1980s [6–8]. In [6], an exemplary FB AEF is presented to cancel out the disturbances of switched-mode power supplies. In [7], different topologies of AEFs are investigated to virtually enhance the values of filtering capacitors or inductors. In [8], the four basic FB topologies of AEFs are introduced and analyzed for the first time.

Since the 1990s, there has been a large amount of scientific publications on various aspects and applications of AEFs. The content relevant for this work is categorized and summarized in the following sections.

In the 2000s, a fundamental theory for the topologies of AEFs has been developed. In [22], the AEFs are abstracted and classified. The two basic FF types are added to the theory and the achievable EMI reduction for each topology is calculated. Furthermore, passive circuit realizations are discussed. In [2], active filters are further generalized for the application in EMC and power quality. The achievable EMI reduction and the influence on low frequency (e.g. power-line) impedances are analyzed.

In 2019, the numerous publications on AEFs have been comprehensively summarized in [23].

4.3 Topologies

The topologies are generally divided in FB and FF types. These AEFs are analyzed in regard to their possible configurations and their systematic limitations. The limitations comprise the impedance and gain ratios, the amplifier's frequency-dependent gain and the limited signal propagation speed.

4.3.1 Feedback AEFs

The topologies of AEFs are distinguished by the sensed and injected quantity. There are four topologies for FB AEFs that are also presented in Figure 4.3 [2, 8, 22]:

1. CSVI: **c**urrent **s**ense **v**oltage **i**nject
2. CSCI: **c**urrent **s**ense **c**urrent **i**nject
3. VSCI: **v**oltage **s**ense **c**urrent **i**nject
4. VSVI: **v**oltage **s**ense **v**oltage **i**nject

The voltage injecting topologies compensate the disturbing voltage V_{EMI} by injecting the cancellation voltage V_{anti}. By doing so, the EMI source becomes isolated from the EMI victim (in regard to the high-frequency disturbances) [2]. The current injecting topologies basically reroute the disturbing current from the victim into the AEF by introducing the current I_{anti} [2]. Although only a current or a voltage is sensed, both quantities are equally suppressed. This is due to the direct correlation between $V^{@\mathrm{victim}}$ and $I^{@\mathrm{victim}}$ by the victim's impedance Z_{victim} (assuming a linear system). So, if one quantity is reduced, the other is reduced by the same relative value. In the following, systematic limitations of FB AEFs are analyzed.

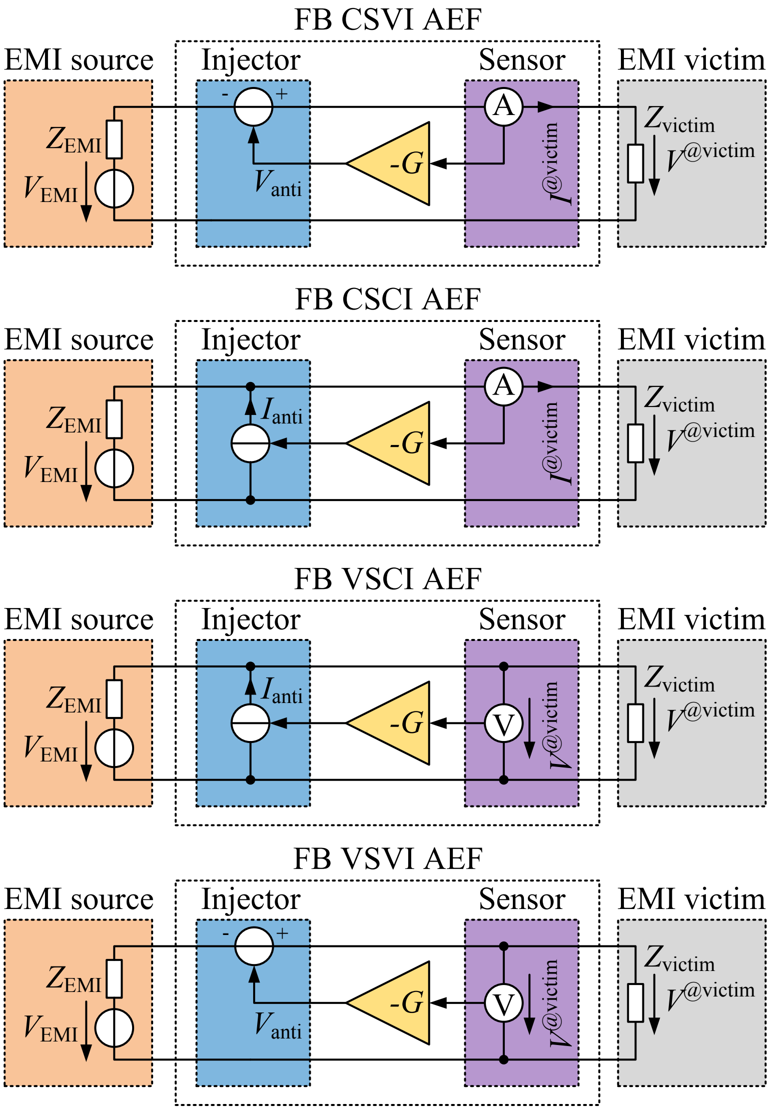

Figure 4.3: Topologies of FB AEFs [2]

a) Limitations due to Impedance and Gain Ratios

The achievable EMI reduction $\Delta V_{\mathrm{dB}}^{\mathrm{@victim}}$ can be calculated by setting $V_{\mathrm{EMI}}^{\mathrm{@victim}}$ (disturbances at victim without active AEF) and $V_{\mathrm{res}}^{\mathrm{@victim}}$ (disturbances at victim with active AEF) according to (4.1) into relation:

$$\Delta V_{\mathrm{dB}}^{\mathrm{@victim}} = 20\ \mathrm{dB} \cdot \log_{10} \left| \frac{V_{\mathrm{EMI}}^{\mathrm{@victim}}}{V_{\mathrm{res}}^{\mathrm{@victim}}} \right| \tag{4.1}$$

The analytical solutions for the achievable EMI reductions are summarized in Table 4.1. Noteworthy, all internal impedances of the sensor, injector and amplifier are neglected at this point. So, the AEF is ideal except for its gain G. [2]

It can be found that the performance of all FB AEFs depends on the gain G of the amplifier and the impedances of the system. From a systematic point of view, it would be beneficial

Topology	Reduction $\Delta V_{\mathrm{dB}}^{\mathrm{@victim}}$	Condition for maximum $\Delta V_{\mathrm{dB}}^{\mathrm{@victim}}$
FB CSVI	$20\ \mathrm{dB} \cdot \log_{10} \left\| 1 + \frac{1}{Z_{\mathrm{EMI}} + Z_{\mathrm{victim}}} \cdot G \right\|$	$\|G\| \gg \|Z_{\mathrm{EMI}} + Z_{\mathrm{victim}}\|$
FB CSCI	$20\ \mathrm{dB} \cdot \log_{10} \left\| 1 + \frac{Z_{\mathrm{EMI}}}{Z_{\mathrm{EMI}} + Z_{\mathrm{victim}}} \cdot G \right\|$	$\|Z_{\mathrm{EMI}}\| \gg \|Z_{\mathrm{victim}}\|$
FB VSCI	$20\ \mathrm{dB} \cdot \log_{10} \left\| 1 + \frac{1}{Y_{\mathrm{EMI}} + Y_{\mathrm{victim}}} \cdot G \right\|$	$\|G\| \gg \|Y_{\mathrm{EMI}} + Y_{\mathrm{victim}}\|$
FB VSVI	$20\ \mathrm{dB} \cdot \log_{10} \left\| 1 + \frac{Z_{\mathrm{victim}}}{Z_{\mathrm{EMI}} + Z_{\mathrm{victim}}} \cdot G \right\|$	$\|Z_{\mathrm{victim}}\| \gg \|Z_{\mathrm{EMI}}\|$

Table 4.1: Analytical solution for the performance of the four FB AEFs [2]

to separate signal generation, injector and sensor from each other and to analyze them individually. However, this is not possible for AEFs since the theoretical performance always depends on the complete setup. This is why each individual topology must be discussed.

For **FB CSVI AEFs**, the amplifier's gain should be much larger than the sum of the source and victim impedances [2]. This can be problematic if the EMI source is close to an ideal current source and/or if the victim is close to an open port. This effect can be understood by considering Figure 4.3. If Z_{EMI} is an open port, there are no disturbances affecting the victim. So, there are no disturbances that can be suppressed by the AEF and the EMI reduction drops to 0 dB. If Z_{victim} is an open port (and Z_{EMI} is not), V_{EMI} equals $V_{\mathrm{EMI}}^{\mathrm{@victim}}$. In this case, there can be significant voltage disturbances, but no currents $I_{\mathrm{EMI}}^{\mathrm{@victim}}$ flow (due to the open circuit). Therefore, no disturbances can be detected and no cancellation signal is generated. This is why FB CSVI AEFs fail for high victim impedances.

For **FB CSCI AEFs**, the source impedance should be much larger than the victim impedance [2]. This effect can easily be understood by considering the current divider for the cancellation current I_{anti}. The current is divided by Z_{EMI} and Z_{victim}. It should flow to the EMI victim so that the cancellation can take effect. So, the impedance of the victim must be lower than the one of the source. If the impedance of the source is too low, the cancellation current is diverted into the EMI source and causes only little cancellation at the victim.

For **FB VSCI AEFs**, the amplifier's gain should be much larger than the sum of the source and victim admittances for best results [2]. This causes issues if the EMI source is close to an ideal voltage source or if the victim is close to a short. If Y_{victim} is a short, there are no voltage disturbances at the victim. So, the FB VSCI AEF cannot measure any disturbances, even though there may be significant current disturbances flowing through the victim. If Y_{EMI} is a short (ideal voltage source), V_{EMI} equals $V_{\mathrm{EMI}}^{\mathrm{@victim}}$. So, the disturbances can be measured by the AEF. The cancellation current I_{anti} is divided between the EMI source and victim. Assuming the EMI source to be an ideal voltage source, it diverts all of the injected cancellation current away from the EMI victim. Therefore, the AEF has no cancellation effect at the EMI victim.

For **FB VSVI AEFs**, the impedance of the EMI victim should be much larger than the impedance of the source [2]. For understanding, the voltage divider for the cancellation source V_{anti} is discussed. The cancelling voltage is divided by the impedances Z_{EMI} and Z_{victim}. Since the cancelling signal must take effect at the EMI victim, its impedance must be higher than the one of the source.

If the source impedance is too large or too small, it could be altered by adding a decoupling circuit as discussed in Chapter 3. For example, the performance of the FB CSCI topology could be improved by adding a series inductance between EMI source and AEF [24]. If the victim impedance is too large for the FB CSCI topology, [24] proposes the introduction of a parallel capacitance at the EMI victim.

The consideration of the system's impedances is very important since it has a large impact on the achievable EMI reduction. Until now, it is assumed that the FB AEF is stable. However, this is not always the case. The amplifier may be intrinsically instable, and the impedances of source, victim, sensor and injector may also negatively affect the stability. Stabilizing the feedback loop is an essential step in the design of FB AEFs, but it can be a limiting factor for the performance [22, 25, 26]. This problem becomes even worse if parameter variations or changing impedances are considered since the designed FB AEF must be stable and effective for all possible configurations.

b) Limitations due to Amplifier's Gain

In the following, the systematic limitations due to the amplifier's gain are discussed. The maximum EMI reduction $\Delta V_{\text{dB}}^{\text{@victim}}(f)$ can be achieved if the conditions of Table 4.1 are fulfilled. Considering each topology individually, the achievable EMI reduction can be described by (4.2). So, under the assumption of an ideal system, the achievable EMI reduction directly depends on the gain of the amplifier.

$$\Delta V_{\text{dB}}^{\text{@victim}}(f) = 20\text{ dB} \cdot \log_{10} |1 + G(f)| \tag{4.2}$$

For further analysis, the amplifier is assumed to be an analog device consisting of, e.g., bipolar transistors [27, p. 281]. The high-frequency gain of these devices is usually limited by time constants that result from internal capacitances [27, p. 385 ff.]. The frequency response can be described by a first order low-pass filter according to (4.3) where G_0 is the amplification at very low frequencies (or DC) and f_{c} is the -3 dB cutoff frequency [27, p. 384]. For frequencies above cutoff, the gain drops with 20 dB per decade. For later use, the absolute value of the gain is calculated in (4.4).

$$G(f) = \frac{G_0}{1 + jf/f_{\text{c}}} \tag{4.3}$$

$$\Rightarrow |G(f)| = \frac{G_0}{\sqrt{1+f^2/f_c^2}} \tag{4.4}$$

To give an idea of the technological limitations, some exemplary **op**erational **amp**lifiers (OpAmps) are considered (Table 4.2) that have already been mentioned or used in publications on AEFs. The uA741 is a general purpose OpAmp going back to a design from 1968. The other elements are more recent and designed for, e.g., video applications. The low-frequency (or DC) gains G_0 are extracted from data sheets. The values of the cutoff frequency f_c are usually not directly given in the data sheets. However, the so-called unity-gain bandwidth can be used that is defined as the frequency f_{unity} at which the absolute value of the gain $|G(f)|$ drops to 1 (unity, 0 dB). This value also directly equals the gain-bandwidth product that can often be found in data sheets. The cutoff frequencies f_c are calculated by using (4.4), G_0 and $\left|G(f = f_{unity})\right| = 1$.

OpAmp	G_0	f_{unity}	f_c	Reference
uA741 [28]	200.000 $\approx$ 106 dB	1 MHz	5 Hz	Mentioned in [29]
LM6172 [30]	20.000 $\approx$ 86 dB	100 MHz	5 kHz	Used in [31,32]
AD829 [33]	100.000 $\approx$ 100 dB	750 MHz	7.5 kHz	Used in [24,34,35]
OPA847 [36]	80.000 $\approx$ 98 dB	3.9 GHz	49 kHz	Used in [37]

Table 4.2: Relevant specifications of exemplary OpAmps

The equations (4.2), (4.3) and the values of Table 4.2 are used to calculate the achievable EMI reduction $\Delta V_{dB}^{@victim}(f)$ for the four exemplary OpAmps. The results are depicted in Figure 4.4. All OpAmps show the best performance for lower frequencies due to the declining magnitude response of the gain $G(f)$. Although the uA741 has the highest G_0, it shows the worst performance in the considered frequency range. This is due to the fact that the cutoff frequency f_c is extremely low. The other OpAmps have a lower G_0, but their cutoff frequencies are much higher. Therefore, they show a much better performance in the considered frequency range. In this comparison, the OPA847 enables the highest EMI reduction. Characteristic values are 91 dB at 100 kHz and 42 dB at 30 MHz.

For a better understanding of the influence of the OpAmps' frequency-dependent gain, the time-domain signals are depicted in the following. As an example, the FB VSVI topology is considered. It is assumed that the condition for maximum EMI reduction is still valid. Considering the schematic of Figure 4.3, (4.5) can be derived (note $|Z_{victim}| \gg |Z_{EMI}|$). For the cancellation signal (4.6)-(4.8) follow.

$$V_{res}^{@victim}(f) = V_{EMI}(f) + V_{anti}(f) \tag{4.5}$$

$$V_{anti}(f) = -G(f) \cdot V_{res}^{@victim}(f) \tag{4.6}$$

$$= -G(f) \cdot (V_{EMI}(f) + V_{anti}(f)) \tag{4.7}$$

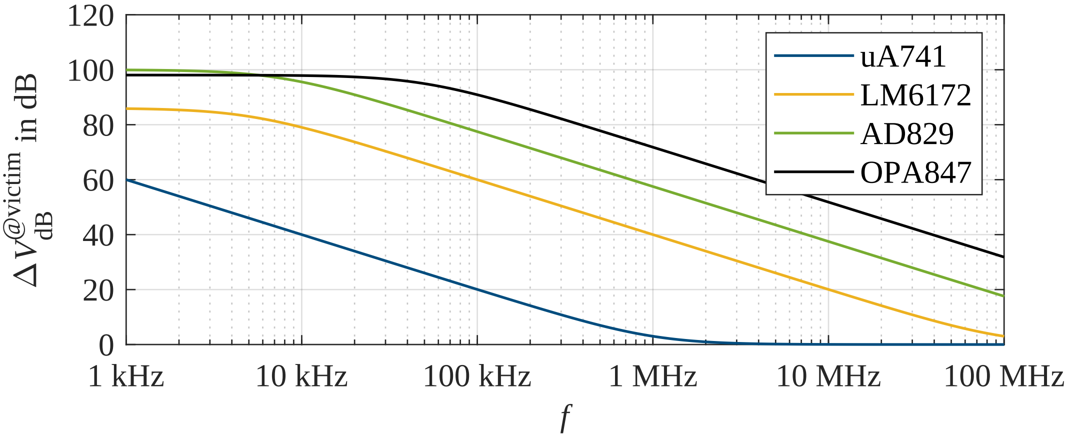

Figure 4.4: Theoretical performance of FB AEFs for exemplary OpAmps

$$\Rightarrow V_{\mathrm{anti}}(f) = -\frac{G(f)}{1+G(f)} \cdot V_{\mathrm{EMI}}(f) \tag{4.8}$$

The time-domain signals of anti-EMI and residual EMI are calculated by the following procedure: At first, the time-domain EMI $v_{\mathrm{EMI}}(t)$ is transferred to the frequency domain ($V_{\mathrm{EMI}}(f)$) and used to calculate the anti-EMI $V_{\mathrm{anti}}(f)$ by (4.8). By using (4.5), the residual EMI $V_{\mathrm{res}}^{@\mathrm{victim}}(f)$ is found. The time-domain signals $v_{\mathrm{anti}}(t)$ and $v_{\mathrm{res}}^{@\mathrm{victim}}(t)$ are determined from the respective complex spectra by using (2.8).

As an example, the frequency-dependent gain $G(f)$ of the OpAmp uA741 is considered. The EMI $v_{\mathrm{EMI}}(t)$ is a PWM signal with a fundamental frequency of 100 kHz, a relative pulse width of 25%, an amplitude of 0.9 V and no DC component. The time-domain signals are depicted in Figure 4.5. If the EMI's voltage jumps, the anti-EMI starts to rise or fall. The corresponding slew rate is fundamentally limited by the time constant of the amplifier (that is directly linked to its bandwidth). Due to this effect, spikes remain in the residual EMI. These spikes contain high-frequency contents. This is plausible since FB AEFs are most effective at lower frequencies (see also Figure 4.4) since the amplifiers show a low-pass characteristic according to (4.3). By improving the slew rate, the spikes in the residual EMI can be reduced leading to a better high-frequency performance. This can be achieved by advances in the design and technology of amplifiers.

c) Limitations due to Finite Signal Propagation Speed

The amplifier's gain is not the only limitation in FB AEFs. Another systematic limitation is the finite propagation speed of electrical signals that is at most the speed of light c_0. Due to the resulting delay, EMI and anti-EMI will never be exactly simultaneous. In the following, the consequences of this effect are discussed.

As depicted in Figure 4.6, the propagation delay t_{d} is defined by the time the signal needs to propagate from sensor through amplifier through injector back to sensor. The delay time

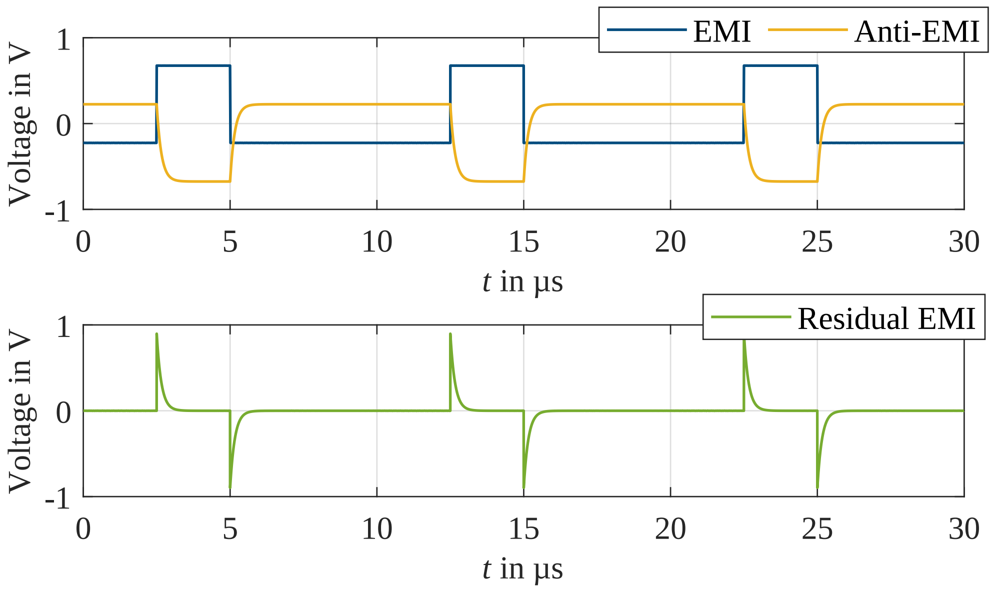

Figure 4.5: Theoretical time-domain signals for an FB VSVI AEF with uA741

can be estimated by considering the geometrical length of the signal loop l_{loop} according to (4.9):

$$t_{\text{d}} \geq \frac{l_{\text{loop}}}{c_0} \tag{4.9}$$

It can be expected that these lengths are in the range from a few centimeters to a few decimeters. One centimeter causes a propagation delay of at least 33 ps. The propagation delay of one decimeter is already over 333 ps. These values may appear insignificant, but they are actually very relevant for the performance of AEFs as shown in the following.

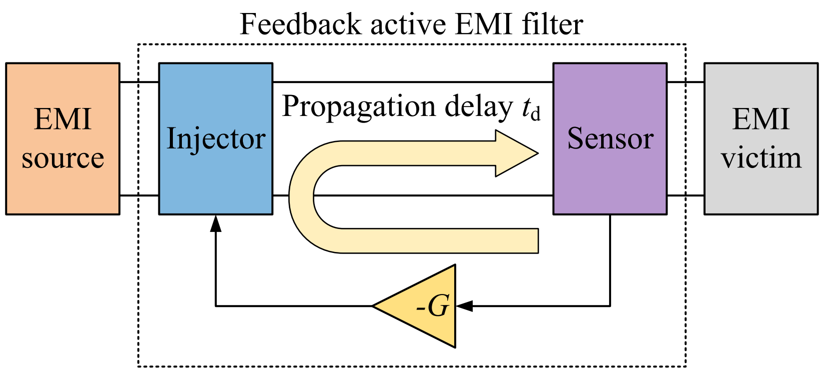

Figure 4.6: Systematic signal propagation delay in FB AEFs

It is assumed that the conditions for a maximum EMI reduction are still fulfilled (Table 4.1). So, the simplification of (4.2) still holds true. In this analysis, only the influence of the propagation delay shall be analyzed. To do so, it is assumed that the amplifier's absolute gain is not deteriorated by its frequency response. Thus, $|G(f)|$ equals G_0 over the complete frequency range. The propagation delay introduces a phase shift according to (4.10):

$$G_{\text{delayed}}(f) = G_0 \cdot e^{-j2\pi f \cdot t_{\text{d}}} \tag{4.10}$$

Delay times can generally lead to instable feedback loops [38, p. 449]. For an evaluation of the stability, the Nyquist stability criterion can be applied. This criterion says that there must be a positive **p**hase **m**argin (PM, defined by (4.11)) for the frequency f_{x} at which the absolute value of the open-loop transfer function $G_{\text{delayed}}(f)$ meets unity (according to (4.12)) [38, p. 453]. The condition of (4.12) is fulfilled for all $f_{\text{x}} \in \mathbb{R}^+ \setminus \{0\}$ if G_0 equals 1. However, the requirement of (4.11) is only fulfilled for $f_{\text{x}} < 1/(2 \cdot t_{\text{d}})$. So, the FB AEF will be instable for all delay times (no matter how small) and it must be stabilized.

$$\text{PM} = \pi + \angle G_{\text{delayed}}(f_{\text{x}}) \overset{!}{>} 0 \tag{4.11}$$

$$\text{for } \left|G_{\text{delayed}}(f_{\text{x}})\right| \overset{!}{=} 1 \tag{4.12}$$

The feedback loop can be stabilized by introducing an integrating element. Therefore, the open-loop transfer function is changed to (4.13) and (4.14).

$$G_{\text{delayed}}(f) = G_0 \cdot \frac{1}{j2\pi f} \cdot e^{-j2\pi f \cdot t_{\text{d}}} \tag{4.13}$$

$$= \frac{G_0}{2\pi f} \cdot e^{-j2\pi f \cdot t_{\text{d}} - j\pi/2} \tag{4.14}$$

The condition of (4.12) is fulfilled for (4.15):

$$\overset{(4.12)}{\Rightarrow} \quad f_{\text{x}} = \frac{G_0}{2\pi} \tag{4.15}$$

With this information, the requirement of (4.11) can be solved to (4.16) and (4.17):

$$\overset{(4.11)}{\Rightarrow} \quad \text{PM} = \pi - 2\pi \frac{G_0}{2\pi} \cdot t_{\text{d}} - \frac{\pi}{2} \tag{4.16}$$

$$= \frac{\pi}{2} - G_0 \cdot t_{\text{d}} \overset{!}{>} 0 \tag{4.17}$$

To ensure that the PM is larger than 0, the gain G_0 must be adjusted depending on the propagation delay t_{d}. In theory, a PM of 0 would be enough for a stable feedback loop. Nevertheless, higher PM are beneficial since oscillations can be reduced [38, p. 454]. A typical value for the PM is $60° \mathrel{\widehat{=}} \pi/3$ [38, p. 454]. Using (4.17), the necessary value of the gain G_0 can be calculated by (4.18):

$$\Rightarrow G_0(t_{\text{d}}) = \frac{\pi}{6 \cdot t_{\text{d}}} \tag{4.18}$$

The achievable EMI reduction for different propagation delays is calculated by using (4.2), (4.14) and (4.18) and depicted in Figure 4.7. It can be found that these propagation delays pose a significant limitation to FB AEFs. Due to the integrating element, the achievable EMI reduction declines for increasing frequencies. Considering the propagation delay of 1 ns, the FB AEF reaches unity (0 dB) at approximately 83 MHz. For frequencies around 180 MHz, the disturbances are amplified by approximately 4 dB. This effect becomes worse for smaller PMs. For very high frequencies, the achievable EMI reduction closes in on 0 dB.

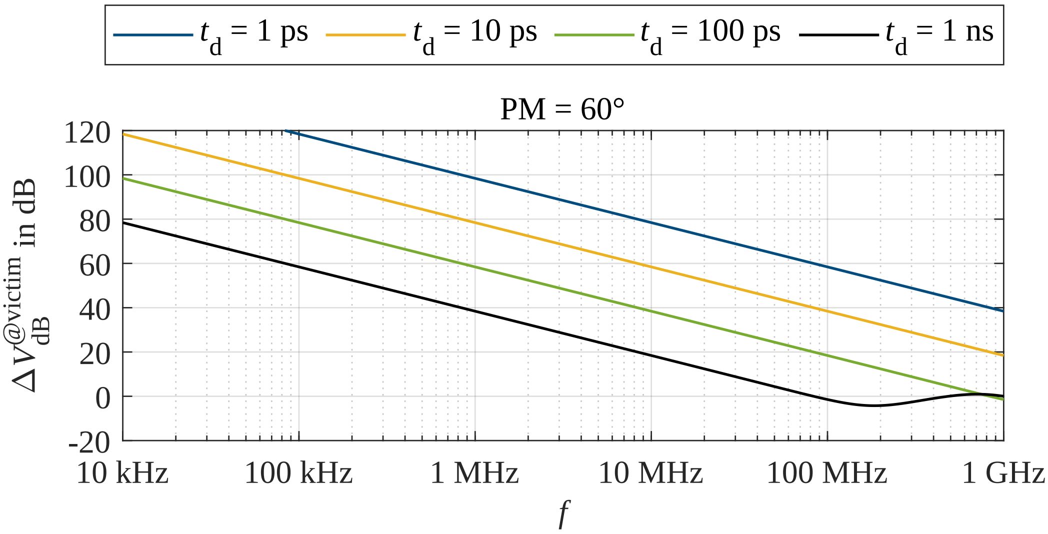

Figure 4.7: Theoretical performance of FB AEFs for different propagation delays

For a reasonable propagation delay of 100 ps (loop length of approximately 3 cm), the achievable EMI reduction will be limited to 78 dB at 100 kHz and 29 dB at 30 MHz. Considering the results of Figure 4.4 for the different OpAmps, it can be found that the FB AEF using OPA847 would already be limited by the propagation delay of the signals. In this case, an improvement of the OpAmp's gain would be of no use. Since the propagation speed of the signals cannot be increased, the only option is to minimize the geometrical length of the signal's path. This could be done by, e.g., integration and miniaturization.

To give an idea of the influence of delay times, the time-domain signals in the FB VSVI topology are discussed again by using the same procedure as in the example of Section 4.3.1.b). The amplifiers frequency-dependent gain is calculated according to (4.14) and (4.18). It is assumed that the signal loop l_{loop} has a length of 10 cm. So, the resulting propagation delay t_{d} is approximately 333 ps. To make the effect of this propagation delay visible, the frequency of the PWM signal is increased to 50 MHz. The other parameters are the same as before (relative pulse width of 25%, amplitude of 0.9 V and no DC component). The resulting time-domain signals can be found in Figure 4.8. The propagation time causes a delay of 333 ps between EMI and anti-EMI as marked by dashed lines. After this delay, the anti-EMI rises or falls with a finite slew rate. This additional time constant results from the integrator that had to be implemented for the stabilization of the feedback loop. As in the example of Section 4.3.1.b), spikes with high-frequency contents remain. Due to the delay times, these spikes also have short plateaus.

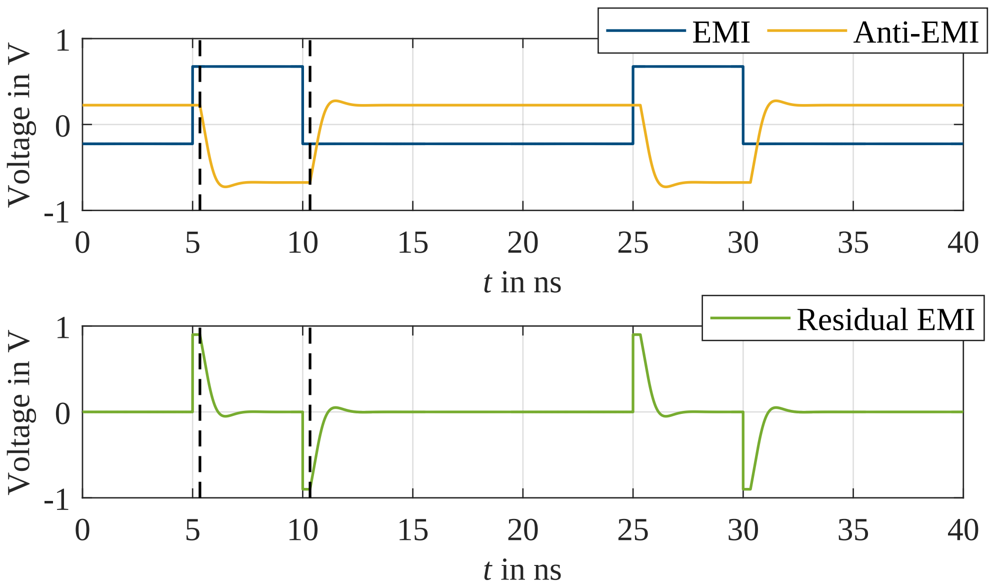

Figure 4.8: Theoretical time-domain signals for an FB VSVI AEFs with a propagation delay of 333 ps

4.3.2 Feedforward AEFs

The two fundamental topologies (i.e. CSCI and VSVI) of FF AEFs are depicted in Figure 4.9 [2]. CSVI and VSCI topologies are less convenient since a different quantity is measured than injected. Therefore, a transfer from current to voltage (or vice versa) is necessary.

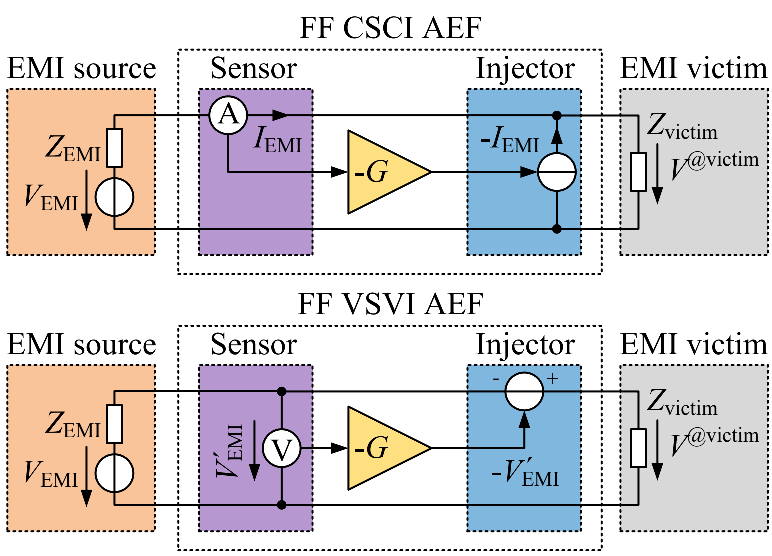

Figure 4.9: Topologies of FF AEFs [2]

To do so, the external impedances must be known and respected in the gain of the amplifier. This can be especially problematic if the source and victim impedances change over time. In this case, it would be necessary to adjust the gain during operation. This is much less convenient than the CSCI and VSVI topologies that ideally only require an inversion of the measured signal (as shown in the next section). [2]

a) Limitations due to Impedance Ratios and Variations

The achievable EMI reductions are summarized in Table 4.3. Again, all internal impedances of the sensor, injector and amplifier are neglected at this point [2]. The FF AEFs offer an infinite EMI reduction if the amplifier's gain G is exactly 1. By the same logic as in Section 4.3.1.a), current injectors require the source's impedance to be much higher than the one of the victim. For the voltage injector it is vice versa.

Topology	Reduction $\Delta V_{\mathrm{dB}}^{@\mathrm{victim}}$	Cond. for max. $\Delta V_{\mathrm{dB}}^{@\mathrm{victim}}$
FF CSCI	$20\ \mathrm{dB} \cdot \log_{10} \left\| \frac{1}{1-G} \cdot \left(1 - \frac{G \cdot Z_{\mathrm{victim}}}{Z_{\mathrm{EMI}} + Z_{\mathrm{victim}}}\right) \right\|$	$G = 1,\ \|Z_{\mathrm{EMI}}\| \gg \|Z_{\mathrm{victim}}\|$
FF VSVI	$20\ \mathrm{dB} \cdot \log_{10} \left\| \frac{1}{1-G} \cdot \left(1 - \frac{G \cdot Z_{\mathrm{EMI}}}{Z_{\mathrm{EMI}} + Z_{\mathrm{victim}}}\right) \right\|$	$G = 1,\ \|Z_{\mathrm{EMI}}\| \ll \|Z_{\mathrm{victim}}\|$

Table 4.3: Analytical solution for the performance of the two FF AEFs [2]

Since FF AEFs have no correcting feedback loop, the complete signal path (from sensor through amplifier through injector into the system) must be extremely close to -1. As analyzed in Section 3.1.3.a), small deviations in amplitude or phase already degrade the performance of the system significantly. Therefore, the FF AEF must be implemented with exact gain, minimal phase shift and low distortion. This is a difficult task that becomes significantly worse if parameter variations are considered. [26]

b) Limitations due to Amplifier's Gain

Assuming that the source and victim impedances fulfill the conditions of Table 4.3, the EMI reduction $\Delta V_{\mathrm{dB}}^{@\mathrm{victim}}$ can be calculated by (4.19):

$$\Delta V_{\mathrm{dB}}^{@\mathrm{victim}}(f) = 20\ \mathrm{dB} \cdot \log_{10} \left| \frac{1}{1 - G_{\mathrm{unity}}(f)} \right| \tag{4.19}$$

The gain of the amplifier $G(f)$ must "only" be set to 1 (here denoted by $G_{\mathrm{unity}}(f)$) to achieve an infinite EMI reduction. However, even in theory, this is no trivial requirement. The amplifier is still assumed to be an analog device with the same characteristics as in (4.3). The low-frequency (or DC) gain and the cutoff frequency of the amplifier are still denoted by G_0 and f_{c}. Now, the gain is set to unity by external circuitry (denoted by $G_{0,\mathrm{unity}}$). Due to the constant gain-bandwidth product, the cutoff frequency $f_{\mathrm{c,unity}}$ is shifted to the unity-gain bandwidth f_{unity}. [27, pp. 385-387]

In the following, the four OpAmps of Table 4.2 are investigated again. The new cutoff frequencies $f_{\mathrm{c,unity}}$ directly equal the unity-gain bandwidths f_{unity}. Using (4.3), $G_{0,\mathrm{unity}}$ and $f_{\mathrm{c,unity}}$, the amplifiers' frequency-dependent gains $G_{\mathrm{unity}}(f)$ are calculated. The achievable EMI reductions $\Delta V_{\mathrm{dB}}^{@\mathrm{victim}}(f)$ are determined by (4.19). The results are depicted in Figure 4.10.

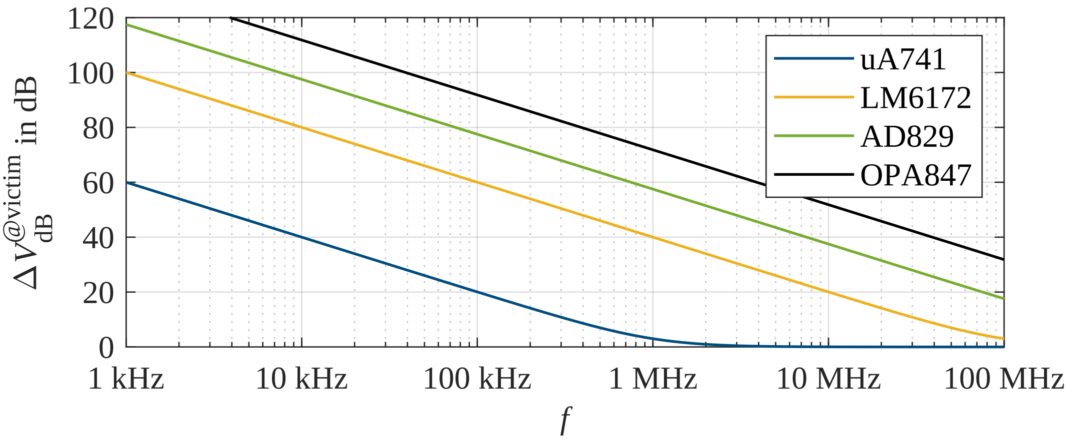

Figure 4.10: Theoretical performance of FF AEFs for exemplary OpAmps

FF AEFs are also most effective for lower frequencies. The decline in the achievable EMI reduction can still be explained by the amplifier's frequency-dependent gain. The low-frequency (or DC) gain may be set to 1 and the cutoff frequency may be shifted to very high frequencies, but the frequency-dependent gain will still slightly deviate in amplitude and phase from the necessary gain of 1. As analyzed in Section 3.1.3.a), these tiny deviations are enough to limit the performance significantly. Interestingly, FF AEFs show an even better performance than FB AEFs (Figure 4.4) for low frequencies. In this frequency range, the FB AEFs are limited by the low-frequency (or DC) gain G_0. Since the gain is set to unity for FF AEFs, this limitation does not apply anymore. It can be expected that the frequency-dependent gain will be closest to unity for low frequencies.

For better understanding, time-domain signals are shown again. Considering the FF VSVI topology (Figure 4.9) with the fulfilled requirement $|Z_{\mathrm{EMI}}| \ll |Z_{\mathrm{victim}}|$, the residual EMI can also be calculated by (4.5). The cancellation signal is found by (4.20). The rest of the calculation procedure is the same as in Section 4.3.1.b).

$$V_{\mathrm{anti}}(f) = -G_{\mathrm{unity}}(f) \cdot V_{\mathrm{EMI}}(f) \tag{4.20}$$

As an example, the OpAmp uA741 and a PWM EMI voltage with a fundamental frequency of 100 kHz, relative pulse width of 25%, an amplitude of 0.9 V and no DC component are considered. The resulting time-domain signals are shown in Figure 4.11. It can be found that the signals are very similar to the ones of the FB AEF (Figure 4.5). The method of signal generation may be different (feedforward vs. feedback), but both types suffer from the same time constant of the amplifier. So, a similar performance is plausible.

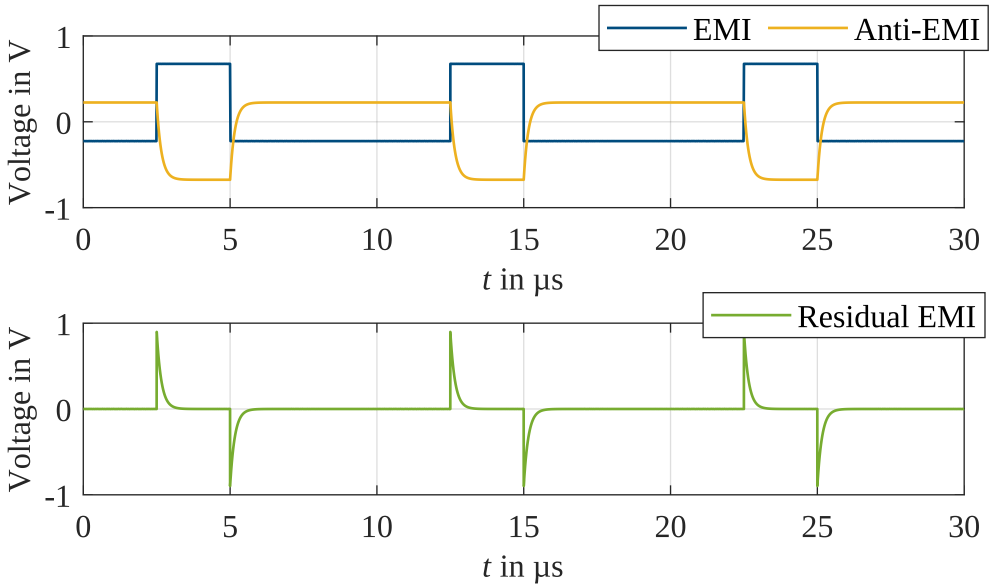

Figure 4.11: Theoretical time-domain signals for an FF VSVI AEF with uA741

c) Limitations due to Finite Signal Propagation Speed

Next, the limitations of FF AEFs due to signal propagation delays are discussed. The fundamental problem can be depicted by Figure 4.12. It is assumed that sensor and injector are ideal and that the requirements of Table 4.3 are met (i.e. $G = 1$). Due to the geometrical lengths of the signal paths from sensor to injector, there will be a signal propagation delay for both the EMI $t_{\mathrm{d,EMI}}$ and anti-EMI $t_{\mathrm{d,anti}}$. If these delay times are not the same, there will be a shift between EMI and anti-EMI degrading the performance of the FF AEF. The propagation delays can both be estimated in analogy to (4.9) by considering the speed of light c_0 and the respective lengths of the signal paths.

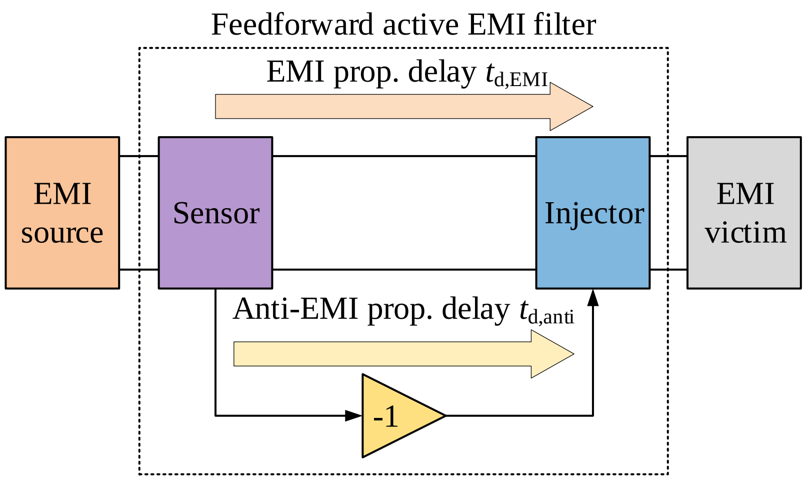

Figure 4.12: Systematic signal propagation delay in FF AEFs

Since the description of the signals is fundamentally the same for the CSCI and the VSVI topology, the signals are universally denoted by $X(f)$ that can be either a current or a voltage. Since the EMI is delayed by $t_{\mathrm{d,EMI}}$, (4.21) follows (the impedances can be neglected since the requirements of Table 4.3 are assumed to be fulfilled):

$$X_{\mathrm{EMI}}^{@\mathrm{victim}}(f) = X_{\mathrm{EMI}}(f) \cdot e^{-j2\pi f \cdot t_{\mathrm{d,EMI}}} \tag{4.21}$$

In analogy, (4.22) can be formulated for the anti-EMI:

$$X_{\mathrm{anti}}^{@\mathrm{victim}}(f) = X_{\mathrm{anti}}(f) \cdot e^{-j2\pi f \cdot t_{\mathrm{d,anti}}} \tag{4.22}$$

Due to the requirement of $X_{\mathrm{anti}}(f) \stackrel{!}{=} -X_{\mathrm{EMI}}(f)$, (4.23) follows:

$$\stackrel{(4.22)}{\Rightarrow} X_{\mathrm{anti}}^{@\mathrm{victim}}(f) = -X_{\mathrm{EMI}}(f) \cdot e^{-j2\pi f \cdot t_{\mathrm{d,anti}}} \tag{4.23}$$

The residual EMI can be described by (4.24)-(4.26):

$$\begin{aligned} X_{\mathrm{res}}^{@\mathrm{victim}}(f) &= X_{\mathrm{EMI}}^{@\mathrm{victim}}(f) + X_{\mathrm{anti}}^{@\mathrm{victim}}(f) && (4.24)\\ &= X_{\mathrm{EMI}}(f) \cdot e^{-j2\pi f \cdot t_{\mathrm{d,EMI}}} - X_{\mathrm{EMI}}(f) \cdot e^{-j2\pi f \cdot t_{\mathrm{d,anti}}} && (4.25)\\ &= X_{\mathrm{EMI}}(f) \cdot \left(e^{-j2\pi f \cdot t_{\mathrm{d,EMI}}} - e^{-j2\pi f \cdot t_{\mathrm{d,anti}}}\right) && (4.26) \end{aligned}$$

The achievable EMI reduction $\Delta X_{\mathrm{dB}}^{@\mathrm{victim}}(f)$ is calculated by (4.27):

$$\Delta X_{\mathrm{dB}}^{@\mathrm{victim}}(f) = 20\ \mathrm{dB} \cdot \log_{10} \left| \frac{X_{\mathrm{EMI}}^{@\mathrm{victim}}(f)}{X_{\mathrm{res}}^{@\mathrm{victim}}(f)} \right| \tag{4.27}$$

Since only the deviation Δt_{d} between the propagation delays is relevant for this calculation, (4.28) can be followed:

$$\begin{gathered} \Rightarrow \Delta X_{\mathrm{dB}}^{@\mathrm{victim}}(f) = -10\ \mathrm{dB} \cdot \log_{10} \left[2 - 2 \cdot \cos\left(2\pi f \cdot \Delta t_{\mathrm{d}}\right)\right] \\ \text{with } \Delta t_{\mathrm{d}} := t_{\mathrm{d,EMI}} - t_{\mathrm{d,anti}} \end{gathered} \tag{4.28}$$

The achievable EMI reduction is depicted in Figure 4.13 for different deviations of the propagation times. The deviation in the propagation delays should be as small as possible to achieve the best cancellation results. If there is a deviation in the signal paths, they could be symmetrized by increasing or decreasing the geometrical lengths. For a perfect symmetry, the signal propagation delay poses no limitation for the FF AEFs. Note that this symmetrization is not possible for FB AEFs since they suffer from a signal loop (and not two "racing" signals). Interestingly, the achievable EMI suppression increases for a deviation of 1 ns at 1 GHz again. In this case, the signals are shifted so far that they are in phase again.

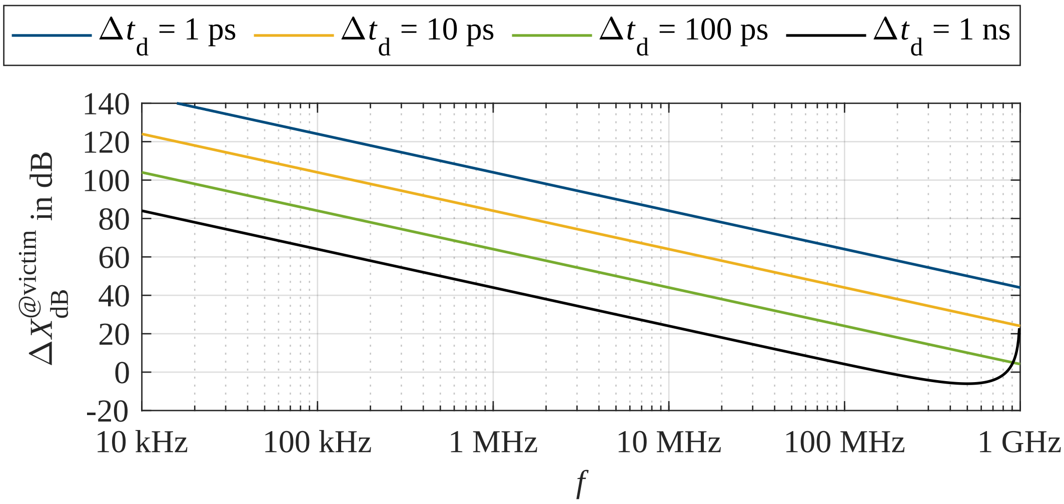

Figure 4.13: Theoretical performance of FF AEFs for different propagation delay deviations

In the following, the time-domain signals are discussed. The EMI is constructed in time domain. The anti-EMI is the delayed inverse of the EMI (calculated in time domain). The residual EMI is the superposition of both signals. It is assumed that the two signal propagation paths have a length difference of 10 cm leading to a deviation of 333 ps. The EMI is a PWM signal again with a high fundamental frequency of 50 MHz, a relative pulse width of 0.25%, an amplitude of 0.9 (V or A) and no DC component. The time-domain signals can be found in Figure 4.14. In comparison to Figure 4.8, the same plateau can be found in the residual EMI that results from the shift between EMI and anti-EMI. In contrast to FB AEFs, the FF AEFs need no settling time after this plateau phase.

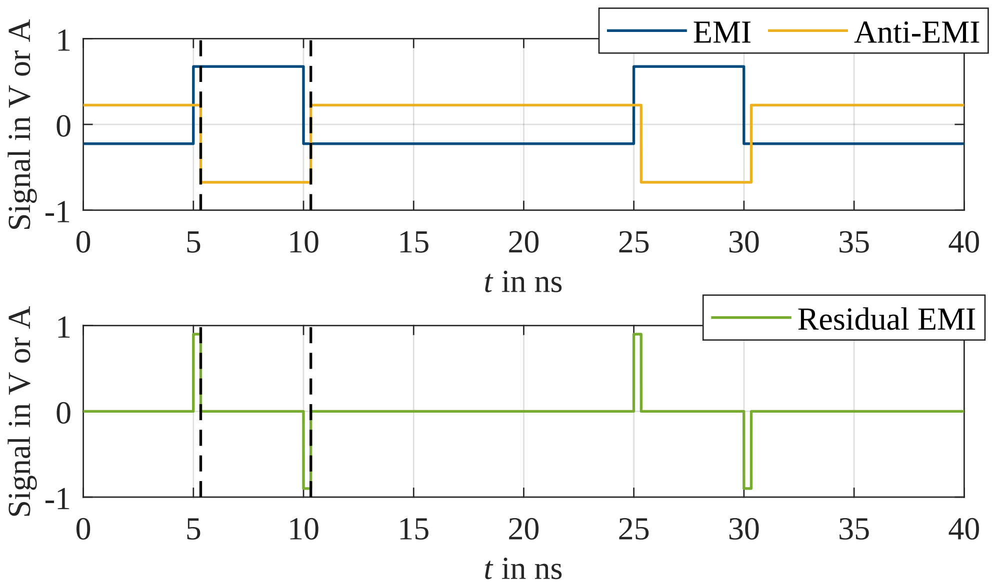

Figure 4.14: Theoretical time-domain signals for FF AEFs with a propagation delay deviation of 333 ps

4.4 Building Blocks

In this section, the fundamental building blocks of AEFs are summarized. These comprise the active analog circuitry, the injecting circuits and the sensing circuits. These injecting and sensing circuits can also directly be used for further active EMI cancellation techniques.

4.4.1 Active Circuitry

In AEFs, discrete transistors and integrated operational amplifiers are commonly used for the active circuitry. The application of these elements is summarized in the following.

In [7,8], two bipolar transistors are used in specialized configurations since they offer high gains and bandwidths. The amount of active devices is limited to two in order to achieve a system with a high bandwidth [7] that can be stabilized with reasonable effort [8].

In, e.g., [39], bipolar class-A amplifiers are used as output driving stages for the signals generated by operational amplifiers. In, e.g., [29], MOSFET class-A amplifiers are used for the same purpose. These stages suffer from a lower efficiency since the transistor needs a substantial DC bias in this configuration. However, the circuit is simple and requires only few components [29, 39]. In [40], only bipolar transistors (without operational amplifiers) are used for a class-A amplifier.

In, e.g., [41–45], bipolar class-B amplifiers are used without additional operational amplifiers. In, e.g., [46–48], the class-B amplifier's current gain is further increased by Darlington transistors. In, e.g., [22, 49], bipolar class-B amplifiers are used as driving stages for the signals generated by operational amplifiers.

In, e.g., [24, 34, 35, 50, 51], bipolar class-AB amplifiers are used to amplify the signals of operational amplifiers.

In, e.g., [1, 26, 31, 32, 37, 52–62], various operational amplifiers are exclusively applied in many different configurations.

As shown before, the AEF's performance is fundamentally limited by the gain-bandwidth product of the amplifiers. As long as only "small" ripple currents or voltages are suppressed, small devices with large gain-bandwidth products can be applied. For higher EMI levels, larger active devices are necessary that may have lower gain-bandwidth products [8]. So, high EMI reductions can be more difficult to be realized for higher EMI levels.

The active circuitry of AEFs can potentially be overdriven by the low-frequency or DC operating voltages and currents of the power electronic systems. To avoid this issue, high-pass filters can be applied. Fortunately, all of the sensing circuits discussed later show a high-pass characteristic. Additional high-pass filters can be applied if necessary. [2, 25]

Transients can be a potential harm to the cancellation circuitry of AEFs [8]. For protection, Zener diodes can be placed at the input and output of the AEF [8]. However, during the transients, the AEF's amplifier will generally saturate and the Zener diodes will carry the current [8]. Therefore, no proper cancellation signal can be injected into the system and a noise burst will result [8]. In [51], varistors are proposed in addition to Zener diodes. The selection and design of the protective circuit is not trivial since the parasitics of the protective components can degrade the AEF's performance [51].

4.4.2 Injecting Circuits

Injecting circuits in general have two purposes: First, they couple the high-frequency cancellation signals into the system. Second, they protect the AEF from possibly high operating voltages and currents of the power electronic system that could otherwise destroy the cancellation circuitry. Two basic injecting circuits are depicted in Figure 4.15. These use capacitive or inductive coupling elements that reject the low-frequency or DC operating voltages and pass the high-frequency cancellation signals. Since this functionality cannot be realized by resistive coupling elements alone, such injecting circuits are not applied.

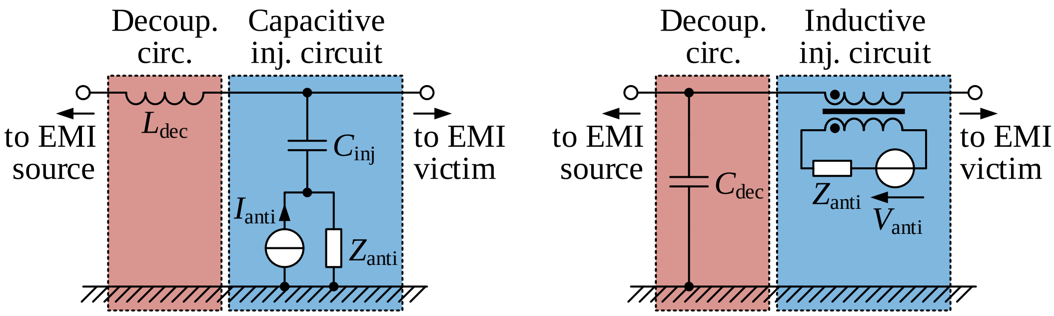

Figure 4.15: Capacitive current injector (left), inductive voltage injector (right)

a) Single-Wire Capacitive Current Injector

The capacitive current injector (Figure 4.15, left) uses a current source that generates the current I_{anti}. This source has an internal impedance of Z_{anti}. The capacitor C_{inj} is used to **inj**ect the high-frequency cancellation signal into the overall system. This element blocks the potentially high operating voltages of the power electronic system.

In a single-wire system with ground as return conductor, there are only DM disturbances that must be cancelled out. In this case, the coupling capacitor is a X-capacitor since it is installed between the supply and return conductor. There are usually no restrictions on the capacitance value of this element. In, e.g., [8, 29, 39, 49, 52], such an injector is applied. In, e.g., [39], an additional high-frequency transformer is used to galvanically isolate the cancellation circuitry from the power system. Since only a small cancellation signal must be transferred by the transformer, very small designs are possible.

In a multi-wire system (isolated from ground or remotely grounded), there are not only DM but also CM disturbances on each line. In this case, one capacitive current injector will be needed per wire. Since each injector will suppress the EMI on its wire individually, it will suppress DM and CM EMI. So, in this setup, it is actually a mixed mode injector. This concept is used in, e.g., [63]. The introduced coupling capacitors can be interpreted as

Y-capacitors. Obviously, they must withstand the voltages between the wires and ground. In many devices, there are very high safety regulations for the isolation. To fulfill these requirements, Y-capacitors with approved insulation properties must be used. Furthermore, the introduced capacitance can cause leakage currents against ground at, e.g., 50 or 60 Hz. To minimize shock hazards from these leakage currents, the value of the system's total Y-capacitance is usually restricted. These are critical constraints for passive and active EMI filters since the allowed filtering or coupling capacitance may be limited to the one- or two-digit nF range. [19, p. 390]

From the requirements in Tables 4.1 and 4.3, it can be found that the EMI source's impedance should be much larger than the one of the EMI victim. If this condition is not fulfilled, a **dec**oupling inductance L_{dec} can be added between injector and EMI source [24]. In many cases, this inductance is necessary since the impedance of power electronic systems can be very low. Realizing this inductance is not trivial since the operating currents of the power electronic system can be quite high. The wires for, e.g., coils must have a sufficient cross-section area to carry the currents without overheating. Usually, ferrite cores will be used to increase the inductance. However, a saturation due to the operation currents must be avoided since ferrites would lose most of their inductance in this case. Due to these effects, compact decoupling inductors may be difficult to realize.

b) Single-Wire Voltage Injector with Transformer

The inductive voltage injector (Figure 4.15, right) uses a voltage source with the voltage V_{anti} and the internal impedance of Z_{anti}. A high-frequency transformer is the coupling element. The DC or low-frequency operating currents of the power electronic system can pass through the primary side of the transformer. The high-frequency cancellation signals are coupled into the system by the magnetic coupling. The turns ratio is a convenient way to adjust signal ranges. The primary side of the transformer must be capable to pass the operating currents without magnetic saturation or overheating. As discussed in Section 4.4.2.a), this can lead to a rather large inductive element.

In this single-wire setup with ground as return conductor, the injector cancels out DM EMI. Such an injector is applied in, e.g., [1, 26, 53]. In a multi-wire system (isolated from ground or remotely grounded), one two-winding transformer can be used per wire. In this case, it is a mixed mode injector. In both cases, the mutual inductance of the transformer is in parallel with the overall system (seen from the cancellation source). Since the signal must be coupled into the overall system (and not into the mutual inductance), the impedance of the mutual coupling must be higher than the one of the overall system.

To fulfill the requirements depicted in Tables 4.1 and 4.3, the EMI source's impedance should be much smaller than the one of the EMI victim. If the source impedance is too large, it can be reduced by introducing a parallel capacitance C_{dec} as **dec**oupling element. In a single-wire system with ground as return conductor, the capacitance value is usually not restricted (X-capacitor). For an isolated multi-wire system, there are the same restrictions as for the capacitive coupling element in Section 4.4.2.a) (Y-capacitor).

c) Further Topologies

There are many more topologies suited for different systems. In Table 4.4, some options for isolated (or remotely grounded) multi-wire systems are summarized.

Injection	System	EMI	Coupling circuit	Reference
Voltage	Two-wire	DM	Three-wind. transf.	[56, 58]
Voltage	Two-wire	CM	Three-wind. transf.	[54, 56]
Voltage	Three-wire	CM	Four-wind. transf.	[31, 32, 37, 41–43, 45–48, 64, 65]
Current	Two-wire	DM	One X-capacitor	[24, 25, 34, 35]
Current	Two-wire	CM	Two Y-capacitors	[25, 40, 44, 50, 51, 55–57, 60–62]
Current	Three-wire	CM	Three Y-capacitors	[44, 65, 66]

Table 4.4: Overview of further injector topologies for isolated (or remotely grounded) multi-wire systems (abbreviations: **wind**ing, **transf**ormer)

4.4.3 Sensing Circuits

Like injecting circuits, sensing circuits must couple the high-frequency EMI for the cancellation system while rejecting the operating voltages and currents of the power electronic system. In analogy to injecting circuits, there are capacitive and inductive coupling circuits for sensing. However, for sensing, the capacitive variant couples a voltage and the inductive variant couples a current. So, the coupling is inversed in comparison to the injecting circuits. Two basic sensors are depicted in Figure 4.16 and discussed in the following.

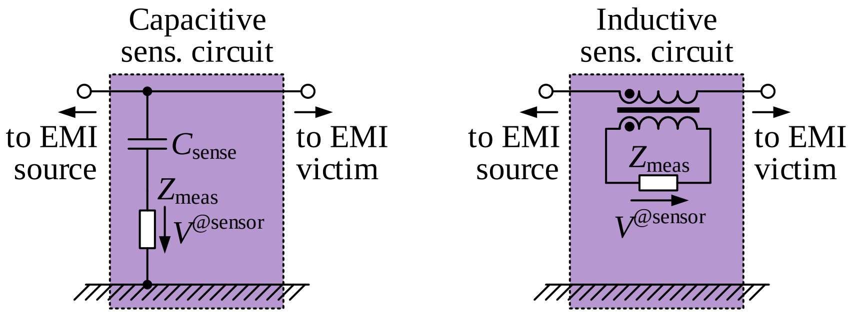

Figure 4.16: Capacitive voltage sensor (left), inductive current sensor (right)

a) Single-Wire Capacitive Voltage Sensor

The elements of the capacitive voltage sensor (Figure 4.16, left) are a coupling element C_{sense} and a measuring impedance Z_{meas}. The coupling element must be dimensioned in such way that it rejects the possibly high operating voltage of the power electronic system and passes the high-frequency EMI without significant voltage drops.

In a single-wire system, the sensing circuit measures DM EMI and there are usually no restrictions for the capacitance value of C_{sense} (X-capacitor). This sensor is applied in, e.g., [1, 6, 8, 26, 58].

In an isolated multi-wire system, the sensing circuit can be applied to each line individually (as done in, e.g., [63]). By the same logic as in Section 4.4.2.a), it measures mixed mode EMI consisting of DM and CM. In this case, the coupling elements introduce an additional Y-capacitance that is often restricted (as described in Section 4.4.2.a)).

b) Single-Wire Inductive Current Sensor

The inductive current sensor (Figure 4.16, right) consists of a high-frequency transformer and a shunt impedance Z_{meas} for measurement. The low-frequency or DC operating currents flow through the primary side of the transformer and only the high-frequency currents are coupled into the measurement impedance. By measuring the voltage drop over this known element, the disturbing currents can be found. The turns ratio is a convenient way to adjust the signal range.

In a single-wire system (e.g. [29, 39, 49, 53]), the sensor measures the DM currents. In a multi-wire system (isolated from ground or remotely grounded), one of these sensors can be applied to each wire. Since the operating currents must be conducted through the primary side of the inductive transformer, large components may be necessary as discussed in Section 4.4.2.a).

To resolve this issue, Rogowski coils are proposed in [39]. For comparison, a current transformer with a ferrite core and a Rogowski coil are designed for the same operating current of 20 A in [39]. It is shown that the Rogowski coil and the current transformer have approximately the same size while the Rogowski coil is much lighter due to the absence of a ferrite core. It is stated that the Rogowski coil should be smaller for higher currents and larger for lower currents in comparison to the current transformer. [39]

c) Further Topologies

In Table 4.5, further sensing circuits for isolated (or remotely grounded) multi-wire systems are summarized.

Sensing	System	EMI	Coupling circuit	Reference
Voltage	Two-wire	CM	Two Y-capacitors	[37, 40, 51]
Voltage	Three-wire	CM	Three Y-capacitors	[31, 32, 41–43, 45–48, 59, 64–66]
Current	Two-wire	DM	Three-wind. transf.	[34]
Current	Two-wire	CM	Three-wind. transf.	[44, 50, 54–57, 60–62]
Current	Three-wire	CM	Four-wind. transf.	[44]

Table 4.5: Overview of further sensor topologies for isolated (or remotely grounded) multi-wire systems (abbreviations: **wind**ing, **transf**ormer)

4.5 Applications

In this section, the performance of AEFs in different applications is discussed. These comprise DC-to-DC converters, motor inverters and AC-to-DC converters. In the literature, the EMI reductions of AEFs are given in different manners. In most publications, the disturbances with and without the AEF are compared (denoted by "AEF vs. raw"). In these comparisons, the EMI reduction consists of the active suppression of the injected signals and the passive attenuation of the introduced analog circuitry. In some publications, the combination of a **p**assive **E**MI **f**ilter (PEF) and an AEF is compared to the same PEF without AEF (denoted by "PEF&AEF vs. PEF"). Also in these comparisons, the active suppression and passive attenuation of the AEFs can be found. In some other cases, the EMI is compared for the activated and deactivated AEF (denoted by "AEF: on vs. off"). Thus, only the active suppression is evaluated. This is the same for the combination "PEF&AEF: on vs. off". The EMI reductions are quoted by using characteristic values for specific frequencies or frequency ranges. In between, the EMI reductions may be interpolated.

4.5.1 DC-to-DC Converters

At first, AEFs for DC-to-DC converters are discussed. There are DM and CM realizations.

a) DM EMI

In Table 4.6, AEFs for the suppression of DM EMI are summarized. In general, AEFs work best for lower frequencies due to their frequency responses as discussed in Section 4.3.

In [22], an experimental comparative study is presented. It is shown that voltage-injecting AEFs are best suited for the suppression of DM EMI of typical DC-to-DC converters since they usually pose a very low DM impedance due to their rather large stabilizing capacitances at the input and output ports. So, the requirements for voltage-injecting AEFs are usually fulfilled (Table 4.1 and 4.3).

The combination of FF and FB AEFs shows the best results in this comparison [1, 26, 29]. In [26], the FF AEF suppresses the lower frequencies up to the point where its slight magnitude and phase deviations limit its performance. The FB AEF is used to suppress higher frequencies. However, the FB AEF increases the EMI around 875 kHz due to the control loop. A similar effect occurs in [29].

It is shown that the AEF's relative power consumption is below 1% of the transfer power of the DC-to-DC converters [26,58]. This is due to the fact that the EMI is already filtered by the stabilizing capacitors. Therefore, only a small ripple remains that contains little power.

In [26], it is shown that the value of filtering capacitors can be decreased by 99% while still maintaining the necessary EMI reduction. This is achieved by applying a combination of one FF and one FB VSVI AEF. In [58], an integrated hybrid filter is proposed that has the same performance as a passive solution. The filter's volume and mass are reduced by 76% and 53%, respectively. So, AEFs are effective in reducing the required effort for passive filtering.

It can be found that the practical results for the AEFs are below the theoretical limits identified in Section 4.3. So, the performance of AEFs may be limited by practical issues like parasitic influences, parameter variations or the necessary stabilization of feedback loops.

Topology	Circuitry	Results	Publ.
FB CSVI	Bipolar class-B	DM EMI: -17 dB at 100 kHz (AEF vs. raw)	[22]
FB CSCI	Bipolar class-B	DM EMI: -10 dB at 100 kHz (AEF vs. raw)	[22]
FB VSVI	Bipolar class-B	DM EMI: -14 dB at 100 kHz (AEF vs. raw)	[22]
FB VSCI	Bipolar class-B	DM EMI: -12 dB at 100 kHz (AEF vs. raw)	[22]
FF&FB VSVI	OpAmp	DM EMI: -13 dB at 200 Hz DM EMI: -40 dB at 1 kHz DM EMI: -60 dB at 8 kHz DM EMI: -51 dB at 60 kHz (AEF vs. raw)	[1]
FF VSVI and FB VSVI	OpAmp OpAmp	DM EMI: -40 dB at 125 kHz DM EMI: -4 dB at 500 kHz DM EMI: +20 dB at 875 kHz DM EMI: -0 dB at 1 MHz (AEF: on vs. off) Needed filter capacitance: -99% AEF rel. power cons.: $\leq$ 0.9%	[26]
FF CSCI and FB CSCI	OpAmp & MOSFET class-A OpAmp & bipolar class-A	DM EMI: -70 dB at 100 kHz DM EMI: -0 dB at 5 MHz DM EMI: +20 dB at 9 MHz (AEF: on vs. off)	[29]
FB VSVI	OpAmp	DM EMI: -13 dB at 200 kHz DM EMI: -5 dB at 2 MHz (PEF&AEF vs. PEF) Filter volume: -76% Filter mass: -53% AEF rel. power cons.: 1%	[58]
FF CSCI	OpAmp	DM EMI: -30 dB at 125 kHz DM EMI: -3 dB at 250 kHz (PEF&AEF: on vs. off)	[39]

Table 4.6: Demonstrator results of DM AEFs for DC-to-DC converters

b) CM EMI

In Table 4.7, a summary of CM AEFs is presented. Again, all AEFs show the best results for lower frequencies. Here, current-injecting topologies are applied. Since DC-to-DC converters are usually coupled by very small parasitic capacitances to ground, large CM impedances result. Current-injecting AEFs can be expected to perform well in this setup since the requirements of Tables 4.1 and 4.3 are fulfilled. Also here, the theoretical limits identified in Section 4.3 are not met.

Topology	Circuitry	Results	Publ.
FB VSCI	Bipolar class-AB	CM EMI: -18 dB at 200 kHz CM EMI: -24 dB at 1 MHz CM EMI: -0 dB at 7.5 MHz (PEF&AEF vs. PEF)	[51]
FB CSCI	OpAmp	CM EMI: -25 dB at 150 kHz CM EMI: -0 dB at 700 kHz (AEF vs. raw)	[55]
FB CSCI	OpAmp	CM EMI: -27 dB at 300 kHz CM EMI: -13 dB at 3 MHz CM EMI: -0 dB at 5.1 MHz (PEF&AEF: on vs. off)	[60]

Table 4.7: Demonstrator results of CM AEFs for DC-to-DC converters

4.5.2 Motor Inverters

In this section, publications on AEFs for motor inverter systems are summarized. These systems are either DC or AC fed, but all of them drive motors at the output. In all publications, the CM disturbances are suppressed. However, the AEFs are applied either to the input or output wires.

a) Motor Side

At first, AEFs for the motor side of the inverter are discussed. Here, the fundamental goal is to minimize the CM EMI towards the motor. The first and obvious reason is the reduction of EMI. The second reason is a reliability issue: The CM voltage generated by the PWM inverter couples capacitively through the motor air-gap and causes a shaft voltage. This shaft voltage can cause electric discharges through the bearing lubrication. This process damages the motor's bearings and shortens the motor's lifetime. So, suppressing the EMI improves not only the EMC but also the lifetime of the motor drive system. [32]

Di Piazza et al. have made numerous publications on this topic that are summarized in Table 4.8 (note that RMS stands for "**r**oot **m**ean **s**quare"). All of these AEFs utilize the VSVI topology. It can be found that the CM peak currents and voltages on the motor side can be reduced by up to 93% and 90%, respectively [46]. Since the supply and motor sides are coupled through the inverter, an AEF installed on the motor side can positively or negatively affect the CM EMI at the **l**ine **i**mpedance **s**tabilization **n**etwork (LISN) of the supply side [47]. However, in [47], the overall effect is positive enabling the reduction of the input CM choke's inductance by 41%. The relative power consumption of the AEFs can be quite high ranging from 0.5% to 3.8% of the transfer power of the inverter [48].

Topology	Circuitry	Results	Publ.
FF VSVI	Bipolar darlington class-B	CM motor peak current: -93% CM motor RMS current: -88% CM motor peak-to-peak voltage: -90% CM motor RMS voltage: -96% (AEF vs. raw)	[46]
FF VSVI	Bipolar darlington class-B	CM motor peak current: -89% CM EMI LISN: -10 dB until 1 MHz CM EMI LISN: -0 dB at 1.5 MHz CM EMI LISN: +30 dB at 4.1 MHz (AEF vs. raw) $\Rightarrow$ Needed input CM choke inductance: -41%	[47]
FB VSVI	OpAmp	CM motor peak-to-peak voltage: -50% CM motor voltage: -16 dB at 20 kHz CM motor voltage: -2 dB at 200 kHz (AEF vs. raw)	[31]
FF VSVI	Bipolar darlington class-B	AEF relative power consumption: 0.5-3.8%	[48]
FB VSVI and FF VSVI	OpAmp OpAmp	CM motor peak voltage: -50% CM motor voltage: -8 dB at 20 kHz CM motor current: -34 dB at 240 kHz CM motor current: -17 dB at 401 kHz CM motor current: -2 dB at 720 kHz (AEF vs. raw)	[32]

Table 4.8: Demonstrator results of CM AEFs for the motor side of inverters (Di Piazza et al.)

In Table 4.9, further publications of various authors are summarized. There are similar results compared to Table 4.8. The reduction of the potential harmful bearing currents is explicitly shown in [45]. In [65], extraordinary results are presented regarding the frequency range of the AEF: An FF VSVI AEF is used to suppress the CM motor voltage up to approximately 2.5 MHz. An additional FB VSCI AEF is applied to suppress the CM motor voltage for frequencies of up to 100 MHz.

Topology	Circuitry	Results	Publ.
FF VSVI	Bipolar class-B	CM motor peak current: -91% CM EMI LISN: -20 dB up to 1 MHz Shaft peak voltage: -60% (AEF vs. raw)	[41]
FF VSVI	Bipolar class-B	CM motor peak current: -97% Shaft peak voltage: -84% Bearing peak current: -87% (AEF vs. raw)	[45]
FF VSVI	OpAmp	CM motor peak-to-peak voltage: -85% CM motor current: -20 dB at 20 kHz CM motor current: -15 dB at 200 kHz CM motor current: -0 dB at 2 MHz (AEF vs. raw)	[59]
FF VSVI and FB VSCI	Bipolar class-B OpAmp	CM motor peak voltage: -95% CM motor voltage: -35 dB at 100 kHz CM motor voltage: -30 dB at 1 MHz CM motor voltage: -0 dB at 2.5 MHz CM motor voltage: -19 dB at 10 MHz CM motor voltage: -15 dB at 100 MHz (AEF vs. raw)	[65]

Table 4.9: Demonstrator results of CM AEFs for the motor side of inverters (various authors)

b) Supply side

In Table 4.10, publications on CM AEFs for the supply side (DC or AC) are summarized. For this side, the CM EMI is measured by either LISNs or PLIPs (**p**ower **l**ine **i**nterference **p**robes). PLIPs can be used if the operating currents are high and/or if the connection of the LISN to the circuit is difficult to realize [44].

Topology	Circuitry	Results	Publ.
FF CSCI	OpAmp	CM EMI LISN: -38 dB at 12 kHz CM EMI LISN: -0 dB above 3 MHz AEF relative power consumption: $\leq$ 0.08% (PEF&AEF vs. PEF)	[50]
FF CSCI	Bip. class-B	CM EMI PLIP: -5 dB at 150 kHz CM EMI PLIP: $\approx$ -20 dB from 250 kHz to 6 MHz CM EMI PLIP: -5 dB at 10 MHz (AEF vs. raw) CM EMI PLIP: -5 dB at 150 kHz CM EMI PLIP: -14 dB at 200 kHz CM EMI PLIP: $\approx$ -5 dB at 300 kHz to 500 kHz CM EMI PLIP: $\approx$ -15 dB from 800 kHz to 5 MHz CM EMI PLIP: -4 dB at 10 MHz (AEF: on vs. off)	[44]
FB VSCI	Bip. transistors	CM EMI LISN: -10 dB at 150 kHz CM EMI LISN: -0 dB at 600 kHz (AEF: on vs. off)	[66]
FB CSCI	OpAmp	CM EMI LISN: -27 dB at 10 kHz CM EMI LISN: -20 dB at 60 kHz CM EMI LISN: -38 dB from 100 kHz to 300 kHz CM EMI LISN: -35 dB at 600 kHz CM EMI LISN: -25 dB at 1 MHz CM EMI LISN: -13 dB at 3 MHz CM EMI LISN: -8 dB at 6 MHz CM EMI LISN: -0 dB at 10 MHz (PEF&AEF vs. PEF)	[57]

Table 4.10: Demonstrator results of CM AEFs for the supply side of inverter systems

Here, various topologies are used. It can be found that the maximum achievable EMI reduction is below 40 dB. The frequency range appears to be limited to 10 MHz. The AEF's relative power consumption is much lower on the supply side ($\leq$ 0.08%, [50]) than on the motor side (0.5-3.8%). This may be due to the fact that the AEF on the motor side is placed *inside* of the power converting system. Therefore, the EMI has much power, and much power is needed to suppress it. On the input side, the AEF can be installed *outside* of the power converting system. So, the AEF must only suppress a residual ripple that has already been partially filtered by the X- and Y-capacitors at the input of the inverter. This EMI has usually only little power in comparison to the rated power of the power electronic system.

4.5.3 AC-to-DC Converters

In this section, AEFs for AC-to-DC converters are summarized and discussed. The converters are specified as **s**witched-**m**ode **p**ower **s**upplies (SMPS) or **p**ower **f**actor **c**orrections (PFC) with rectifiers (and in some cases with additional DC-to-DC stages). The AEFs are all applied to the AC input side of the converters, but suppress either DM or CM EMI.

a) DM EMI

At first, DM AEFs for SMPS are summarized in Table 4.11. In [56], a comparative study is done for the topologies FB VSVI and FB VSCI. Due to the low DM input impedance of the AC-to-DC converter, the VSVI topology shows better results than the VSCI. In [34], the volume of a passive filter is reduced by approximately 50% by applying an AEF. The relative power consumption is relatively low (0.7%) since only ripple currents and voltages are suppressed. In [35], combinations of FB and FF AEFs are investigated. There are good results for two series FB CSCI AEFs.

b) CM EMI

In Table 4.12, CM AEFs are summarized. In [56], a comparative study is done for the topologies FB CSCI and FB CSVI. As discussed in Section 4.5.1.b), the CM impedances of power electronic systems are usually high. So, current-injecting topologies can be expected to perform well. This is confirmed in [56].

In [40], an integrated hybrid filter is realized from an FB AEF and a passive EMI filter. In comparison to a discrete filter, the filter volume is reduced by up to 55%. However, the efficiency is reduced by 1 pp (**p**ercentage **p**oint). In comparison to an integrated passive filter, the volume is reduced by 22% and the efficiency is degraded by 0.7 pp.

In [37], another hybrid filter is considered. Here, the overall volume can be reduced by 50% by applying the AEF. In [61], a CM choke is used for passive attenuation and also as sensing circuit for the AEF. By doing so, the volume of the passive filter can be reduced by up to 85% in comparison to a purely passive EMI filter. So, AEFs can be an effective solution to reduce the sizes of passive EMI filters. However, there is a small impact on the efficiency of the device.

Topology	Circuitry	Results	Publ.
FB VSVI	OpAmp	DM EMI: -5 dB at 150 kHz DM EMI: -34 dB at 1 MHz DM EMI: -13 dB at 10 MHz DM EMI: -0 dB at 20 MHz (AEF vs. raw)	[56]
FB VSCI	OpAmp	DM EMI: +15 dB at 150 kHz DM EMI: -7 dB at 1 MHz DM EMI: -0 dB at 6 MHz (AEF vs. raw)	[56]
FB CSCI	OpAmp & bip. class-AB	DM EMI: -23 dB at 120 kHz DM EMI: -28 dB at 240 kHz DM EMI: -0 dB above 3 MHz (AEF vs. raw)	[24]
FB CSCI	OpAmp & bip. class-AB	DM EMI: -23 dB at 120 kHz DM EMI: -28 dB at 240 kHz DM EMI: -0 dB at 3 MHz (AEF vs. raw) Filter volume: -50% AEF relative power cons.: 0.7%	[34]
2× FB CSCI	OpAmp & bip. class-AB	DM EMI: -25 dB at 120 kHz DM EMI: -45 dB at 240 kHz DM EMI: -20 dB at 1 MHz DM EMI: -0 dB at 4 MHz (AEF vs. raw)	[35]

Table 4.11: Demonstrator results of DM AEFs for AC-to-DC converters

Topology	Circuitry	Results	Publ.
FB CSCI	OpAmp	CM EMI: -31 dB at 150 kHz CM EMI: -36 dB at 1 MHz CM EMI: -18 dB at 10 MHz CM EMI: -0 dB at 30 MHz (AEF vs. raw)	[56]
FB CSVI	OpAmp	CM EMI: +2 dB at 150 kHz CM EMI: -23 dB at 1 MHz CM EMI: -18 dB at 10 MHz CM EMI: -0 dB at 30 MHz (AEF vs. raw)	[56]
FB VSCI	Bipolar class-A	CM EMI: -0 dB at 200 kHz CM EMI: -20 dB at 1 MHz CM EMI: -11 dB at 2 MHz CM EMI: -3 dB at 7 MHz (AEF: on vs. off) Efficiency: -0.7 pp to -1 pp Filter volume: -22% to -55%	[40]
FF VSVI	OpAmp	CM EMI: -5 dB at 150 kHz CM EMI: -9 dB at 1.5 MHz CM EMI: -12 dB at 2.5 MHz CM EMI: -6 dB at 9 MHz (PEF&AEF vs. PEF) Filter volume: -50%	[37]
FB CSCI	OpAmp	Filter volume: -77% to -85%	[61]
FB CSCI	OpAmp	CM EMI: -15 dB at 64 kHz CM EMI: -0 dB at 500 kHz CM EMI: -7 dB at 10 MHz (PEF&AEF vs. PEF) AEF relative power consumption: $< 0.2\%$	[62]

Table 4.12: Demonstrator results of CM AEFs for AC-to-DC converters

4.6 Chapter Summary

From the literature, it can be found that AEFs are an effective solution to suppress CM or DM EMI for frequencies of up to a few MHz. Since these frequency components usually cause the necessity of large inductors and capacitors in passive EMI filters, AEFs can be a good solution for volume reduction. The field of application is very wide and comprises, e.g., DC-to-DC converters, motor inverters and AC-to-DC converters. There are many possibilities regarding the injecting and sensing circuits. So, active EMI cancellation is a promising approach to reduce the necessary passive filtering effort.

However, the achievable EMI reduction and the bandwidth of AEFs are systematically limited by the amplifier's gain-bandwidth product (that results in an unavoidable time constant) and unavoidable signal propagation delays. To oppose the limited gain-bandwidth products of analog amplifiers, digital active EMI filters have been developed in [9–11]. These are analyzed in the following chapter.

5 Analysis of Digital Active EMI Filter (DAEF) Approaches

To overcome the limitations of analog circuitry due to restricted gain-bandwidth products, **d**igital **a**ctive **EMI f**ilters (DAEFs) have been proposed in 2013 [9–11] and further analyzed in 2018 [63]. In these publications, the control of both the power electronic system and the DAEF are implemented on the same digital device. In DAEFs, the EMI is sensed, analog-to-digital converted, digitally processed, digital-to-analog converted and injected back into the system. Since the inversion and amplification are done in digital domain, there is no systematically limited gain-bandwidth product like for analog amplifiers. However, this method has its own limitations that are discussed in this chapter.

At first, the fundamental feedback and feedforward topologies of DAEFs are introduced. Then, the limitations resulting from the digital cancellation system are analyzed. To give an idea of the achievable EMI reduction, demonstrator results are discussed. The chapter closes with a summary that motivates the next steps.

5.1 Topologies

DAEFs use feedback [9, 10, 63] or feedfoward [11] topologies as depicted in Figure 5.1. The fundamental structure of EMI source, injector, sensor and EMI victim is unchanged in comparison to AEFs (Chapter 4). The main difference is that digital signal processing hardware is used for inversion and amplification. As interfaces between the digital and analog domain, **a**nalog-to-**d**igital **c**onverters (ADC) and **d**igital-to-**a**nalog **c**onverters (DAC) are necessary. In the following, the limitations resulting from the digital hardware are evaluated.

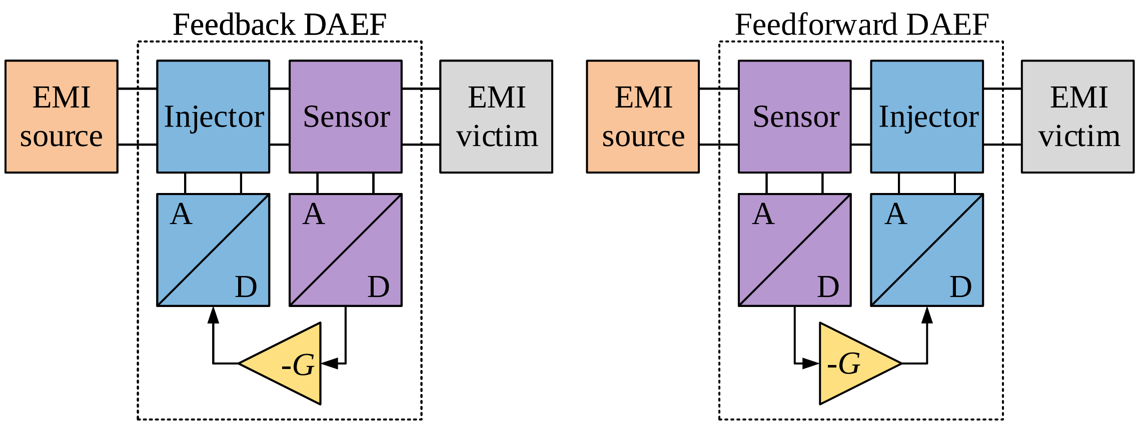

Figure 5.1: Feedback vs. feedforward digital active EMI filters

5.1.1 Limitations due to Vertical Resolution

In DAEFs, ADCs and DACs are the interface circuits between the analog and digital domains. They are used for sensing the (residual) EMI and injecting the anti-EMI. These interface circuits can be a limiting factor for the achievable EMI reduction due to their quantization noise (given that the digital signal processor has a sufficient precision in its calculations). An important measure is the **s**ignal-to-**n**oise **r**atio (SNR) that defines the quotient of the highest measurable/producible sine wave and the noise floor (both in RMS values) in dependence of the amount of bits n_{bits}. The SNR can be estimated by (5.1). Note that the SNR assumes a single sine wave for calculation.

$$\text{SNR} \approx 6.02\ \text{dB} \cdot n_{\text{bits}} + 1.76\ \text{dB} \tag{5.1}$$

In the following, the influence of the SNR will be discussed for the ADC. It is assumed that the ADC has a symmetric voltage range of $V_{\text{ADC,max}}$. To calculate its noise floor $V_{\text{ADC,NF,RMS}}$, the RMS value of the maximum measurable sine wave $V_{\text{ADC,sine,max,RMS}}$ must be determined. Since the maximum measurable amplitude equals the voltage range $V_{\text{ADC,max}}$, its RMS value can be calculated by $V_{\text{ADC,sine,max,RMS}} = V_{\text{ADC,max}}/\sqrt{2}$. The SNR can be calculated by (5.1) for a given amount of bits n_{bits}. A first approximation of the noise floor $V_{\text{ADC,NF,RMS}}$ can be calculated by (5.2). This calculation is also valid for DACs according to (5.3).

$$V_{\text{ADC,NF,RMS}} \approx \frac{V_{\text{ADC,max}}}{\sqrt{2}} - \text{SNR} \tag{5.2}$$

$$V_{\text{DAC,NF,RMS}} \approx \frac{V_{\text{DAC,max}}}{\sqrt{2}} - \text{SNR} \tag{5.3}$$

In Figure 5.2, the restrictions due to the dynamic range of the ADC are visualized. At first, a single sine wave is considered as a measured signal. It has a fundamental frequency of f_0 and the maximum allowed amplitude $V_{\text{ADC,max}}$ (Figure 5.2, top). Larger signals cannot be measured by the ADC. The level $V_{\text{ADC,sine,max,RMS}}$ of the sine wave can theoretically be suppressed down to the noise floor $V_{\text{ADC,NF,RMS}}$ (Figure 5.2, center). Lower signals can generally not be measured by the ADC. So, the single sine wave can be suppressed by the ADC's dynamic range that can be described by the SNR (Figure 5.2, bottom).

In practical systems with, e.g., quasi-periodic EMI, the signals consist of many harmonics that superpose each other. In Figure 5.2, a PWM signal is chosen as a second example. It has also a fundamental frequency of f_0 and the maximum allowed amplitude of $V_{\text{ADC,max}}$. Due to the duty cycle of 50%, the fundamental wave f_0 has even a higher level than $V_{\text{ADC,sine,max,RMS}}$. So, the fundamental wave could theoretically be suppressed further than the SNR. The higher harmonics have a lower level than the fundamental wave. Since they can also only be suppressed down to the noise floor $V_{\text{ADC,NF,RMS}}$, the achievable reduction is less than the SNR.

Last, a measured EMI signal of a DC-to-DC converter is discussed. This signal consists of a voltage ripple and voltage ringings due to the switching power transistors. Since also this signal must not overdrive the ADC, the high-frequency ringing defines the measurement range. Although the signal has no DC component, it is not symmetric around 0 V. Due to this effect, it is not possible to utilize the complete frequency range of the ADC. Even though the ringing has a relatively high amplitude, it consists of harmonics with relatively small levels. The fundamental wave is close to the level $V_{\text{ADC,sine,max,RMS}}$, but the higher harmonics are far below. Due to all of these reasons, the achievable EMI reduction is worse than for the PWM signal.

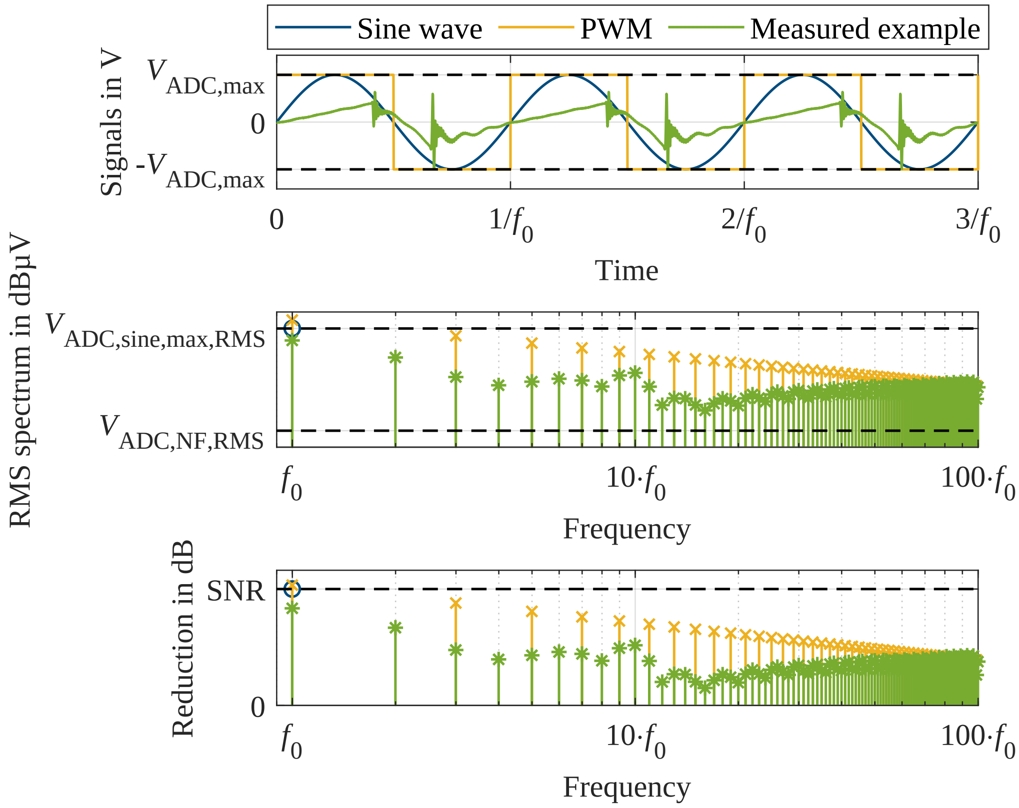

Figure 5.2: Theoretical performance of DAEFs considering the ADC's dynamic range and different disturbance signals

In theory, the EMI can be suppressed down to the noise floor of the ADC. Therefore, the relative EMI reduction increases with a rising EMI level (as long as the ADC is not overdriven). In other words, given quantization steps result in larger relative deviations for small signals. So, the achievable EMI reduction declines with decreasing amplitudes. A single sine wave may be reduced by the ADC's SNR if its voltage range is completely used. The individual harmonics of a broadband signal cannot be reduced by the same value due to the limited voltage range of the ADC.

In a similar manner, this description also applies to DACs. The highest producible cancellation signal is limited by the DAC's voltage range. The precision of this signal is limited by the DAC's quantization noise floor.

5.1.2 Limitations due to Sampling Rate

The ADCs and DACs as interfaces between the analog and digital domains do not only limit the achievable EMI reduction, but also the suppressible frequency range.

The first limiting factor for the interfaces' frequency range is the sampling rate f_s. According to the Nyquist-Shannon theorem, only frequencies below half the sampling rate (Nyquist frequency) can be measured and generated. So, the suppressible frequency range is limited by half of the sampling rate. Obviously, the rest of the digital cancellation system must be capable to operate the interface circuits at this rate.

Although the Nyquist-Shannon theorem is the hard limit for the suppressible frequency range, it is not the only one. The other important limit results from the aliasing effect that occurs if the signal's frequency range exceeds the Nyquist frequency. This effect distorts the signal and hinders a successful EMI cancellation. So, frequencies above the Nyquist frequency must be avoided. For both the ADC and DAC, this can be done by low-pass filtering the signals in analog domain. However, since low-pass filters have a limited steepness beyond their cutoff frequency, it must be set well below the Nyquist frequency to ensure a sufficient attenuation for higher frequencies. Therefore, the introduced low-pass filters are an additional limiting factor for the suppressible frequency range.

The theoretical limitations due to the sampling rate and vertical resolution are depicted in Figure 5.3. The sampling rate is assumed to be 200 MHz in reference to Table 5.1. A vertical resolution of 10 to 16 bits is reasonable considering already available components (Table 5.1). Assuming a single sine wave, the EMI can be suppressed by the SNR. This is the assumed theoretical limit. Since the SNR should be frequency-independent, the achievable EMI reduction will theoretically be constant up the Nyquist frequency and then drop to 0 dB. This performance is very promising since it is much higher than all previously discussed for high frequencies.

5.1.3 Limitations due to Delays in Signal Processing

There may be no limited gain-bandwidth product for digital systems (in comparison to analog amplifiers), but there are unavoidable delay times due to the analog-to-digital conversion, signal processing and digital-to-analog conversion. In Table 5.1, different digital components are summarized that have already been used in the realization of DAEFs. These comprise a **d**igital **s**ignal **p**rocessor (DSP), a **f**ield **p**rogrammable **g**ate **a**rray (FPGA), ADCs and DACs. The sampling rates (or clock frequencies) are extracted from the data sheets. It can be found that the ADCs have a conversion time (or pipeline delay) of 8.5 to 16 clock periods. Considering the sampling rate, significant delay times result for the acquisition of

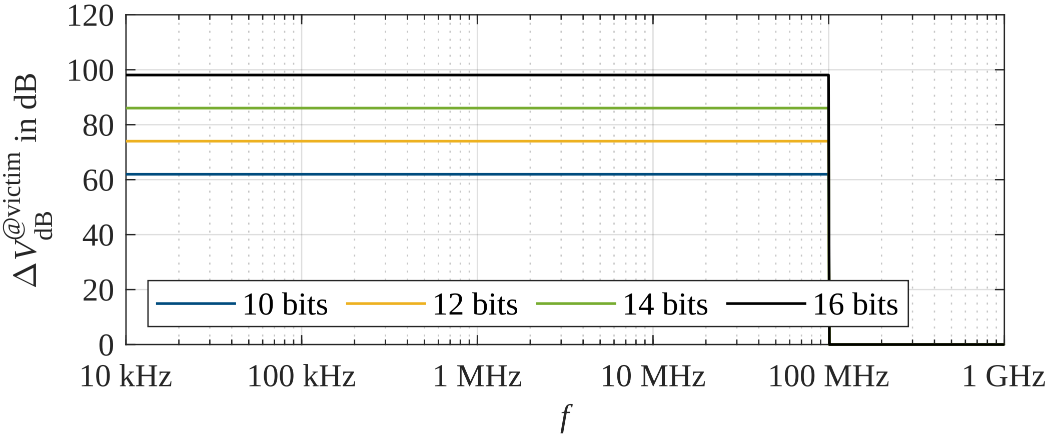

Figure 5.3: Theoretical performance of DAEFs for a sampling rate of 200 MHz and different vertical resolutions

signals. DACs may take only one clock period to output the analog signal. In the following, it is assumed that the DSP and FPGA only need one clock period to process the signal (inversion and amplification).

Component	Type	Sampling rate	Operations	Delay	Bits	Publ.
TMS320F28335	DSP	150 MHz [67]	1 (assumed)	$\approx$ 7 ns		[9]
XC2C64A	FPGA	240 MHz [68]	1 (assumed)	$\approx$ 4 ns		[10]
KAD5514P	ADC	250 MSPS [69]	8.5 [69]	34 ns	14	[9, 10]
ADS4229	ADC	250 MSPS [70]	16 [70]	64 ns	12	[63]
ISL5957	DAC	260 MSPS [71]	1	$\approx$ 4 ns	14	[9, 10]
DAC5662A	DAC	275 MSPS [72]	1	$\approx$ 4 ns	12	[63]

Table 5.1: Digital components of DAEFs

The total delay time for sensing, amplifying and injecting may be in the range of several tens of ns for these high-end components. The feedback and feedforward DAEFs will be limited by this delay time like their analog counterparts in Sections 4.3.1.c) and 4.3.2.c). For feedforward DAEFs, there is a race between EMI and anti-EMI. By increasing the length of the EMI path, the signal processing times of the feedforward AEF can theoretically be compensated (the delay times of feedback topologies cannot be compensated since there is no race between EMI and anti-EMI). Here, it is beneficial that signals travel slower through, e.g., cables and printed circuit boards since shorter geometrical lengths are required to compensate the signal processing delays. For typical dielectrics between and around the conductors, the propagation speed of electrical signals is reduced to values between $0.29c_0$ and $0.70c_0$ [19, p. 20]. Considering a total delay time of at least 40 ns and a “slow” propagation of $0.29c_0$, the EMI signal’s path must be extended by approximately 3.5 m. Since this length is too much for most practical realizations, this approach is not feasible.

By using the equations of the Sections 4.3.1.c) and 4.3.2.c) for the propagation delays, the achievable EMI reduction can be calculated to the results presented in Figure 5.4. The delay times pose a significant restriction for the performance of this concept. Since the time-domain signals are fundamentally the same as for the FB and FF AEFs, they are not depicted again.

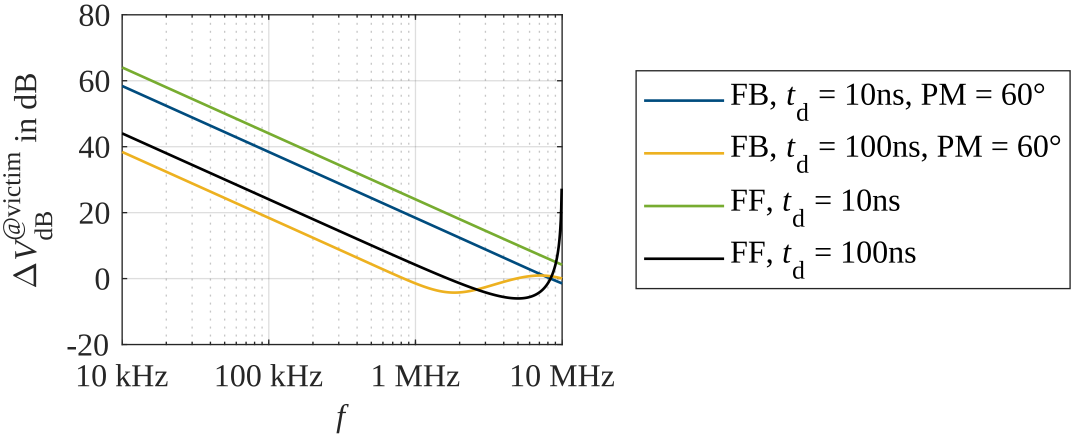

Figure 5.4: Theoretical performance of DAEFs for different propagation delays

To overcome the issue of unavoidable delay times, another strategy is proposed in [73]. Assuming quasi-periodic disturbances, the EMI can be measured in one period, processed and injected back into the system in following periods. By doing so, there is enough time for the digital signal processing. To compensate remaining delay times (e.g. of the DAC), the digital hardware can output the cancellation signal earlier than the EMI occurs. A similar approach will be pursued in the later chapters of this thesis.

5.2 Applications

In Table 5.2, some application results of DAEFs are summarized (PV stands for **p**hoto**v**oltaic). In all of these publications, the EMI reduction is given by a comparison of the disturbances with and without the DAEF. So, the quoted EMI reductions comprise the active suppression of the injected signals and the passive attenuation of the analog components of the DAEFs. The found results are significantly better than the ones expected from the discussion of the signal processing delay times (Figure 5.4). So, a significant portion of the EMI reduction may be contributed by the passive attenuation of the DAEFs. Since the passive attenuation is not clearly stated in these publications, this point cannot be fully analyzed. However, it can be found that the results are far below the theoretical limitations of the digital hardware in regard to sampling rate and vertical resolution (Figure 5.3).

Application	at 150 kHz	at 1 MHz	at 10 MHz	at 30 MHz	Publ.
DC-to-DC converter	25 dB	20 dB	30 dB	20 dB	[9]
Switched-mode power supply	20 dB	10 dB	10 dB	5 dB	[10]
Grid-tied PV microinverter	5 dB	20 dB	25 dB	15 dB	[11]
Arc welding inverter	18 dB	30 dB	20 dB	15 dB	[63]

Table 5.2: Achieved EMI reductions of DAEFs in the literature

5.3 Chapter Summary

In this chapter, it has been found that DAEFs are limited by the signal processing delay, sampling rate and vertical resolution of the digital system. The sampling rates and vertical resolutions of already available digital devices would allow for very good cancellation results, especially for high frequencies. However, the delay times resulting from the feed-forward or feedback signal processing can hinder the DAEF from reaching the digital hardware's limitations. This leads to the question if there are other possibilities to generate the cancellation signal in order to better utilize the performance of digital cancellation systems. To answer this question, cancellation techniques of other disciplines are investigated. The considered fields are power quality and acoustics.

6 Analysis of Active Power Filter (APF) Approaches for Active EMI Cancellation

As analyzed in Chapter 5, the performance of DAEFs is systematically limited by delay times that result from the feedback or feedforward approach for signal generation. To resolve this issue, methods used in power quality are analyzed and evaluated in regard to their applicability to active EMI cancellation.

One may think that the field of power quality is completely different to the field of EMC since the frequencies are much lower and the considered power is much higher. In EMC, high-frequency disturbances must be suppressed that are mostly decoupled from the low-frequency or DC operating currents and voltages. In power quality, the operating currents and voltages must be adjusted by compensating, e.g., low-frequency harmonics (of the grid frequency), reactive power, imbalances and/or neutral currents [13, 74–76]. Despite the differences in the application, the topologies of AEFs discussed in Chapter 4 are very similar to the ones in power quality [2]. So, from a topological point of view, **a**ctive **p**ower **f**ilters (APFs) are related to AEFs.

In the first section, the fundamentals of power quality and APFs are briefly discussed. A generic structure is presented that allows a general discussion of methods for cancellation signal generation. A promising approach for active EMI cancellation is identified and transferred. It is mathematically described and analyzed in regard to its limitations and robustness. The chapter closes with a short summary on the new insights.

6.1 Fundamentals

Due to the uprise of power electronics, there is an increasing number of nonlinear loads in the power grid that can cause harmonic currents, reactive power, imbalances between the phases and high neutral currents. These effects can degrade the system's efficiency and power factor. They can also cause EMI problems for other consumers and communication networks. [13]

The conventional solution to this problem were passive filters made of inductors and capacitors. Although passive filters are cheap and simple [76], they suffer from, e.g., fixed compensations, resonances with the grid and large sizes [13]. To resolve this issue, APFs were proposed first by [12] in 1971. Interestingly, AEFs were basically introduced at the same time by [1].

APFs are applied to single- and three-phase power systems with high ratings in the range from 100 kVA to over 10 MVA [74]. Since the APF must compensate low-frequency harmonics, reactive power and imbalances in these systems, the power rating of APFs is much higher than the one of AEFs [55]. Therefore, linear electronics are not feasible anymore and switching power electronics must be applied for the generation of the cancellation signals [55]. At first, bipolar transistors and MOSFETs were used for small ratings. Afterward, static induction thyristors and gate-turn-off thyristors were applied. The development of APFs got a boost by newly introduced IGBTs. This development was supported by improved sensor technologies. [13]

Another important factor is the control hardware for the APFs. At first, discrete analog and digital components were used. Later, microprocessors, microcontrollers and digital signal processors enabled the realization of complex algorithms. These digital devices were already available at reasonable costs in 1999. [13]

It is plausible that APFs were digitized much earlier than AEFs (2013, Chapter 5) since the considered frequencies are only low multiples of the power systems frequency. As discussed in Chapter 5, there are fast digital devices that are applicable to high-frequency EMI today. Considering the rapid development of APFs, digital EMI cancellation strategies could experience a similar rise in the following years.

6.2 Generic Structure

A generic structure for APFs is derived from the descriptions in [13, 74] and depicted in Figure 6.1. This representation is very simplistic and shows only the basic building blocks. For the sake of simplicity, a feedforward system is discussed. In practical applications, feedback systems are commonly applied to improve the precision of the cancellation signals [74, 77]. There is much more to the design and realization of APFs that is beyond the scope of this work.

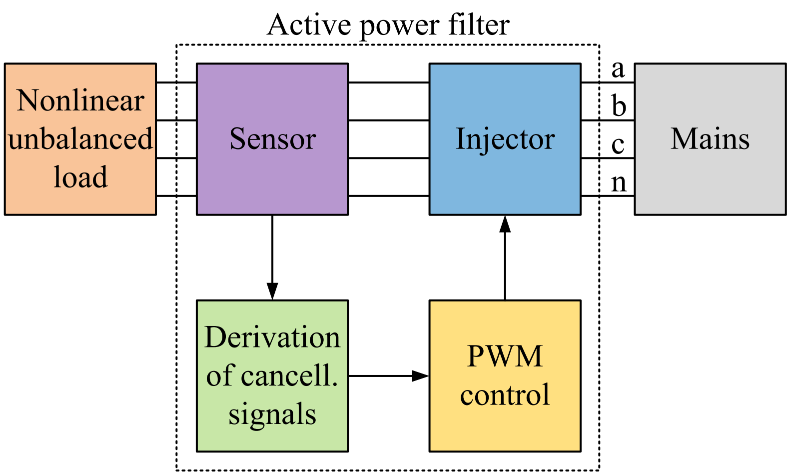

Figure 6.1: A generic structure for active power filters

Compared to the fundamental topologies of AEFs in Figure 4.1, the relatedness between these active filters becomes quite obvious. In both cases, there is a source of unwanted signals or disturbances. Here, it is a nonlinear unbalanced load in a three-phase (a, b, c) system with neutral conductor (n) that generates harmonics, reactive power and imbalances. The mains are the victim.

The sensor is used to measure the voltage and current signals on the lines. For voltage measuring, voltage transformers, Hall-effect voltage sensors or isolation amplifiers can be applied [13]. For current measuring, current transformers or Hall-effect current sensors can be used [13]. From these measured quantities, the necessary compensation (i.e. cancellation) signals can be derived.

As stated before, APFs use inverter stages with switching power devices as injectors due to the high power rating. Interestingly, these systems do not need an additional power supply. The injectors comprise storage elements (capacitors and injectors) that are charged by the mains through the injector and provide the necessary energy for cancellation [13].

There are different methods to find the necessary cancellation signals. These are discussed and evaluated in more detail in the next section.

6.3 Review of Methods for Cancellation Signal Generation

In this section, methods of APFs for the generation of cancellation signals are discussed. Fundamentally, there are methods using the frequency or time domain [13, 74–76, 78].

6.3.1 Frequency Domain

A pragmatic and effective approach for the generation of the cancellation signals is the Fourier analysis. At first, the signals at the lines are measured (Figure 6.2, top left). These can be transferred to the frequency domain (Figure 6.2, top right) by using the Fourier transform [13] (i.e. an FFT on digital hardware [74–77]). By doing so, the unwanted harmonics can easily be identified in the frequency domain (Figure 6.2, center right). The cancellation signal is synthesized from the inverted unwanted harmonics (Figure 6.2, center left) [13, 77]. By superposing the cancellation signals with the signals on the lines (Figure 6.2, bottom left), only the desired harmonics remain (Figure 6.2, bottom right).

This method enables the compensation of complex frequency responses (and, therefore, time constants) and delay times by adjusting the amplitudes and phases of the inverted harmonics before synthesizing the cancellation signal. This compensation can significantly improve the performance of APFs (and also AEFs and DAEFs).

The APF must be synchronized to the grid's fundamental frequency. If there is only a slight frequency deviation between the APF and the grid, the signals will slide apart and degrade the cancellation performance. For an accurate APF, the acquisition time must be exactly one or multiple grid periods and the acquisition reference point must be synchronized to the grid [77]. This can be realized by, e.g., a **p**hase-**l**ocked **l**oop (PLL) [77, 78] or a voltage observer [77].

Despite the potentials, there are some drawbacks. The system must acquire the disturbed

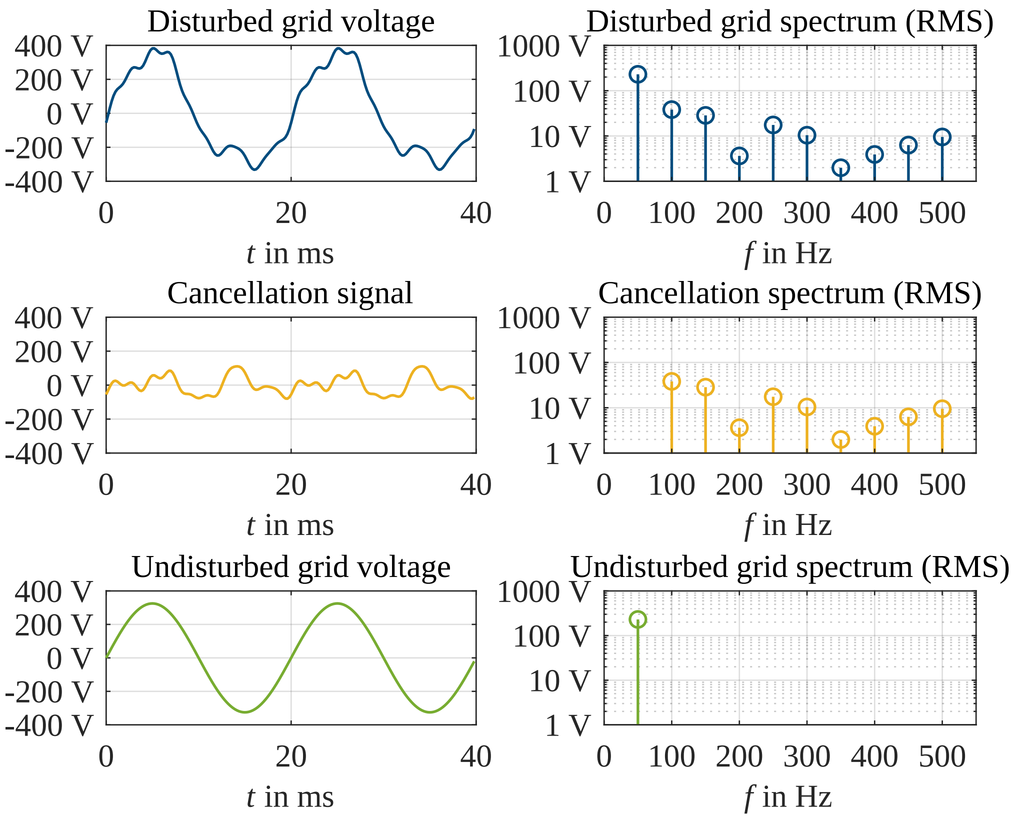

Figure 6.2: Exemplary signals for one line of the power grid

signals of at least one complete period so that the FFT is applicable [74, 76, 77]. Afterward, the FFT must be calculated that is a time-consuming operation, especially for a large number of harmonics [13]. The computation time also increases with the number of considered harmonics [75, 78]. Due to the required calculation, the cancellation signal will be applied in a later period than the disturbed signals are acquired. Therefore, this method requires a stationary operation of the power system so that the information of the previous periods is still valid for the periods in which the cancellation signal is injected [75, 77].

This approach is very promising for the active cancellation of quasi-periodic EMI since complex frequency responses and delay times can be compensated by adjusting the harmonics for cancellation. Therefore, an active EMI cancellation concept for this method will be derived later.

6.3.2 Time Domain

In time domain, a very simple approach with a band-stop filter can be used to find the right cancellation signals for the suppression of harmonics. The lines' signals comprising the wanted fundamental wave and the unwanted harmonics are measured. To find the cancellation signal for the unwanted harmonics, the measured signals are filtered by a band-stop filter that removes the fundamental wave. Now, this filtered signal only contains the unwanted harmonics. This signal is inverted and used as cancellation signal [79, 80]. This method is simple, but it is fundamentally limited by the bandwidths and delays of the system [77, 80]. This structure can directly be compared to AEFs where the unwanted EMI is extracted by applying high-pass filters. So, this time-domain method is no solution to improve the performance of AEFs.

There are many more control methods in time domain that are based on specialized theories for the application in power systems [13]. These comprise, e.g., the instantaneous power theory or the synchronous frame d-q theory [13]. Since there is no direct connection to EMI of power electronic systems, these methods are not investigated further.

6.4 Application of the FFT Method to Active Cancellation of Quasi-Periodic EMI

In this section, the FFT method of APFs is transferred for the application to quasi-periodic EMI. At first, the concept is presented. The resulting system is mathematically described and an algorithm is developed. The potential limitations of the method are elaborated and analyzed. The method's robustness against measurement or identification deviations is investigated in detail.

6.4.1 Concept

A possible concept for a digital active EMI cancellation system using the FFT method is depicted in Figure 6.3. As for AEFs and DAEFs, there is an EMI source, an EMI victim, an injector and a sensor. The decoupling circuit is motivated by the theory of Chapter 3. In this concept, a feedback topology is chosen that enables a successive correction of the cancellation signal as discussed later.

The sensed signal $x^{\text{@sensor}}(t)$ (x as either a voltage or current signal) is passed through an ADC to the calculation block (hence the time-discrete quantity $x^{\text{@sensor}}(n)$). This element identifies the harmonics by an FFT, corrects amplitude and phase responses and passes the respective harmonics $X_{\text{anti}}(kf_0)$ to the synthesizer that generates the time-discrete cancellation signal $x_{\text{anti}}(n)$. The DAC transfers the signal back to the time-continuous analog domain ($x_{\text{anti}}(t)$).

This method requires quasi-periodic EMI since the FFT is not applicable otherwise. The system acquires the (residual) EMI in one time interval, calculates the parameters for cancellation in another interval and injects the cancellation signal in all following intervals. So, the cancellation signal is based on information of the past. Without periodicity, the injected anti-EMI will not match with the current EMI. AEFs and DAEFs do not have the same requirement since they generate their cancellation signals directly from the measured quantity.

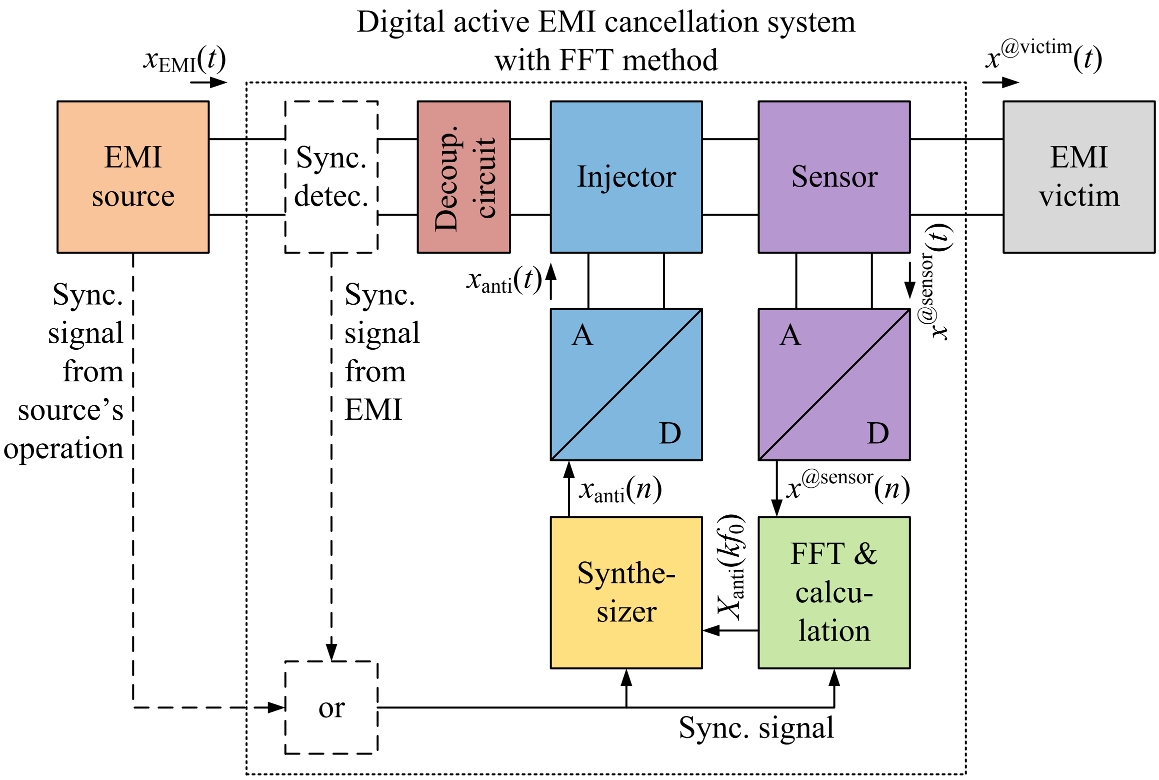

Figure 6.3: Concept for a digital active EMI cancellation system applying the FFT method

For this procedure of acquisition, calculation and generation, the cancellation system must be synchronized to the EMI source. In many cases, the EMI source can provide a synchronization signal for the synthesizer. In power electronic systems, the control signals for the power transistors are convenient signals since they are usually very stable and digitally available. If such a signal is unavailable, the system can be synchronized to the EMI by a suitable detection circuit (e.g. voltage observer or PLL, Section 6.3.1). One could come to the idea to use the sensor signal $x^{@\mathrm{sensor}}(t)$ since it is measured in any case. This approach can be problematic since the cancellation system suppresses the signal $x^{@\mathrm{sensor}}(t)$. Therefore, it is possible that the cancellation system eliminates its own synchronization signal. In this case, additional effort is necessary so that the cancellation system maintains synchronicity with the EMI.

If the fundamental frequency of the EMI is known (e.g. the switching frequency of a power electronic system), the length of the required acquisition window and the length of the necessary cancellation signal can be calculated. Using the synchronization signal, these windows can be locked to the EMI. For many power electronic systems, there may be some frequency drift or the fundamental frequency may even be completely unknown. In these cases, the system must identify the actual fundamental frequency. There is no trivial solution for this problem [21, co-author].

6.4.2 Proposed Algorithm

In the following, an algorithm is derived for the application of the FFT method to active EMI cancellation. At first, the formula for the calculation of the necessary cancellation signal is derived. This formula requires information on the EMI without active cancellation and on the coupling of the cancellation source to the overall system. There are different possibilities for the acquisition of this information. Some of these are briefly discussed. An algorithm is proposed that characterizes the system and calculates the required cancellation signals. An iterative application of the algorithm is suggested to improve the cancellation results.

a) Calculation of the Required Cancellation Signal

For the FFT method, the mathematical description of Section 3.1.2.c) can be applied again. To do so, the spectral frequency f is replaced by the harmonics kf_0 (where f_0 is the fundamental frequency). Here, the signals at the sensor and the propagation to the sensor are considered. The superscripts are changed accordingly to '@sensor' and '$\rightarrow$ sensor'. Since the EMI at the sensor $X_{\mathrm{EMI}}^{@\mathrm{sensor}}(kf_0)$ can directly be measured, it is not necessary to identify the EMI source $X_{\mathrm{EMI}}(kf_0)$ and propagation path $H_{\mathrm{EMI}}^{\rightarrow\mathrm{sensor}}(kf_0)$. The signals are denoted by X since they can represent voltages or currents. The resulting equations are given in (6.1)-(6.3):

$$X_{\mathrm{res}}^{@\mathrm{sensor}}(kf_0) = X_{\mathrm{EMI}}^{@\mathrm{sensor}}(kf_0) + H_{\mathrm{anti}}^{\rightarrow\mathrm{sensor}}(kf_0) \cdot X_{\mathrm{anti}}(kf_0) \tag{6.1}$$

$$\stackrel{!}{=} 0 \tag{6.2}$$

$$\Rightarrow X_{\mathrm{anti}}(kf_0) = -\frac{X_{\mathrm{EMI}}^{@\mathrm{sensor}}(kf_0)}{H_{\mathrm{anti}}^{\rightarrow\mathrm{sensor}}(kf_0)} \tag{6.3}$$

b) Options for System Characterization

To be able to calculate the necessary harmonics $X_{\mathrm{anti}}(kf_0)$ for cancellation, only the EMI at the sensor $X_{\mathrm{EMI}}^{@\mathrm{sensor}}(kf_0)$ and the transfer function $H_{\mathrm{anti}}^{\rightarrow\mathrm{sensor}}(kf_0)$ must be found. $X_{\mathrm{EMI}}^{@\mathrm{sensor}}(kf_0)$ can be found by measuring the time-domain EMI at the sensor and applying an FFT. $H_{\mathrm{anti}}^{\rightarrow\mathrm{sensor}}(kf_0)$ could be found by using, e.g., a **v**ector **n**etwork **a**nalyzer (VNA). It is also possible to use the cancellation system for this identification. This method is convenient since the hardware will be needed anyway. Furthermore, the identification can be done during operation of, e.g., the power electronic system. This is an interesting feature since the transfer functions can be determined for the actual operating point. This can make a significant difference if, e.g., inductors show saturation behavior due to large operating currents. In the following, the identification process with the cancellation system is described.

c) Algorithm

The complete signal generation procedure of the FFT method is illustrated in Figure 6.4. At the top, the EMI at the sensor $x_{\mathrm{EMI}}^{@\mathrm{sensor}}(t)$ is shown for 5 periods. The generated anti-EMI $x_{\mathrm{anti}}(t)$ and the anti-EMI at the sensor $x_{\mathrm{anti}}^{@\mathrm{sensor}}(t)$ are depicted in the middle. The sensor signal $x^{@\mathrm{sensor}}(t)$ results from superposing EMI and anti-EMI and can be found at the bottom.

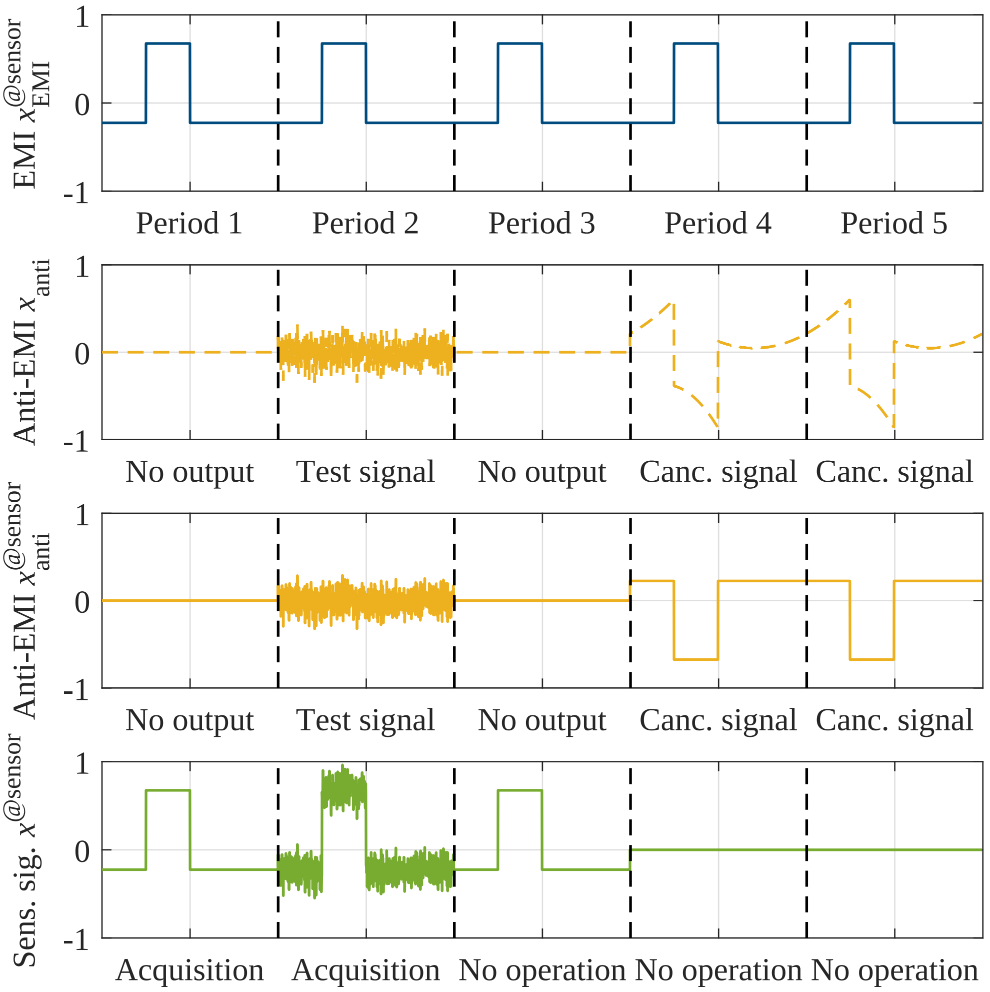

Figure 6.4: Signal generation procedure of the FFT method

The goal is to find the right cancellation signal so that the sensor signal is constant 0. The cancellation system takes at least three periods to eliminate the EMI:

1. In the first period, the cancellation system acquires the signal $x_{\text{EMI}}^{@\text{sensor}}(t)$ in time domain.

2. In the second period, the cancellation system injects an arbitrary test signal $x_{\text{anti,test}}(t)$ to identify the transfer function $H_{\text{anti}}^{\rightarrow\text{sensor}}(kf_0)$. During this period, the cancellation system acquires the superposition of $x_{\text{EMI}}^{@\text{sensor}}(t)$ and $x_{\text{anti,test}}^{@\text{sensor}}(t)$.

3. During the third period, the cancellation system calculates the necessary anti-EMI. To do so, $X_{\text{EMI}}^{@\text{sensor}}(kf_0)$ and $H_{\text{anti}}^{\rightarrow\text{sensor}}(kf_0)$ must be determined.
   The disturbing harmonics at the sensor $X_{\text{EMI}}^{@\text{sensor}}(kf_0)$ can immediately be found by applying an FFT on the time-domain signal $x_{\text{EMI}}^{@\text{sensor}}(t)$.
   To find the transfer function $H_{\text{anti}}^{\rightarrow\text{sensor}}(kf_0)$, the influence of the test signal $x_{\text{EMI}}(t)$ on

the sensor signal must be identified. The time-domain response $x_{\text{anti,test}}^{@\text{sensor}}(t)$ is found by subtracting the known disturbances $x_{\text{EMI}}^{@\text{sensor}}(t)$ from the superposed sensor signal $x_{\text{EMI}}^{@\text{sensor}}(t) + x_{\text{anti,test}}^{@\text{sensor}}(t)$ of period 2. Afterward, the harmonics $X_{\text{anti,test}}^{@\text{sensor}}(kf_0)$ are determined from the time-domain signal $x_{\text{anti,test}}^{@\text{sensor}}(t)$ by an FFT. Now, the transfer function $H_{\text{anti}}^{\rightarrow\text{sensor}}(kf_0)$ can be found by dividing the systems response $X_{\text{anti,test}}^{@\text{sensor}}(kf_0)$ by the known test signals $X_{\text{anti,test}}(kf_0)$ according to (6.4):

$$H_{\text{anti}}^{\rightarrow\text{sensor}}(kf_0) = \frac{X_{\text{anti,test}}^{@\text{sensor}}(kf_0)}{X_{\text{anti,test}}(kf_0)} \tag{6.4}$$

By using (6.3), the cancellation signal's harmonics $X_{\text{anti}}(kf_0)$ can be calculated. In the last step, the time-domain signal $x_{\text{anti}}(t)$ is constructed by (2.8) or an inverse FFT. This signal is injected for period 4 and onward. By doing so, the EMI should be eliminated leading to a residual EMI of ideally constant 0.

Note that the shapes of $x_{\text{anti}}(t)$ and $x_{\text{anti}}^{@\text{sensor}}(t)$ differ due to the transfer function $H_{\text{anti}}^{\rightarrow\text{sensor}}(kf_0)$. The injected cancellation signal $x_{\text{anti}}(t)$ has the required shape so that the signals at the sensors $\left(x_{\text{anti}}^{@\text{sensor}}(t) \text{ and } x_{\text{EMI}}^{@\text{sensor}}(t)\right)$ cancel each other out.

d) Iterative Application for Improved Results

In practical implementations, there may be no ideal cancellation after one iteration due to, e.g., measurement noise or numerical errors. To oppose this problem, the procedure described above can be applied again to refine the cancellation signal. To do so, the found anti-EMI is continuously injected by the cancellation system. The cancellation system acquires the residual EMI $x_{\text{res}}^{@\text{sensor}}(t)$ and transfers it to $X_{\text{res}}^{@\text{sensor}}(kf_0)$ by an FFT. The transfer function can also be identified anew to account for, e.g., weak nonlinear effects. To find the cancellation harmonics, (6.3) is adjusted to (6.5):

$$X_{\text{anti,new}}(kf_0) = X_{\text{anti,old}}(kf_0) - \frac{X_{\text{res}}^{@\text{sensor}}(kf_0)}{H_{\text{anti,new}}^{\rightarrow\text{sensor}}(kf_0)} \tag{6.5}$$

The new cancellation signal is found by superposing the "old" cancellation signal with the new portion that eliminates the residual EMI. This process can be repeated indefinitely to optimize the cancellation signal and, therefore, the cancellation results.

6.4.3 Limitations due to Frequency Deviations

Frequency deviations have a twofold influence on the active cancellation system: one on the signal acquisition and one on the signal generation. To achieve a precise FFT result, the time-domain signal must repeat itself perfectly in regard to the considered time window. If this window is only a few samples too long or too short, the identified harmonics will differ in amplitude, phase and frequency from the actual harmonics of the signal. In Sections 6.4.7 and 6.4.8, it will be shown that the method is rather robust against deviations in amplitude and phase.

The influence of frequency deviations on the signal generation has already been analyzed in Section 3.1.3.b). If there is a frequency deviation, EMI and anti-EMI will shift apart over time leading to a decreasing cancellation performance. To prevent this shift, the cancellation system must repeatedly be synchronized to the EMI. However, this synchronization may also cause limitations that are discussed in the next section.

6.4.4 Limitations due to Synchronization Deviations

In this section, the limitations due to deviations in the synchronization are analyzed [15, author]. The cancellation signal is assumed to be ideally synthesized (no amplitude, phase or frequency deviations) but with deviations in the synchronization. The origin of these deviations depends on the implementation. As a very simple example, it is assumed that the power electronic system sends a trigger signal to the active cancellation system. This trigger must be detected by the digital hardware.

In Figure 6.5, exemplary signals are depicted. It is assumed that the external trigger is completely stable. The digital cancellation system checks at each of its sample points for a change in the trigger signal. In the best case, the system samples right after the external trigger signal, and there is basically no synchronization deviation t_{dev}. In the worst case, the system samples right before the external trigger signal. So, the system detects the trigger signal almost one sampling period later. This is the maximum deviation that can occur.

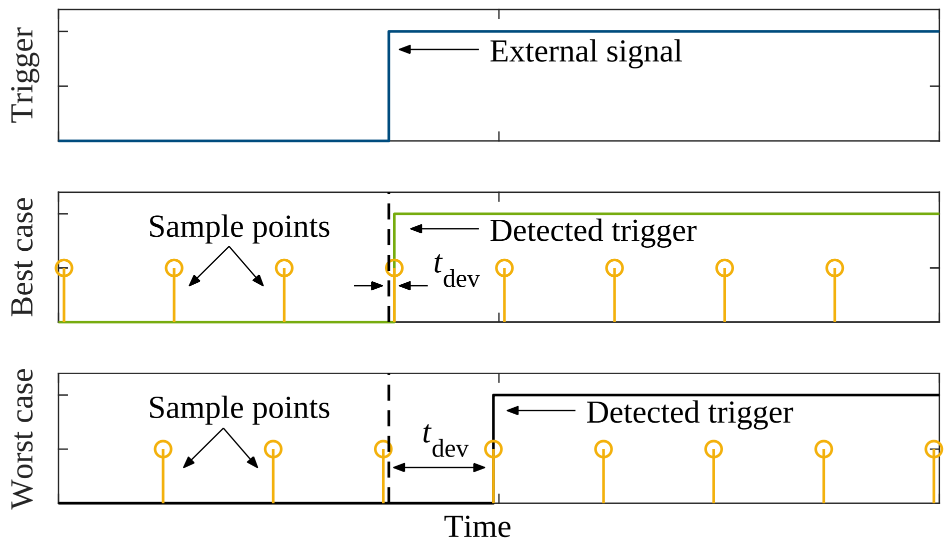

Figure 6.5: Example for a source of synchronization deviations: trigger detection

This synchronization deviation is basically stochastic. If the deviation was deterministic, it would be possible to compensate it by phase-shifting the anti-EMI's harmonics. Since this is not possible in the stochastic case, this source of deviation must be avoided. Stochastic synchronization deviations will cause the match between anti-EMI and EMI to be randomly rather good or rather bad from period to period. This issue is visualized in Figure 6.6 for a fundamental frequency of 10 MHz and a potential synchronization deviation of 10 ns.

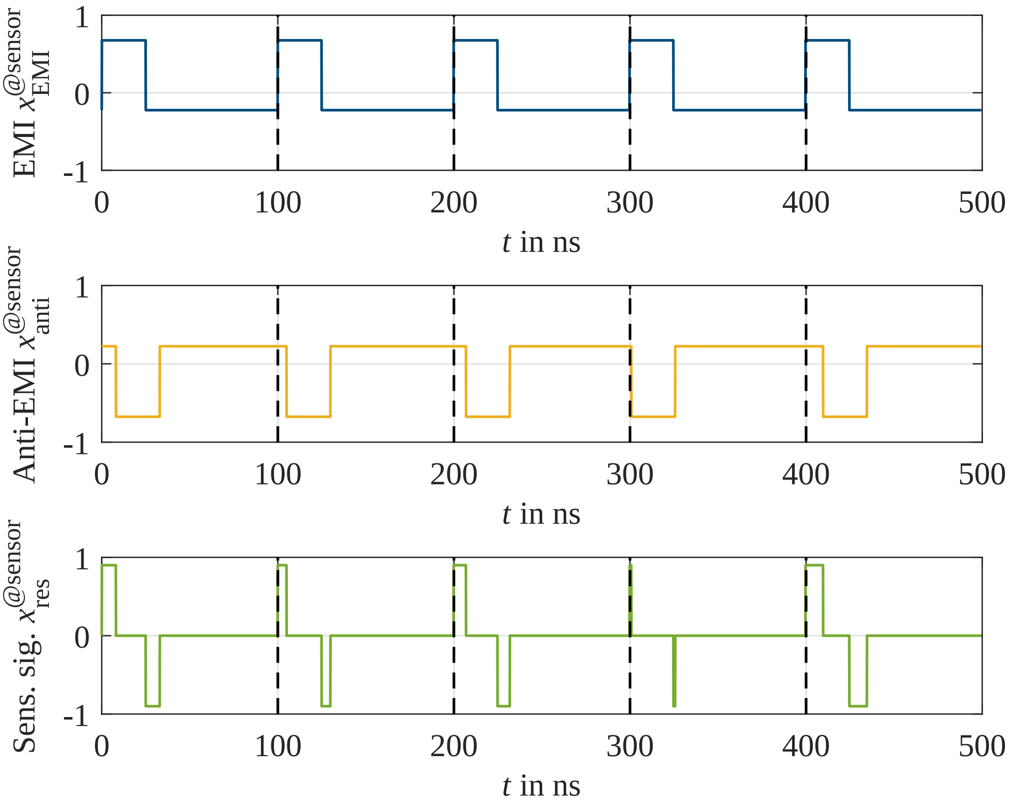

Figure 6.6: Signals for stochastic synchronization deviations

a) Mathematical Description

In the following, the influence of synchronization deviations on the achievable EMI reduction is mathematically described. For the sake of simplicity, the signals are evaluated at the victim. The EMI $x_{\text{EMI}}^{\text{@victim}}$ is defined by (6.6) with $A \in \mathbb{R}^+ \setminus \{0\}$ and $\varphi \in \mathbb{R}$:

$$x_{\text{EMI}}^{\text{@victim}}(t,f) = A \cdot e^{j2\pi f \cdot t + j\varphi} \tag{6.6}$$

It is assumed that the cancellation signal is randomly shifted by $t_{\text{dev}}(t) \in [0, T_{\text{dev}}]$ where $t_{\text{dev}}(t)$ is evenly distributed. Therefore, (6.7) follows:

$$x_{\text{anti}}^{\text{@victim}}(t,f) = -A \cdot e^{j2\pi f \cdot (t - t_{\text{dev}}(t)) + j\varphi} \tag{6.7}$$

The residual EMI is defined by (6.8) and (6.9):

$$x_{\text{res}}^{\text{@victim}}(t,f) = x_{\text{EMI}}^{\text{@victim}}(t,f) + x_{\text{anti}}^{\text{@victim}}(t,f) \tag{6.8}$$

$$\Rightarrow x_{\text{res}}^{\text{@victim}}(t,f) = A \cdot e^{j2\pi f \cdot t + j\varphi} - A \cdot e^{j2\pi f \cdot (t - t_{\text{dev}}(t)) + j\varphi} \tag{6.9}$$

For further analysis, the absolute values of the EMI and the residual EMI are introduced in (6.10)-(6.14):

$$\left|x_{\mathrm{EMI}}^{\mathrm{@victim}}(f)\right| = \left|A \cdot e^{j2\pi f \cdot t + j\varphi}\right| \tag{6.10}$$

$$= A \tag{6.11}$$

$$\left|x_{\mathrm{res}}^{\mathrm{@victim}}(t,f)\right| = \left|A \cdot e^{j2\pi f \cdot t + j\varphi} - A \cdot e^{j2\pi f \cdot (t - t_{\mathrm{dev}}(t)) + j\varphi}\right| \tag{6.12}$$

$$= A \cdot \left|1 - e^{-j2\pi f \cdot t_{\mathrm{dev}}(t)}\right| \tag{6.13}$$

$$= A \cdot \sqrt{2 - 2 \cdot \cos\left(2\pi f \cdot t_{\mathrm{dev}}(t)\right)} \tag{6.14}$$

Since the synchronization deviation changes randomly over time, also the achievable EMI reduction changes over time. In the following, two different criteria are discussed. The first is the worst-case EMI reduction that can occur. The second is the time-averaged EMI reduction.

b) Worst-Case EMI Reduction

The achievable EMI reduction $\Delta X_{\mathrm{dB}}^{\mathrm{@victim}}(f)$ is defined by (6.15):

$$\Delta X_{\mathrm{dB}}^{\mathrm{@victim}}(f) = 20\ \mathrm{dB} \cdot \log_{10}\left|\frac{x_{\mathrm{EMI}}^{\mathrm{@victim}}(f)}{x_{\mathrm{res}}^{\mathrm{@victim}}(t,f)}\right| \tag{6.15}$$

The worst-case $\Delta X_{\mathrm{dB,worst}}^{\mathrm{@victim}}(f)$ is defined by (6.16) and (6.17):

$$\Delta X_{\mathrm{dB,worst}}^{\mathrm{@victim}}(f) = \min\left\{\Delta X_{\mathrm{dB}}^{\mathrm{@victim}}(t,f)\right\} \tag{6.16}$$

$$= \min\left\{20\ \mathrm{dB} \cdot \log_{10}\left|\frac{x_{\mathrm{EMI}}^{\mathrm{@victim}}(f)}{x_{\mathrm{res}}^{\mathrm{@victim}}(t,f)}\right|\right\} \tag{6.17}$$

After inserting (6.11) and (6.14) and some solving, (6.18) results. The different cases for the minimum function can be solved to (6.19). Note that a negative reduction equals an amplification of the EMI.

$$\Rightarrow \Delta X_{\mathrm{dB,worst}}^{\mathrm{@victim}}(f) = \min\left\{-10\ \mathrm{dB} \cdot \log_{10}\left(2 - 2 \cdot \cos\left(2\pi f \cdot t_{\mathrm{dev}}(t)\right)\right)\right\} \tag{6.18}$$

$$= \begin{cases} -10\ \mathrm{dB} \cdot \log_{10}\left(2 - 2 \cdot \cos\left(2\pi f \cdot T_{\mathrm{dev}}\right)\right) & \text{for } f < 1/\left(2 \cdot T_{\mathrm{dev}}\right) \\ -10\ \mathrm{dB} \cdot \log_{10}(4) \approx -6\ \mathrm{dB} & \text{for } f \geq 1/\left(2 \cdot T_{\mathrm{dev}}\right) \end{cases} \tag{6.19}$$

In Figure 6.7, the worst-case EMI reduction $\Delta X_{\mathrm{dB,worst}}^{\mathrm{@victim}}(f)$ is depicted for different values of the potential synchronization deviation T_{dev}. For the implementation with trigger detection, T_{dev} equals the sampling period of the digital hardware. Considering common sampling rates (e.g. Table 5.1), the deviation may be in the range of a few ns. The value of 100 ps is given to account for prospective digital hardware or more stable implementations. Considering a frequency of 1 MHz and $T_{\mathrm{dev}} = 1$ ns, the worst-case EMI reduction is already decreased to approximately 44 dB. For $T_{\text{dev}} = 10$ ns, the achievable reduction drops already to 24 dB. So, it is very important to maintain a very precise synchronization.

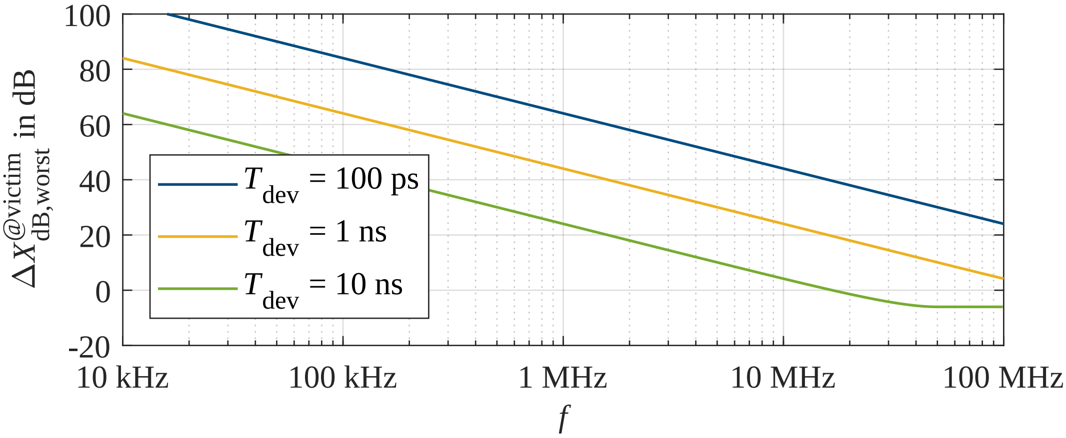

Figure 6.7: Worst-case EMI reduction for different potential synchronization deviations

c) Time-Averaged EMI Reduction

Of course, the worst-case does not apply all the time. Therefore, the time-averaged EMI reduction is discussed in the following. To do so, the RMS values of the signals are considered by (6.20)-(6.22) with (6.11) and (6.14):

$$\text{RMS}\left\{\left|x_{\text{EMI}}^{\text{@victim}}(f)\right|\right\} = \sqrt{\frac{1}{T_2 - T_1} \cdot \int_{T_1}^{T_2} A^2 \, dt} = A \tag{6.20}$$

$$\text{RMS}\left\{\left|x_{\text{res}}^{\text{@victim}}(f)\right|\right\} = \sqrt{\frac{1}{T_2 - T_1} \cdot \int_{T_1}^{T_2} \left(A \cdot \sqrt{2 - 2 \cdot \cos\left(2\pi f \cdot t_{\text{dev}}(t)\right)}\right)^2 dt} \tag{6.21}$$

$$= A \cdot \sqrt{\frac{1}{T_2 - T_1} \cdot \int_{T_1}^{T_2} \left(2 - 2 \cdot \cos\left(2\pi f \cdot t_{\text{dev}}(t)\right)\right) \, dt} \tag{6.22}$$

Since $t_{\text{dev}}(t)$ is stochastic, its period T can be assumed to be infinite. Therefore, T_1 and T_2 are pushed to $\pm\infty$ s in (6.23):

$$\Rightarrow \text{RMS}\left\{\left|x_{\text{res}}^{\text{@victim}}(f)\right|\right\} = A \cdot \sqrt{\lim_{T \to \infty \text{ s}} \left\{\frac{1}{2T} \cdot \int_{-T}^{+T} \left(2 - 2 \cdot \cos\left(2\pi f \cdot t_{\text{dev}}(t)\right)\right) \, dt\right\}} \tag{6.23}$$

Due to the assumption of an evenly distributed $t_{\text{dev}}(t) \in [0, T_{\text{dev}}]$, the integral can be rewritten to (6.24):

$$\Rightarrow \text{RMS}\left\{\left|x_{\text{res}}^{\text{@victim}}(f)\right|\right\} = A \cdot \sqrt{\frac{1}{T_{\text{dev}}} \cdot \int_{0}^{T_{\text{dev}}} \left(2 - 2 \cdot \cos\left(2\pi f \cdot t_{\text{dev}}\right)\right) \, dt_{\text{dev}}} \tag{6.24}$$

After calculating the integral, (6.25) follows:

$$\Rightarrow \mathrm{RMS}\left\{\left|x_{\mathrm{res}}^{@\mathrm{victim}}(f)\right|\right\} = A \cdot \sqrt{\frac{1}{T_{\mathrm{dev}}} \cdot \left[2t_{\mathrm{dev}} - \frac{1}{\pi f} \cdot \sin\left(2\pi f \cdot t_{\mathrm{dev}}\right)\right]_0^{T_{\mathrm{dev}}}} \tag{6.25}$$

(6.26) results from some more solving:

$$\Rightarrow \mathrm{RMS}\left\{\left|x_{\mathrm{res}}^{@\mathrm{victim}}(f)\right|\right\} = A \cdot \sqrt{2 - 2 \cdot \mathrm{sinc}\left(2\pi f \cdot T_{\mathrm{dev}}\right)} \;\text{ with }\; \mathrm{sinc}(x) = \frac{\sin(x)}{x} \tag{6.26}$$

So, the time-averaged EMI reduction $\Delta X_{\mathrm{dB,RMS}}^{@\mathrm{victim}}(f)$ can be calculated by (6.27)-(6.29):

$$\Rightarrow \Delta X_{\mathrm{dB,RMS}}^{@\mathrm{victim}}(f) = 20\ \mathrm{dB} \cdot \log_{10}\left(\frac{\mathrm{RMS}\left\{\left|x_{\mathrm{EMI}}^{@\mathrm{victim}}(f)\right|\right\}}{\mathrm{RMS}\left\{\left|x_{\mathrm{res}}^{@\mathrm{victim}}(f)\right|\right\}}\right) \tag{6.27}$$

$$= 20\ \mathrm{dB} \cdot \log_{10}\left(\frac{A}{A \cdot \sqrt{2 - 2 \cdot \mathrm{sinc}\left(2\pi f \cdot T_{\mathrm{dev}}\right)}}\right) \tag{6.28}$$

$$= -10\ \mathrm{dB} \cdot \log_{10}\left(2 - 2 \cdot \mathrm{sinc}\left(2\pi f \cdot T_{\mathrm{dev}}\right)\right) \tag{6.29}$$

In Figure 6.8 the time-averaged EMI reduction $\Delta X_{\mathrm{dB,RMS}}^{@\mathrm{victim}}(f)$ is depicted for different potential synchronization deviations T_{dev}. The results are similar to the ones of Figure 6.7, but $\Delta X_{\mathrm{dB,RMS}}^{@\mathrm{victim}}(f)$ is approximately 3 dB higher than $\Delta X_{\mathrm{dB,worst}}^{@\mathrm{victim}}(f)$ for the considered frequency range. This is plausible since the worst-case applies only rarely in time.

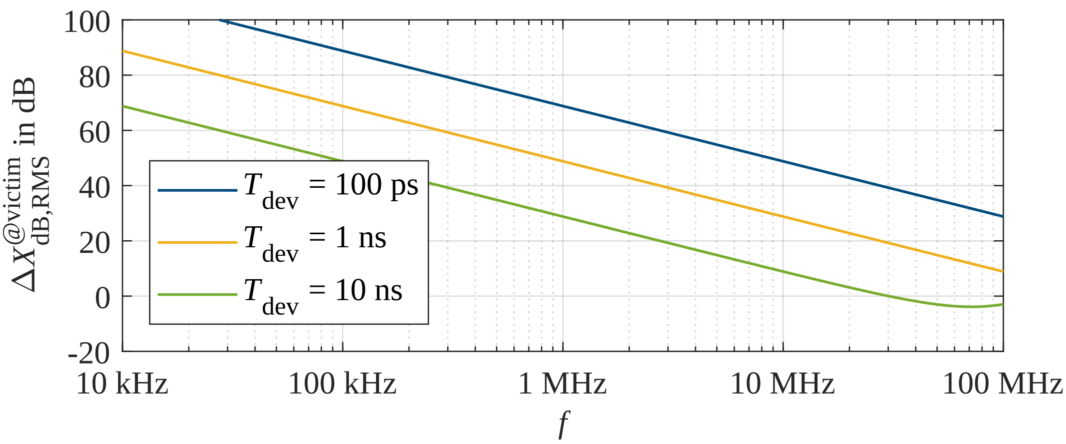

Figure 6.8: Time-averaged EMI reduction for different potential synchronization deviations

The stochastic synchronization deviation causes non-periodic changes of the residual EMI that can lead to an increased noise floor. This noise floor takes up some of the power of the signals. This contribution is already respected in $\mathrm{RMS}\left\{\left|x_{\mathrm{res}}^{@\mathrm{victim}}(f)\right|\right\}$ and, therefore, also in $\Delta X_{\mathrm{dB,RMS}}^{@\mathrm{victim}}(f)$.

Synchronization deviations can potentially have a large impact on the achievable EMI reduction. Therefore, synchronization deviations should be minimized to maximize the effectivity of the proposed method. One very simple solution is to implement the control of the power electronic device and the generation of the cancellation signal on the same digital device. In this case, there is an intrinsic synchronization and no synchronization deviations occur.

6.4.5 Limitations due to Digital Hardware

Like DAEFs (5), the FFT method is also limited by the digital hardware. The achievable reduction is limited by the vertical resolution as discussed in Section 5.1.1. The frequency limitations are described in Section 5.1.2.

Regarding the FFT, there are some special requirements and potentials. For a precise result, the FFT must be done very precisely for one or multiple periods of the (residual) EMI. Just a few sample points too much or too few in the acquisition time window can deteriorate the performance of the algorithm significantly.

It is recommended to acquire multiple periods of the EMI so that the FFT's precision is enhanced by the so-called “processing gain”. The FFT result may also be improved by oversampling in which the Nyquist frequency (Section 5.1.2) is set far above the highest relevant harmonic of the signal.

6.4.6 Limitations due to Amplitude and Phase Deviations

As analyzed in Section 3.1.3.a), the amplitudes and phases of the cancellation signal must be set very precisely to achieve convincing cancellation results. One could assume that the system and signal identification of the FFT method must also be extremely precise. However, it can be found that the method is rather robust against deviations. This is analyzed in the following section.

6.4.7 Robustness against Deviations in Identified Transfer Function

Considering the calculation of the cancellation signal in (6.3), it can be found that there are two potential error sources: deviations in the determined transfer function and deviations in the determined EMI. At first, deviations in the transfer function $H_{\text{anti}}^{\rightarrow\text{sensor}}(kf_0)$ are discussed. This analysis extends the description of [81, supervisor].

a) Mathematical Description

For analysis, it is assumed that the **det**ermined transfer function $H_{\text{anti,det}}^{\rightarrow\text{sensor}}(kf_0)$ deviates from the real transfer function $H_{\text{anti}}^{\rightarrow\text{sensor}}(kf_0)$ by $a_{\text{dev}} \in \mathbb{R}$, $a_{\text{dev}} > -1$ in amplitude and $\varphi \in \mathbb{R}$ in phase according to (6.30):

$$H_{\text{anti,det}}^{\rightarrow\text{sensor}}(kf_0) = (1 + a_{\text{dev}}) \cdot e^{j\varphi_{\text{dev}}} \cdot H_{\text{anti}}^{\rightarrow\text{sensor}}(kf_0) \tag{6.30}$$

Considering that (6.3) is calculated with the determined transfer function (and not the real one), the cancellation signal will deviate from the ideal one according to (6.31):

$$\overset{(6.3)}{\Rightarrow} X_{\text{anti,1}}(kf_0) = -\frac{X_{\text{EMI}}^{@\text{sensor}}(kf_0)}{H_{\text{anti,det}}^{\rightarrow\text{sensor}}(kf_0)} \tag{6.31}$$

This is the cancellation signal for the first iteration $X_{\text{anti,1}}(kf_0)$. In reference to (6.1), the residual EMI after the first iteration $X_{\text{res,1}}^{@\text{sensor}}(kf_0)$ can be calculated by (6.32):

$$\overset{(6.1)}{\Rightarrow} X_{\text{res,1}}^{@\text{sensor}}(kf_0) = X_{\text{EMI}}^{@\text{sensor}}(kf_0) + H_{\text{anti}}^{\rightarrow\text{sensor}}(kf_0) \cdot X_{\text{anti,1}}(kf_0) \tag{6.32}$$

This calculation represents the superposition of EMI and anti-EMI in the real system. Therefore, the actual transfer function $H_{\text{anti}}(kf_0)$ (and not the identified one) is used to find the residual EMI of the system. By inserting (6.30) and (6.31), (6.33) follows:

$$\Rightarrow X_{\text{res,1}}^{@\text{sensor}}(kf_0) = X_{\text{EMI}}^{@\text{sensor}}(kf_0) \cdot \left(1 - \frac{1}{(1+a_{\text{dev}}) \cdot e^{j\varphi_{\text{dev}}}}\right) \tag{6.33}$$

The refined cancellation signal for the second iteration can be calculated by (6.5). To do so, the determined transfer function and the previously found cancellation signal according to (6.31) are inserted. So, (6.34) follows for $X_{\text{anti,2}}(kf_0)$:

$$\overset{(6.5)}{\Rightarrow} X_{\text{anti,2}}(kf_0) = -\frac{X_{\text{EMI}}^{@\text{sensor}} + X_{\text{res,1}}^{@\text{sensor}}}{H_{\text{anti,det}}^{\rightarrow\text{sensor}}(kf_0)} \tag{6.34}$$

Combining (6.1), (6.30), (6.33) and (6.34) leads to (6.35) and (6.36) after some solving:

$$\overset{(6.1)}{\Rightarrow} X_{\text{res,2}}^{@\text{sensor}}(kf_0) = X_{\text{EMI}}^{@\text{sensor}}(kf_0) + H_{\text{anti,det}}^{\rightarrow\text{sensor}}(kf_0) \cdot X_{\text{anti,2}}(kf_0) \tag{6.35}$$

$$= X_{\text{EMI}}^{@\text{sensor}}(kf_0) \cdot \left(1 - \frac{1}{(1+a_{\text{dev}}) \cdot e^{j\varphi_{\text{dev}}}}\right)^2 \tag{6.36}$$

This process can be repeated indefinitely. By continuing the pattern of (6.33) and (6.36), the residual EMI of the n-th iteration (with $n \in \mathbb{N} \cup \{0\}$) can be calculated by (6.37). Ideally, the residual EMI is further decreased from iteration to iteration.

$$\Rightarrow X_{\text{res,n}}^{@\text{sensor}}(kf_0) = X_{\text{EMI}}^{@\text{sensor}}(kf_0) \cdot \left(1 - \frac{1}{(1+a_{\text{dev}}) \cdot e^{j\varphi_{\text{dev}}}}\right)^n \tag{6.37}$$

b) Stability

For a further analysis, it must be found for which amplitude and phase the algorithm remains stable. This stability is defined by the capability of reducing the residual EMI in each iteration. The residual EMI decreases if the absolute value of the base of (6.37) is below one. This requirement is stated in (6.38) and solved to (6.39):

$$\left|1-\frac{1}{(1+a_{\mathrm{dev}})\cdot e^{j\varphi_{\mathrm{dev}}}}\right|<1 \tag{6.38}$$

$$\Rightarrow \frac{\left|(1+a_{\mathrm{dev}})\cdot e^{j\varphi_{\mathrm{dev}}}-1\right|}{|1+a_{\mathrm{dev}}|\cdot|e^{j\varphi_{\mathrm{dev}}}|}<1 \tag{6.39}$$

Since $|1+a_{\mathrm{dev}}|$ is larger than 0 by definition and the absolute value of $e^{j\varphi_{\mathrm{dev}}}$ is 1, (6.40) can be followed:

$$\Rightarrow \left|(1+a_{\mathrm{dev}})\cdot e^{j\varphi_{\mathrm{dev}}}-1\right|<1+a_{\mathrm{dev}} \tag{6.40}$$

Since both sides of the inequation are positive, they can be squared according to (6.41):

$$\Rightarrow \left|(1+a_{\mathrm{dev}})\cdot e^{j\varphi_{\mathrm{dev}}}-1\right|^2<(1+a_{\mathrm{dev}})^2 \tag{6.41}$$

After solving, the stability condition of (6.42) follows:

$$\Rightarrow (1+a_{\mathrm{dev}})\cdot\cos(\varphi_{\mathrm{dev}})>\frac{1}{2} \tag{6.42}$$

This condition is visualized in Figure 6.9. It can be found that the algorithm is very stable. If there is no phase deviation, the amplitude could deviate by nearly -50% and the residual EMI is still reduced in each iteration. If there is no amplitude deviation, the phase could deviate by nearly ±60°.

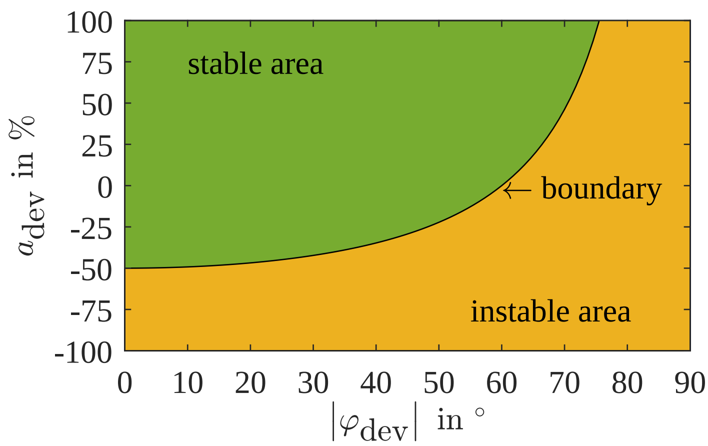

Figure 6.9: Stability area for amplitude and phase deviations in the determined transfer function

c) Convergence Rate

Although the algorithm is very stable, its convergence is reduced by amplitude and phase deviations. The achieved EMI reduction after each iteration can be expressed by (6.43):

$$\Delta X_{\mathrm{dB,n}}^{\mathrm{@sensor}}(kf_0) = 20\ \mathrm{dB} \cdot \log_{10} \left| \frac{X_{\mathrm{EMI}}^{\mathrm{@sensor}}(kf_0)}{X_{\mathrm{res,n}}^{\mathrm{@sensor}}(kf_0)} \right| \tag{6.43}$$

By inserting (6.37), (6.44) follows:

$$\overset{(6.37)}{\Rightarrow} \Delta X_{\mathrm{dB,n}}^{\mathrm{@sensor}}(kf_0) = 20\ \mathrm{dB} \cdot \log_{10} \left| \left(1 - \frac{1}{(1+a_{\mathrm{dev}}) \cdot e^{j\varphi_{\mathrm{dev}}}} \right)^{-n} \right| \tag{6.44}$$

This can be solved according to (6.45)-(6.47):

$$\Rightarrow \Delta X_{\mathrm{dB,n}}^{\mathrm{@sensor}}(kf_0) = 20\ \mathrm{dB} \cdot \log_{10} \left(\left| 1 - \frac{1}{(1+a_{\mathrm{dev}}) \cdot e^{j\varphi_{\mathrm{dev}}}} \right|^{-n} \right) \tag{6.45}$$

$$= -n \cdot 20\ \mathrm{dB} \cdot \log_{10} \left| 1 - \frac{1}{(1+a_{\mathrm{dev}}) \cdot e^{j\varphi_{\mathrm{dev}}}} \right| \tag{6.46}$$

$$= -n \cdot 10\ \mathrm{dB} \cdot \log_{10} \left(1 - \frac{2 \cdot \cos(\varphi_{\mathrm{dev}})}{1+a_{\mathrm{dev}}} + \frac{1}{(1+a_{\mathrm{dev}})^2} \right) \tag{6.47}$$

(6.48) describes the achievable EMI reduction per iteration. So, it represents the convergence rate of the method.

$$\Rightarrow \frac{\Delta X_{\mathrm{dB,n}}^{\mathrm{@sensor}}(kf_0)}{n} = -10\ \mathrm{dB} \cdot \log_{10} \left(1 - \frac{2 \cdot \cos(\varphi_{\mathrm{dev}})}{1+a_{\mathrm{dev}}} + \frac{1}{(1+a_{\mathrm{dev}})^2} \right) \tag{6.48}$$

For a better understanding, (6.48) is depicted in Figure 6.10 for different amplitude and phase deviations. It becomes obvious that the convergence rate is basically infinitely high if there are no amplitude ($a_{\mathrm{dev}} = 0\%$) and phase ($\varphi_{\mathrm{dev}} = 0.0°$) deviations. However, an amplitude deviation of 1% or a phase deviation of 0.5° result in an EMI reduction per iteration of only approximately 40 dB. If the deviations are further increased, the convergence rate drops even more.

One could now come to the conclusion that the transfer function $H_{\mathrm{anti}}(kf_0)$ must be identified very precisely in order to get a sufficient convergence rate. While this is in general true, the total achievable EMI reduction is limited by the digital system's SNR as discussed in Section 6.4.5. Considering an already high resolution of 14 bit, the SNR is approximately 86 dB according to (5.1). So, for a convergence rate of 40 dB, the limits are nearly reached after two iterations. Even for larger deviations (e.g. $a_{\mathrm{dev}} = 5\%$ and $\varphi_{\mathrm{dev}} = 2.0°$), the limits are already reached after four iterations. Considering the digital system's limitations, the algorithm will convergence reasonably fast for small deviations in the identified transfer function.

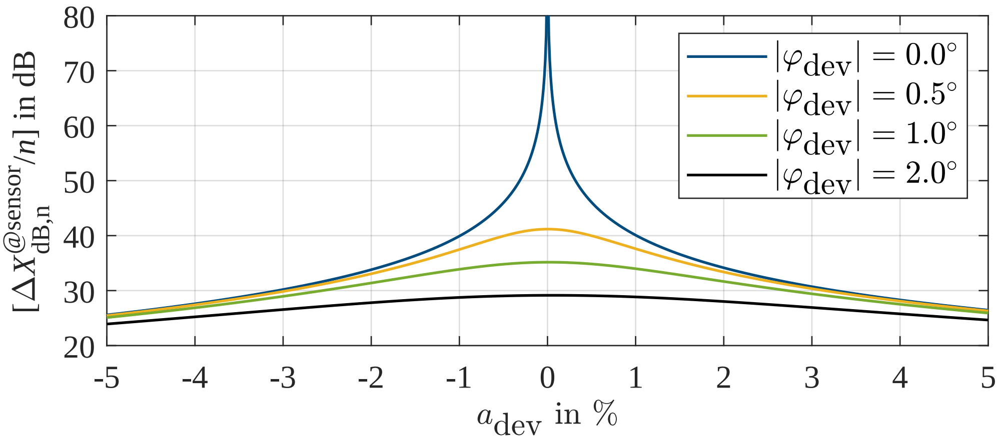

Figure 6.10: Convergence rate for different amplitude and phase deviations in the determined transfer function

6.4.8 Robustness against Deviations in (Residual) EMI Measurement

Another error source is the measurement of the original and residual EMI. Its effect is discussed in the following. Also this analysis extends the description of [81, supervisor].

a) Mathematical Description

For analysis, it is assumed that there is a deviation of $a_{\text{dev}} \in \mathbb{R}$, $a_{\text{dev}} > -1$ in amplitude and $\varphi \in \mathbb{R}$ in phase of the measured signals according to (6.49) and (6.50):

$$X^{@\text{sensor}}_{\text{EMI,det}}(kf_0) = (1+a_{\text{dev}}) \cdot e^{j\varphi_{\text{dev}}} \cdot X^{@\text{sensor}}_{\text{EMI}}(kf_0) \tag{6.49}$$

$$X^{@\text{sensor}}_{\text{res,det}}(kf_0) = (1+a_{\text{dev}}) \cdot e^{j\varphi_{\text{dev}}} \cdot X^{@\text{sensor}}_{\text{res}}(kf_0) \tag{6.50}$$

The transfer function is assumed to be ideally identified. The cancellation signal for the first iteration is calculated by (6.51):

$$\overset{(6.3)}{\Rightarrow} X_{\text{anti},1}(kf_0) = -\frac{X^{@\text{sensor}}_{\text{EMI,det}}}{H_{\text{anti}}(kf_0)} \tag{6.51}$$

According to (6.1), the residual EMI after the first iteration can be found by (6.52):

$$\overset{(6.1)}{\Rightarrow} X^{@\text{sensor}}_{\text{res},1}(kf_0) = X^{@\text{sensor}}_{\text{EMI}}(kf_0) + H^{\rightarrow\text{sensor}}_{\text{anti}}(kf_0) \cdot X_{\text{anti},1}(kf_0) \tag{6.52}$$

Since this calculation represents the physical superposition of EMI and anti-EMI, the actual EMI $X^{@\text{sensor}}_{\text{EMI}}(kf_0)$ must be respected. By inserting (6.49) and (6.51) and some solving, (6.53) can be found:

$$\Rightarrow X^{@\text{sensor}}_{\text{res},1}(kf_0) = X^{@\text{sensor}}_{\text{EMI}}(kf_0) \cdot \left[1-(1+a_{\text{dev}}) \cdot e^{j\varphi_{\text{dev}}}\right] \tag{6.53}$$

The cancellation signal for the second iteration can be calculated by (6.5). Here, the calculated cancellation signal and the measured residual EMI of the first iteration must be considered. Therefore, (6.54) follows:

$$\overset{(6.5)}{\Rightarrow} X_{\text{anti},2}(kf_0) = -\frac{X_{\text{EMI,det}}^{@\text{sensor}} + X_{\text{res,det},1}^{@\text{sensor}}}{H_{\text{anti}}^{\rightarrow\text{sensor}}(kf_0)} \tag{6.54}$$

By inserting (6.49) and (6.50), (6.55) can be derived:

$$\Rightarrow X_{\text{anti},2}(kf_0) = -\frac{\left(X_{\text{EMI}}^{@\text{sensor}} + X_{\text{res},1}^{@\text{sensor}}\right)\cdot(1+a_{\text{dev}})\cdot e^{j\varphi_{\text{dev}}}}{H_{\text{anti}}^{\rightarrow\text{sensor}}(kf_0)} \tag{6.55}$$

The residual EMI of the second iteration according to (6.56) and (6.57) can be found by combining (6.1), (6.53) and (6.55):

$$\overset{(6.1)}{\Rightarrow} X_{\text{res},2}^{@\text{sensor}}(kf_0) = X_{\text{EMI}}^{@\text{sensor}}(kf_0) + H_{\text{anti}}^{\rightarrow\text{sensor}}(kf_0)\cdot X_{\text{anti},2}(kf_0) \tag{6.56}$$

$$= X_{\text{EMI}}^{@\text{sensor}}(kf_0)\cdot\left[1-(1+a_{\text{dev}})\cdot e^{j\varphi_{\text{dev}}}\right]^2 \tag{6.57}$$

Repeating the pattern of (6.53) and (6.57), the residual EMI of the n-th iteration (with $n \in \mathbb{N}\cup\{0\}$) can be calculated by (6.58). This residual EMI should be decreased after each iteration.

$$\Rightarrow X_{\text{res,n}}^{@\text{sensor}}(kf_0) = X_{\text{EMI}}^{@\text{sensor}}(kf_0)\cdot\left[1-(1+a_{\text{dev}})\cdot e^{j\varphi_{\text{dev}}}\right]^n \tag{6.58}$$

b) Stability

For stability, the absolute value of the base of (6.58) must be smaller than 1 according to (6.59):

$$\left|1-(1+a_{\text{dev}})\cdot e^{j\varphi_{\text{dev}}}\right| < 1 \tag{6.59}$$

Since both sides are positive, the inequation can be squared according to (6.60):

$$\Rightarrow \left|1-(1+a_{\text{dev}})\cdot e^{j\varphi_{\text{dev}}}\right|^2 < 1 \tag{6.60}$$

Afterward, the absolute value can be solved to (6.61):

$$\Rightarrow (1+a_{\text{dev}})^2 - 2\cdot(1+a_{\text{dev}})\cdot\cos(\varphi_{\text{dev}}) + 1 < 1 \tag{6.61}$$

After subtracting 1 on both sides, the inequation can be divided by $(1+a_{\text{dev}})$ since this term is larger than zero by definition. So, (6.62) and (6.63) follow:

$$\Rightarrow 1 + a_{\text{dev}} - 2 \cdot \cos(\varphi_{\text{dev}}) < 0 \tag{6.62}$$

$$\Rightarrow a_{\text{dev}} < 2 \cdot \cos(\varphi_{\text{dev}}) - 1 \tag{6.63}$$

The stability area is depicted in Figure 6.11. It can be found that the algorithm is also very tolerant against deviations in the disturbance measurement.

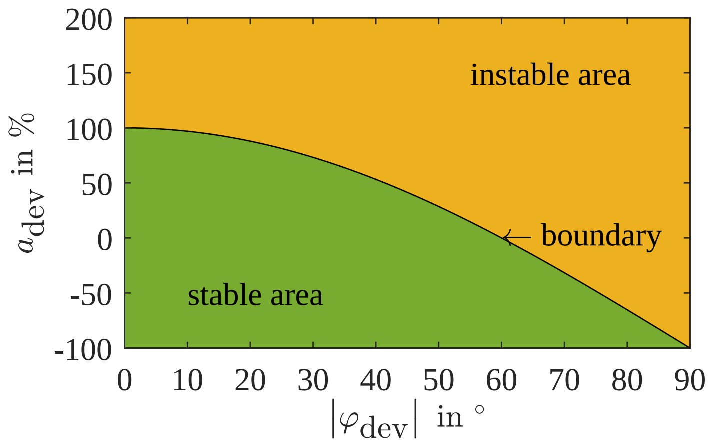

Figure 6.11: Stability area for amplitude and phase deviations in the disturbance measurements

c) Convergence Rate

To analyze the convergence rate, (6.64) is evaluated:

$$\Delta X^{\text{@sensor}}_{\text{dB,n}}(kf_0) = 20\text{ dB} \cdot \log_{10} \left| \frac{X^{\text{@sensor}}_{\text{EMI}}(kf_0)}{X^{\text{@sensor}}_{\text{res,n}}(kf_0)} \right| \tag{6.64}$$

By inserting (6.58), (6.65) follows:

$$\overset{(6.58)}{\Rightarrow} \Delta X^{\text{@sensor}}_{\text{dB,n}}(kf_0) = 20\text{ dB} \cdot \log_{10} \left| \left(1 - (1 + a_{\text{dev}}) \cdot e^{j\varphi_{\text{dev}}}\right)^{-n} \right| \tag{6.65}$$

This equation can be solved to (6.66)-(6.68):

$$\Rightarrow \Delta X^{\text{@sensor}}_{\text{dB,n}}(kf_0) = 20\text{ dB} \cdot \log_{10} \left(\left|1 - (1 + a_{\text{dev}}) \cdot e^{j\varphi_{\text{dev}}}\right|^{-n} \right) \tag{6.66}$$

$$= -n \cdot 20\text{ dB} \cdot \log_{10} \left|1 - (1 + a_{\text{dev}}) \cdot e^{j\varphi_{\text{dev}}}\right| \tag{6.67}$$

$$= -n \cdot 10\text{ dB} \cdot \log_{10} \left((1 + a_{\text{dev}})^2 - 2(1 + a_{\text{dev}}) \cdot \cos(\varphi_{\text{dev}}) + 1 \right) \tag{6.68}$$

The achievable EMI reduction per iteration can be described by (6.69):

$$\Rightarrow \frac{\Delta X^{@\text{sensor}}_{\text{dB,n}}(kf_0)}{n} = -10\ \text{dB} \cdot \log_{10}\left((1+a_{\text{dev}})^2 - 2\,(1+a_{\text{dev}}) \cdot \cos(\varphi_{\text{dev}}) + 1 \right) \qquad (6.69)$$

The result is visualized in Figure (6.12) for different amplitude and phase deviations. Interestingly, the result is very similar to Figure 6.10 in the considered parameter range. Deviations in amplitude and phase may slow down the convergence, but high EMI reductions are still achievable after a few iterations.

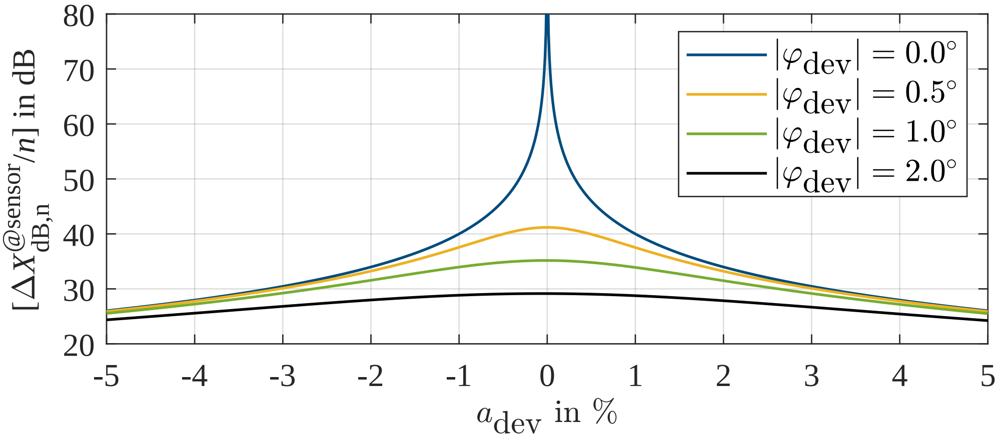

Figure 6.12: Convergence rate for different amplitude and phase deviations in the disturbance measurements

6.5 Chapter Summary

In this chapter, different methods for active cancellation in the field of power quality have been evaluated. The FFT method has shown to be a promising approach to cancel out quasi-periodic disturbances. Therefore, a concept for an active EMI cancellation system has been developed that applies this method. For quasi-periodic EMI, the cancellation signal can be constructed very precisely in frequency domain. So, there are no bothersome time constants (resulting from, e.g., limited gain-bandwidth products) like for AEFs. Otherwise problematic delay times are respected in the identified transfer functions. By inverting the problem, these delay times are compensated by phase shifts of the cancellation signal's harmonics. The FFT method requires the EMI to be periodic over a sufficient period of time. It must be noted that this requirement is not necessary for AEFs or DAEFs.

There are many possible sources for limitations. Frequency and synchronization deviations can be an issue if the active cancellation system must synchronize itself to the EMI. However, if the cancellation system is integrated with the power electronic system in the same device, an ideal synchronization is achievable. Amplitude and phase deviations are, in general, a limiting factor for active EMI cancellation. One could assume that the signal acquisition and system identification must be extremely precise to mitigate the problem of amplitude and phase deviations. In contrary, the FFT method has been found to be very robust against deviations in system and signal identification. Good cancellation results can be achieved after only a few iterations (as long as the deviations are not too large). The last remaining limitations are the ones of the digital hardware that comprise the sampling rate and the vertical resolution. So, by applying this method for signal generation, the active cancellation system can be brought close to the digital hardware's limits that could not be reached by the feedforward or feedback signal generation approaches of DAEFs.

7 Analysis of Active Noise Cancellation (ANC) Approaches for Active EMI Cancellation

In this chapter, **a**ctive **n**oise **c**ancellation (ANC) in acoustics is analyzed for the possible transfer to active EMI cancellation. In acoustics, the fundamental problem is very similar to the one in EMC since there are disturbing signals that must be cancelled out. In general, these disturbances have a relatively high frequency and a low power considering the respective physical domain. So, evaluating the methods of ANC in acoustics is a nearby step.

At first, some selected fundamentals are summarized. Then, three different methods are discussed and evaluated regarding their applicability to active EMI cancellation. A promising approach is transferred to active EMI cancellation. The fundamental limitations and possible solutions are discussed.

7.1 Fundamentals

In acoustics, there are basically the same issues regarding noise as in EMC. Noise signals must be attenuated, and this is conventionally done by passive structures (e.g. enclosures, barriers and silencers). Like passive attenuating structures in EMC, these components are often large, costly and ineffective at low frequencies. To resolve these issues, ANC systems can be applied that are especially effective for lower frequencies. [3]

Similar to AEFs, ANC systems use sensors, injectors and some active circuitry to suppress (acoustic) noise [3]. However, this fundamental method has been patented much earlier, in 1936 [5]. In comparison, AEFs are a much younger method that has not been discussed until 1970 [1]. So, ANC is a very interesting field due to its level of maturity.

In acoustics, the characteristics of the noise source and the environment are usually time-varying [3]. Therefore, some form of feedback is necessary for the correction of the cancellation signals [3, 82]. One could expect that this feedback loop would immediately lead to the same restrictions as AEFs suffer from. This may indeed be true for simple feedback types, but there are also specialized adaptive techniques that are even capable of suppressing random noise if the right conditions are met. So, a review of the methods developed for ANC is very promising.

At the first glance, one could expect that the geometrical problem for acoustic and electromagnetic noise is completely different since different physical domains are considered. However, there are many similarities. Conducted electromagnetic noise of, e.g., power electronic systems propagates through wires. In acoustics, noise can also be conducted if it propagates through, e.g., a duct. In both cases, this is basically a one-dimensional problem that can be solved by one injector, one signal generator and one sensor. Electromagnetic and acoustic noise can also be radiated. In this case, the problem becomes immediately threedimensional and multiple injectors and sensors can become necessary [3]. For a clear review of the methods, the simpler case of conducted noise is discussed.

7.2 Review of Methods for Cancellation Signal Generation

In the following, three methods of ANC are evaluated. These comprise the broadband non-adaptive feedback ANC, the broadband adaptive feedforward ANC and the narrowband adaptive feedforward ANC.

7.2.1 Broadband Non-Adaptive Feedback ANC

In Figure 7.1, an exemplary ANC system is depicted. It contains a noise source, a duct that conducts the noise and a noise victim at the end. The ANC system contains an error microphone to pick up the residual noise x_{res} (superscripts are neglected in this section) that would propagate to the noise victim. This measured (and now electrical) quantity is amplified by an analog device, inverted and injected back into the system via a cancelling loudspeaker [82].

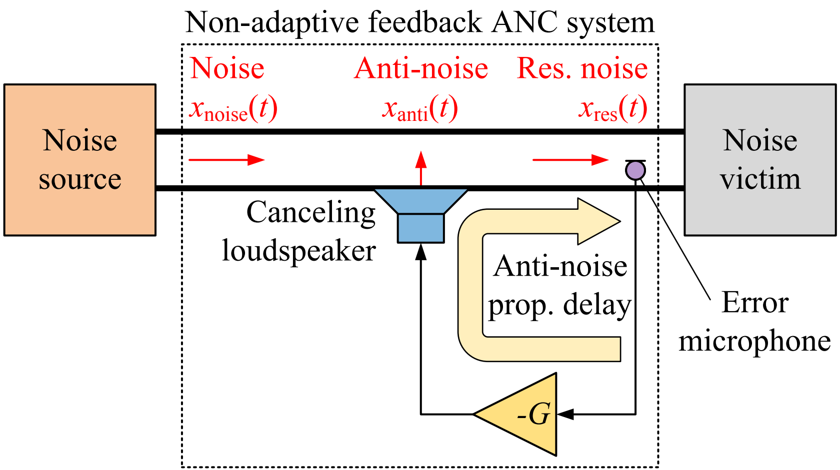

Figure 7.1: Broadband non-adaptive ANC system with feedback controller

This system is fundamentally the same as feedback AEFs and has unfortunately the same limitations. Again, the gain-bandwidth product of the amplifier limits the performance of the system [82]. The feedback loop also tends to instabilities and the necessary stabilization limits the performance [82]. As for the AEFs, this problem is even worsened since the properties of the system may change during operation [82]. Like for AEFs and DAEFs, delay times are also an issue for this ANC system. Here, the propagation speed of sound is problematic since it is only about 343 meters per second. Therefore, the residual noise is measured much later than the anti-noise is injected. This can lead to instabilities and also limits the performance [82]. These issues lead to the question if feedforward strategies are better suited for the application to ANC systems.

7.2.2 Broadband Adaptive Feedforward ANC

In feedforward systems, the noise is measured at the noise source, processed and injected back into the system. As stated before, the noise signal and environment are usually time-varying. Therefore, the ANC system must adapt itself [3]. This adaption can be realized by applying the adaptive filter theory. Early publications on adaptive ANC systems for duct systems are [83] and [84] from the year 1981. Digital signal processing hardware is a convenient way to realize real-time capable and adaptive ANC systems [85, 86]. Already in the 1980s, powerful adaptive algorithms could be realized at low costs [14]. This fact accelerated the development and application of ANC [87].

There are many different concepts for the realization of adaptive ANC systems, and the evaluation of the entirety is beyond the scope of this work. Fundamentally, there are feedforward and feedback types. Feedforward types have a straight-forward topology that can be evaluated more easily. Furthermore, the performance of feedback types depends on the predictability of the noise that is, in general, a limitation for the method [3]. As discussed in the next section, this is no requirement for feedforward ANC systems that can even suppress stochastic noise if the right conditions are met. So, feedforward types are discussed in this work.

a) Exemplary System with Conducted Acoustic Noise

An exemplary adaptive feedforward ANC system is depicted in Figure 7.2. A noise source injects noise that propagates through a duct to a noise victim. The ANC system uses a reference microphone to pick up the noise $x_{\text{noise}}(t)$. This signal is processed to generate the cancellation signal $x_{\text{anti}}(t)$ in a feedforward approach. The cancellation signal is injected by a loudspeaker. The noise and anti-noise superpose each other and result in a residual noise $x_{\text{res}}(t)$ that is measured by an error microphone. An optimizer uses the information of the residual noise to optimize the signal processing for the cancellation signal. This is the characteristic adaptive process that is discussed in more detail in the following section.

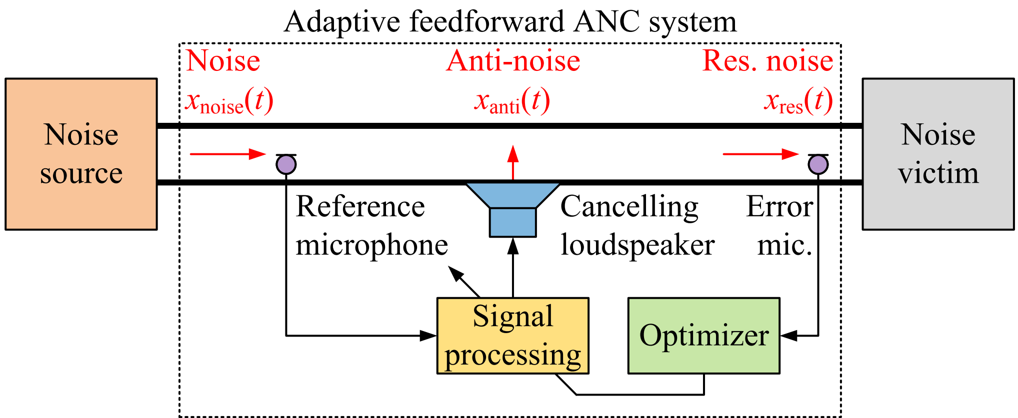

Figure 7.2: Single-channel broadband feedforward ANC system for conducted acoustic noise [3]

b) Systems Theory

A block diagram of an ANC system using the adaptive filter theory is depicted in Figure 7.3 [3]. There are still the noise source and noise victim that are coupled in the acoustic domain. However, the propagation path is now represented by the transfer function $H_{\text{noise}}(f)$ (superscripts for the transfer functions are neglected in this section).

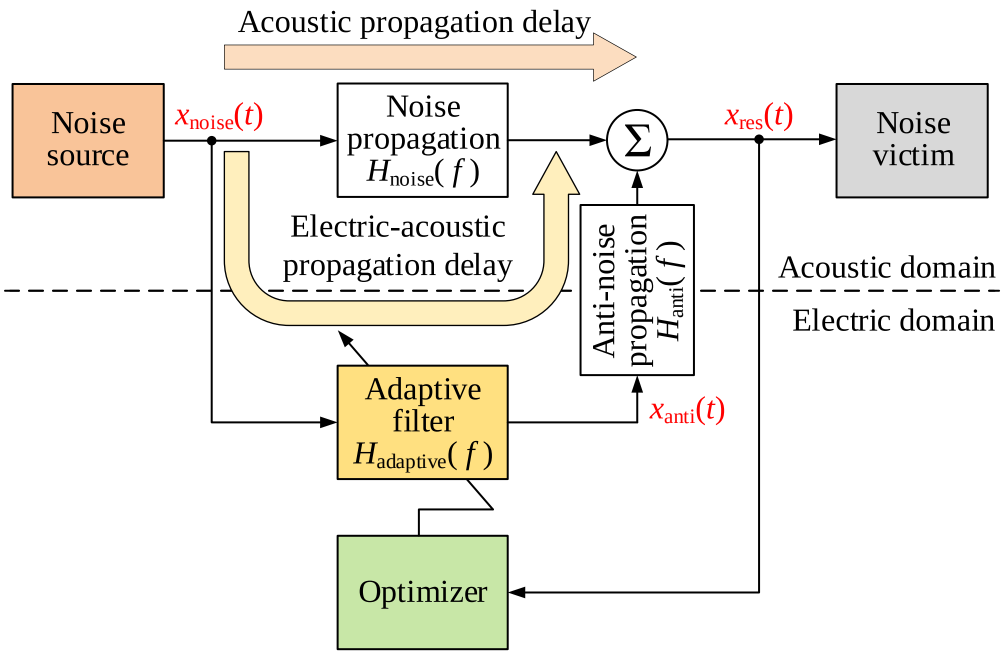

Figure 7.3: Block diagram of a broadband adaptive ANC system [3]

The adaptive ANC system picks up the acoustic noise and shapes it by an adaptive filter in the electric domain. This signal is brought into the acoustic domain again where it superposes itself with the noise. The residual noise is picked up and evaluated by an optimizer that adjusts the properties of the adaptive filter so that the residual noise is minimized. The propagation of the anti-noise back to the optimizer must be respected by the transfer function $H_{\text{anti}}(f)$. This block comprises, e.g., the digital-to-analog conversion of the anti-noise, the loudspeaker, the acoustic path from the loudspeaker to the error microphone, the error microphone and the analog-to-digital conversion of the residual noise. The adaptive filter is most commonly realized by a **f**inite **i**mpulse **r**esponse (FIR) filter. The optimizer is usually a **l**east-**m**ean-**s**quare (LMS) algorithm. As stated before, DSPs can be used for a real-time adaption at low costs. [3]

The residual noise $X_{\text{res}}(f)$ can fundamentally be described by (7.1):

$$X_{\text{res}}(f) = H_{\text{noise}}(f) \cdot X_{\text{noise}}(f) + H_{\text{anti}}(f) \cdot H_{\text{adaptive}}(f) \cdot X_{\text{noise}}(f) \tag{7.1}$$

For an ideal cancellation, $X_{\text{res}}(f)$ should equal zero as stated in (7.2):

$$0 \stackrel{!}{=} H_{\text{noise}}(f) \cdot X_{\text{noise}}(f) + H_{\text{anti}}(f) \cdot H_{\text{adaptive}}(f) \cdot X_{\text{noise}}(f) \tag{7.2}$$

So, it can be found by (7.3) that the adaptive filter $H_{\text{adaptive}}(f)$ must model $H_{\text{noise}}(f)$ and inversely model $H_{\text{anti}}(f)$ [3]:

$$\Rightarrow H_{\text{adaptive}}(f) = -\frac{H_{\text{noise}}(f)}{H_{\text{anti}}(f)} \tag{7.3}$$

The filter corresponding to the transfer function $H_{\text{adaptive}}(f)$ can be causal or non-causal. If the acoustic delay from the reference microphone to cancelling loudspeaker is longer than the electro-acoustic delay of the ANC system (also from the reference microphone to the loudspeaker), there is some time for calculating the cancellation signal (note Figure 7.3). If the time difference is large enough, a causal filter can be realized. In this case, the condition for causality is met and the ANC system can suppress even random noise. However, if the electro-acoustic delay is longer than the acoustic, there is no time for the calculation of the cancellation signals. In this case, the condition for causality is not met anymore and the performance of the system is severely degraded. There is still a theoretical non-causal solution for the adaptive filter. However, since non-causal systems cannot be realized, this solution is not feasible. [3]

c) Evaluation for Active EMI Cancellation in Power Electronic Systems

Considering EMC, EMI and anti-EMI will propagate by the same speed. Therefore, it is almost guaranteed that the sensed, processed and injected signal is too late. So, random EMI will not be suppressible by such a system.

In power electronic systems, the EMI is usually a deterministic result of the control signals. There are applications in which the control signals can be known beforehand for the next few switching periods. In this case, future control signals could be used to compensate the unavoidable delay times of the signal processing. So, a predictive method could significantly improve the applicability. Such a method has been pursued in [88, supervisor]. However, it has been shown that the precise modeling of transfer functions by FIR- or IIR-filters (**i**nfinite **i**mpulse **r**esponse) can become a cumbersome and inconvenient task.

Considering quasi-periodic EMI, the (too late) cancellation signal could be delayed even further to be in sync with a later period of the EMI. Since the quasi-periodic signal will consist of numerous discrete harmonics, it is also completely viable to generate a cancellation signal from sine waves. A possible strategy utilizing the Fourier transform has been discussed in Section 6.3.1. This approach is rather slow since it only uses historic data. Fortunately, there is a specialized method for the suppression of individual harmonics by injecting continuously adapted sine waves in acoustics. This method is discussed and evaluated in the following section.

7.2.3 Narrowband Adaptive Feedforward ANC

A narrowband adaptive feedforward ANC system has already been proposed by [89] in 1956. In [89], a large power transformer is investigated that generates acoustic noise at the harmonics of the grid frequency. To suppress the acoustic noise of one harmonic, a cancelling sine wave can be generated by a a loudspeaker. Obviously, the cancelling wave must be an exact opposite of the harmonic. For broadband realizations, this is no trivial task since complex transfer functions must be compensated. The parameters of a single cancelling sine wave can easily be found since there is only an amplitude and a phase. In [89], the adaption of amplitude and phase is done manually to minimize the noise picked up by an error microphone. Self-adapting narrowband ANC systems have been presented in [90] and [91].

a) Exemplary System with Conducted Noise

An exemplary adaptive feedforward ANC system is depicted in Figure 7.4. Again, the noise source, ANC system and noise victim are connected by a duct. In this case, the noise source generates quasi-periodic noise. There is a signal source that creates an artificial sine wave for cancellation. This sine wave must have the same frequency as the harmonic that should be suppressed.

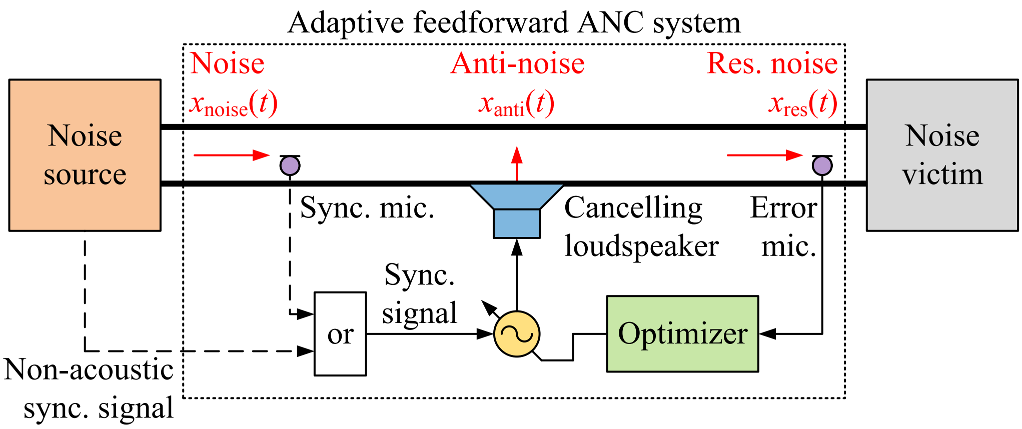

Figure 7.4: Single-channel narrowband feedforward ANC system for conducted acoustic noise

Noise and anti-noise must be synchronized to each other. There are different possibilities: It is possible to synchronize the ANC system to the acoustic noise picked up by a synchronization microphone. As stated in Section 6.3.1, this could be achieved by, e.g., a PLL. In many cases, there are non-acoustic control or sensor signals that are correlated to the noise. One example is a tachometer signal from an automotive engine that is correlated to the acoustic noise [3]. One could come up with the idea to use the error signal that is picked up by the error microphone. However, this may be no convenient approach since harmonics of this signal are eliminated by the ANC system. In this setup, the ANC system may cancel its own synchronization signal. Maintaining the synchronization can still be possible, but it will require some more implementation effort.

The cancellation signal must be adjusted so that the respective harmonic of the noise is suppressed. This is done by an optimizer that adapts the amplitude and phase of the cancelling sine wave in such way that the residual noise picked up by the error microphone is minimized.

This method has some interesting features. For example, the method is applicable to nonlinear systems that cannot be described by broadband FIR-filters. Delay times can easily be compensated by phase-shifting the sine waves (for quasi-periodic noise). So, the causality requirement is no constraint for the method. [3]

b) Single-Frequency Adaptive Notch Filter with Delayed LMS Algorithm

One possible realization of a narrowband adaptive feedforward ANC system is a single-frequency adaptive notch filter as depicted in Figure 7.5 [3]. The name is due to the transfer characteristic of the ANC system that passes all frequencies except for a narrow band that is cancelled out. This method can be digitally realized by using, e.g., a DSP or an FPGA with ADCs and DACs. Since these digital devices operate in a sampled time domain, all signals are represented accordingly (n instead of t). The transfer functions are represented as impulse responses $h(n)$ in this domain.

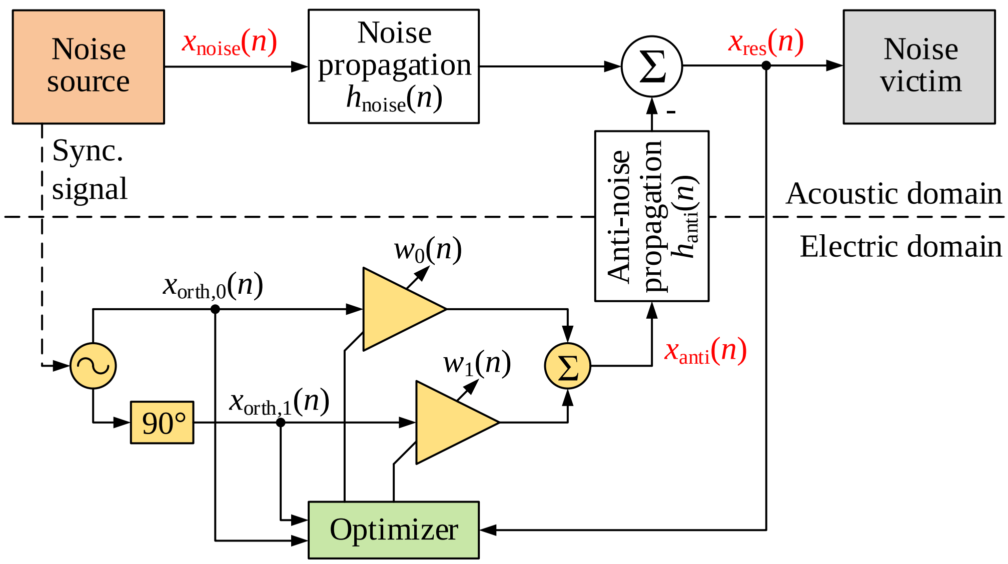

Figure 7.5: Block diagram of a single-frequency adaptive notch filter [3]

The fundamental goal is to generate the right sine wave $x_{anti}(n)$ that cancels out a specific harmonic of the noise signal. To do so, an adjustable sine wave is necessary. Therefore, an orthogonal system $\vec{x}_{orth}(n)$ of cosine and sine is generated in synchronicity with the noise according to (7.4):

$$\vec{x}_{\text{orth}}(n) = \begin{pmatrix} A \cdot \cos\left(2\pi \frac{kf_0}{f_\text{s}} n\right) \\ A \cdot \sin\left(2\pi \frac{kf_0}{f_\text{s}} n\right) \end{pmatrix} \tag{7.4}$$

A is an arbitrary amplitude, f_0 is the fundamental frequency of the noise and f_s is the sampling rate of the digital system. The generated orthogonal system has a frequency of kf_0 and it will cancel out the k-th harmonic. The cosine and sine of the orthogonal system are multiplied by the filter weights $\vec{w}(n)$ according to (7.5):

$$\vec{w}(n) = \begin{pmatrix} w_0(n) \\ w_1(n) \end{pmatrix} \tag{7.5}$$

Note that these filter weights may change for each sample. The cancellation signal $x_{\text{anti}}(n)$ is found by (7.6) and (7.7):

$$x_{\text{anti}}(n) = \vec{w}(n) \cdot \vec{x}_{\text{orth}}(n) \tag{7.6}$$

$$= A \left[w_0(n) \cdot \cos\left(2\pi \frac{kf_0}{f_\text{s}} n\right) + w_1(n) \cdot \sin\left(2\pi \frac{kf_0}{f_\text{s}} n\right) \right] \tag{7.7}$$

So, by adjusting the filter weights $\vec{w}(n)$, an arbitrary sine wave with the frequency kf_0 can be generated according to (7.8) [92]:

$$\Rightarrow x_{\text{anti}}(n) = A \left[\operatorname{sgn}(w_0(n)) \sqrt{w_0^2(n) + w_1^2(n)} \cdot \cos\left(2\pi \frac{kf_0}{f_\text{s}} n + \arctan\left\{ -\frac{w_1(n)}{w_0(n)} \right\} \right) \right] \tag{7.8}$$

Finding the correct filter weights $\vec{w}(n)$ is obviously not trivial. However, there are simple and efficient algorithms for the optimizer that are described in the following. To derive the algorithm for optimization, the superposition of noise and anti-noise is evaluated by (7.9)-(7.10):

$$x_{\text{res}}(n) = h_{\text{noise}}(n) * x_{\text{noise}}(n) - h_{\text{anti}}(n) * x_{\text{anti}}(n) \tag{7.9}$$

$$= h_{\text{noise}}(n) * x_{\text{noise}}(n) - h_{\text{anti}}(n) * (\vec{w}(n) \cdot \vec{x}_{\text{orth}}(n)) \tag{7.10}$$

Note that the negative sign is for conformity with the existing theory in acoustics. According to [3], a steepest descent algorithm (with the step size μ) is used to minimize the instantaneous squared residual noise $x_{\text{res}}(n)$ as depicted in (7.11):

$$\vec{w}(n+1) = \vec{w}(n) - \frac{\mu}{2} \cdot \operatorname{grad}\left(x_{\text{res}}^2(n)\right) \tag{7.11}$$

So, in each sample step the filter weights $\vec{w}(n)$ will be updated in negative direction of the gradient (derivated by $\vec{w}(n)$). This approach can easily be made plausible by considering the fact that the squared residual noise will be minimized if the k-th harmonic is cancelled out. There may also be lower or higher harmonics (or even random noise) in the signal so that the residual noise will not drop to zero. This does not change the fact that there is exactly one minimum for the problem and that the k-th harmonic can ideally be completely cancelled out by this approach. The gradient of the squared residual noise can be solved to (7.12)-(7.14):

$$\mathrm{grad}\left(x_{\mathrm{res}}^2(n)\right) = 2 \cdot \mathrm{grad}\left(x_{\mathrm{res}}(n)\right) \cdot x_{\mathrm{res}}(n) \tag{7.12}$$

$$\overset{(7.10)}{\Rightarrow} \mathrm{grad}\left(x_{\mathrm{res}}(n)\right) = -h_{\mathrm{anti}}(n) * \vec{x}_{\mathrm{orth}}(n) \tag{7.13}$$

$$\overset{(7.12)}{\Rightarrow} \mathrm{grad}\left(x_{\mathrm{res}}^2(n)\right) = -2 \cdot \left(h_{\mathrm{anti}}(n) * \vec{x}_{\mathrm{orth}}(n)\right) \cdot x_{\mathrm{res}}(n) \tag{7.14}$$

Inserting (7.14) into the update rule (7.11) leads to (7.15):

$$\overset{(7.11)}{\Rightarrow} \vec{w}(n+1) = \vec{w}(n) + \mu \cdot \left(h_{\mathrm{anti}}(n) * \vec{x}_{\mathrm{orth}}(n)\right) \cdot x_{\mathrm{res}}(n) \tag{7.15}$$

In this update rule, the orthogonal system must be digitally filtered by the anti-noise propagation path $h_{\mathrm{anti}}(n)$. Therefore, this algorithm is called **f**iltered-**x** **l**east **m**ean **s**quare (FXLMS) algorithm [93] that was independently developed by [83] and [94]. The filtering is very important since the algorithm will generally become instable without it [95]. For digital filtering, $h_{\mathrm{anti}}(n)$ must be identified. In most ANC applications with a time-invariant propagation path, $h_{\mathrm{anti}}(n)$ is estimated in initial training stages [3]. In a time-variant case, online estimation techniques can be applied to follow changes of the system in real-time [3]. The algorithm is very tolerant against errors made in the estimation of $h_{\mathrm{anti}}(n)$. In [96], it is shown that the algorithm even converges for an error of $\pm 90°$. In [97] and [98], it is shown that phase errors of up to $\pm 40°$ affect the convergence speed of the algorithm only little. The algorithm will significantly slow down for higher phase errors (until it becomes instable). One may be tempted to compensate the slower convergence speed by a larger step size μ. But too large step sizes can cause the algorithm to become instable as well. So, there are systematic restrictions that are further discussed in [3].

Considering the fact that only a single sine wave is injected into the system, a broadband filtering by $h_{\mathrm{anti}}(n)$ is actually not necessary. The phase information can conveniently be respected by estimating the propagation delay Δ (in amount of sample periods) of the cancellation signal. Hence, the **delayed LMS algorithm** results according to (7.16) [99,100]. Note that the delay times can vary for different harmonics since they comprise not only frequency-independent delays but also frequency-dependent phase shifts of the transfer function.

$$\overset{(7.15)}{\Rightarrow} \vec{w}(n+1) = \vec{w}(n) + \mu \cdot \vec{x}_{\mathrm{orth}}(n-\Delta) \cdot x_{\mathrm{res}}(n) \tag{7.16}$$

If multiple harmonics must be suppressed, the presented structure can be implemented for each harmonic individually. In parallel implementations, all harmonics can be optimized at the same time. There is still only one error microphone necessary that finds the broadband residual noise. The found cancelling sine waves can be superposed digitally to form a broadband cancellation signal. To inject this signal, only one cancelling loudspeaker is necessary. [3]

It must be noted that the description of this section scratches at most the surface of the algorithms used for active cancellation of acoustic noise. There are many possible extensions for the proposed algorithm like a variable step size or an online secondary path modeling that have not been discussed yet. There are also many other algorithms and structures that are beyond the scope of this work. [3] gives a good overview of the field with many references to in-depth analyzes.

c) Exemplary Time Domain Signals

For a better understanding of the algorithm, some exemplary time domain signals for the single-frequency adaptive notch filter with delayed LMS algorithm are shown in Figure 7.6. The noise signal is a sine wave with a fundamental frequency of 1 kHz and an amplitude of nearly 1. The transfer functions are idealized to 1. Considering (7.9), the residual EMI can be calculated by subtracting the anti-noise from the noise. The orthogonal system is generated according to (7.4). The filter weights for each step are calculated according to the update rule (7.16). The anti-EMI is calculated by the orthogonal system and the filter weights according to (7.6). This idealized system has no delay times. Therefore, the delay time estimation Δ can be set to 0. In this example, the algorithm starts to adapt the filter weights $\vec{w}(n)$ at 2 ms. These converge respectively to values of 0.75 and -0.5 for the cosine and sine of the orthogonal system. The anti-noise slowly builds up to the required sine wave. The residual noise is reduced accordingly.

d) Evaluation for EMC in Power Electronic Systems

The presented method is capable of cancelling harmonics of quasi-periodic disturbances. The delayed LMS algorithm adapts the amplitude and phase of the cancelling sine wave by adjusting the filter weights $\vec{w}(n)$. It compensates the transfer function (including the propagation delays) and provides very precise cancellation signals.

In difference to the FFT method discussed for APFs in Section 6.3.1, the algorithm adapts itself continuously over time. The complete adaption process may still take a few fundamental periods, but the algorithm immediately starts to adjust its parameters if changes occur. So, the algorithm can be expected to perform well for slowly changing disturbances or transfer functions.

Since the single-frequency adaptive notch filter with delayed LMS algorithm is a promising approach for active EMI cancellation, it will be transferred to this field in the next section.

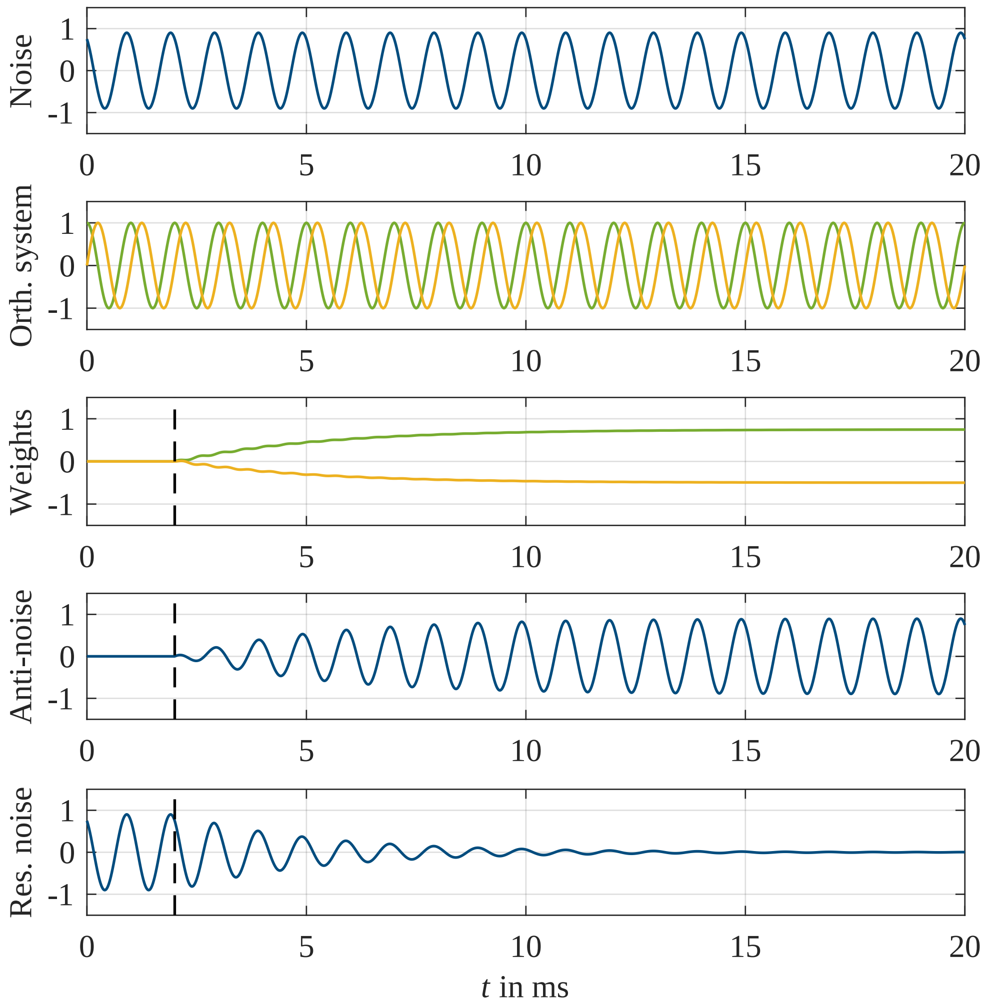

Figure 7.6: Exemplary time-domain signals for the single-frequency adaptive notch filter with delayed LMS algorithm

7.3 Application of the Single-Frequency Adaptive Notch Filter with Delayed LMS Algorithm to Active Cancellation of Quasi-Periodic EMI

In this section, the single-frequency adaptive notch filter with delayed LMS algorithm (in the following abbreviated by “notch filter method”, Section 7.2.3.b)) is transferred to active EMI cancellation. A suitable concept is derived and limitations are discussed.

7.3.1 Concept and Mathematical Description

To realize an active EMI cancellation system using the notch filter method, the same hardware concept as Figure 6.3 can be used. The only differences lie within the synthesizer and calculation blocks. The synthesizer consists of the single-frequency adaptive notch filter with its orthogonal system according to (7.4) and the calculation of the cancelling sine wave according to (7.6). The orthogonal system requires a synchronization signal that can be obtained by one of the two ways depicted in Figure 6.3. In the calculation block, the delayed LMS algorithm is used with its update rule of (7.16). This element optimizes the filter weights by using the current value of the residual EMI, the delayed values of the orthogonal system and the previous values of the filter weights. These optimized filter weights are passed to the synthesizer. To realize the single-frequency adaptive notch filter with delayed LMS algorithm, only the formulas (7.4), (7.6) and (7.16) are necessary. To adapt the cancelling sine wave to the EMI, these three formulas must be calculated multiple times during one period of the EMI. Due to the adaptive process, the EMI and transfer function of the anti-EMI must not be identified (in contrast to the FFT method, e.g. Section 6.4.2) as long as the algorithm is stable. [15, 101, 102, author]

7.3.2 Limitations due to Frequency Deviations

Frequency deviations discussed in Section 3.1.3.b) can also be a limiting factor for the notch filter method. The notch filter method provides some robustness against this kind of deviation since the notch does not only affect its center frequency but also frequencies around it. This bandwidth depends on the used step size μ [103]. Larger step sizes increase this bandwidth at the potential cost of a less precise result at the center frequency.

7.3.3 Limitations due to Synchronization Deviations

Synchronization deviations may cause the anti-EMI and EMI to be randomly shifted against each other. The analysis done for the FFT method (Section 6.4.4) is also viable for the notch filter method [15, author]. In contrast to the FFT method, the notch filter method offers some robustness against this deviation due to the possibility of continuously adapting the cancelling sine wave.

7.3.4 Limitations due to Digital Hardware

If the cancellation system is ideally synchronized to the EMI, the notch filter method is only limited by the digital hardware. The vertical resolution limits the achievable EMI reduction and the sampling rate limits the suppressible frequency range as discussed in Sections 5.1.1 and 5.1.2. [15, 102, author]

There is one additional limit that results from the necessity of doing multiple calculations during one period of the considered harmonic. The digital hardware must be fast enough to perform these calculations in time. This may be a limitation for the highest suppressible harmonic for a given digital hardware (since the periods become shorter for higher harmonics).

If multiple harmonics shall be suppressed, the calculations must be done individually for each cancelling sine wave. So, the digital hardware must be capable of doing numerous calculations, ideally at the same time. Modern FPGAs are a good option since complex calculations may be done in only a few sample periods. Calculations can also be parallelized very well with these devices. Nevertheless, the calculation resources of FPGAs are finite and limit the number of implementable single-frequency adaptive notch filters with delayed LMS algorithm. Therefore, only a limited number of harmonics can be suppressed by this approach.

To resolve this issue, a successive signal generation method can be pursued [104, author]. In this strategy, one single-frequency adaptive notch filter is successively applied to numerous harmonics. The cancelling sine waves for each harmonic are individually identified and superposed with each other. By doing so, a broadband cancellation signal results. It must be noted that the signal generation will be slowed down in comparison to the parallel implementation since the optimization is done one by one for each harmonic.

7.4 Chapter Summary

In this chapter, methods of active noise cancellation in acoustics have been reviewed in regard to their applicability to active EMI cancellation in power electronic systems. In acoustics, many sophisticated methods can be applied since the propagation speed difference of acoustic and electric signals offers some leeway for complex calculations. These systems may even suppress stochastic noise. In active EMI cancellation, all quantities are electric and there is basically no time for calculations. Therefore, the methods of ANC are not applicable to stochastic EMI. Nevertheless, the single-frequency adaptive notch filter with delayed LMS algorithm (notch filter method) is a promising approach to suppress the harmonics of quasi-periodic EMI.

This method has been transferred to active EMI cancellation. The concept and its limitations have been discussed. Like the FFT method (Section 6.4), the notch filter method can compensate the influence of complex transfer functions and delay times. The remaining limitations result from the digital hardware. Numerous single-frequency adaptive notch filters can be applied in parallel to suppress a large number of harmonics. This may lead to very high requirements for the digital calculation system. Successive signal generation approaches can help to solve this problem.

8 Active EMI Cancellation with Synthesized and Synchronized Signals

In this chapter, a new active EMI cancellation technique using synthesized and synchronized signals is derived from the FFT method (of power quality) and the notch filter method (of acoustics). At first, the fundamental concept is presented. The predictability of the upcoming EMI as a fundamental requirement of this new method is discussed. Different variants (e.g. self-adapting and taught systems) for practical realizations are depicted. Afterward, different methods for the signal optimizer are discussed. These include the FFT method, the notch filter method and also new, original approaches. Assuming an ideal determination of the necessary cancellation signal, the cancellation system will be limited by the digital hardware. The resulting restrictions are briefly described.

8.1 Concept

The two most promising approaches for active EMI cancellation (FFT method, Section 6.4 and notch filter method, Section 7.3) may appear to be very different at the first glance. But considering the fundamental principle, they are closely related. In both strategies, the cancellation signals are artificially synthesized by digital hardware. To maintain the destructive interference between EMI and anti-EMI, the injection is done in synchronicity with the EMI source. Optimizers find the right cancellation parameters to minimize the sensed residual EMI. This is a completely different strategy than in AEFs and DAEFs that use feedback or feedforward topologies to directly generate the cancellation signal from a sensed quantity.

Considering the similarities between the identified methods, a new concept can be derived according to Figure 8.1. This active EMI cancellation system uses digital hardware to inject synthesized and synchronized signals [16, author]. Most of the elements are the same as in Figure 6.3, but there are two major differences: The first is the abstraction of the synthesizer and the optimizer. The second is the option to use a feedback signal of an actual EMI victim instead of a sensor signal. In the case that the system is completely known, the cancellation signal can immediately be calculated and no feedback signal is necessary at all. However, in most practical applications, some form of feedback is needed to account for, e.g., parasitic or nonlinear effects of the system.

8.2 Predictability as Fundamental Requirement

The main feature of the proposed method is the injection of an artificially synthesized cancellation signal that is synchronized to the EMI source's operation. This anti-EMI must match very precisely with the EMI. To account for time constants and delay times (that are the limiting factors of AEFs and DAEFs), the anti-EMI must be generated before the EMI

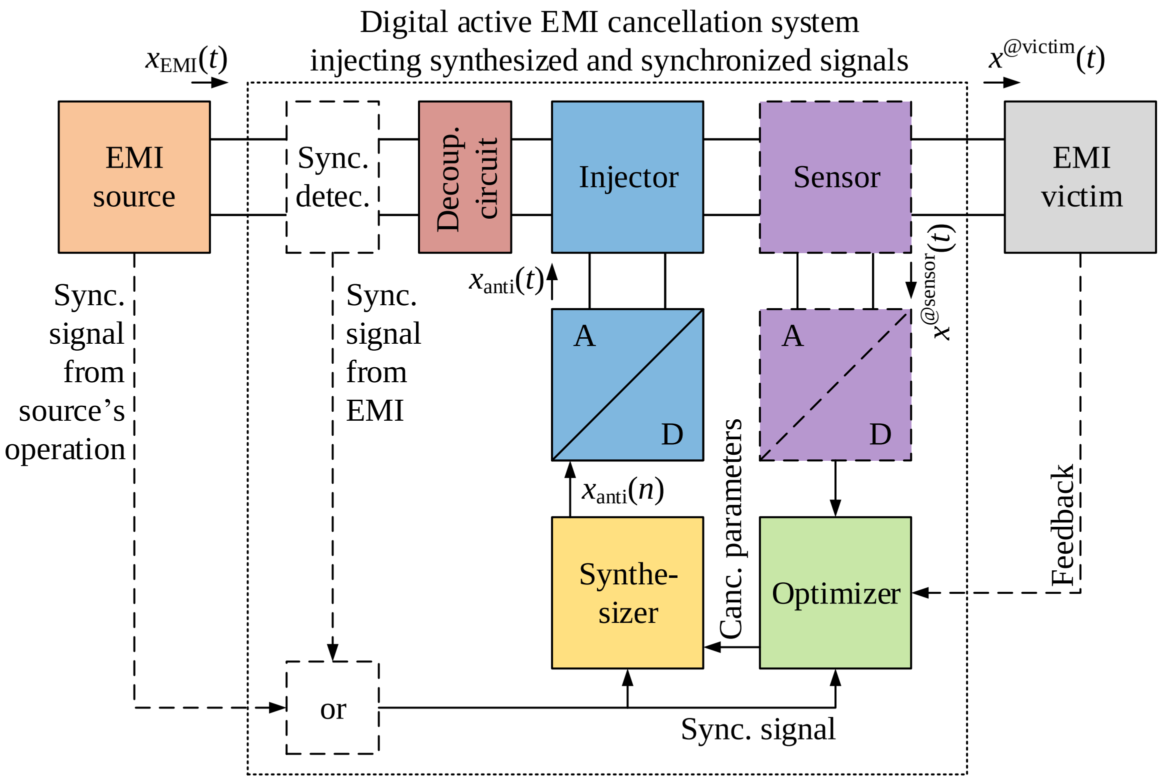

Figure 8.1: Concept of digital active EMI cancellation systems using synthesized and synchronized signals

occurs at the victim. This approach requires a predictability over the upcoming EMI.

This requirement is intrinsically fulfilled for quasi-periodic EMI since the information of the last period is still valid for the next. The synchronization of the cancellation system to the EMI source should also be no issue for a quasi-periodic operation.

The requirement of predictability is more complex for non-periodic EMI since the cancellation system cannot simply use the information from the past. Here, the possibilities and potential problems will be discussed for a power electronic system. The operation of these systems is usually defined by controllers. These controllers have information on the current operating mode and may also calculate the next control signals in advance. If these control signals as the origin of EMI are known beforehand, an EMI forecast is generally possible. However, changes in the EMI may not only result from the EMI source but also from the EMI victim by, e.g., rapid changes in loads. These changes of external systems may be difficult to predict. Therefore, external changes can lead to unpredictable EMI. Another interesting approach would be a self-learning cancellation system that gets to know its environment (EMI source and EMI victim). Such a system may detect characteristic changes and extrapolate the upcoming EMI. Recent advances in the field of artificial intelligence may offer interesting possibilities for practical realizations.

8.3 Variants for Realization

In the following, two important variants for practical implementations are discussed. Here, it is assumed that EMI source and cancellation system are installed in the same device. So, the synchronization should be convenient and a communication between the systems should generally be possible. It is assumed that the feedback signal is acquired by a sensor (and not by the EMI victim). The first variant for realization are self-adapting systems. The second variant are taught systems.

8.3.1 Self-Adapting Systems

An important variant are self-adapting systems according to Figure 8.2. For the self-adaption, the system needs sensor, optimizer, synthesizer and injector. This process could be done, e.g., continuously (e.g. notch filter method) or repeatedly (e.g. FFT method). In both cases, the resulting EMI at the output of the device is measured by the sensor and passed to the optimizer. The optimizer adjusts the cancellation parameters to minimize the resulting disturbances. So, the cancellation system can compensate changes of the signals or system by itself.

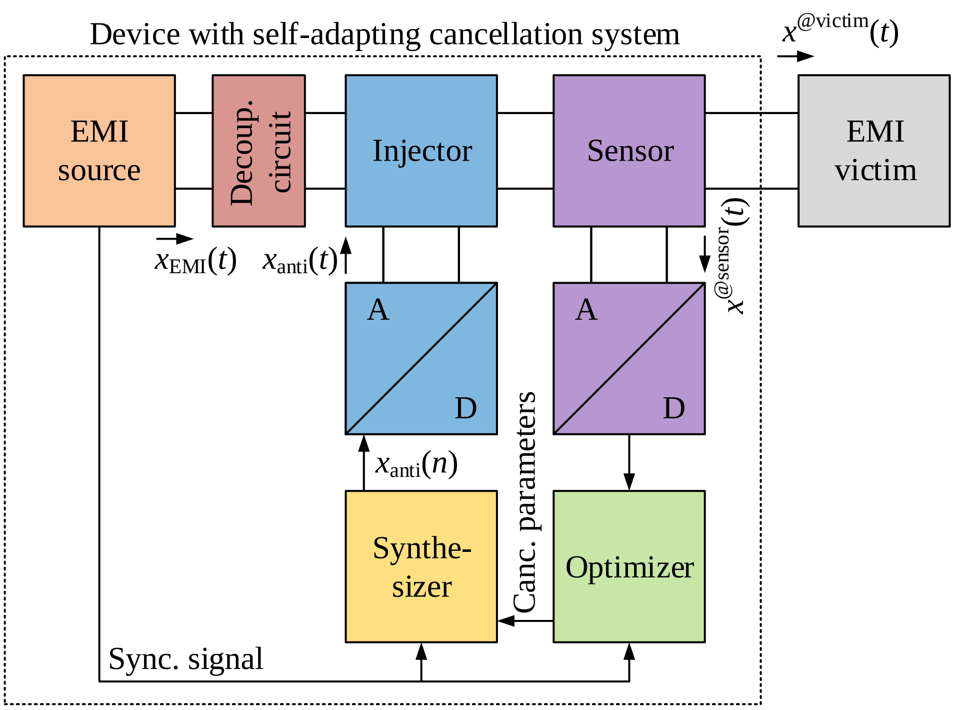

Figure 8.2: Digital realization with a self-adapting system

8.3.2 Taught Systems

Another important variant are systems taught by an external trainer according to Figure 8.3. Here, the cancellation system does not adapt itself. Instead, it is temporarily connected to an external trainer for teach-in. Afterward, the cancellation system uses the found parameters for cancellation. In this variant, sensor, optimizer and an optional signal preprocessor are outsourced to the external trainer that can teach numerous cancellation systems. The remaining cancellation system can be significantly reduced to injector, synthesizer and memory.

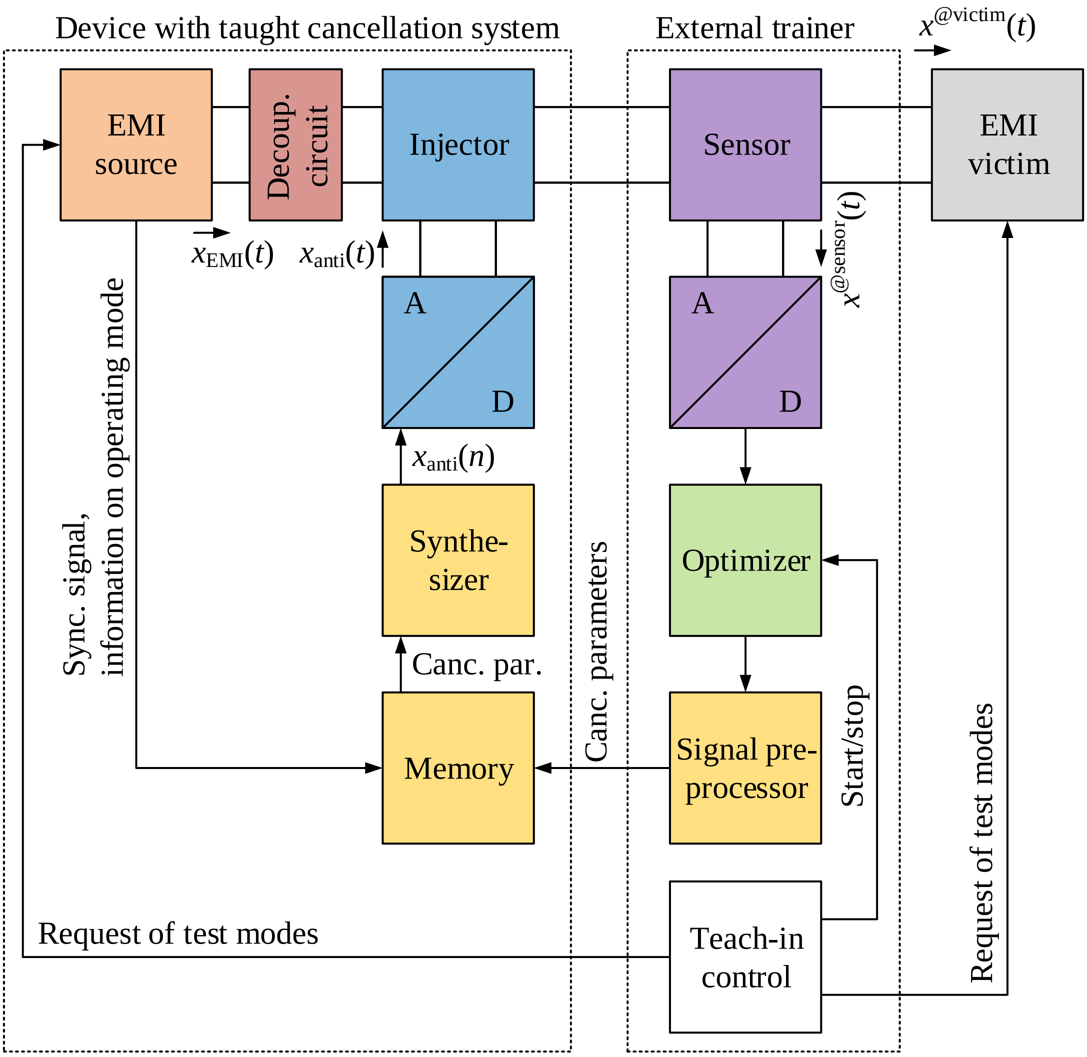

Figure 8.3: Digital realization with an external trainer and a taught system

During training, the cancellation system and the external trainer are connected. The teach-in control of the external trainer requests specific test operation modes from the EMI source and victim. The optimizer finds the right parameters for cancellation. These parameters can be prepared by a signal preprocessor and stored in the memory of the remaining cancellation system. Of course, the system must be taught for all relevant operating modes. For, e.g., power electronic systems, input and output voltages, transfer powers and temperatures are important parameters. Interpolation strategies may help to reduce the teach-in time. The training can be done in different schemes. It is possible to train only with a prototype and to use these parameters for all products of the same type. It is also possible to train each product individually, e.g., after manufacturing or installment in the destined environment. Furthermore, the system could be trained again after some time (for example during a planned maintenance).

In stand-alone operation, the EMI source informs the synthesizer about the current operating mode. This information is usually available from the controller of the EMI source. In, e.g., power electronics, the controller may have information on the operating parameters like transfer power, input voltage, output voltage and duty cycle. The cancellation system uses this information to synthesize the cancelling waveform from the corresponding parameters found in the memory.

Note that the removal of the external trainer can change the transfer functions and disturbances of the system. Due to this effect, the previously found cancellation signals may differ from the ones necessary after removal of the trainer. To avoid this issue, sensors can be chosen that influence the transfer functions as little as possible, or the impedance of the sensors can be substituted after removal.

In taught systems, the hardware effort for the cancellation system can be reduced significantly since sensor, optimizer and the optional signal preprocessor are outsourced. It must be noted that the training process can be bothersome since many different operating modes must be taught-in. Furthermore, slight deviations from the originally considered operating modes can lead to incorrect cancellation signals. As shown in Section 3.1.3.a), this can decrease the cancellation system's performance. The overall setup could also change (e.g. in its configuration) leading to different disturbances and transfer functions. Aging of the components may also pose a problem. To encounter these problems, it is possible to use some form of additional feedback to correct the cancellation signals during operation. This would lead to a hybrid (self-adapting and taught) system.

8.4 Methods for the Optimizer

There are numerous methods that can be applied to optimize the cancellation signal. In the following, some possibilities are listed and discussed:

- FFT method (Section 6.4)
- Notch filter method (Section 7.3)
- Narrowband power method [16, author]
- Broadband power method

The FFT method and the notch filter method have already been described and analyzed in the respective sections. Both of these methods require a high-frequency time-domain acquisition of the (residual) EMI. So, the ADC must have a high sampling rate. To reduce the hardware expenses of the signal acquisition, methods using narrowband or broadband power meters are discussed in the following. Afterward, the methods are compared in regard to the hardware requirements and the optimization speed. Last, the applicability to typical power electronic systems is discussed.

8.4.1 Narrowband Power Method

To avoid a high-frequency time-domain signal acquisition, a narrowband power meter can be applied (hence "narrowband power method"). This is motivated by the superheterodyne measurement principle used in, e.g., EMI test receivers and spectrum analyzers that detect the frequency spectrum of the EMI. This is usually done by filtering the signal with a band-pass filter and sensing the power. Since this band-pass filter has usually a fixed center frequency, the signal's frequency must be shifted so that different spectral frequencies can be evaluated. This can be done by a local oscillator and a mixer. The bandwidth of the band-pass filter must be much smaller than the fundamental frequency so that the individual harmonics can be measured precisely. As a downside, the phase information is usually unavailable and difficult to measure. A simple solution would be the usage of an iterative search algorithm that finds the correct phases for the cancelling sine waves by minimizing the power of the respective harmonic. However, search algorithms usually take numerous iterations for a convenient result. In [16, author], an effective algorithm is derived that needs only a few test measurements to identify the relevant characteristics of the system. The required sine waves for cancellation can easily be calculated by using the parameters of the identified system.

EMI test receivers or spectrum analyzers may be feasible components for an external trainer in a teach-in concept since they are very precise. The high cost can be reasonable if the number of external trainers is low in comparison to the number of taught systems. This standard measurement equipment can be especially interesting if the optimization is done for the measurement methods of the standards (e.g. artificial networks or antennas in automobiles [4]) that evaluate the EMI with the same device. [16, author]

Using EMI test receivers or spectrum analyzers can be expected to be no feasible approach for self-adapting systems due to the high costs. However, the required functionality could be replicated by using integrated circuits. This solution is interesting since the frequency selection is done in analog domain. So, the cancellation system must only acquire a DC value. In comparison to the FFT method, the requirements for the signal acquisition can be reduced significantly by doing so. Furthermore, no calculation-heavy FFT must be done since the signal has already been measured frequency-selective. This is another advantage in comparison to the FFT method. However, the FFT method must (theoretically) acquire only one fundamental period of the signal while the narrowband power method must detect the absolute value of each harmonic. Since the band-pass filter needs some time to settle, each harmonic must be measured for more than one period. So, the narrowband power method reduces the requirements of the digital system at the cost of additional analog components and a slower signal acquisition.

8.4.2 Broadband Power Method

It is also possible to optimize the cancellation signal in regard to the total power of the broadband (residual) EMI (and not in regard to the narrowband power of individual harmonics). In this case, the signal acquisition can be further simplified in comparison to the narrowband power method. Due to the broadband power measurement, there is no need for frequency selection. Therefore, a superheterodyne receiver is not necessary anymore. Common broadband power measurement techniques comprise, e.g., diode, thermoelectric and thermistor sensors [105]. Possible dynamic ranges are 90 dB for diode sensors, 50 dB for thermoelectric sensors and 20 dB for thermistor sensors [105]. These ranges can be a limiting factor for this method.

Since the total broadband power is measured without frequency selection, it is not possible to distinguish the influence of individual harmonics. So, in difference to the other discussed methods, the broadband power method can only optimize one harmonic at a time. Therefore, the cancellation signal must be constructed successively for each harmonic. This is a downside of the simplified hardware.

In the following, a method is presented on how to the find the right cancellation signals using a broadband power meter. At first, a mathematical description is developed. Afterward, the optimization problem is discussed and an efficient strategy for parameter identification is proposed.

a) Mathematical Representation of the Signals

For a mathematical representation, the cancelling sine wave for the κ-th harmonic is described by (8.1):

$$y_{\text{anti}}(t, \kappa f_0) = \begin{pmatrix} a(\kappa f_0) \\ b(\kappa f_0) \end{pmatrix} \cdot \vec{e}(t, \kappa f_0) \ \text{ with } \ \vec{e}(t, \kappa f_0) = \begin{pmatrix} \cos(2\pi\kappa f_0 \cdot t) \\ \sin(2\pi\kappa f_0 \cdot t) \end{pmatrix} \tag{8.1}$$

The factors $a(\kappa f_0)$ and $b(\kappa f_0)$ are the cancellation parameters that must be found. As before, the cancellation signal propagates through the system to the sensor (and/or victim). This propagation can be divided into a change in amplitude $|H_{\text{anti}}^{\rightarrow\text{sensor}}(\kappa f)|$ and phase $\angle H_{\text{anti}}^{\rightarrow\text{sensor}}(\kappa f_0)$. So, the anti-EMI at the sensor can be described by (8.2) with the amplitude response $G(\kappa f_0)$ of (8.3) and the rotation matrix $\boldsymbol{R}(\kappa f_0)$ of (8.4):

$$\Rightarrow y_{\text{anti}}^{@\text{sensor}}(t, \kappa f_0) = G(\kappa f_0) \cdot \boldsymbol{R}(\kappa f_0) \cdot \begin{pmatrix} a(\kappa f_0) \\ b(\kappa f_0) \end{pmatrix} \cdot \vec{e}(t, \kappa f_0) \tag{8.2}$$

$$\text{with } \ G(\kappa f_0) = |H_{\text{anti}}^{\rightarrow\text{sensor}}(\kappa f_0)| \geq 0 \tag{8.3}$$

$$\text{and } \boldsymbol{R}(\kappa f_0) = \begin{bmatrix} \cos(\angle H_{\text{anti}}^{\to\text{sensor}}(\kappa f_0)) & -\sin(\angle H_{\text{anti}}^{\to\text{sensor}}(\kappa f_0)) \\ \sin(\angle H_{\text{anti}}^{\to\text{sensor}}(\kappa f_0)) & \cos(\angle H_{\text{anti}}^{\to\text{sensor}}(\kappa f_0)) \end{bmatrix} \tag{8.4}$$

The EMI at the sensor is described by the real-valued Fourier series in (8.5):

$$y_{\text{EMI}}^{@\text{sensor}}(t) = \frac{c(0)}{2} + \sum_{k\in\mathbb{N}} \begin{pmatrix} c(kf_0) \\ d(kf_0) \end{pmatrix} \cdot \vec{e}(t, kf_0) \ \text{ with } \vec{e}(t, kf_0) = \begin{pmatrix} \cos(2\pi kf_0 \cdot t) \\ \sin(2\pi kf_0 \cdot t) \end{pmatrix} \tag{8.5}$$

The residual EMI at the sensor is the superposition of EMI and anti-EMI according to (8.6) and (8.7). Note that a, b, c and d are real numbers:

$$y_{\text{res}}^{@\text{sensor}}(t, \kappa f_0) = y_{\text{anti}}^{@\text{sensor}}(t, \kappa f_0) + y_{\text{EMI}}^{@\text{sensor}}(t) \tag{8.6}$$

$$= G(\kappa f_0) \cdot \boldsymbol{R}(\kappa f_0) \cdot \begin{pmatrix} a(\kappa f_0) \\ b(\kappa f_0) \end{pmatrix} \cdot \vec{e}(t, \kappa f_0)$$

$$+ \frac{c(0)}{2} + \sum_{k\in\mathbb{N}} \begin{pmatrix} c(kf_0) \\ d(kf_0) \end{pmatrix} \cdot \vec{e}(t, kf_0) \tag{8.7}$$

In (8.8), the κ-th harmonic of the EMI is drawn out of the sum and added to the first summand:

$$\Rightarrow y_{\text{res}}^{@\text{sensor}}(t, \kappa f_0) = \left[\begin{pmatrix} c(\kappa f_0) \\ d(\kappa f_0) \end{pmatrix} + G(\kappa f_0) \cdot \boldsymbol{R}(\kappa f_0) \cdot \begin{pmatrix} a(\kappa f_0) \\ b(\kappa f_0) \end{pmatrix} \right] \cdot \vec{e}(t, \kappa f_0)$$

$$+ \frac{c(0)}{2} + \sum_{k\in\mathbb{N}\setminus\{\kappa\}} \begin{pmatrix} c(kf_0) \\ d(kf_0) \end{pmatrix} \cdot \vec{e}(t, kf_0) \tag{8.8}$$

The superposition of EMI and anti-EMI for the κ-th harmonic is described by the first summand, the DC value is represented by the second and the other harmonics are denoted by the sum. Therefore, all harmonics are separated. In (8.9) and (8.10), the squared RMS value of $y_{\text{res}}^{@\text{sensor}}(t, \kappa f_0)$ is calculated:

$$\Rightarrow Y_{\text{res,RMS}}^{@\text{sensor}^2}(\kappa f_0) = \sqrt{f_0 \cdot \int_0^{1/f_0} y_{\text{res}}^{@\text{sensor}^2}(t, \kappa f_0)\, dt}^{\,2} \tag{8.9}$$

$$= f_0 \cdot \int_0^{1/f_0} y_{\text{res}}^{@\text{sensor}^2}(t, \kappa f_0)\, dt \tag{8.10}$$

The integral is solved by the squared RMS values of the individual harmonics according to Parseval's theorem. To do so, the norms are calculated, divided by $\sqrt{2}$, squared and added up in (8.11):

$$
\begin{aligned}
\Rightarrow Y_{\text{res,RMS}}^{\text{@sensor}^2}(\kappa f_0) = &\left[\frac{1}{\sqrt{2}}\left\|\begin{pmatrix} c(\kappa f_0) \\ d(\kappa f_0)\end{pmatrix} + G(\kappa f_0)\cdot \boldsymbol{R}(\kappa f_0)\cdot \begin{pmatrix} a(\kappa f_0) \\ b(\kappa f_0)\end{pmatrix}\right\|\right]^2 \\
&+\left[\frac{c(0)}{2}\right]^2 + \sum_{k\in\mathbb{N}\setminus\{\kappa\}}\left[\frac{1}{\sqrt{2}}\left\|\begin{pmatrix} c(kf_0) \\ d(kf_0)\end{pmatrix}\right\|\right]^2
\end{aligned}
\tag{8.11}
$$

The solution can be found in (8.12):

$$
\begin{aligned}
\Rightarrow Y_{\text{res,RMS}}^{\text{@sensor}^2}(\kappa f_0) = &\frac{1}{2}\cdot G^2(\kappa f_0)\cdot a^2(\kappa f_0) + \frac{1}{2}\cdot G^2(\kappa f_0)\cdot b^2(\kappa f_0) \\
&+ G(\kappa f_0)\left[c(\kappa f_0)\cdot\cos(...) + d(\kappa f_0)\cdot\sin(...)\right]\cdot a(\kappa f_0) \\
&+ G(\kappa f_0)\left[-c(\kappa f_0)\cdot\sin(...) + d(\kappa f_0)\cdot\cos(...)\right]\cdot b(\kappa f_0) \\
&+ \frac{1}{2}\cdot\left(c^2(\kappa f_0) + d^2(\kappa f_0)\right) \\
&+ \frac{c^2(0)}{4} + \sum_{k\in\mathbb{N}\setminus\{\kappa\}}\frac{c^2(kf_0)+d^2(kf_0)}{2}
\end{aligned}
\tag{8.12}
$$

In (8.13), $c^2(\kappa f_0)/2$ and $d^2(\kappa f_0)/2$ are added to the sum again:

$$
\begin{aligned}
\Rightarrow Y_{\text{res,RMS}}^{\text{@sensor}^2}(\kappa f_0) = &\frac{1}{2}\cdot G^2(\kappa f_0)\cdot a^2(\kappa f_0) + \frac{1}{2}\cdot G^2(\kappa f_0)\cdot b^2(\kappa f_0) \\
&+ G(\kappa f_0)\left[c(\kappa f_0)\cdot\cos(...) + d(\kappa f_0)\cdot\sin(...)\right]\cdot a(\kappa f_0) \\
&+ G(\kappa f_0)\left[-c(\kappa f_0)\cdot\sin(...) + d(\kappa f_0)\cdot\cos(...)\right]\cdot b(\kappa f_0) \\
&+ \frac{c^2(0)}{4} + \sum_{k\in\mathbb{N}}\frac{c^2(kf_0)+d^2(kf_0)}{2}
\end{aligned}
\tag{8.13}
$$

By introducing new variables, the term can be simplified to (8.14) that equals the square RMS value of the complete residual signal:

$$
\begin{aligned}
\Rightarrow Y_{\text{res,RMS}}^{\text{@sensor}^2}(\kappa f_0) = &\alpha(\kappa f_0)\cdot a^2(\kappa f_0) + \alpha(\kappa f_0)\cdot b^2(\kappa f_0) \\
&+ \beta(\kappa f_0)\cdot a(\kappa f_0) + \gamma(\kappa f_0)\cdot b(\kappa f_0) \\
&+ \delta(\kappa f_0)
\end{aligned}
\tag{8.14}
$$

b) Optimization Problem

Considering the structure of (8.14), it can be found that the equation describes a circular paraboloid. First of all, the paraboloid is larger (or equal) zero since RMS values (here of $y_{\text{res}}^{\text{@sensor}}(t, \kappa f_0)$) are always positive. Moreover, it is opened in positive direction of $Y_{\text{res,RMS}}^{\text{@sensor}^2}$ since $\alpha(\kappa f_0)$ is positive by definition of $G(\kappa f_0)$ in (8.3). So, this is a convex optimization problem. This paraboloid has exactly one unambiguous minimum that is reached if the κ-th harmonic is completely cancelled out. It has to be found for which cancellation parameters $a(\kappa f_0)$ and $b(\kappa f_0)$ this minimum is reached. To do so, the squares for $a(\kappa f_0)$ and $b(\kappa f_0)$ are completed in (8.15)-(8.17):

$$\begin{aligned}
\Rightarrow Y_{\text{res,RMS}}^{@\text{sensor}^2}(\kappa f_0) &= \alpha(\kappa f_0)\cdot\left(a^2(\kappa f_0)+\frac{\beta(\kappa f_0)\cdot a(\kappa f_0)}{\alpha(\kappa f_0)}\right)\\
&\quad+\alpha(\kappa f_0)\cdot\left(b^2(\kappa f_0)+\frac{\gamma(\kappa f_0)\cdot b(\kappa f_0)}{\alpha(\kappa f_0)}\right)\\
&\quad+\delta(\kappa f_0) \qquad (8.15)\\
&=\alpha(\kappa f_0)\cdot\left(a^2(\kappa f_0)+\frac{\beta(\kappa f_0)\cdot a(\kappa f_0)}{\alpha(\kappa f_0)}+\frac{\beta^2(\kappa f_0)}{4\alpha^2(\kappa f_0)}-\frac{\beta^2(\kappa f_0)}{4\alpha^2(\kappa f_0)}\right)\\
&\quad+\alpha(\kappa f_0)\cdot\left(b^2(\kappa f_0)+\frac{\gamma(\kappa f_0)\cdot b(\kappa f_0)}{\alpha(\kappa f_0)}+\frac{\gamma^2(\kappa f_0)}{4\alpha^2(\kappa f_0)}-\frac{\gamma^2(\kappa f_0)}{4\alpha^2(\kappa f_0)}\right)\\
&\quad+\delta(\kappa f_0) \qquad (8.16)\\
&=\alpha(\kappa f_0)\cdot\left(a(\kappa f_0)+\frac{\beta(\kappa f_0)}{2\alpha(\kappa f_0)}\right)^2\\
&\quad+\alpha(\kappa f_0)\cdot\left(b(\kappa f_0)+\frac{\gamma(\kappa f_0)}{2\alpha(\kappa f_0)}\right)^2\\
&\quad+\delta-\frac{\beta^2(\kappa f_0)}{4\alpha(\kappa f_0)}-\frac{\gamma^2(\kappa f_0)}{4\alpha(\kappa f_0)} \qquad (8.17)
\end{aligned}$$

Considering the form of (8.17), the **opt**imum values for the cancellation parameters $a(\kappa f_0)$ and $b(\kappa f_0)$ can be expressed by (8.18) and (8.19):

$$\Rightarrow a_{\text{opt}}(\kappa f_0) = -\frac{\beta(\kappa f_0)}{2\alpha(\kappa f_0)} \qquad (8.18)$$

$$\Rightarrow b_{\text{opt}}(\kappa f_0) = -\frac{\gamma(\kappa f_0)}{2\alpha(\kappa f_0)} \qquad (8.19)$$

Since the problem is convex, search or gradient descent algorithms can be used to find $a_{\text{opt}}(\kappa f_0)$ and $b_{\text{opt}}(\kappa f_0)$. However, iterative methods may need numerous steps for convenient results. To resolve this issue, the system's parameters $\alpha(\kappa f_0)$, $\beta(\kappa f_0)$, $\gamma(\kappa f_0)$ and $\delta(\kappa f_0)$ can also be identified by test measurements. Afterward, the ideal parameters $a_{\text{opt}}(\kappa f_0)$ and $b_{\text{opt}}(\kappa f_0)$ for the cancelling sine wave can immediately be calculated by (8.18) and (8.19). One possible method for parameter identification is presented in the next section.

c) Parameter Identification

In the following, a method for parameter identification is developed that requires only four test measurements per harmonic.

At first, $\delta(\kappa f_0)$ is identified. This can easily be done by deactivating the cancelling sine wave for the κ-th harmonic $(a(\kappa f_0)=0$ and $b(\kappa f_0)=0)$ and measuring the EMI of the system $Y^{@\text{sensor}}_{\text{EMI,RMS,meas}}(\kappa f_0)$. From (8.14), the relationship of (8.20) can be found:

$$\overset{(8.14)}{\Rightarrow} \delta(\kappa f_0) = \left[Y^{@\text{sensor}}_{\text{EMI,RMS,meas}}(\kappa f_0)\right]^2 \tag{8.20}$$

The parameters $\alpha(\kappa f_0)$, $\beta(\kappa f_0)$ and $\gamma(\kappa f_0)$ can be found by applying three different test signals with arbitrary values $a_{\text{test,i}}(\kappa f_0)$ and $b_{\text{test,i}}(\kappa f_0)$ and measuring the system's response $Y^{@\text{sensor}}_{\text{res,RMS,meas,i}}(\kappa f_0)$ (with $i = 1,2,3$). To do so, (8.14) is formulated as a linear set of equations according to (8.21):

$$\overset{(8.14)}{\Rightarrow} \begin{pmatrix} {Y^{@\text{sensor}}_{\text{res,RMS,meas,1}}}^2(\kappa f_0) \\ {Y^{@\text{sensor}}_{\text{res,RMS,meas,2}}}^2(\kappa f_0) \\ {Y^{@\text{sensor}}_{\text{res,RMS,meas,3}}}^2(\kappa f_0) \end{pmatrix} = \begin{bmatrix} a^2_{\text{test,1}}(\kappa f_0) + b^2_{\text{test,1}}(\kappa f_0) & a_{\text{test,1}}(\kappa f_0) & b_{\text{test,1}}(\kappa f_0) \\ a^2_{\text{test,2}}(\kappa f_0) + b^2_{\text{test,2}}(\kappa f_0) & a_{\text{test,2}}(\kappa f_0) & b_{\text{test,2}}(\kappa f_0) \\ a^2_{\text{test,3}}(\kappa f_0) + b^2_{\text{test,3}}(\kappa f_0) & a_{\text{test,3}}(\kappa f_0) & b_{\text{test,3}}(\kappa f_0) \end{bmatrix} \cdot \begin{pmatrix} \alpha(\kappa f_0) \\ \beta(\kappa f_0) \\ \gamma(\kappa f_0) \end{pmatrix} + \delta(\kappa f_0) \tag{8.21}$$

This set of equations can be solved according to (8.22):

$$\Rightarrow \begin{pmatrix} \alpha(\kappa f_0) \\ \beta(\kappa f_0) \\ \gamma(\kappa f_0) \end{pmatrix} = \begin{bmatrix} a^2_{\text{test,1}}(\kappa f_0) + b^2_{\text{test,1}}(\kappa f_0) & a_{\text{test,1}}(\kappa f_0) & b_{\text{test,1}}(\kappa f_0) \\ a^2_{\text{test,2}}(\kappa f_0) + b^2_{\text{test,2}}(\kappa f_0) & a_{\text{test,2}}(\kappa f_0) & b_{\text{test,2}}(\kappa f_0) \\ a^2_{\text{test,3}}(\kappa f_0) + b^2_{\text{test,3}}(\kappa f_0) & a_{\text{test,3}}(\kappa f_0) & b_{\text{test,3}}(\kappa f_0) \end{bmatrix}^{-1} \cdot \left[\begin{pmatrix} {Y^{@\text{sensor}}_{\text{res,RMS,meas,1}}}^2(\kappa f_0) \\ {Y^{@\text{sensor}}_{\text{res,RMS,meas,2}}}^2(\kappa f_0) \\ {Y^{@\text{sensor}}_{\text{res,RMS,meas,3}}}^2(\kappa f_0) \end{pmatrix} - \delta(\kappa f_0) \right] \tag{8.22}$$

After identification, the ideal parameters $a_{\text{opt}}(\kappa f_0)$ and $b_{\text{opt}}(\kappa f_0)$ for the cancelling sine wave can be found by (8.18) and (8.19). The ideal cancellation signal is calculated by (8.1) using these parameters.

This strategy can successively be applied to all disturbing harmonics to suppress the EMI in a wide frequency range. Since the overall EMI is reduced, the parameter $\delta(\kappa f_0)$ decreases for each cancelled harmonic. The cancellation result can be further improved by doing multiple iterations.

Note that $\alpha(\kappa f_0)$ could also be identified beforehand by measuring the amplitude response $\left|H^{\to\text{sensor}}_{\text{anti}}(f)\right|$. By doing so, the number of necessary measurements per harmonic can be reduced by one. However, it must be considered that the transfer functions can change if there are variations in the overall system.

8.4.3 Overview of Optimizer Methods

In Table 8.1, an overview of the discussed methods for cancellation signal generation is given. Important aspects are the required hardware for signal acquisition, the requirements for the digital signal processing hardware and the optimization speed. The methods are broadly classified in regard to these aspects to enable a more convenient comparison.

Method	Acquisition hardware	Requirements for signal processing hardware	Optimization speed	Section
FFT	High-speed ADC	Moderate	High	6.4
Notch filter (parallel)	High-speed ADC	High	Very high	7.3
Notch filter (successive)	High-speed ADC	Moderate	High	7.3.4
Narrowband power	Superhet. receiver	Low	Moderate	8.4.1
Broadband power	Power meter	Low	Low	8.4.2

Table 8.1: Overview of methods to determine broadband cancellation signals

The notch filter method using multiple parallel single-frequency adaptive notch filters with, e.g., multiple delayed LMS algorithms can be expected to be the fastest since it adapts itself immediately after changes in the system. To do so, high-speed ADCs are necessary for signal acquisition. Since multiple real-time calculations must be done during each period of the cancelling sine waves, the requirements for the digital signal processing hardware are quite high. The adaption may still take some fundamental periods of the EMI, but it does not need acquisition and calculation intervals like, e.g., the FFT method. Due to the continuous adaption, this method may not only be applied to quasi-periodic, but also to moderately changing EMI (e.g. of PFCs [106, 107, author, supervisor]). All of the other discussed methods are only capable of handling very slow changes in the quasi-periodic EMI (e.g. due to temperature drifts).

In the successive notch filter method, the cancelling sine waves are optimized one by one. Since the calculations are only done for, e.g., one or a few harmonics at a time, the requirements for the digital hardware are significantly reduced. Due to the successive approach for signal generation, the optimization speed of the method is reduced in comparison to the parallel implementation.

The FFT method still requires a high-speed signal acquisition. Calculating the FFT for numerous harmonics may be a time-consuming task for the digital signal processing hardware. However, since acquisition, calculation and cancellation signal injection are separated in different time intervals, there are no real-time requirements for the digital signal processing hardware. The optimization speed can still be high since the broadband signal acquisition must only be done for one or multiple fundamental periods of the EMI.

In the narrowband power method, the calculations for each harmonic are significantly less demanding. Furthermore, the high-speed ADC can be replaced by superheterodyne receivers. Since the band-pass filter for frequency selection must settle for each considered harmonic, a broadband signal acquisition may take some time.

The requirements for the signal processing hardware are also low for the broadband power method since the calculations are rather simple. The optimization speed can be expected to be low since the broadband power measurement will take some time (e.g. due to thermal time constants of the sensing principle). Furthermore, the optimization can only be done for one harmonic at a time since the method is not frequency-selective.

8.4.4 Suggestions for Typical Power Electronic Systems

Until now, the different methods for cancellation signal determination have been discussed on a general and abstract level. Choosing the right method that will lead to an overall optimized power electronic system is no trivial task. Although there is no simple solution to this problem, some broad recommendations are given in the following.

At first, DC-to-DC converters are discussed. In a stationary mode of operation (constant switching frequency, duty cycle, transfer power, temperature, etc.), quasi-periodic disturbances can be expected. So, all of the proposed methods are applicable. The narrowband and broadband methods can be especially interesting since they require only a simple signal processing hardware leading to a cost-efficient cancellation system. If changes in the operating mode of the power electronic system are common, the cancellation system may need a faster optimization method with a more expensive cancellation hardware. The FFT and successive notch filter method may be a good solution in this case. If the time intervals of stationary operation are too brief for these methods, the computation-heavy parallel notch filter method may be necessary.

Motor inverters may also operate in a stationary mode. In this case, the EMI will repeat itself with the fundamental frequency of the generated three-phase voltage system (in a first approximation). Therefore, a very long cancellation signal with the respective fundamental period is necessary. This signal could be generated by each of the discussed methods. If the operation is not stationary, it is best to apply the parallel notch filter method to the relevant switching harmonics. Predictive approaches may be a good extension to compensate remaining time delays due to, e.g., signal processing. If there is a non-periodic operation with unpredictable changes, the application of synchronized and synthesized cancellation signals is not feasible. In this case, AEFs or DAEFs may be a better solution.

AC-to-DC converters (e.g. PFCs or SMPS) have a different function than motor inverters, but the resulting disturbances are quite similar. So, the suggestions for motor inverters are also applicable to these converters.

8.5 Limitations due to Digital Hardware

By using synthesized and synchronized cancellation signals, limitations due to time constants and delay times can be compensated. Remaining limitations result from the vertical resolution (Section 5.1.1) and the sampling rate (Section 5.1.2) of the digital signal processing hardware with its ADCs and DACs (further limitations may result from the dynamic range of the broadband power measurement if this method is applied). This leads to the question how the digital cancellation system must be designed so that specific requirements can be fulfilled. The required dimensioning directly depends on the analog system (decoupling, injecting and sensing circuits, EMI source and EMI victim). So, a purposeful design of the overall cancellation system is necessary. In the Chapters 10 and 11, single- and multi-port active EMI cancellation systems are systematically designed for a DC-to-DC converter. With adjustments, the proposed strategies may also be applied to other systems.

8.6 Demonstrator Results of the Proposed Method

Numerous demonstrator results have been achieved and published for the proposed method. Most of these are summarized in Table 8.2. The active EMI cancellation using synthesized and synchronized signals has been mostly applied to DC-to-DC converters. There are also some recent results for the application to the input side of PFCs and motor inverters. There are many results for the suppression of DM EMI and also some in which both DM and CM EMI have been suppressed.

The method has been applied to the frequency range of 100 kHz to 30 MHz. The highest achieved reductions for the EMI of DC-to-DC converters are 66 dB for 300 kHz and 46 dB for 30 MHz. These results are much better than the ones of AEFs (Section 4.5.1) and DAEFs (Section 5.2). Note that the values given for the achieved EMI reduction only comprise the active suppression due to the injected cancellation signals. The injecting, sensing and decoupling circuits also introduce some passive attenuation (not quoted here) that comes on top.

The method has been applied to various injector and sensor concepts. The hardware for realization comprises FPGA systems, **a**rbitrary **w**aveform **g**enerators (AWGs), EMI test receivers, PCs and oscilloscopes. The used methods comprise the notch filter method (in parallel and successive implementation), the narrowband power method and the FFT method. As shown by these works, the proposed method offers a high potential and also a high degree of freedom for the realization.

Some chosen results on a self-adapting FPGA system using the notch filter method will be presented in the following chapter. In the subsequent chapters, new results are presented in which single- and multi-port active EMI cancellation systems are purposefully designed after a system identification. In these chapters, the FFT method will be applied with AWGs, a PC and an oscilloscope.

Application	EMI mode	Frequencies	Reductions	Injector	Sensor	Hardware	Method	Reference
DC-to-DC	DM	300 kHz -1.8 MHz	66 dB 48 dB	Inductive	Artificial network	FPGA	Notch filter $(6\times)$	[102, author]
DC-to-DC	DM	300 kHz -1.8 MHz	53 dB 48 dB	Inductive	Capacitive	FPGA	Notch filter $(6\times)$	[15, author]
DC-to-DC	DM	300 kHz -30 MHz	$\underline{42}$-48 dB $\underline{21}$-33 dB	Capacitive	Artificial network	EMI test receiver & PC & AWG/$\underline{\text{FPGA}}$	Frequency-domain measurement	[16, author]
DC-to-DC	DM	300 kHz -30 MHz	60 dB 38 dB	Inductive	Capacitive	FPGA	Notch filter (successive)	[104, author]
DC-to-DC	DM & CM	1 MHz -30 MHz	$\approx$ 50 dB $\approx$ 40 dB	Capacitive	Capacitive	AWG & PC & oscilloscope	FFT method	[17, author]
DC-to-DC	DM & CM	1 MHz -30 MHz	$\approx$ 53 dB $\approx$ 40 dB	Capacitive	Capacitive	AWG & PC & oscilloscope	FFT method	[108, supervisor]
DC-to-DC	DM & CM	1 MHz -30 MHz	$\approx$ 57 dB $\approx$ 46 dB	Inductive	Artificial network	AWG & PC & oscilloscope	FFT method	[108, 109, supervisor and co-author]
PFC (input)	DM	@100 kHz	46 dB	Inductive	Capacitive	FPGA	Notch filter $(1\times)$	[106, 107, author and supervisor]
Motor inverter (input)	DM	200 kHz -500 kHz -1.8 MHz	33-42 dB 30-40 dB 17 dB	Capacitive	Capacitive	AWG & PC & oscilloscope	FFT method	[81, 110, supervisor and author]
Motor inverter (input)	DM	100 kHz -400 kHz -30 MHz	48-49 dB 50-54 dB 24-27 dB	Capacitive	Capacitive	AWG & PC & oscilloscope	FFT method	[111, author]

Table 8.2: Demonstrator results of the proposed method

8.7 Chapter Summary

In this chapter, a new active EMI cancellation method has been derived that achieves the destructive interference between EMI and anti-EMI by injecting synthesized and synchronized cancellation signals. Since delay times and time constants can be compensated by shaping the cancellation signal and injecting it in advance, the performance can be significantly improved in comparison to AEFs and DAEFs.

To do so, this new method requires the EMI to be predictable. For quasi-periodic EMI, the signals can always be predicted since the information from the previous period is also valid for the next. For non-periodic EMI, more sophisticated methods are necessary to forecast the upcoming EMI. Some possibilities have been briefly discussed.

Assuming an ideal prediction of the EMI and an ideal calculation of the anti-EMI, the digital hardware limits the achievable performance. So, it must be purposefully dimensioned to fulfill specific requirements in the overall system. A possible approach for single- and multi-port active EMI cancellation systems will be presented in the demonstrations of the Chapters 10 and 11.

During the work on this thesis, various promising demonstrator results could be achieved. These have been briefly summarized. The best results show an active EMI reduction of 66 dB for 300 kHz and 46 dB for 30 MHz (for the EMI of a DC-to-DC converter). This is a much better performance than the one of AEFs (Section 4.5.1) and DAEFs (Section 5.2). Some of the demonstrator results on the notch filter method will be summarized and discussed in the following chapter.

9 Investigation and Demonstration of the Notch Filter Method for Active EMI Cancellation

In this chapter, the notch filter method is applied to a DC-to-DC converter and a **p**ower **f**actor **c**orrection (PFC). At first, the used FPGA system is presented. The performance of the algorithm and the FPGA is investigated in a simplified test setup using a 50 Ω power splitter. Both the parallel and successive implementation variant are applied to the DM EMI of a DC-to-DC converter. Last, the method is tested for the applicability to the DM EMI of a common boost PFC.

9.1 FPGA Signal Processing System

To realize the single-frequency adaptive notch filter with delayed LMS algorithm, digital hardware with high-frequency capabilities is necessary. During the work on this thesis, a programmable FPGA evaluation system Red Pitaya STEMlab 125-14 (Figure 9.1) has been used. Among other features, this evaluation system comprises a capable FPGA for high-frequency signal processing and two high-frequency ADCs and DACs with a voltage range of ±1 V, a vertical resolution of 14 bit, a sampling rate of 125 MS/s and a bandwidth of 50 MHz.

Figure 9.1: Photograph of an FPGA evaluation system Red Pitaya STEMlab 125-14

For programming, an automated tool chain has been realized in different works (e.g. [112, supervisor]) and published in [102, author]. This tool chain is briefly explained in the following. The logic can be designed by using MATLAB Simulink. This graphic programming is very convenient and enables also a prior simulation of the functionality of the logic. Based on this Simulink model, HDL (**h**ardware **d**escription **l**anguage) models are generated by the HDL Coder of MATLAB. Afterward, these are embedded into a standard frame in Xilinx Vivado.

In Xilinx Vivado, three steps are necessary to realize the logic on an FPGA: First, during synthesis, a netlist of logic elements is generated based on the functional description. Second, during implementation, the netlist is modified for the specific FPGA. There are many important requirements (e.g. timing constraints). If some signal propagation times are too long, the timing between signals may deviate. So, the logic will most likely not work properly. In this case, Xilinx Vivado may show warnings, errors or even suggestions for the designer on where to place delay blocks in the original model in order to correct the timing problem. Third, a bit stream is generated that includes all necessary information for configuring the FPGA according to the intended logic.

The Red Pitaya STEMlab 125-14 contains a CPU running a Linux operating system that can program the FPGA and communicate via Ethernet. So, a binary file is generated from the bit stream on the developer's computer and sent to the Red Pitaya STEMlab via Ethernet and an FTP connection. This logic can be activated on the FPGA by using a SSH remote connection to the Linux operating system.

This complete tool chain is automated by a batch file that offers a convenient way to program the prototype hardware.

9.2 Performance in a Simplified System

The single-frequency adaptive notch filter with delayed LMS algorithm is implemented on a Red Pitaya STEMlab 125-14. This implementation goes back to [112, supervisor]. For a systematic investigation of the performance, a defined test setup according to Figure 9.2 is used.

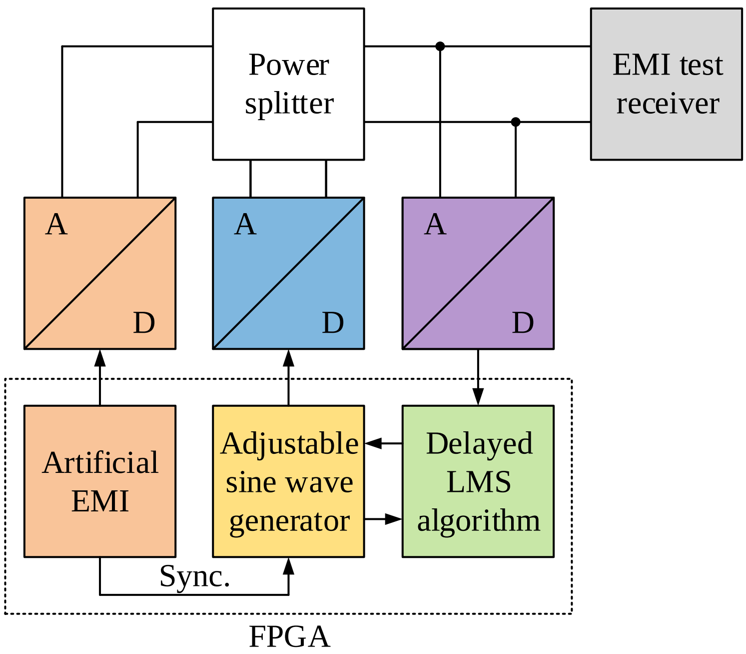

Figure 9.2: Test setup for investigations of the performance of the FPGA system

For full control of the system, the EMI is artificially generated by the FPGA itself, converted by an ADC and injected into a 50 Ω power splitter. Since EMI source and cancellation system are realized on the same hardware, they can be perfectly synchronized. The cancellation signal of the adjustable sine wave generator is also converted to the analog domain and injected into a power splitter. EMI and anti-EMI superpose each other in the power splitter and result in a residual EMI. This signal is digitized by an ADC and evaluated by the delayed LMS algorithm that optimizes the cancelling sine wave. The algorithm uses the same sampling rate as the ADCs and DACs (125 MS/s).

An EMI test receiver is used as reference measurement device. According to [4], a measurement bandwidth of 9 kHz and a measurement time of at least 50 ms is used. Since repeating EMI signals are considered, average and peak detector show basically the same results. However, the average detector is more precise since it evens out stochastic noise. So, it is chosen for the measurements in this section. The coupling by a power splitter results in simplistic transfer functions (ideally only some attenuation without significant phase shifts). The influence of external EMI sources is minimized by the shielded system. So, clean and precise measurements can be conducted.

In the following, different aspects are investigated. These comprise the suppression limit, the harmonic distortion and the frequency performance. To do so, a simple sine wave is generated as artificial EMI. The step size μ is set very low to achieve precise results. This investigation has also been published in [102, author].

9.2.1 Suppression Limits

To investigate the suppression limit, the amplitude of the artificial EMI (sine wave) is varied. Both EMI and anti-EMI have a fundamental frequency of 1 MHz. The amplitude of the artificial EMI and the anti-EMI is limited by the voltage range of the DACs (± 1 V). A sine wave with this amplitude corresponds to an effective value of 117 dBµV. The 50 Ω power splitter and the termination impedance of the EMI test receiver (50 Ω) lead to some attenuation. The results for four different amplitudes of the EMI are depicted in Figure 9.3.

Independent from the original amplitude of the EMI, the residual EMI is reduced to the same level of approximately 20-35 dBµV for each measurement. This can be explained by the noise floor of the ADC. The noise floor can be calculated by subtracting the SNR (approximately 86 dB for a vertical resolution of 14 bit according to (5.1)) from the upper limit (± 1 V $\widehat{=}$ 117 dBµV). So, a noise floor of approximately 31 dBµV results. This value matches well with the residual EMI since the cancelling sine wave is continuously optimized by the delayed LMS algorithm until the sensed signal becomes so small that it is indistinguishable from the ADC's noise floor. Note that the noise floor of the EMI test receiver has been no limiting factor in these measurements.

This result is very interesting since conventional methods for EMI reduction (e.g. passive

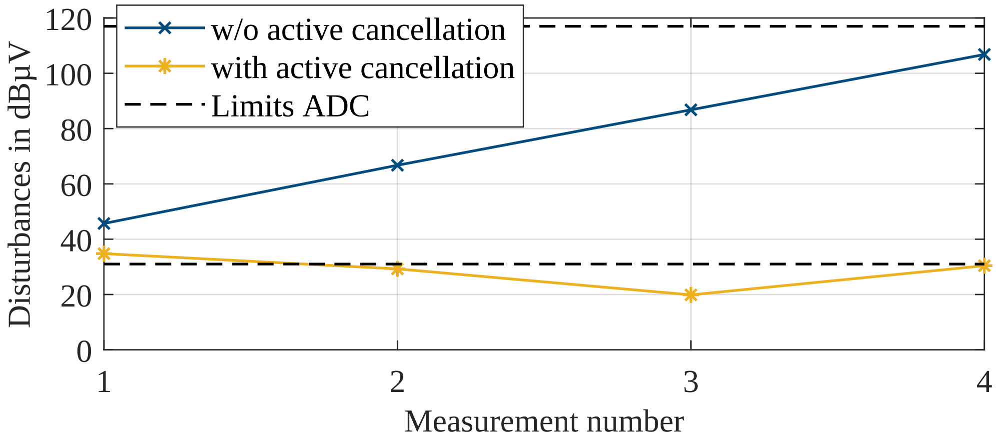

Figure 9.3: Measurement results for the achievable EMI reduction of the used FPGA system

filters or shields) introduce a relative attenuation that is independent from the EMI level (as long as they behave linearly). Even AEFs can be expected to introduce a relative reduction as long as they are not overdriven or limited by their noise floors. In the proposed system, the achievable EMI reduction depends on the disturbances before cancellation (since the residual EMI with cancellation is suppressed to the same limit independent from the original EMI). So, the system shows the highest EMI reduction if the original level of the EMI is high. However, it must be noted that the ADCs must not be overdriven since the system may fail in this scenario. The maximum achievable EMI reduction for a single sine wave is defined by the SNR of the interface circuits (note also the description of Section 5.1.1).

9.2.2 Frequency Performance

Next, the frequency performance of the cancellation system is analyzed. To do so, the amplitude of the artificial disturbing sine wave is kept constant and the frequency is successively increased from 1 MHz to 50 MHz (limited by the bandwidth of the Red Pitaya STEMlab 125-14). The frequency of the cancelling sine wave is increased respectively. The measurement result can be found in Figure 9.4.

The EMI with active cancellation matches relatively well with the noise floor of the ADC. The curves for the EMI with and without active cancellation drop for higher frequencies. This may be due to a frequency-dependent transfer behavior of the overall circuitry. However, this measurement still shows that the cancelling sine wave is optimized until the residual EMI falls into the noise floor of the ADC. The performance of the cancellation system is independent from the fundamental frequency. As discussed in Section 5.1.2, the suppressible frequency range is limited by the Nyquist-Shannon theorem and the bandwidth of the analog filters.

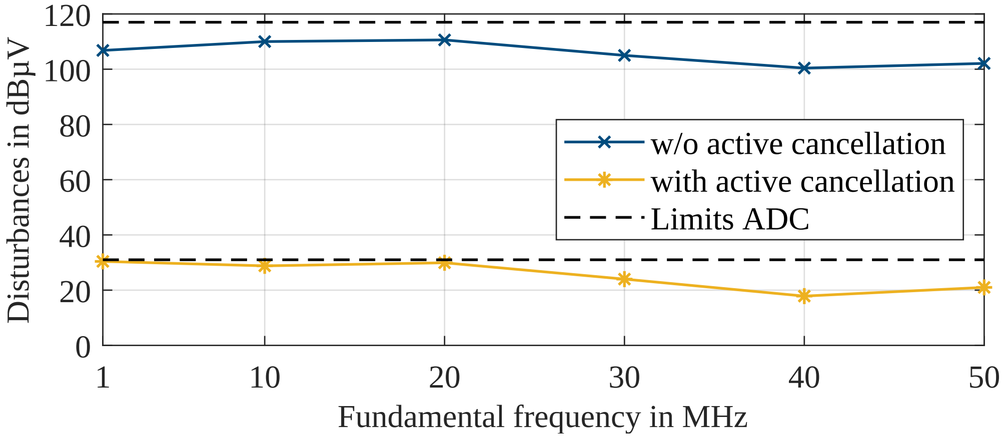

Figure 9.4: Measurement results for the frequency performance of the used FPGA system

9.2.3 Harmonic Distortion

Since all DACs have a finite resolution, they will cause harmonic distortion. This effect is investigated in the measurement of Figure 9.5. Note that the EMI test receiver's measurement bandwidth is increased to 120 kHz for better visibility of the harmonics. By doing so, the noise floor of the measurement equipment is increased but it is still below the measured harmonics. The fundamental frequency of the sine waves is set to 1 MHz again.

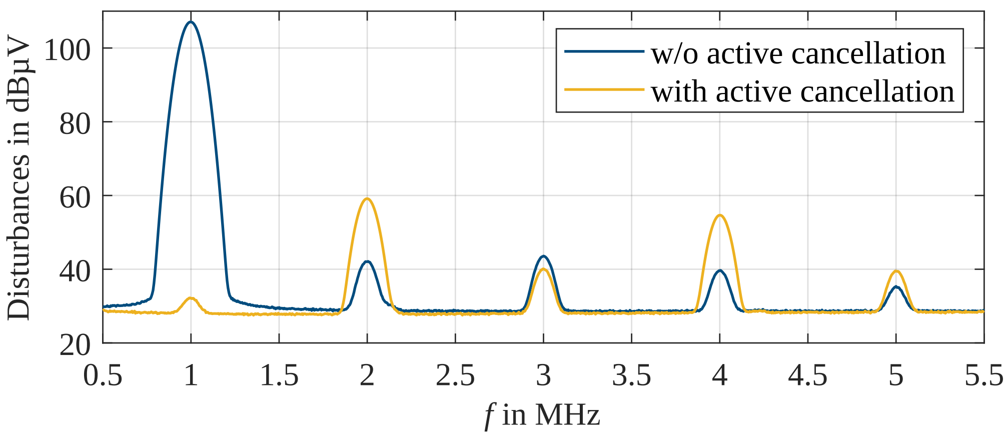

Figure 9.5: Measurement results for the harmonic distortion of the used FPGA system

Since the artificial EMI is a sine wave, most of the signals power can be found for the fundamental frequency of 1 MHz. However, due to the limited precision, harmonic distortion occurs for multiples of this frequency. With active cancellation, the fundamental wave is widely suppressed (almost by 75 dB). Since the cancelling sine wave also introduces harmonic distortion, the harmonics at higher frequencies are increased. It must be noted that the power of these harmonics is significantly lower than the one of the fundamental wave. Nevertheless, such high levels of harmonic distortion would not be acceptable considering common EMC standards.

To remove the harmonic distortion of the cancelling sine wave, the signal could be filtered in the analog domain. Since the harmonic distortion repeats itself quasi-periodically, it could also be cancelled out by an appropriate cancelling sine wave. This effect will be addressed in the demonstrations of the Sections 9.4 and 9.5 again.

9.3 Convergence Rate vs. EMI Suppression in a Simplified System

In this section, the influence of the step size μ of the delayed LMS algorithm is investigated for **p**ulse-**w**idth **m**odulated (PWM) signals. The test system is the same as in Figure 9.2. The EMI test receiver is used with the same settings. The artificial EMI is changed to a PWM signal. At first, a periodic PWM signal is considered. Afterward, the duty cycle is continuously changed with a frequency of 100 Hz. This investigation has been conducted in [107, supervisor] and published in [106, author].

9.3.1 Convergence for a Quasi-Periodic PWM Signal

For investigation, a repeating PWM signal with an amplitude of 0.5 V, a fundamental frequency of 100 kHz and a duty cycle of 77% is investigated. There are two important parameters for the convergence speed of the algorithm (note the description in Section 7.2.3.b)): the step size μ and the estimated propagation delay Δ. Deviations in the estimated propagation delay may slow down the algorithm's convergence. Here, the propagation delay is dominated by the combined signal conversion times of the ADC and DAC of approximately 14 samples. To maximize the convergence speed, Δ is set exactly to this value. The only free parameter is the step size μ of the algorithm. In the following, the cancellation system's performance is investigated for various step sizes.

At first, the fundamental wave is suppressed. The cancellation system generates a corresponding cancelling sine wave of 100 kHz. To illustrate the effect of different step sizes μ, the resulting cancellation signal is simulated for different step sizes and depicted in Figure 9.6. It can be found that the cancellation signal is a clean sine wave for a very small step size μ of $6.7 \cdot 10^{-5}$. However, the cancellation signal will deviate from a sine wave for larger step sizes. This is due to the fact that the algorithm updates its parameters in each sample step (here at a rate of 125 MS/s). If the step size is too large, the algorithm will become too sensitive to the residual EMI and modulate the cancelling sine wave. So, the algorithm starts to affect not only the fundamental wave but also higher harmonics. This effect can be problematic since the algorithm may lose some of its precision for the originally considered harmonic. In a worst-case scenario, the algorithm may even become unstable. There are analytical solutions for the bandwidth and the stability of the single-frequency adaptive notch filter in dependency of the step size μ that can be found in, e.g., [3].

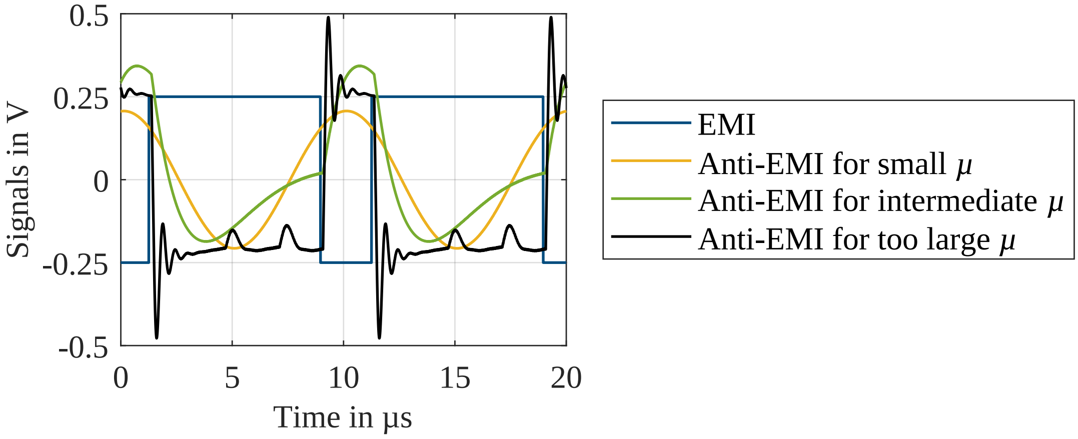

Figure 9.6: Simulated signals for a quasi-periodic PWM signal and different step sizes of the delayed LMS algorithm

This effect can also be observed in the EMI test receiver measurements in Figure 9.7. As long as the step size μ is below approximately $1.7 \cdot 10^{-2}$, the fundamental wave can be suppressed very precisely. For higher step sizes, the cancelling sine wave becomes overmodulated or the algorithm becomes unstable. So, the achieved EMI reduction degrades substantially for a too high μ.

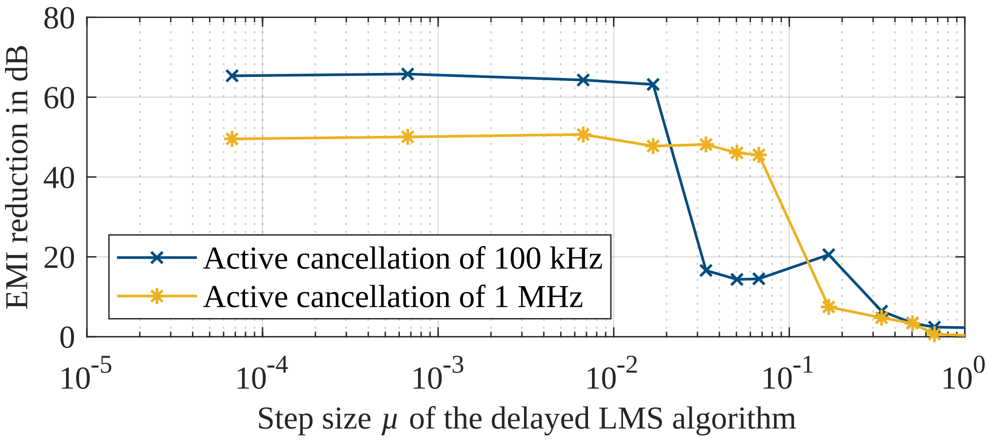

Figure 9.7: Measurement results of the achievable EMI reduction for a repeating PWM signal and different step sizes of the delayed LMS algorithm

For the suppression of the harmonic at 1 MHz, similar results can be found. However, the step size μ can potentially be increased to $6.7 \cdot 10^{-2}$. The achievable EMI reduction for 1 MHz is lower than for 100 kHz since the original harmonic at 1 MHz is lower than for 100 kHz. So, a lower EMI reduction results as discussed in Section 9.2.1.

9.3.2 Convergence for a Slowly Changing PWM Signal (e.g. PFCs)

In the following, the PWM signal is slowly changing according to Figure 9.8. Such a scheme occurs for, e.g., the switching node of an active boost **p**ower **f**actor **c**orrection (PFC) in continuous conduction mode. Note that the switching frequency of the PWM signal is still at 100 kHz. The duty cycle will vary widely over the range of a few milliseconds.

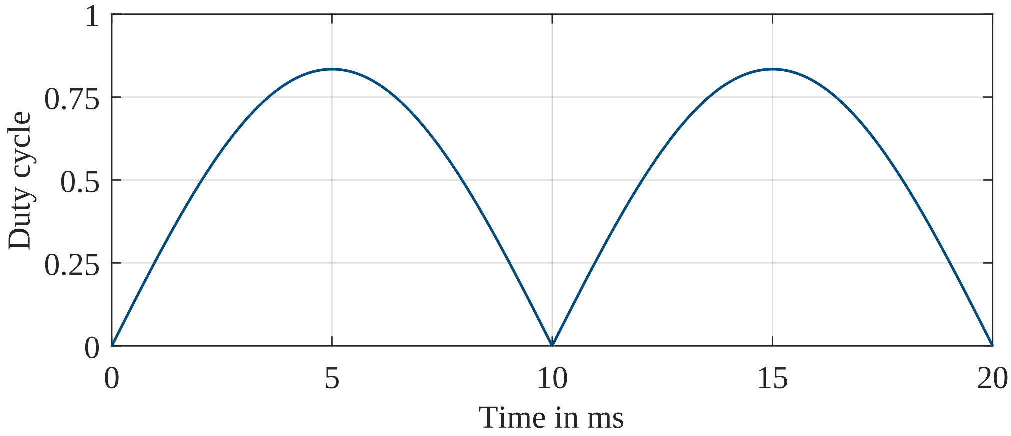

Figure 9.8: Scheme for the changing duty cycle

To investigate the performance of the system, the step sizes μ are varied again in Figure 9.9. From Figure 9.7, it is clear that the algorithm will become imprecise or even unstable for step sizes over $6.7 \cdot 10^{-3}$ or $5 \cdot 10^{-2}$ for respectively 100 kHz or 1 MHz. For small step sizes μ, the performance also degrades since the algorithm will become simply too slow for the changes of the EMI.

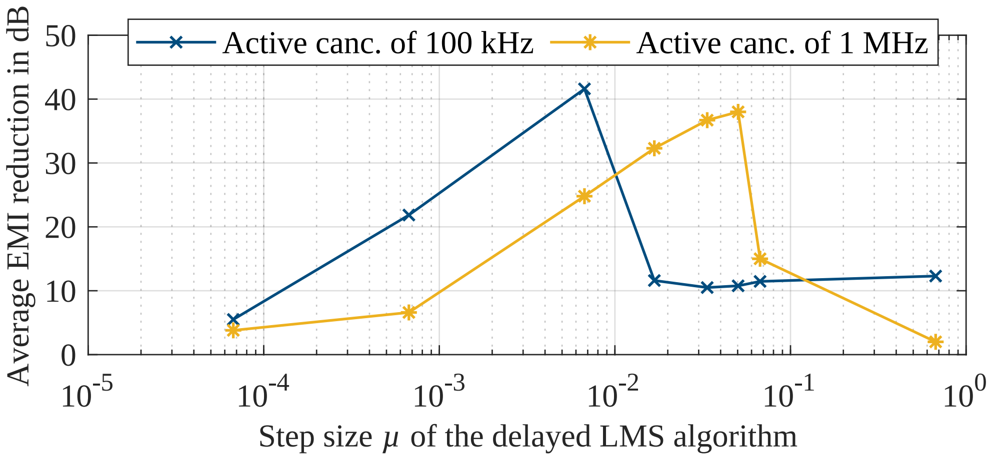

Figure 9.9: Measurement results of the achievable average EMI reduction for an exemplary PFC PWM signal and different step sizes of the delayed LMS algorithm

So, the algorithm will show the best performance for the largest step size that achieves precise results without overmodulation. Here, optimum step sizes μ of $6.7 \cdot 10^{-3}$ and $5 \cdot 10^{-2}$

can be identified for 100 kHz and 1 MHz, respectively. It is plausible that the cancellation of the higher harmonic will require a larger step size μ since it changes more quickly than the fundamental wave. The peak measurement shows similar results that are only a few dB below the average measurement.

9.4 Application of a Parallel Implementation to a DC-to-DC Converter

In the demonstration of this section, multiple single-frequency adaptive notch filters with delayed LMS algorithms are implemented in parallel on an FPGA evaluation system Red Pitaya STEMlab 125-14. This implementation goes back to [112, supervisor]. The demonstrator setup was developed in [15, 101, 102, author].

9.4.1 Demonstrator Setup

The schematics and a photograph of the realized **d**evice **u**nder **t**est (DUT) are depicted in Figure 9.10 and Figure 9.11, respectively. The DC-to-DC converter is a GaN evaluation board GS61008P-EVBBK from GaN Systems operating with a switching frequency of 300 kHz. It steps the input voltage of 48 V down to 12 V for, e.g., an automotive application. At the input, the DC-to-DC converter has a rather large capacitance of 43 µF. Due to the load resistance of 1 Ω, the converter transfers a power of approximately 144 W.

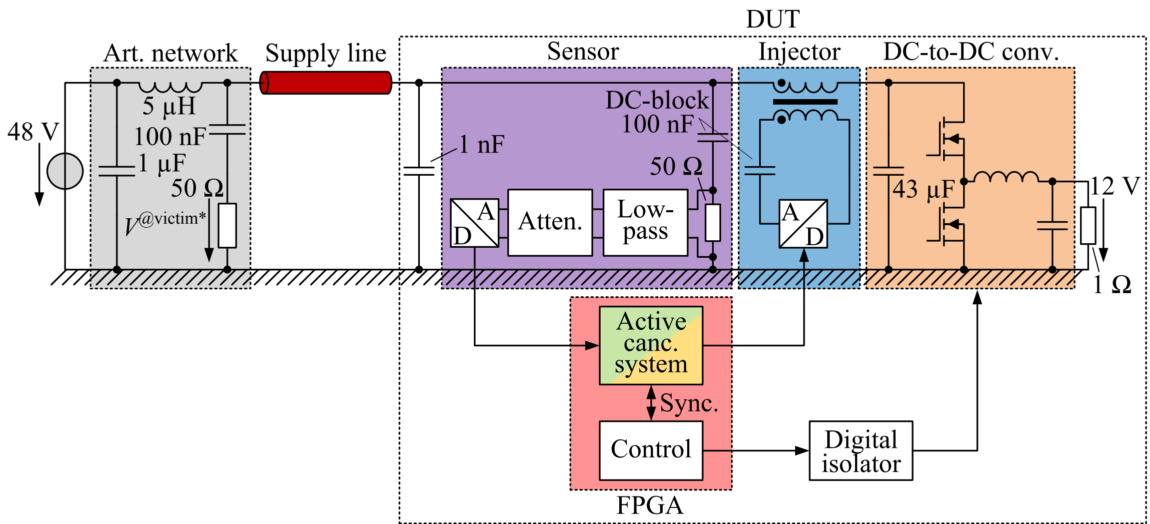

Figure 9.10: Schematics of the demonstrator setup

On the FPGA system, the notch filter method is implemented in parallel for the first six harmonics. The residual EMI is measured by a capacitive sensor consisting of a 100 nF DC-block capacitor and a 50 Ω resistor. The sensed signal is filtered with a 2.5 MHz low-pass filter (50 Ω) to avoid an overdrive of the ADC due to high-frequency signals. A 50 Ω attenuator of 3 dB is applied to avoid a resonance between the reactive elements of the low-pass

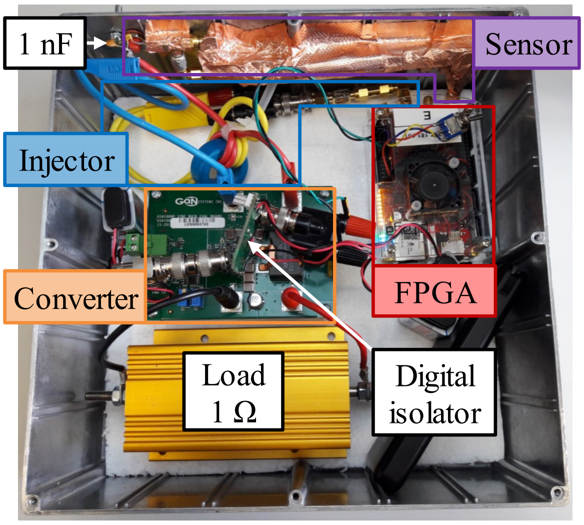

Figure 9.11: Photograph of the realized DUT (shielding case opened)

filter and the overall system. The injecting circuit is realized by a high-frequency transformer (two windings with each two turns on a toroidal EMC ferrite EPCOS B64290L0048X830) and a DC-block capacitor of 100 nF. The FPGA system generates the control signal for the DC-to-DC converter. So, a perfect synchronization is achieved between the systems. To avoid ground loops, a digital isolator is installed in this path. The DC-to-DC converter, cancellation system and load resistor are placed inside of a closable shielding case. This case is very important so that only little internal EMI couples to the outside. The DUT is placed on a reference ground plane that is used as return conductor for the operating currents of the power electronic system.

According to the automotive standard CISPR 25 [4], the conducted emissions are measured via an artificial network that provides a standardized impedance for the disturbances and a coaxial measurement port. Furthermore, the emissions on the supply line are evaluated by using a rod antenna according to [4]. To avoid an overdrive of the broadband antenna amplifier due to high-frequency signals, a 1 nF capacitor is placed at the input of the DUT. A photograph of the test setup can be found in Figure 9.12.

9.4.2 Measurement Results at Artificial Network

The disturbances at the measurement port of the artificial network are evaluated by using an EMI test receiver with a resolution bandwidth of 9 kHz and an average detector. The measurement results with and without active cancellation are depicted in Figure 9.13. The first six harmonics are suppressed by 53, 56, 51, 38, 48 and 48 dB, respectively, and they comply with the strictest limit class of [4].

The harmonics are basically reduced to the ADC's noise floor that has a level of 31 dBµV (as shown in Section 9.2.1). The higher residual EMI for the fundamental wave may be due to transfer functions that lower the precision of the cancellation system. In Section 9.2.3,

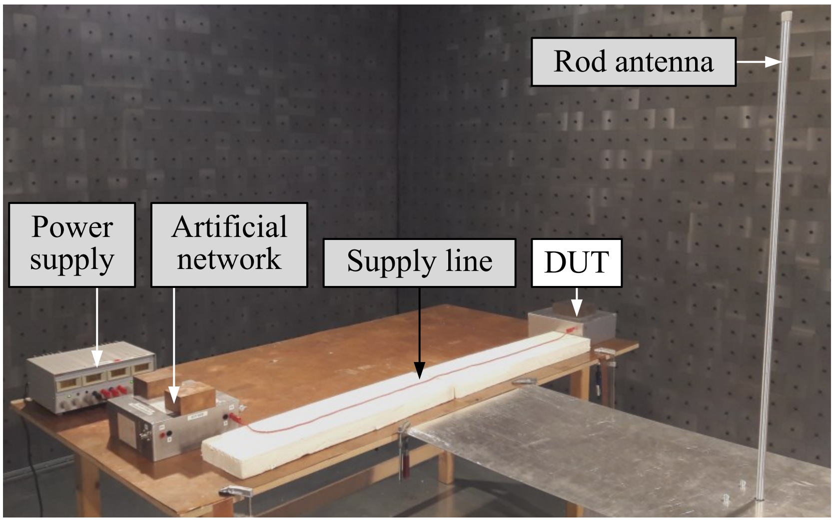

Figure 9.12: Photograph of the complete test setup

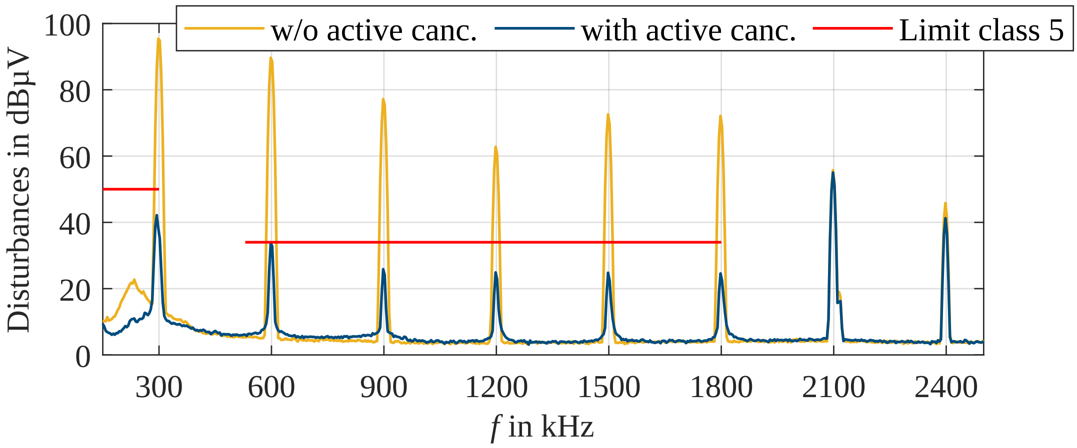

Figure 9.13: Measurement results with and without active EMI cancellation at the artificial network

significant harmonic distortion has been found during the cancellation of a single sine wave (e.g. 60 dBµV for the “overtone”). However, in this measurement, no significant harmonic distortion can be found. This is due to the parallel structure of the cancellation system: The cancelling sine wave of, e.g., 300 kHz injects harmonic distortion into the system that falls directly onto the subsequent disturbing harmonics. Since the harmonic distortion is deterministic, it can be compensated by the single-frequency adaptive notch filter for the respective higher harmonic. By this measure, the effect of harmonic distortion is compensated by the cancellation system itself. So, in regard to the cancellation signal, the harmonic distortion of the previous sine wave is compensated by the subsequent. Since the harmonic distortion is rather low compared to the unsuppressed harmonics, there is only little influence on the harmonics above 1800 kHz.

9.4.3 Measurement Results at Rod Antenna

In Figure 9.14, the average measurements for a rod antenna are depicted. Also in this measurement, the disturbances are suppressed below the given limit. It can be found that the EMI reduction appears to be worse for the rod antenna than for the artificial network. Due to the non-ideal attenuation of the shielding case, the rod antenna may measure some of the internal EMI of the DUT leading to a worse measurement result.

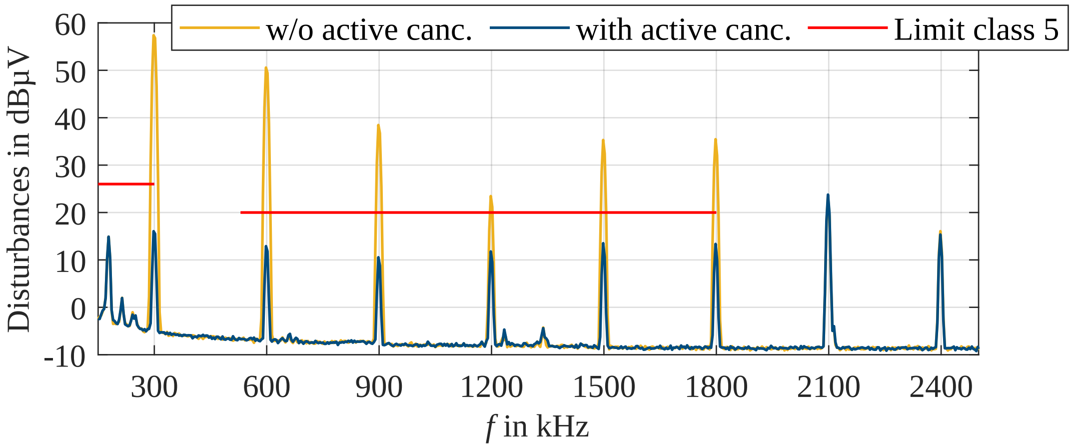

Figure 9.14: Measurement results with and without active EMI cancellation at the rod antenna

9.5 Application of a Successive Implementation to a DC-to-DC Converter

In the following strategy, one single-frequency adaptive notch filter with delayed LMS algorithm is successively applied to numerous harmonics in a much wider frequency range than in Section 9.4. The cancelling sine waves for each harmonic are identified and superposed with each other. By doing so, a successively synthesized cancellation signal results. The results of this section have been published in [104, author].

9.5.1 Algorithm

In Figure 9.15, a flowchart for an exemplary implementation is depicted. The algorithm starts with the first harmonic. The frequency of the cancelling sine wave is set accordingly and the delayed LMS algorithm optimizes the signal. At first, an arbitrary delay time Δ is assumed (the estimated delay time is very important for stability, Section 7.2.3.b)). If the algorithm becomes unstable, the cancellation signal diverges and reaches quickly the limits of the DAC. So, this is a suitable criteria to detect an unacceptable deviation in the delay time estimation. A simple solution for an unstable algorithm is to set a new delay time, to reset the delayed LMS algorithm and to start the optimization again. A stable algorithm will take some time to converge depending on the residual deviation in the estimation of the delay time Δ. As discussed in Section 7.2.3.b), the convergence speed is only marginally affected by deviations of up to $\pm 40°$. But higher deviations of up to $\pm 90°$ will notably slow down the algorithm. Taking this case into account, a sufficient long optimization time must be set. As long as the optimization time is not over, the algorithm continues to optimize the signal. If the optimization time is over, the cancellation signal is saved and the algorithm is set to the next harmonic. By repeating this process, a very large frequency range consisting of numerous harmonics can be suppressed.

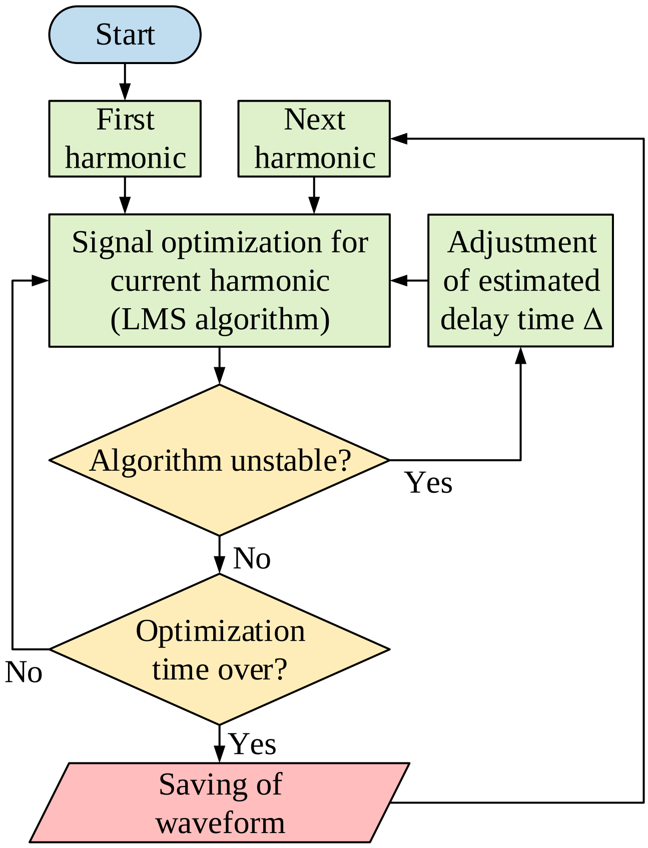

Figure 9.15: Flow chart for a successive signal synthesis with the notch filter method

This successive implementation is slower than the parallel since each harmonic is optimized one by one. Therefore, it is best suited for quasi-periodic EMI. There are many options to improve the speed of the algorithm. Some are summarized in the following.

- A slow convergence (deviations between $40°$ and $90°$ and deviations between $-40°$ and $-90°$) could be detected. Using this information, the delay time Δ could be adjusted in such way that there is always a fast convergence.

- In many cases, the assumed optimization time may be too long. To resolve this issue, it would be possible to detect a steady state of the algorithm and to stop the optimization for the respective harmonic earlier.

- The found delay times Δ for each harmonic could be stored in a memory. By doing so, the trial and error to find the right delay times Δ may only be necessary for the first cycle of the algorithm. Afterward, the delay times must only be corrected if they deviate due to changes in the system.

- As mentioned in Section 7.2.3.b), online methods for secondary path modeling could be used instead of the iterative approach.

9.5.2 Demonstrator Setup

The schematics and a photograph of the realized DUT are depicted in Figure 9.16 and Figure 9.17, respectively. The system is basically the same as in Section 9.4.1. The changes are as follows:

- The GaN evaluation board is replaced by the newer model GS61008P-EVBHF from GaN Systems.

- The 2.5 MHz low-pass filter (50 Ω) of the sensor is replaced by a 32 MHz low-pass filter to enable an active EMI suppression up to 30 MHz.

- The attenuator of the sensor is removed.

- The DC-block capacitor of the injector is removed.

- A 3 dB attenuator (50 Ω) is applied in the injector to adjust its voltage range.

- The load resistor is placed outside of the shielding case.

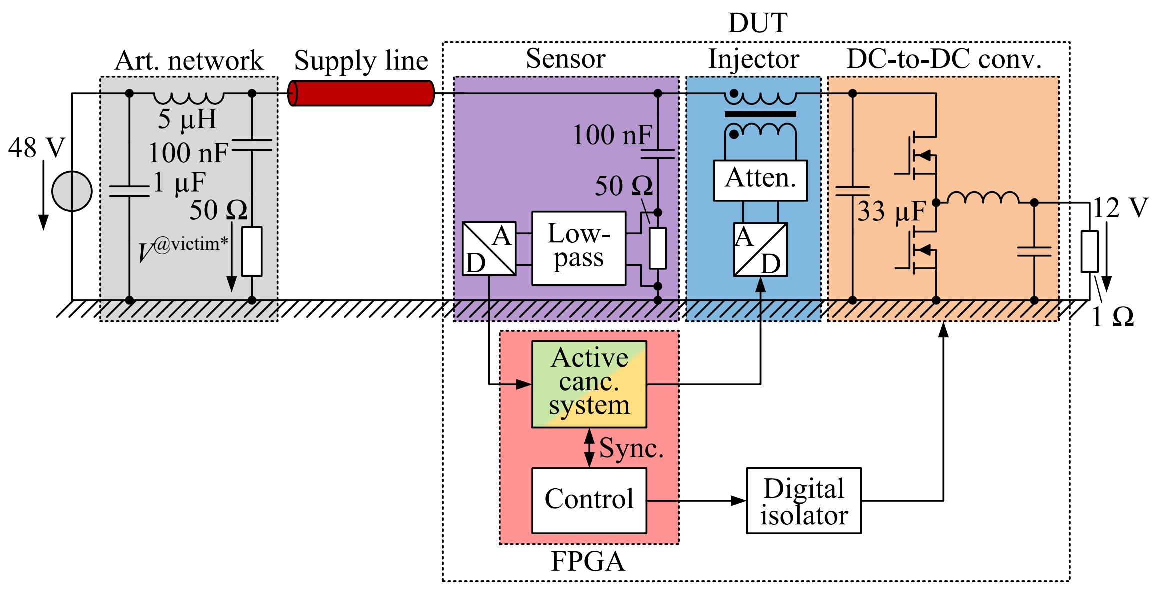

Figure 9.16: Schematics of the realized DUT

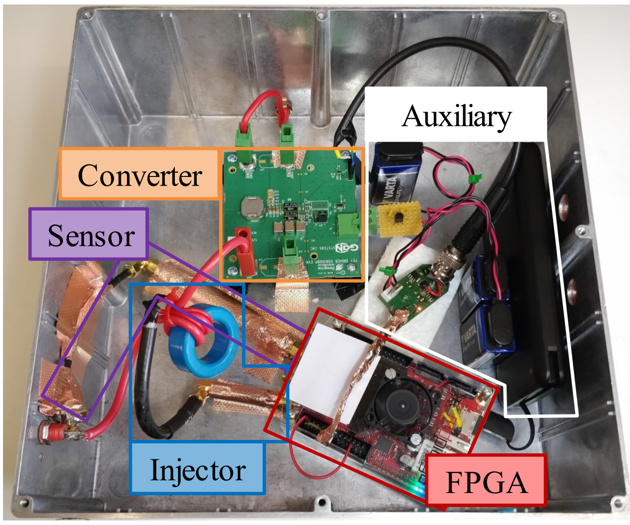

Figure 9.17: Photo of the realized DUT (shielding case opened)

9.5.3 Measurement Results

The measurement results at the artificial network with and without active cancellation are shown in Figure 9.18. The disturbances are successfully suppressed for the complete frequency range of 150 kHz to 30 MHz. The fundamental wave is suppressed by approximately 60 dB and even the very high harmonics of up to 30 MHz are reduced by up to 40 dB. The system's residual disturbances comply with the class 5 limit of CISPR 25 [4]. It can be found that the residual disturbances tend to the noise floors of the ADCs and DACs of 31 dBµV (Section 9.2.1). Deviations from this value may be due to the transfer functions of the system.

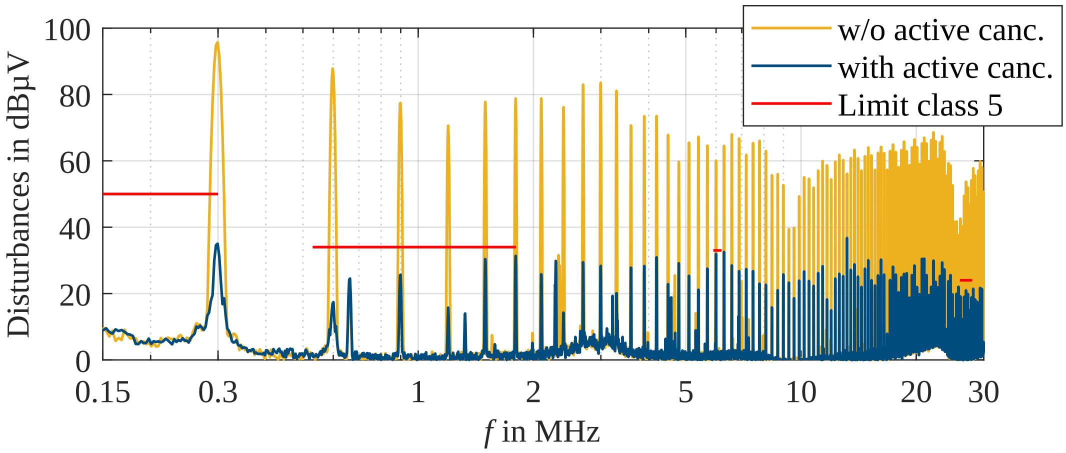

Figure 9.18: Measurement results with and without full active EMI cancellation at the artificial network

9.5.4 Cancellation Signal

The successively adapted cancellation signal has been measured by an oscilloscope and is depicted in Figure 9.19. There is a distinct fundamental wave. The ringing hints to the switching events of the transistors.

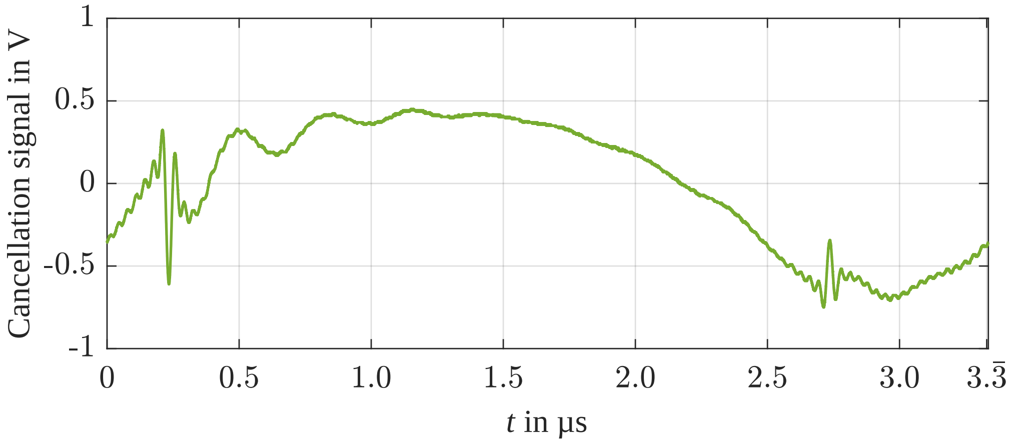

Figure 9.19: Successively synthesized cancellation signal

9.5.5 Power Consumption of the Cancellation Signal

To evaluate the power consumption of the injector, the RMS value of the cancellation signal (Figure 9.19) is determined to $V_{\text{anti,RMS}} \approx 384$ mV. Due to the 3 dB attenuator, the DAC is terminated by approximately 50 Ω. Since the high-frequency output impedance R_{DAC} of the Red Pitaya STEMlab 125-14 varies over frequency, the internal impedance is assumed to be 0 Ω for a worst-case approximation. So, the worst-case power consumption of the cancellation signals can be estimated to 3 mW by $V^2_{\text{anti,RMS}}/50\ \Omega$. In comparison to the transfer power of 144 W, this power consumption is negligible.

One could be surprised that the injection of the cancellation signal requires only so little power although a high voltage of 48 V is chopped by the DC-to-DC converter. However, it must be noted that the chopped voltages and currents are already smoothened by the stabilizing capacitors at the input (and output) of the converter. So, the power of the disturbances is already significantly reduced. However, the resulting emissions are usually still significant (and critical in regard to EMC standards). Due to the small power rating of the emissions, the cancellation also requires little power.

9.5.6 Measurement Results for a Frequency-Selective Approach

Considering the disturbing harmonics and the limit lines, it becomes obvious that the active cancellation system needlessly suppresses numerous harmonics that do not violate any limits. Since the method is frequency selective, it is completely viable to only suppress the harmonics in the frequency ranges of the limits. This special feature is demonstrated by the additional measurement in Figure 9.20.

Here, the critical harmonics are suppressed below the standard's class 5 limit and the other harmonics remain untouched. The slight changes in the untouched harmonics are explained by harmonic distortion since the DAC and the analog circuitry are not ideally linear. Since the cancellation signal must only be optimized for 14 harmonics (instead of 100), the adaption process is significantly accelerated. Additionally, the power consumption of the injector is further reduced to approximately 2.8 mW.

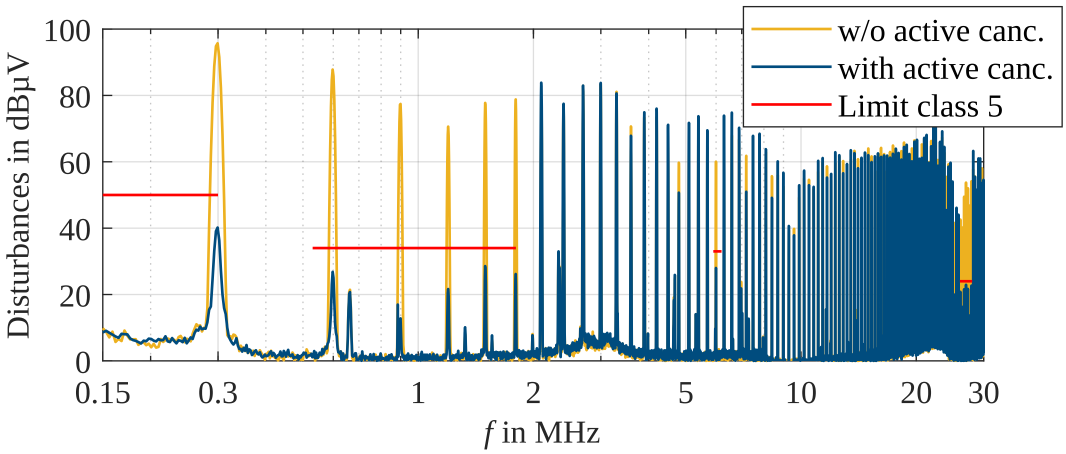

Figure 9.20: Measurement results with and without frequency-selective active EMI cancellation at the artificial network

9.6 Application to the First Harmonic of a PFC

In this section, the notch filter method is applied to the DM EMI on the input side of a common boost PFC. The results go back to [107, supervisor] and have been published in [106, author].

The PFC is an evaluation system IPP60R190P6. It operates with a switching frequency of 100 kHz and transfers a power of approximately 223 W. The notch filter method is implemented on a Red Pitaya STEMlab 125-14 again. The step size is set to the ideal value of $6.7 \cdot 10^{-3}$ according to the investigation of Section 9.3.2. An inductive voltage injector (with transformer) and a capacitive voltage sensor have been chosen. The FPGA system sends a synchronization signal to the controller of the PFC evaluation system.

The DM disturbances are measured with an EMI test receiver at a **l**ine **i**mpedance **s**tabilization **n**etwork (LISN). The measurement is done with a resolution bandwidth of 9 kHz, a measurement time of at least 50 ms and an average detector.

The measurement results are depicted in Figure 9.21. The fundamental wave is suppressed by approximately 46 dB. The active cancellation systems seems to inject overtones of the cancelling sine wave that increase the level of higher harmonics. The chosen step size of $6.7 \cdot 10^{-3}$ generated no significant overtones in the investigation of Section 9.3. So, the increased higher harmonics may be traced back to a nonlinear coupling behavior of the overall system. This issue may be solvable by optimizing the sensing and injecting circuits.

By applying multiple single-frequency adaptive notch filters with delayed LMS algorithm in parallel, a larger frequency range can be suppressed. This method may also be applied to other power electronic systems with “slowly” changing PWM signals. One example could be motor inverters.

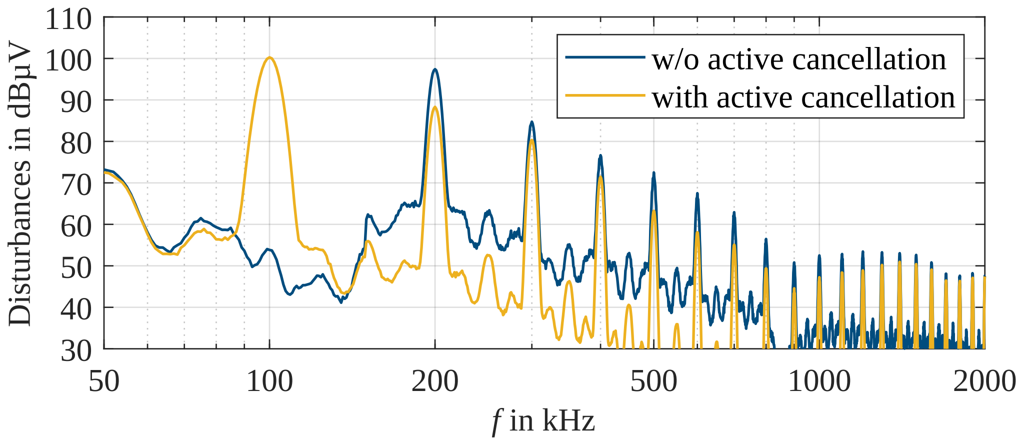

Figure 9.21: Measurement results at the LISN for the average DM EMI at the input of a boost PFC

9.7 Chapter Summary

In this demonstration, the notch filter method has been applied to different test systems. For a DC-to-DC converter, the EMI could actively be reduced by 60 dB for the fundamental wave of 300 kHz. The active EMI suppression for up to 30 MHz is still up to 40 dB. Note that the passive attenuation of the injecting and sensing circuits comes on top. In comparison to AEFs (Table 4.6) and DAEFs (Table 5.2), the proposed cancellation system using synthesized and synchronized cancellation signals shows a very good performance.

Using the notch filter method, the fundamental wave at 100 kHz of a boost PFC could be reduced by approximately 46 dB. The results of Figure 9.9 suggest that this performance may also be achievable for frequencies of up to 1 MHz. This performance is also better than the one of AEFs (Table 4.11) and DAEFs (Table 5.2).

So, the notch filter method proves to be a promising approach to suppress quasi-periodic (e.g. of a DC-to-DC converter) and “slowly” changing (e.g. of a PFC) EMI. The active cancellation systems with their analog and digital components of this chapter have basically been designed by trial and error. In the following chapter, the active EMI cancellation system is systematically designed after a system identification. The FFT method will be used for demonstration.

10 Systematic Design of an FFT-Based Single-Port Active EMI Cancellation System

In this chapter, a single-port active EMI cancellation system is designed to suppress the EMI at one line of a DC-to-DC converter in regard to specific EMC requirements. As an example, the FFT method will be applied with an **a**rbitrary **w**aveform **g**enerator (AWG), a PC and an oscilloscope.

For a systematic realization of the active EMI cancellation system without trial and error, three steps are necessary:

1. Definition of the application and its EMC requirement
2. Identification of the disturbing and disturbed system
3. Design of the active EMI cancellation system

These steps will be exemplary discussed for the given system. With appropriate adjustments, they could also be applied to other systems.

10.1 Application and EMC Requirement

The investigated application is an automotive DC-to-DC converter that steps down an input voltage of 48 V to an output voltage of 12 V. The schematic and a photograph of the overall test setup are depicted in Figure 10.1 and 10.2, respectively. The inside of the **d**evice **u**nder **t**est (DUT) can be found in Figure 10.3.

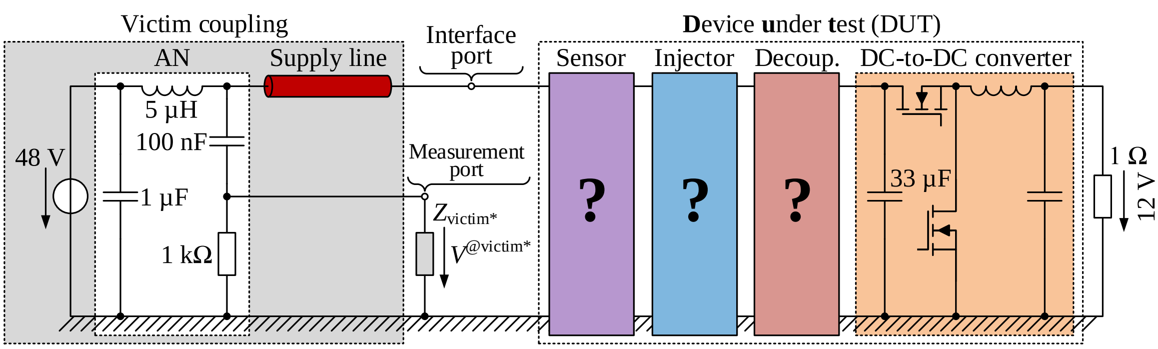

Figure 10.1: Schematics of the overall test setup

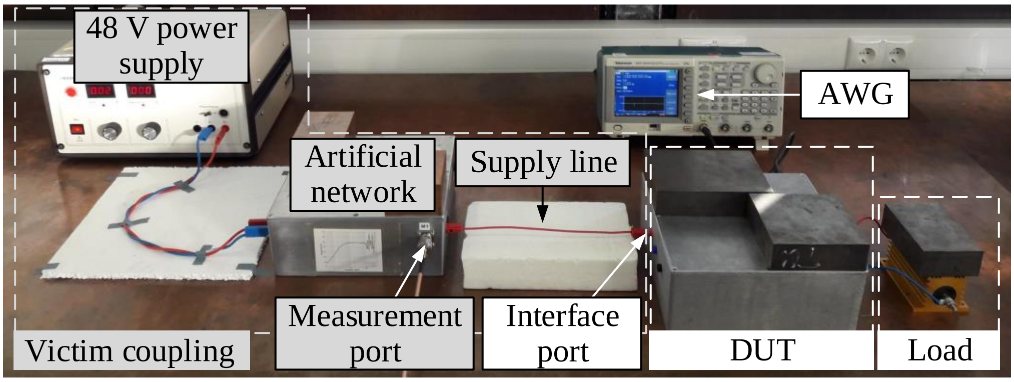

Figure 10.2: Photograph of the overall test setup

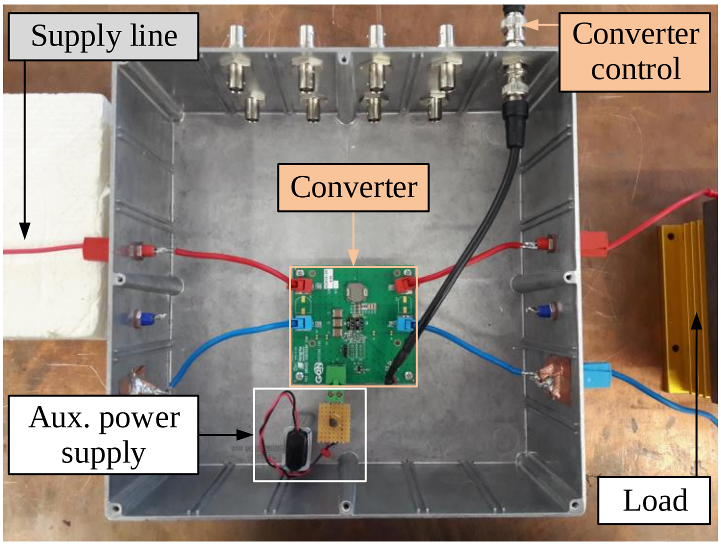

Figure 10.3: Photograph of the inside of the DUT

The DC-to-DC converter is realized by a GaN evaluation board GS61008P-EVBHF from GaN Systems. The switching frequency f_0 and the duty cycle are set to constant 300 kHz and 25%, respectively. This control signal is generated by an AWG AFG3252 from Tektronix. The transistor driver of the evaluation board is powered by an auxiliary power supply. The load is a 1 Ω resistor. So, the converter transfers a power of approximately 144 W. Since all quantities are constant (assuming also a thermal equilibrium), there will be discrete and stable harmonics with a spacing of f_0.

Since this power electronic system uses the reference ground plane as return conductor [4], there are only DM disturbances at the input and output port of the DC-to-DC converter. In this demonstration, the EMI at the input shall be actively cancelled out. Therefore, the active cancellation system with its sensor, injector and decoupler must be applied to DM EMI. The DC-to-DC converter and the active cancellation system will be installed in the same shielding case that represents the DUT. The elements of the active cancellation system will be designed in the following sections.

In reference to the automotive EMC standard CISPR 25 [4], an **ar**tificial **n**etwork (AN) is connected between the 48 V supply and the DUT. ANs represent a standardized impedance for the disturbances and provide a coaxial measurement port. The measurement port is connected with an EMI test receiver. According to [4], its resolution bandwidth is set to 9 kHz and the measurement time for each frequency point is at least 50 ms. Its internal resistance of $Z_{\text{victim*}} = 50\ \Omega$ terminates the AN. There is a short supply line between AN and DUT. In reference to Figure 3.1, the AN, supply line and 48 V source form the victim coupling. Note the interface port connecting the disturbing DUT and the disturbed exterior.

The EMC requirement is to suppress the disturbances below the class 5 limits of the automotive standard CISPR 25 in the frequency range from 150 kHz to 30 MHz [4]. Due to the periodically repeating EMI, peak- and average-detector lead to basically the same results. However, the average limits are much lower than the peak limits. So, if the average limits are fulfilled, the peak limits are also fulfilled. Therefore, only the average EMI will be evaluated. Considering the frequency range and the switching frequency, there will be 100 disturbing harmonics that must be cancelled out.

10.2 System Identification

For the design of the cancellation system in the later steps, the overall system (without cancellation system) shall be described by the form given in Figure 10.4. Note the similarities with the generic descriptions of Figure 3.1 and 3.2.

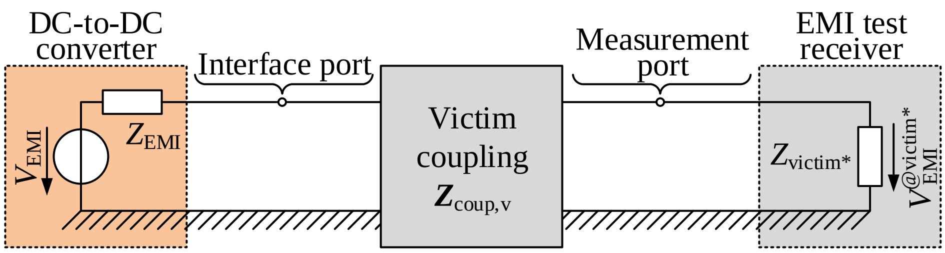

Figure 10.4: Block diagram of the system to be identified

The victim coupling consists of the AN, supply line and 48 V power supply and connects the interface and measurement ports. It can be represented by a 2×2 impedance matrix $\boldsymbol{Z}_{\text{coup,v}}(f)$ for the high-frequency EMI signals. The impedance of the EMI victim $Z_{\text{victim*}}$ equals 50 Ω due to the EMI test receiver. The DC-to-DC converter is represented by an equivalent Thévenin voltage source with $V_{\text{EMI}}(f)$ and $Z_{\text{EMI}}(f)$ in regard to the interface port.

The possibilities for system identification range from analysis over simulations to measurements. Here, a measurement technique is proposed that can be applied without any further knowledge of the system. The required steps are as follows:

1. **Identification of the EMI victim coupling $\mathbf{Z}_{\text{coup,v}}(f)$:**
   This can be done by, e.g., a **v**ector **n**etwork **a**nalyzer (VNA) measurement.

2. **Identification of the EMI source's equivalent impedance $Z_{\text{EMI}}(f)$:**
   Measuring the equivalent impedance of power electronic systems is no trivial task since they usually lack a well-defined coaxial measurement port for VNAs. Connecting the measurement equipment without coaxial cables to the power electronic system can lead to unreliable results. As a solution, the previously identified victim coupling can be used as fixture. By de-embedding its characteristics, the impedance of the EMI source can be found reliably and precisely.

3. **Identification of the EMI source's equivalent voltage source $V_{\text{EMI}}(f)$:**
   The EMI source's equivalent voltage source could theoretically be found by measuring the voltage at an open interface port. However, this poses two practical problems: First, this is no nominal operation point for most systems. So, the system may stop working or its EMI is not representative anymore. Second, there is no coaxial measurement port leading to unreliable measurements as described before. If a Norton equivalent is chosen, the current source could theoretically be found by measuring the short-circuit current at the interface port. This approach suffers from similar problems as the open-port voltage measurement.
   The direct measurement of the equivalent source may not be possible, but its effect on the overall system can be measured. The measurement port (here of the AN) is an ideal choice due to two facts: First, the measurement port is usually coaxial. So, reliable measurements are possible. Second, the coupling from the interface port to the measurement port has already been identified in the first step. Since the internal impedance, the victim coupling and the victim impedance are all known, the equivalent source can be calculated from a measurement of its effect on the measurement port (e.g. with an oscilloscope).

These steps are demonstrated for the given system in the following. The VNA measurements are done with a ZNB 8 from Rohde & Schwarz that is calibrated by using a standard calibrating kit 85033E. The used oscilloscope is an HDO6104A from Teledyne LeCroy.

10.2.1 Step 1: Identification of the EMI Victim Coupling by VNA Measurement

The coupling of the EMI victim $\mathbf{Z}_{\text{coup,v}}(f)$ can be identified by doing a two-port VNA measurement at the measurement port of the AN and the interface port (Figure 10.5). The coaxial measurement port of the AN is well suited for VNA measurement. However, there is no well-defined port for the supply line. To resolve this issue, the DUT is removed and a metal angle is introduced. The reference ground of the VNA is connected with the ground plane via the AN and the metal angle. The later used power supply must also be connected during identification since it will influence the overall coupling. However, its voltage is set to 0 V. To avoid deviations during the measurements, the position of the lines is fixed.

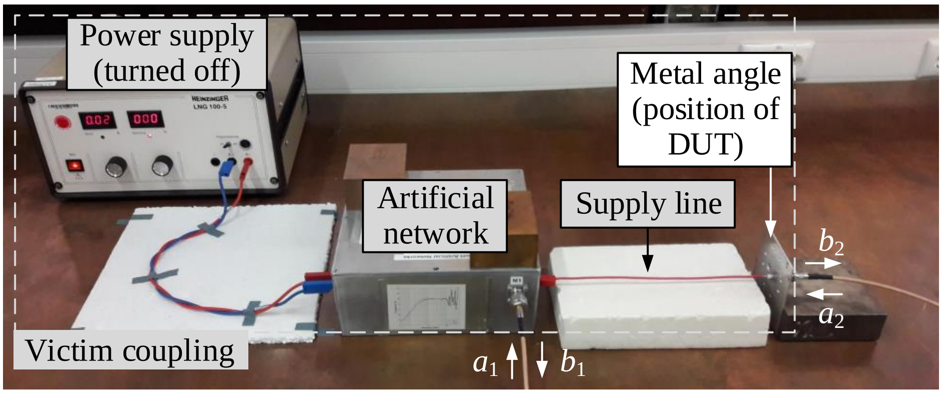

Figure 10.5: Photograph of the test setup for identification of the victim coupling $\boldsymbol{Z}_{\text{coup,v}}(f)$

By doing the VNA measurement, the victim coupling is described by a matrix of scattering parameters $\boldsymbol{S}_{\text{coup,v}}(f)$ according to (10.1):

$$\begin{pmatrix} b_1(f) \\ b_2(f) \end{pmatrix} = \boldsymbol{S}_{\text{coup,v}}(f) \cdot \begin{pmatrix} a_1(f) \\ a_2(f) \end{pmatrix} \tag{10.1}$$

These parameters are also depicted in Figure 10.6. Since only passive elements are used, the system is reciprocal. Therefore, $S_{\text{coup,v,1,2}}(f)$ and $S_{\text{coup,v,2,1}}(f)$ are the same. The system is close to being symmetric, but $S_{\text{coup,v,1,1}}(f)$ and $S_{\text{coup,v,2,2}}(f)$ differ for higher frequencies. The scattering parameters can be made plausible by the fact that the AN poses a very low impedance against ground for low frequencies. So, the incoming waves are mostly reflected and the scattering parameters $S_{\text{coup,v,1,1}}(f)$ and $S_{\text{coup,v,2,2}}(f)$ are close to 0 dB. For higher frequencies, the AN poses a higher impedance against ground and the measurement ports are well coupled. Therefore, the reflection is reduced and the transmission is increased.

For the usage in the next step, the transfer matrix is calculated. There are different definitions for this transfer matrix $\boldsymbol{T}_{\text{coup,v}}(f)$. Here, the definition according to (10.2) is used. For later uses in the systematic design strategy, the scattering parameters are also transferred to impedance parameters $\boldsymbol{Z}_{\text{coup,v}}(f)$.

$$\Rightarrow \begin{pmatrix} a_1(f) \\ b_1(f) \end{pmatrix} = \boldsymbol{T}_{\text{coup,v}}(f) \cdot \begin{pmatrix} b_2(f) \\ a_2(f) \end{pmatrix} \tag{10.2}$$

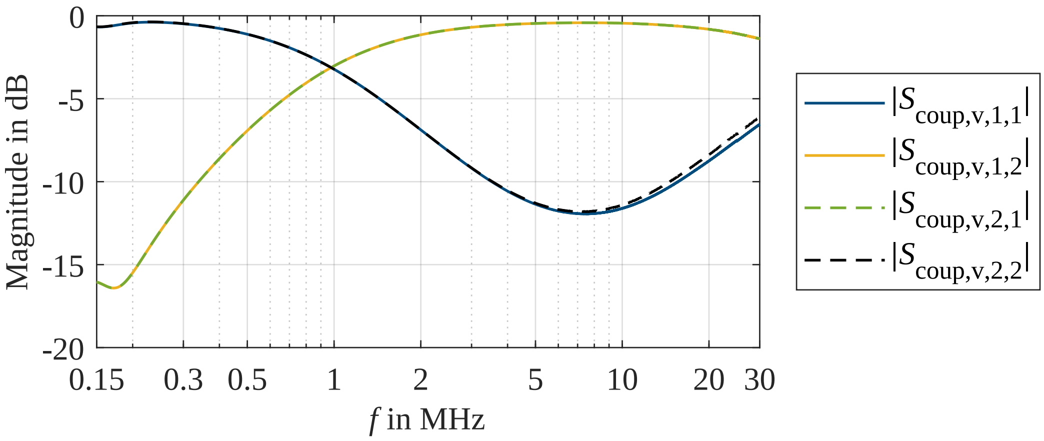

Figure 10.6: Magnitudes of the scattering matrix $\boldsymbol{S}_{\mathrm{coup,v}}(f)$

10.2.2 Step 2: Identification of the EMI Source's Equivalent Impedance by VNA Measurement

Determining the equivalent impedance of an EMI source is no trivial task since measurements are easily degraded by the connection of the measurement device and the system to be measured. Well-defined coaxial measurement ports are best suited, but those can usually not be found on power electronic converters. However, in this test setup, there is the measurement port of the AN that can be used. Since the victim coupling from the measurement port to the interface port is already identified, it can be de-embedded mathematically. For measurement, the metal angle is removed and the DUT is inserted again (note Figure 10.7).

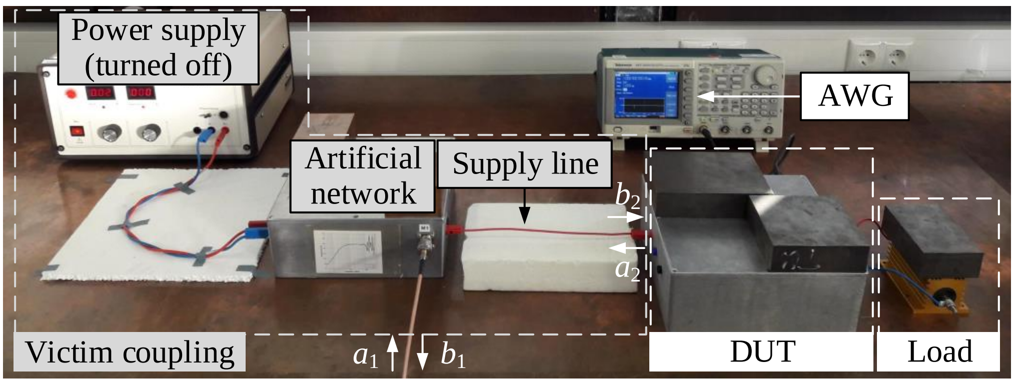

Figure 10.7: Photograph of the test setup for identification of the EMI source's impedance $Z_{\mathrm{EMI}}(f)$

To find the equivalent impedance $Z_{\mathrm{EMI}}(f)$ of the DC-to-DC converter, the power electronic system and the power supply are turned off. The auxiliary power supply of the transistor drivers is activated to provide a nominal condition of the converter. Since the load resistor will affect the equivalent impedance of the DC-to-Dc converter, it must be connected to the system (even though no power is transferred). The result of the one-port VNA measurement at the AN is a scattering parameter $S_{\mathrm{meas}}(f)$ according to (10.3):

$$S_{\mathrm{meas}}(f) = \frac{b_1(f)}{a_1(f)} \tag{10.3}$$

The converter's scattering parameter $S_{\mathrm{EMI}}(f)$ is defined according to (10.4):

$$S_{\mathrm{EMI}}(f) = \frac{a_2(f)}{b_2(f)} \tag{10.4}$$

To find this parameter, (10.2) is rearranged to (10.5):

$$\begin{pmatrix} b_2(f) \\ a_2(f) \end{pmatrix} = \boldsymbol{T}^{-1}_{\mathrm{coup,v}}(f) \cdot \begin{pmatrix} a_1(f) \\ b_1(f) \end{pmatrix} \tag{10.5}$$

For a simpler mathematical representation, the inverse of $\boldsymbol{T}_{\mathrm{coup,v}}(f)$ is replaced by a matrix with the entries $\alpha(f)$, $\beta(f)$, $\gamma(f)$ and $\delta(f)$ according to (10.6):

$$\begin{pmatrix} b_2(f) \\ a_2(f) \end{pmatrix} = \begin{bmatrix} \alpha(f) & \beta(f) \\ \gamma(f) & \delta(f) \end{bmatrix} \cdot \begin{pmatrix} a_1(f) \\ b_1(f) \end{pmatrix} \tag{10.6}$$

Now, it is possible to determine $S_{\mathrm{EMI}}(f)$ by combining (10.4) and (10.6) according to (10.7) and (10.8):

$$\overset{(10.4)}{\Rightarrow} S_{\mathrm{EMI}}(f) = \frac{\gamma(f) \cdot a_1(f) + \delta(f) \cdot b_1(f)}{\alpha(f) \cdot a_1(f) + \beta(f) \cdot b_1(f)} \tag{10.7}$$

$$= \frac{\gamma(f) + \delta(f) \cdot \dfrac{b_1(f)}{a_1(f)}}{\alpha(f) + \beta(f) \cdot \dfrac{b_1(f)}{a_1(f)}} \tag{10.8}$$

By inserting (10.3), the solution of (10.9) follows:

$$\overset{(10.3)}{\Rightarrow} S_{\mathrm{EMI}}(f) = \frac{\gamma(f) + \delta(f) \cdot S_{\mathrm{meas}}(f)}{\alpha(f) + \beta(f) \cdot S_{\mathrm{meas}}(f)} \tag{10.9}$$

The internal impedance $Z_{\mathrm{EMI}}(f)$ can be calculated by (10.10) where Z_0 is the reference impedance (here 50 Ω):

$$\Rightarrow Z_{\mathrm{EMI}}(f) = Z_0 \cdot \frac{1 + S_{\mathrm{EMI}}(f)}{1 - S_{\mathrm{EMI}}(f)} \tag{10.10}$$

The resulting impedance $Z_{\mathrm{EMI}}(f)$ is depicted in Figure 10.8. It can be found that the impedance is mostly inductive in the considered frequency range. This is plausible since the lines inside of the shielding case introduce significant inductances. Note that the stabilizing capacitors at the input of the converter represent a very low impedance.

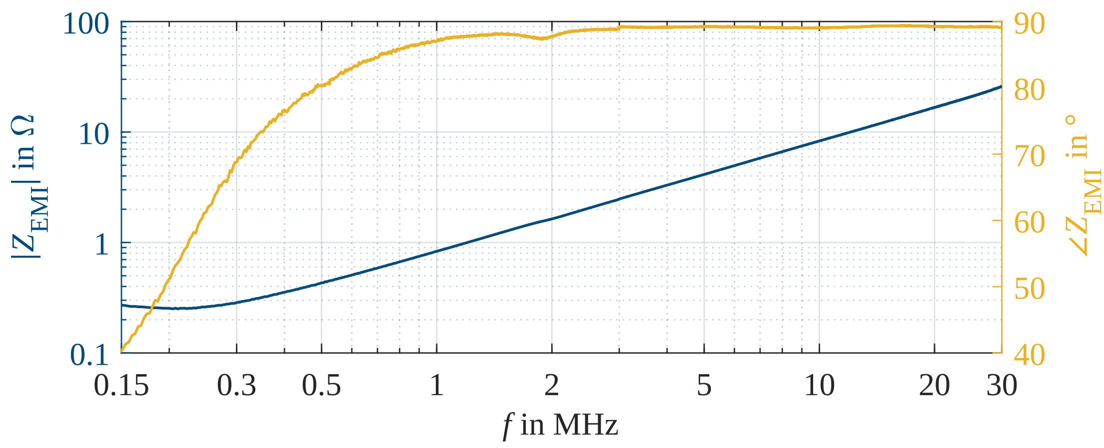

Figure 10.8: Magnitude and phase of the identified equivalent source impedance $Z_{\mathrm{EMI}}(f)$

10.2.3 Step 3: Identification of the EMI Source's Equivalent Voltage Source by Oscilloscope Measurement

In the last step of the identification, the equivalent voltage source of the DC-to-DC converter must be found. Although this voltage cannot be measured directly, its effect on the measurement port of the AN $V_{\mathrm{EMI}}^{@\mathrm{victim}*}(f)$ can be measured. Since the overall system is known, the EMI source's equivalent voltage $V_{\mathrm{EMI}}(f)$ can be calculated.

To do so, the equivalent circuit according to Figure 10.9 is considered. $Z_{\mathrm{EMI}}(f)$ and the victim coupling $\boldsymbol{Z}_{\mathrm{coup,v}}(f)$ are already determined. The oscilloscope measurement is done with a termination impedance $Z_{\mathrm{victim}*}$ of 50 Ω in reference to the input impedance of typical EMI test receivers.

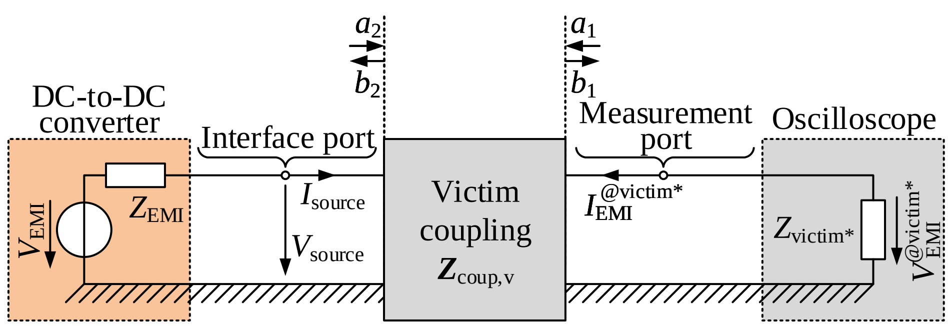

Figure 10.9: Schematic for the calculation of the EMI source's equivalent voltage $V_{\mathrm{EMI}}(f)$

The already known external coupling is translated to a chain parameter matrix $\boldsymbol{A}_{\text{coup,v}}(f)$ according to the definition of (10.11):

$$\begin{pmatrix} V_{\text{EMI}}^{\text{@victim*}}(f) \\ I_{\text{EMI}}^{\text{@victim*}}(f) \end{pmatrix} = \boldsymbol{A}_{\text{coup,v}}(f) \cdot \begin{pmatrix} V_{\text{source}}(f) \\ -I_{\text{source}}(f) \end{pmatrix} \tag{10.11}$$

To find $V_{\text{source}}(f)$ and $I_{\text{source}}(f)$, the formula is rearranged to (10.12):

$$\Rightarrow \begin{pmatrix} V_{\text{source}}(f) \\ -I_{\text{source}}(f) \end{pmatrix} = \boldsymbol{A}_{\text{coup,v}}^{-1}(f) \cdot \begin{pmatrix} V_{\text{EMI}}^{\text{@victim*}}(f) \\ I_{\text{EMI}}^{\text{@victim*}}(f) \end{pmatrix} \tag{10.12}$$

For a simple mathematical description, $\boldsymbol{A}_{\text{coup,v}}^{-1}(f)$ is replaced by a matrix with the new entries $\alpha(f)$, $\beta(f)$, $\gamma(f)$ and $\delta(f)$ in (10.13). Note that these parameters are not the same as the ones used in the second step of the identification.

$$\Rightarrow \begin{pmatrix} V_{\text{source}}(f) \\ -I_{\text{source}}(f) \end{pmatrix} = \begin{bmatrix} \alpha(f) & \beta(f) \\ \gamma(f) & \delta(f) \end{bmatrix} \cdot \begin{pmatrix} V_{\text{EMI}}^{\text{@victim*}}(f) \\ I_{\text{EMI}}^{\text{@victim*}}(f) \end{pmatrix} \tag{10.13}$$

The voltage harmonics $V_{\text{EMI}}(f)$ can be calculated by (10.14):

$$V_{\text{EMI}}(f) = V_{\text{source}}(f) + Z_{\text{EMI}}(f) \cdot I_{\text{source}}(f) \tag{10.14}$$

By applying (10.13), the solution of (10.15) follows:

$$\begin{aligned} \overset{(10.13)}{\Rightarrow} V_{\text{EMI}}(f) = {} & \alpha(f) \cdot V_{\text{EMI}}^{\text{@victim*}}(f) + \beta(f) \cdot I_{\text{EMI}}^{\text{@victim*}}(f) \\ & - Z_{\text{EMI}}(f) \cdot \gamma(f) \cdot V_{\text{EMI}}^{\text{@victim*}}(f) - Z_{\text{EMI}}(f) \cdot \delta(f) \cdot I_{\text{EMI}}^{\text{@victim*}}(f) \end{aligned} \tag{10.15}$$

With $I_{\text{EMI}}^{\text{@victim*}}(f) = -V_{\text{EMI}}^{\text{@victim*}}(f)/Z_{\text{victim*}}(f)$, (10.15) can be solved to (10.16):

$$\Rightarrow V_{\text{EMI}}(f) = V_{\text{EMI}}^{\text{@victim*}} \cdot \left[\alpha - \frac{\beta}{Z_{\text{victim*}}} - \gamma \cdot Z_{\text{EMI}} + \delta \cdot \frac{Z_{\text{EMI}}}{Z_{\text{victim*}}}\right] \tag{10.16}$$

To find $V_{\text{EMI}}^{\text{@victim*}}(f)$, the DC-to-DC converter and the 48 V power supply are turned on. An oscilloscope is used to measure the time-domain EMI $v_{\text{EMI}}^{\text{@victim*}}(t)$ at the well-defined measurement port of the AN. By doing an FFT, the harmonics $V_{\text{EMI}}^{\text{@victim*}}(kf_0)$ are found. These original disturbances and the class 5 limit are depicted in Figure 10.10. Since the limit is given for RMS values, the disturbances must be evaluated accordingly. The EMI must be reduced by up to 57 dB to comply with the required limit.

The magnitude and phase of $V_{\text{EMI}}(kf_0)$ are calculated by (10.16) and depicted in Figure 10.11. It can be found that the phase declines linearly. This may not be obvious due to the logarithmic frequency axis.

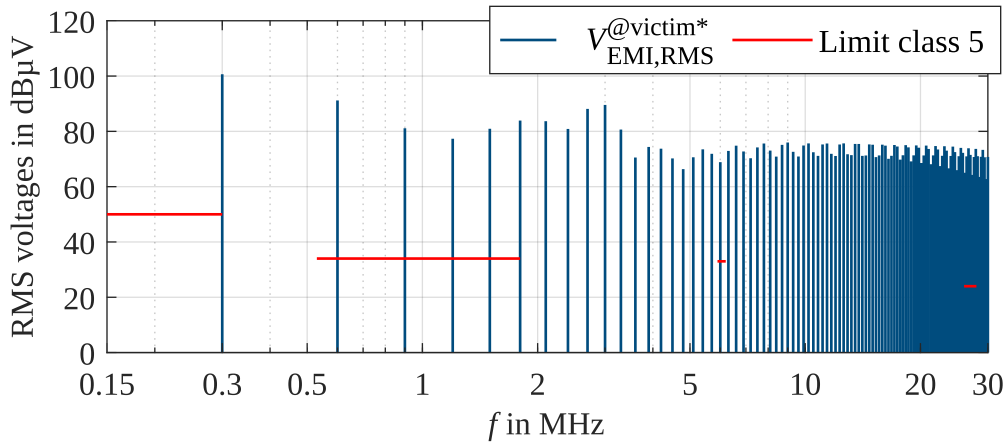

Figure 10.10: Original disturbances at the AN $V_{EMI}^{@victim*}(kf_0)$ vs. required limit (both in RMS values)

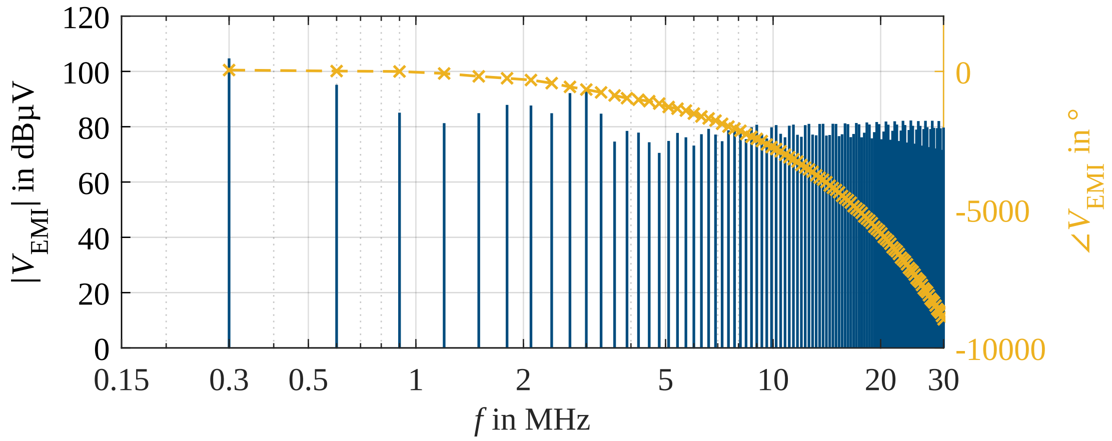

Figure 10.11: Magnitude and phase of the identified equivalent voltage source $V_{EMI}(kf_0)$

By completing this step, all elements of Figure 10.4 are identified and the design of the cancellation system can be started.

10.3 Design of the Active EMI Cancellation System

Designing active cancellation systems is no trivial task since numerous analog and digital devices must be dimensioned. Here, a pragmatic approach is proposed that uses the information on the previously identified system for a purposeful design. In [16, author], a similar, experimental approach is described. At first, the injector is designed.

10.3.1 Design of the Injector

The purposeful design of the injectors is very important since these elements are critical for the performance of the active EMI cancellation system. The design process can be very complex since numerous analog (coupling elements, decoupling elements, attenuators, additional passive filters, etc.) and digital (DAC) components must work together for an optimized system. Note that each of these elements can be a potential bottleneck for the overall performance of the cancellation system. Due to the high number of components and high degree of freedom in the dimensioning, a design by trial and error is usually not feasible. To resolve this problem, a procedure for a first design is proposed and demonstrated in the following. This approach requires the following eight steps:

1. **Selection of the injecting circuit** (and implicitly also of the decoupling circuit):
   In the first step, the topology for the injecting circuit must be chosen. Many of the options have been discussed and summarized in Section 4.4.2. Note that the topology of the decoupling circuit directly depends on the choice of the injecting circuit.

2. **Dimensioning of the decoupling element**:
   In the second step, it may be required to decouple the injecting circuit from the EMI source. The requirements for the impedances have been discussed in Section 4.4.2.

3. **Dimensioning of the coupling element**:
   For an efficient injection of the cancellation signals, the coupling element should be designed in such way that it generates only a small insertion loss. Capacitive injectors may require large capacitance values and inductive injectors may require large mutual inductances. However, the coupling element must still reject the low-frequency or DC operating voltages and currents.

4. **Calculation of the required cancellation source impedance (or admittance)**:
   Also the internal impedance (or admittance) of the cancellation source should cause only a small insertion loss for an efficient cancellation system. For laboratory equipment, this value may be given as 50 Ω. If this value is problematic, impedance converters can be applied.

5. **Estimation of the required cancellation signal**:
   After these first three steps, the actually required cancellation signal can be estimated. This estimation is very important for the design of the DAC.

6. **Adjustment of the DAC voltage range**:
   From the estimation of the required cancellation signal, the required voltage range of the DAC can be found. If the voltage range of the DAC is fixed, the signal range could be adjusted by applying attenuators, amplifiers or high-frequency transformers.

7. **Determination of the required DAC resolution**:
   As discussed in Section 5.1.1, the achievable EMI reduction is restricted by the SNR of the DAC. To find the required noise floor, the given EMC limit must be transferred to the DAC. Since the voltage range has already been defined in the previous step, the

required SNR can be calculated. From this value, the necessary resolution (number of bits) can be determined.

8. **Determination of the required DAC sampling rate**:
Last, the required DAC sampling rate must be determined. According to Section 5.1.2, the sampling rate should be at least twice as high as the highest frequency to be suppressed.

In the following, this procedure is demonstrated for the previously identified system. Here, the second channel of the AWG AFG3252 from Tektronix is used to generate the cancellation signal. The internal voltage source of this device has a symmetric range of ±5 V, a vertical resolution of 14 bits, an effective analog bandwidth (-3 dB) of 225 MHz and an impedance of $Z_{\text{anti}} = 50\ \Omega$. So, there are already some given quantities.

a) Step 1: Selection of the Injecting Circuit

For this demonstration, a capacitive injecting circuit according to Section 4.4.2.a) is chosen. Its design is simple and the decoupling can be described clearly. The required decoupling element is a series inductance. For the sake of simplicity, the cancellation source will be realized by a voltage source instead of a current source. This does not change the functionality of the injector. The resulting system is shown in Figure 10.12.

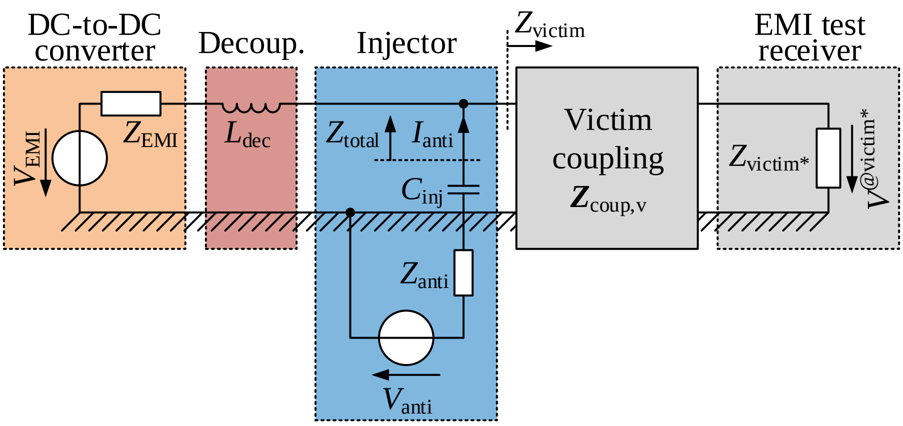

Figure 10.12: Schematic of the overall system with the injecting and decoupling circuits included

In reference to Section 3.1.1.a), the equivalent victim impedance $Z_{\text{victim}}(kf_0)$ is calculated. Since the AN's measurement port is terminated by 50 Ω, it can directly be found from the scattering parameter $S_{\text{coup,v,2,2}}(kf_0)$ by applying (10.17):

$$Z_{\text{victim}}(kf_0) = Z_0 \cdot \frac{1 + S_{\text{coup,v,2,2}}(kf_0)}{1 - S_{\text{coup,v,2,2}}(kf_0)} \tag{10.17}$$

The absolute value of the victim impedance $Z_{\text{victim}}(kf_0)$ is depicted in Figure 10.13. At low frequencies (below 3 MHz), the impedance will be defined by the AN's inductance of 5 µH (note the schematics of Figure 10.1). From approximately 3 MHz to 10 MHz, the termination impedance $Z_{\text{victim*}}$ of 50 Ω becomes dominant. For larger values, the supply line will significantly increase the impedance due to its inductance.

The total impedance $Z_{\text{total}}(kf_0)$ seen by the injecting circuit (note Figure 10.12) into the overall system is introduced for later use.

b) Step 2: Dimensioning of the Decoupling Element

The cancellation source generates a voltage $V_{\text{anti}}(kf_0)$ that causes an injected current $I_{\text{anti}}(kf_0)$ (note Figure 10.12). This current will be divided by the impedances $Z_{\text{victim}}(kf_0)$ and $Z_{\text{EMI}}(kf_0)$ (assuming that there is no decoupling inductance L_{dec} yet). Comparing the impedances in Figure 10.13, it can be found that most of the injected current would flow into the EMI source and not support the cancellation at the EMI victim.

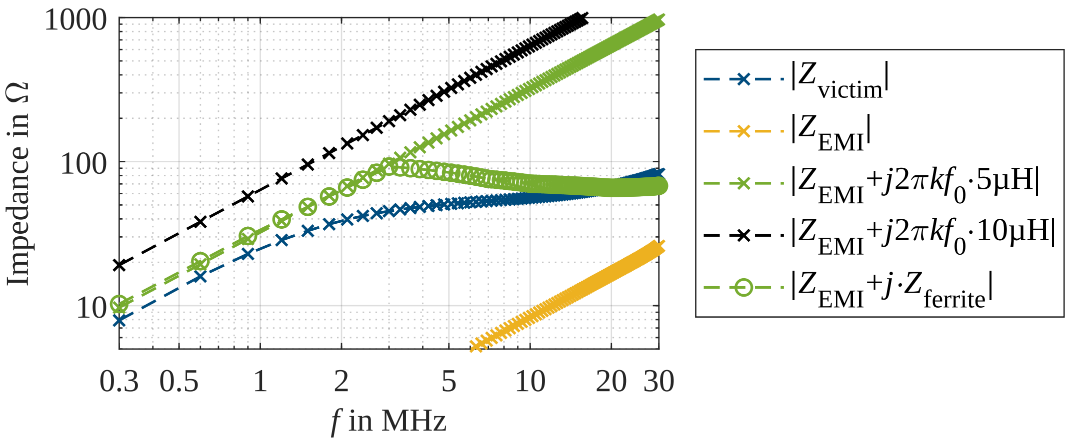

Figure 10.13: Comparison of impedances for different values L_{dec} of the decoupling inductance

This issue can be resolved by the decoupling inductance L_{dec}. Here, it is chosen that at least 50% of the injected current should flow to the EMI victim. So, the combined impedance $|Z_{\text{EMI}}(kf_0) + j2\pi kf_0 \cdot L_{\text{dec}}|$ should be larger than (or at least equal) $|Z_{\text{victim}}(kf_0)|$ as described by (10.18):

$$|Z_{\text{EMI}}(kf_0) + j2\pi kf_0 \cdot L_{\text{dec}}| \overset{!}{\geq} |Z_{\text{victim}}(kf_0)| \tag{10.18}$$

The mismatch is strongest for the lower frequencies at which the AN's impedance is mostly defined by its inductance of 5 µH. So, it can be expected that a decoupling impedance of $L_{\text{dec}} = 5$ µH may be necessary. In Figure 10.13, the impedances are shown for different values of the decoupling inductance L_{dec} (i.e. 0 µH, 5 µH, 10 µH). It can be found that the injector should indeed be sufficiently decoupled for an inductance of 5 µH.

Now, a viable inductor must be selected that poses at least an inductance of 5 μH. Furthermore, it must be effective in the considered frequency range. Here, the split core ferrite MnZn 74272733 from Würth Elektronik [113] is selected. The frequency range is specified from 150 kHz to 30 MHz that matches exactly with the range of interest. It has a one turn impedance of 10 Ω at 300 kHz that corresponds to an inductance of 5.3 μH. The impedance curve of the selected core $Z_{\text{ferrite}}(kf_0)$ is extracted from the datasheet and the resulting impedance $|Z_{\text{EMI}}(kf_0) + j \cdot Z_{\text{ferrite}}(kf_0)|$ is presented in Figure 10.13. It can be found that the injector is well decoupled for frequencies of up to 20 MHz. For higher frequencies, the selected inductor loses some performance and the decoupling declines. This can generally be an issue since the cancelling sine waves may become large for these frequencies. However, the EMI of this demonstrator is rather low for high frequencies (note Figure 10.10). So, this effect is assumed to be negligible in comparison to the cancelling sine waves required for the lower frequencies.

c) Step 3: Dimensioning of the Coupling Element

The voltage $V_{\text{anti}}(kf_0)$ generated by the cancellation source is divided by the series connection of the impedances $Z_{\text{anti}}(kf_0)$, $Z_{\text{total}}(kf_0)$ and $1/(j2\pi kf_0 \cdot C_{\text{inj}})$. Most of the injected voltage should drop over the impedance $Z_{\text{victim}}(kf_0)$ for a strong coupling to the EMI victim. The impedance $Z_{\text{total}}(kf_0)$ can be calculated by (10.19):

$$Z_{\text{total}}(kf_0) = \frac{(Z_{\text{EMI}}(kf_0) + j \cdot Z_{\text{ferrite}}(kf_0)) \cdot Z_{\text{victim}}(kf_0)}{Z_{\text{EMI}}(kf_0) + j \cdot Z_{\text{ferrite}}(kf_0) + Z_{\text{victim}}(kf_0)} \tag{10.19}$$

For a small insertion loss of the coupling capacitance C_{inj}, its impedance should be much smaller than $|Z_{\text{total}}(kf_0)|$ according to (10.20):

$$\left| \frac{1}{j2\pi kf_0 \cdot C_{\text{inj}}} \right| = \frac{1}{2\pi kf_0 \cdot C_{\text{inj}}} \overset{!}{\ll} |Z_{\text{total}}(kf_0)| \tag{10.20}$$

In Figure 10.14, the absolute values of the impedances are compared for different values of the coupling element C_{inj} (i.e. 10 nF, 100 nF, 1 μF). Here, a value of 100 nF is chosen. The small mismatch for the fundamental wave is assumed to be negligible.

A photograph of the resulting DUT is depicted in Figure 10.15. The cancellation signal will be generated by the AWG and brought into the system via a BNC feedthrough. Inside the shielding case, a coaxial cable is used to connect the feedthrough to the injecting capacitor. At both ends, the shield of the coaxial cable is connected with the shielding case and, therefore, ground. Note that the coaxial cable below will be used for the sensor later. The split core ferrite can be seen on the internal supply line to the converter.

d) Step 4: Calculation of the Required Cancellation Source Impedance

In general, the cancellation source impedance $|Z_{\text{anti}}(kf_0)|$ should be much smaller than $|Z_{\text{total}}(kf_0)|$ for a small insertion loss. Here, $Z_{\text{anti}}(kf_0)$ equals 50 Ω due to the application

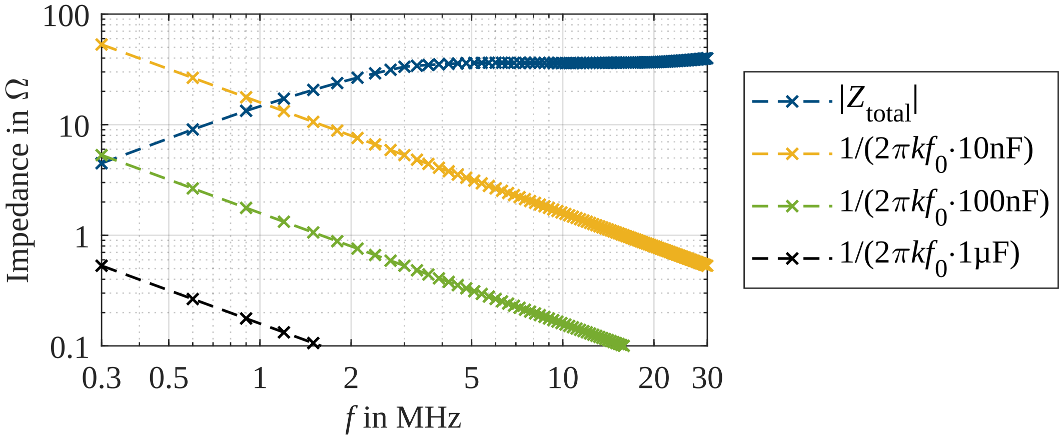

Figure 10.14: Comparison of impedances for different values C_{inj} of the coupling capacitance

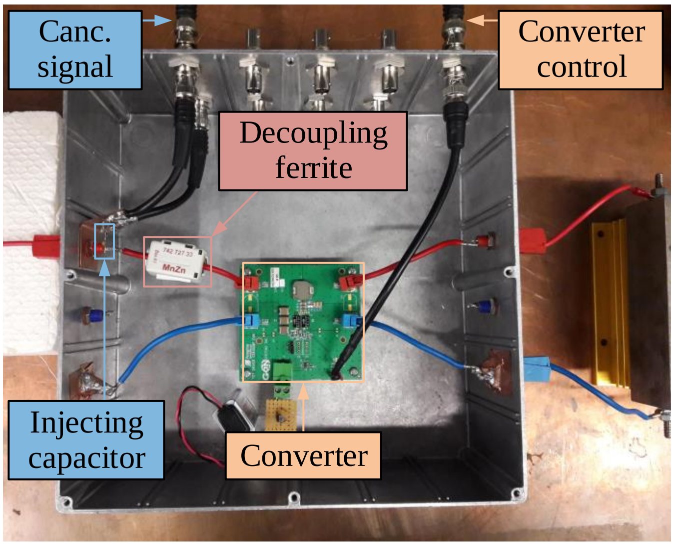

Figure 10.15: Photograph of the DUT with installed decoupling and coupling elements

of an AWG as cancellation source. Considering $|Z_{\text{total}}(kf_0)|$ in Figure 10.14, this value is actually too high. In the following, it will be checked if the AWGs internal voltage range of ± 5 V is still sufficient. In this case, the high cancellation source impedance poses no issue.

e) Step 5: Estimation of the Required Cancellation Signal

Next, a first estimation of the cancellation signal $V_{\text{anti}}(kf_0)$ must be calculated. In general, the cancellation signal is found by considering the EMI at the interface port according to (3.9). For this demonstration, the description of (3.9) is referred to the measurement port of the AN (denoted by 'victim*') leading to (10.21). By doing so, the calculations can be verified at a well-defined measurement port.

$$V_{\text{anti}}(kf_0) = -\frac{H_{\text{EMI}}^{\rightarrow\text{victim*}}(kf_0)}{H_{\text{anti}}^{\rightarrow\text{victim*}}(kf_0)} \cdot V_{\text{EMI}}(kf_0) \tag{10.21}$$

Since $V_{\text{EMI}}(kf_0)$ is known, only the transfer functions $H_{\text{EMI}}^{\rightarrow\text{victim*}}(kf_0)$ and $H_{\text{anti}}^{\rightarrow\text{victim*}}(kf_0)$ must be determined. Both transfer functions can be found by considering the schematic depicted in Figure 10.12. Note that the connection of the injecting circuit and the AWG introduces a parasitic inductance of approximately 250 nH (found by measurements). This inductance is respected between $Z_{\text{anti}}(kf_0)$ and C_{inj}. The calculation of the transfer functions is straightforward, but lengthy. So, only the results are discussed in the following.

The calculated transfer function from the injector to the measurement port $H_{\text{anti}}^{\rightarrow\text{victim*}}(kf_0)$ is depicted in Figure 10.16. For verification of this calculation, the transfer function is also measured in the practical system. To do so, the cancellation source (AWG) and the EMI victim (EMI test receiver) are removed and the VNA is connected to these two ports. The found scattering parameters are transferred to the transfer function of interest. There is a very good agreement between the calculated and measured transfer functions.

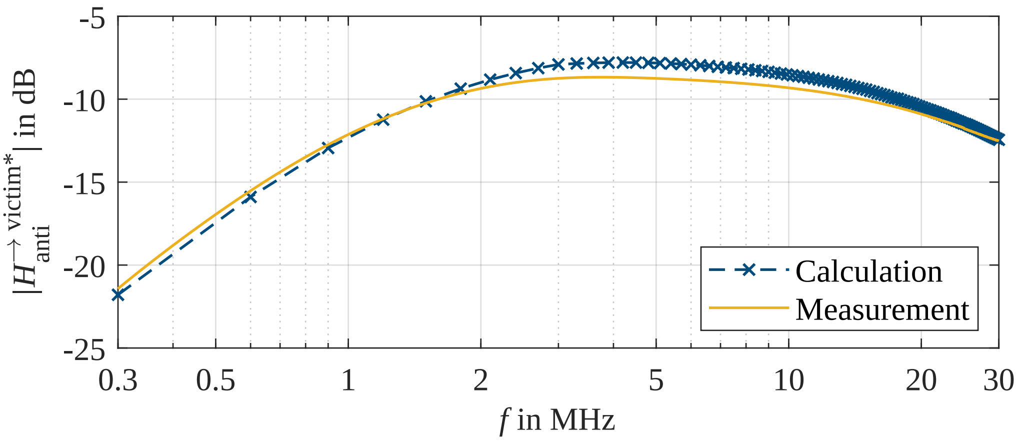

Figure 10.16: Calculated and measured transfer function $H_{\text{anti}}^{\rightarrow\text{victim*}}(kf_0)$

The transfer function $H_{\text{EMI}}^{\rightarrow\text{victim*}}(kf_0)$ (Figure 10.17) can also be calculated by using the schematic of Figure 10.12.

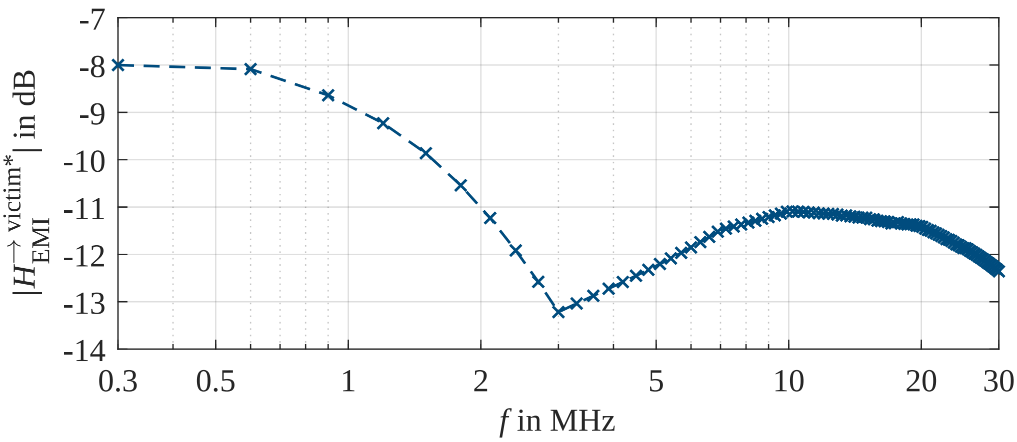

Figure 10.17: Calculated transfer function $H_{\text{EMI}}^{\rightarrow\text{victim*}}(kf_0)$

The verification of this transfer function is not trivial since the DC-to-DC converter with its equivalent impedance $Z_{\mathrm{EMI}}(kf_0)$ cannot simply be replaced by 50 Ω measurement equipment. However, it is possible to evaluate the resulting EMI at the victim $V_{\mathrm{EMI}}^{@\mathrm{victim}^*}(kf_0)$ that can be calculated by (10.22):

$$V_{\mathrm{EMI}}^{@\mathrm{victim}^*}(kf_0) = H_{\mathrm{EMI}}^{\rightarrow\mathrm{victim}^*}(kf_0) \cdot V_{\mathrm{EMI}}(kf_0) \tag{10.22}$$

So, for verification, the cancellation source $V_{\mathrm{anti}}(kf_0)$ is turned off, the EMI source is turned on and the EMI at the measurement port of the AN $v_{\mathrm{EMI}}^{@\mathrm{victim}^*}(t)$ is measured by an oscilloscope. By doing an FFT, the spectrum $V_{\mathrm{EMI}}^{@\mathrm{victim}^*}(kf_0)$ can be found. In Figure 10.18, three different spectra of $V_{\mathrm{EMI}}^{@\mathrm{victim}^*}(kf_0)$ are depicted. The first is the measurement without any injector. The second is the measurement with deactivated injector. The third is the calculation using the identified parameters and the designed (deactivated) injector. Comparing the last two spectra, it can be found that there is a very good agreement between calculation and measurement. So, the calculation proves to be viable. Furthermore, the passive attenuation of the injector can clearly be seen by comparing the spectra with and without (deactivated) injector. The passive attenuation is the highest (approx. 13 dB) for 3.6 MHz and declines for higher and lower frequencies to approximately 6 dB. As stated before, this passive attenuation reduces the EMI and, therefore, the cancellation effort. So, it is advantageous.

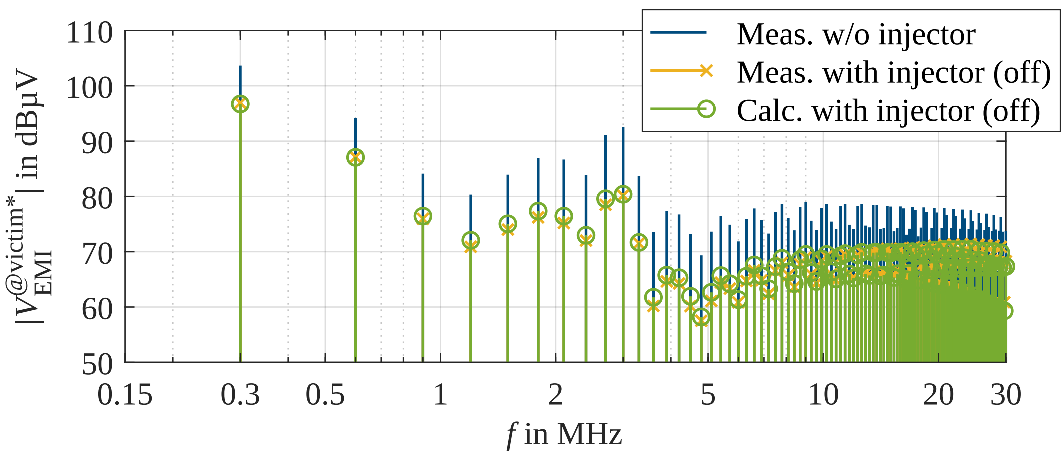

Figure 10.18: EMI spectra at the measurement ports of the ANs without and with deactivated injector, also: comparison of measurement and calculation

Since $H_{\mathrm{EMI}}^{\rightarrow\mathrm{victim}^*}(kf_0)$, $H_{\mathrm{anti}}^{\rightarrow\mathrm{victim}^*}(kf_0)$ and $V_{\mathrm{EMI}}(kf_0)$ are all known, the necessary cancellation signal $V_{\mathrm{anti}}(kf_0)$ can be calculated by (10.21). The spectrum is depicted in Figure 10.19. The time-domain signal $v_{\mathrm{anti}}(t)$ will be discussed in the following.

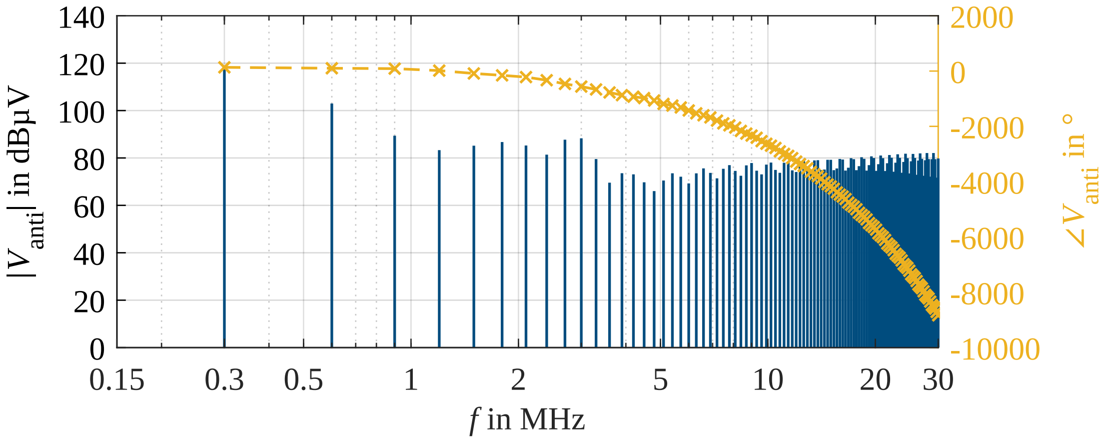

Figure 10.19: Magnitude and phase of the required cancellation signal $V_{\text{anti}}(kf_0)$

f) Step 6: Adjustment of the DAC Voltage Range

Next, the voltage range of the DAC is adjusted for the required cancellation signal. To do so, the time-domain signal is calculated. It is synthesized according to (2.8) and depicted in Figure 10.20. It can be found that the fundamental wave is quite significant (note also Figure 10.19). This is plausible since the EMI at the measurement port $V_{\text{EMI}}^{\text{@victim*}}(kf_0)$ (Figure 10.18) is the highest and the coupling of the injecting circuit $H_{\text{anti}}^{\rightarrow\text{victim*}}(kf_0)$ (Figure 10.16) is the lowest for the fundamental wave ($k = 1$). The high-frequency ringing of the cancellation signal (that results from the superposition of numerous sine waves) corresponds to the switching events of the transistors.

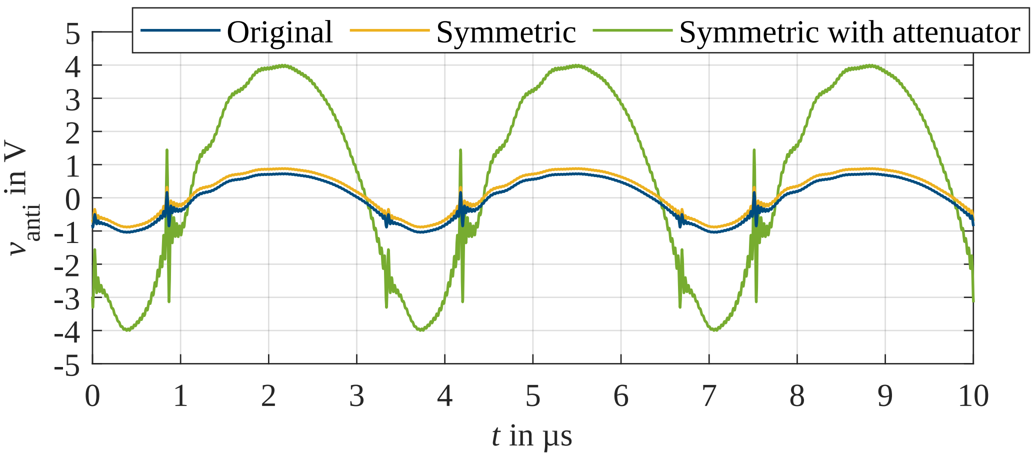

Figure 10.20: Calculated time-domain cancellation signals (original, symmetric and symmetric with attenuator)

To get the most out of the vertical resolution of the DAC, its given voltage range should be fully utilized. The DAC of the AWG AFG3252 has an internal voltage range of ± 5 V. Since the calculated cancellation signal $v_{\text{anti}}(t)$ is only between ± 1 V, the source impedance

$Z_{\text{anti}} = 50\ \Omega$ is no limiting factor in this setup. There should be even more attenuation so that the voltage range (and therefore the given resolution) of the AWG is better used. By introducing attenuators in series with the cancellation source, the transfer function $H_{\text{anti}}^{\rightarrow\text{victim*}}(kf_0)$ is reduced and larger cancellation signals are necessary for the same effect. By doing so, more of the DAC's voltage range is used. Before these attenuators are applied, the signal is symmetrized around 0 V by (10.23):

$$v_{\text{anti,symmetric}}(t) = v_{\text{anti}}(t) - \frac{\max\left(v_{\text{anti}}(t)\right) + \min\left(v_{\text{anti}}(t)\right)}{2} \tag{10.23}$$

The symmetric signal $v_{\text{anti,symmetric}}(t)$ can also be found in Figure 10.20. It is chosen that the DAC's voltage range should be used by 80%. Since the cancellation signal must be increased by the factor 4 that corresponds to an attenuation of approximately 13 dB, an attenuator combination of 10 dB and 3 dB (50 Ω) is applied between AWG and injecting circuit. So, ideally, the cancellation signal should use 80% of the DAC's voltage range (note Figure 10.20).

Since the required cancellation signal is too small, the introduction of an attenuator in the signal path is a convenient solution. If the signal was too large, the problem may be solved by the following measures:

- Increasing the value of the coupling element
- Increasing the value of the decoupling element
- Reducing the internal impedance of the cancellation source
- Introducing an amplifier
- Introducing a high-frequency transformer
- Introducing a passive filter between EMI source and decoupling circuit

g) Step 7: Determination of the Required DAC Resolution

In this step, the required DAC resolution is calculated. This is directly related to the given limits since the quantization noise floor of the DAC determines the minimum achievable residual EMI. To derive the necessary DAC resolution, the given class 5 limit of CISPR 25 $V_{\text{limit,RMS}}^{@\text{victim*}}(kf_0)$ is transferred to the cancellation source by using (10.24). Since only the limits for the harmonics kf_0 are relevant, only these discrete values are considered and transferred. Note that the limit is given in RMS values.

$$V_{\text{limit,RMS}}^{@\text{anti}}(kf_0) = \frac{V_{\text{limit,RMS}}^{@\text{victim*}}(kf_0)}{\left|H_{\text{anti}}^{\rightarrow\text{victim*}}(kf_0)\right|} \tag{10.24}$$

The voltage limit referred to the cancellation source $V_{\mathrm{limit,RMS}}^{\mathrm{@anti}}(kf_0)$ is presented in Figure 10.21. The DAC's quantization noise floor must below the lowest limit. Here, the lowest limit is approximately 49 dBµV.

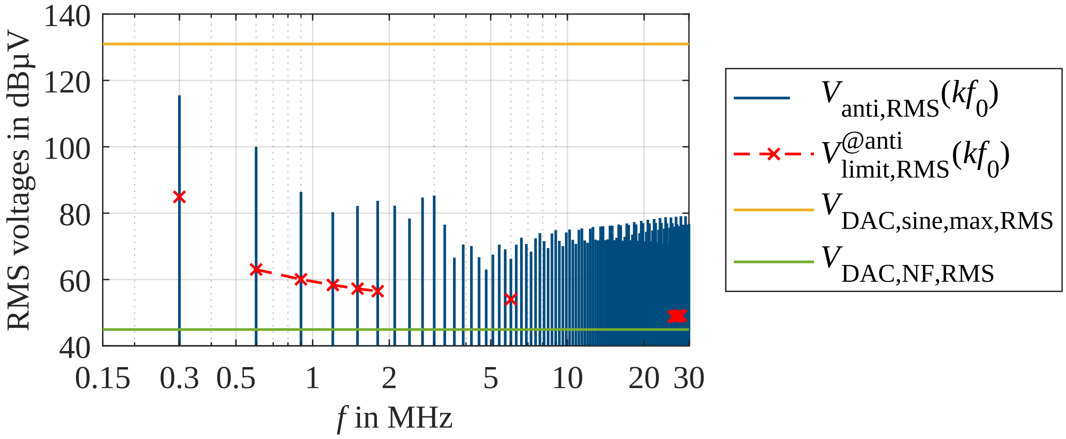

Figure 10.21: RMS voltages of the cancellation signal, the limit (transferred to the injecting source) and the DAC's range

To find the required resolution, the necessary SNR (Section 5.1.1) is considered. For the calculation of the SNR, the highest sine wave producible by the DAC must be calculated (in RMS values). Since the AWG's DAC has a given voltage range of ±5 V, the highest possible sine wave has an RMS value of $V_{\mathrm{DAC,sine,max,RMS}} = 5\ \mathrm{V}/\sqrt{2} \approx 3.54\ \mathrm{V}$. This corresponds to a voltage level of approximately 131 dBµV.

So, the DAC requires an SNR of at least 131 dBµV − 49 dBµV = 82 dB. Using (5.1), it can be found that a resolution of at least 14 bit is necessary. The here used AWG AFG3252 fulfills this requirement. Considering the actual SNR of approximately 86 dB for 14 bits according to (5.1), the actual **n**oise **f**loor of the DAC $V_{\mathrm{DAC,NF,RMS}}$ is calculated to 45 dBµV. This value is also depicted in Figure 10.21.

h) Step 8: Determination of the Required DAC Sampling Rate

Last, the required DAC sampling rate must be determined. Since the highest considered harmonic is 30 MHz, a sampling rate of 60 MHz would theoretically be sufficient (Nyquist-Shannon theorem). The here used AWG AFG3252 has a sampling rate of at least 250 MS/s and an analog bandwidth (-3 dB) of 225 MHz. So, it is well applicable for the considered frequency range.

By finishing this step, the injector is completely dimensioned. In the next few steps, the sensor is added to the system.

10.3.2 Design of the Sensor

In this section, the sensor is designed and dimensioned. The design of the sensors can be done by the following six steps:

a) **Selection of the sensing circuit**:
Also for the sensing circuit, the fundamental topology must be chosen. Some options have been summarized in Section 4.4.3. Note that the choice of the sensing circuit can be made independently from the chosen injecting circuit.

b) **Dimensioning of the sensing circuit**:
The main purpose of the sensing circuit is to measure and not to attenuate. So, it should only marginally affect the overall system. Capacitive voltage sensors should have a large impedance. Inductive current sensors should have a small impedance. Furthermore, the sensing circuit requires a high-pass characteristic that passes the high-frequency EMI signals for the sensing ADC, but rejects the low-frequency or DC operating voltages and currents. The elements of the sensing circuit should be dimensioned accordingly.

c) **Limitation of the sensed frequency range**:
For a precise measurement, the sensed frequency range should be limited to the one that should actually be suppressed.

d) **Adjustment of the ADC voltage range**:
Like for the DAC, the ADC's voltage range should be used as much as possible. So, it should be adjusted according to the expected sensed signals. If the voltage range of the ADC is fixed, the sensed signal can be adjusted by applying attenuators, amplifiers and high-frequency transformers.

e) **Determination of the required ADC resolution**:
As discussed in Section 5.1.1, the achievable EMI reduction is restricted by the SNR of the ADC. To find the required noise floor, the given EMC limit must be transferred to the ADC. Since the voltage range has already been defined in the previous step, the required SNR can be calculated by considering the necessary noise floor. From this value, the required resolution (number of bits) can be determined.

f) **Determination of the required ADC sampling rate**:
Last, the required ADC sampling rate must be determined. According to Section 5.1.2, the sampling rate should be at least twice as high as the highest frequency to be suppressed.

In the following demonstration, an oscilloscope HDO6104A from Teledyne LeCroy is used to acquire the (residual) EMI. It is used with a termination impedance of $Z_{\mathrm{meas}} = 50\ \Omega$. This device has a maximum symmetric voltage range of ± 4 V (with 50 Ω termination), a vertical resolution of 12 bits and an effective analog bandwidth (-3 dB) of 1 GHz (with 50 Ω termination).

a) Step 1: Selection of the Sensing Circuit

At first, a sensing circuit must be selected. Here, a capacitive voltage sensor according to Section 4.4.3.a) is chosen due to its simplicity. The test setup with the added sensor is depicted in Figure 10.22. The parasitic inductance L_{par} of 250 nH due to the connection of the AWG with the injecting capacitor is explicitly shown in this schematic. The same parasitic inductance must also be respected for the connection of the oscilloscope and the sensing capacitor.

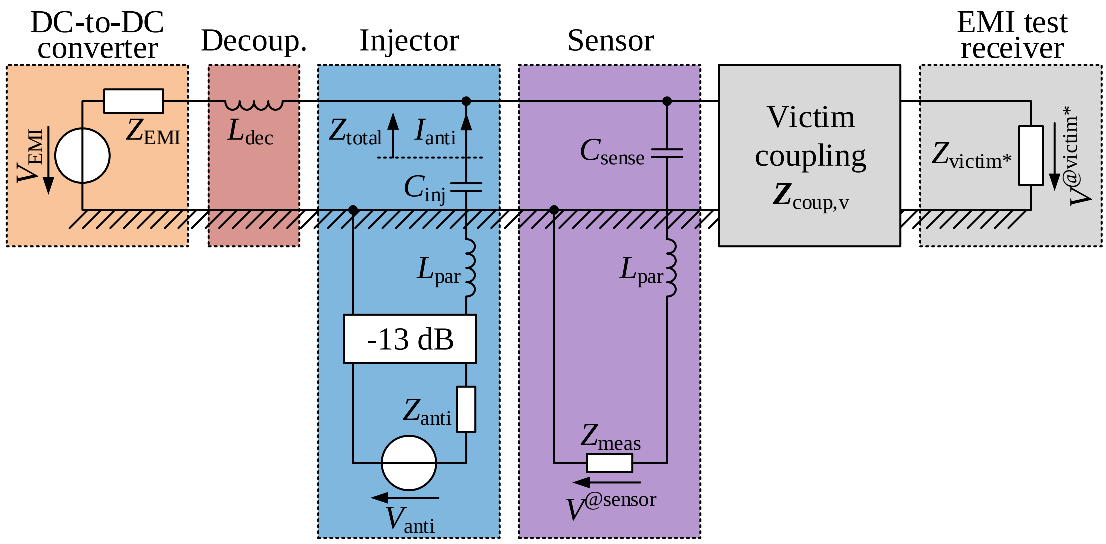

Figure 10.22: Schematic of the overall system with the injecting, decoupling and sensing circuits included

b) Step 2: Dimensioning of the Sensing Circuit

There are basically two requirements for the sensing circuit. First, the sensing circuit should have a high-pass characteristic that passes the high-frequency EMI and rejects the low-frequency or DC operating voltages. Here, it is proposed that its cutoff frequency frequency f_c is set one decade below the fundamental frequency f_0 of the EMI. Since $Z_{meas} = 50\ \Omega$ is actually a pure resistance R_{meas}, f_c can immediately be calculated by (10.25):

$$f_c = \frac{1}{2\pi R_{meas} C_{sense}} \tag{10.25}$$

For $f_c = f_0/10 = 30$ kHz and $R_{meas} = 50\ \Omega$, the required capacitance C_{sense} can be calculated to approximately 106 nF by using (10.25). So, a 100 nF capacitor is chosen.

As a second requirement, the sensing circuit should only marginally affect the overall system for the considered harmonics. Due to the high-pass characteristic, the impedance of the sensing circuit can basically be described by its measurement resistance $R_{meas} = 50\ \Omega$ in the considered frequency range (300 kHz to 30 MHz). This value is in the same range as $|Z_{victim}(kf_0)|$ (note Figure 10.13). So, the sensing circuit may affect the overall system.

This can be problematic for the injector since it was designed without the influence of the sensing circuit. To resolve this issue, the design of the injector could be redone with the sensor included. Another solution would be to use a larger measurement impedance Z_{meas}. For this demonstration, it is assumed that the effect of the too small measurement impedance is bearable.

c) Step 3: Limitation of the Sensed Frequency Range

Since only the frequency range up to 30 MHz is considered, the bandwidth of the sensor is reduced by applying a low-pass filter (50 Ω) with a cutoff frequency of 32 MHz between sensing circuit and oscilloscope. Without this low-pass filter, the higher harmonics (that are not suppressed) may lead to high spikes in time domain. Since the oscilloscope must not be overdriven, the spikes will determine the voltage range and, therefore, the vertical resolution (note also Section 5.1.1). By filtering these high-frequency spikes, only the relevant harmonics remain.

d) Step 4: Adjustment of the ADC Voltage Range

Next, the voltage range of the sensed signal is investigated. The largest signal occurs for the EMI without any cancellation. So, the spectrum $V_{\text{EMI}}^{@\text{sensor}}(kf_0)$ must be considered according to (10.26):

$$V_{\text{EMI}}^{@\text{sensor}}(f) = H_{\text{EMI}}^{\rightarrow\text{sensor}}(f) \cdot V_{\text{EMI}}(f) \tag{10.26}$$

To find the transfer function $H_{\text{EMI}}^{\rightarrow\text{sensor}}(kf_0)$, the schematic of Figure 10.22 can be used. For the sake of brevity, the transfer function and the spectra are not depicted here. Instead, the relevant calculated and measured time-domain signals $v_{\text{EMI}}^{@\text{sensor}}(t)$ are depicted in Figure 10.23. There is a high conformity between the signals. The slight deviations may be due to the low-pass filter that is not respected in the analytical solution.

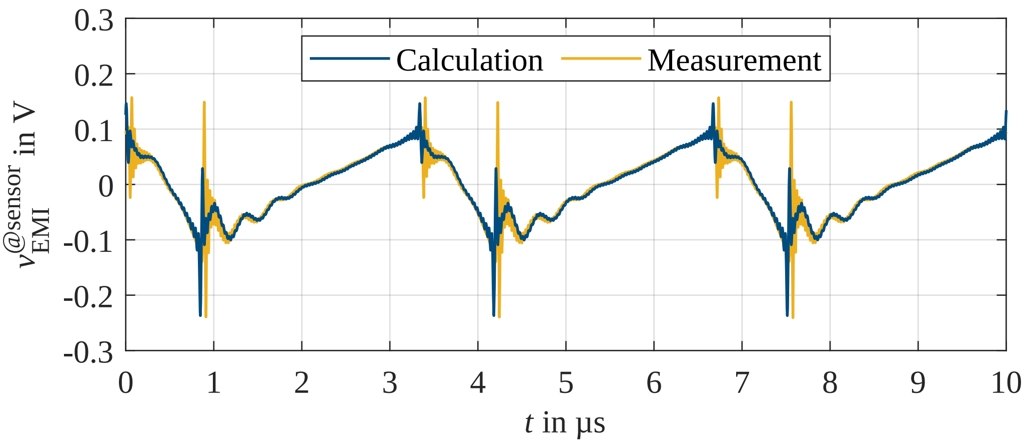

Figure 10.23: Time-domain signal $v_{\text{EMI}}^{@\text{sensor}}(t)$

The here used oscilloscope has a maximum symmetric voltage range of $V_{\text{ADC,max}} = 4$ V if a 50 Ω termination is used. By rescaling its vertical range, the sensed signal can be measured precisely. So, no further adjustments are required.

e) Step 5: Determination of the Required ADC Resolution

Last, the required ADC resolution must be calculated. To do so, the voltage limit at the victim $V_{\text{limit,RMS}}^{@\text{victim*}}(kf_0)$ must be transferred to an equivalent limit at the sensor $V_{\text{limit,RMS}}^{@\text{sensor}}(kf_0)$. In general, this can be done by using the schematics of the complete system according to Figure 10.24.

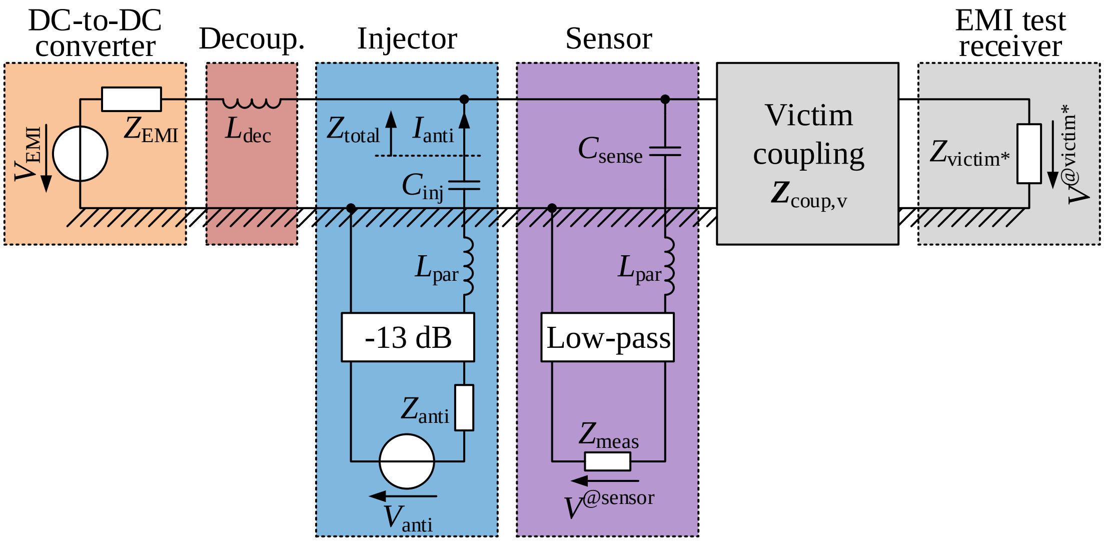

Figure 10.24: Schematic of the overall system with the complete cancellation system

Here, the AN and the sensor pick up the voltage of the same line by using a similar high-pass filter consisting of 100 nF with 50 Ω. In a first approximation, it can be expected that both circuits measure the same signal. So, the EMC requirement at the AN may directly be transferred to the sensor.

Like for the DAC, the noise floor of the ADC must be below the lowest limit. The lowest limit of class 5 [4] is given by 24 dBµV (in RMS) in the considered frequency range. The RMS value of the highest measurable sine wave can be calculated by $4\ \text{V}/\sqrt{2} \approx 2.83\ \text{V} \mathrel{\widehat{=}} 129\ \text{dB}\mu\text{V}$. So, in theory, an SNR of $129\ \text{dB}\mu\text{V} - 24\ \text{dB}\mu\text{V} = 105\ \text{dB}$ would be necessary. The oscilloscope HDO6104A with its resolution of 12 bits only has an SNR of approximately 74 dB according to (5.1).

In theory, the vertical resolution of the oscilloscope's ADC would not be sufficient. However, the vertical range of the oscilloscope can be rescaled after each iteration of the FFT method for more precise measurements. By doing so, the already large dynamic range of 74 dB is widely enhanced.

Since the FFT method will be applied in the following demonstration, the measurement results will be further improved by the FFT gain. To make the most use of this effect, the

FFT will be applied to multiple periods of the signal. It can be expected that the noise floor of the processed sensor signal is far below the given limits.

f) Step 6: Determination of the Required ADC Sampling Rate

Last, the required ADC sampling rate must be determined. Since the highest considered harmonic is 30 MHz, a sampling rate of 60 MHz would theoretically be sufficient (Nyquist-Shannon theorem). The here used oscilloscope HDO6104A from Teledyne LeCroy has a sampling rate of up to 10 GS/s with an analog bandwidth of 1 GHz. So, it is well suited for the application. The very high sampling rate leads to oversampling that can further enhance the precision of the later applied FFT method (note Section 6.4.5).

10.3.3 Designed Active EMI Cancellation System

After this design procedure, the system is completely dimensioned. The schematic is already depicted in Figure 10.24 and a photograph of the realized system can be found in Figure 10.25.

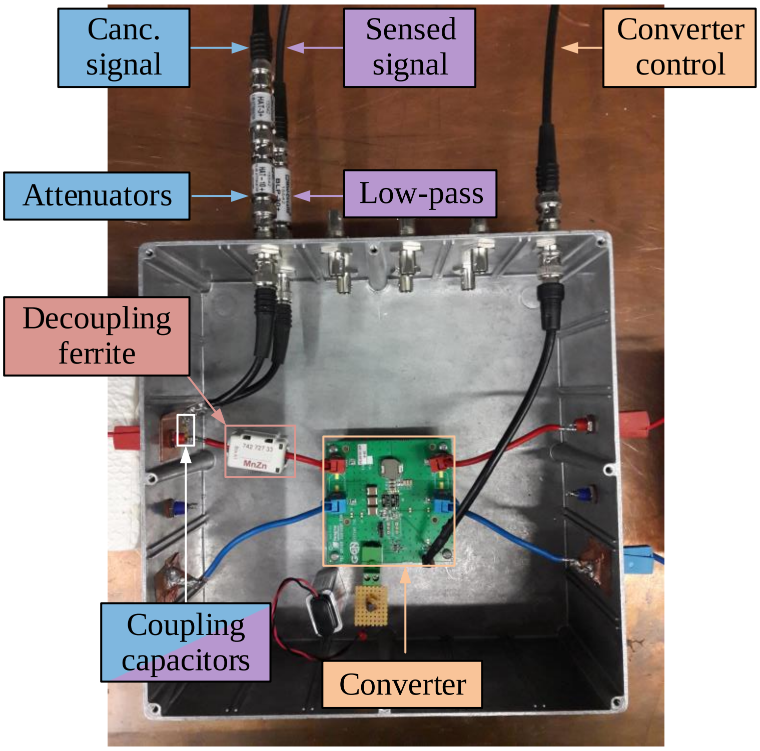

Figure 10.25: Photograph of the converter with the designed cancellation system (shielding case opened)

10.4 Application of the FFT Method

In the following, the cancellation system's performance is demonstrated by using the FFT method. This demonstration shows the effectiveness of both the cancellation hardware and the algorithm. At first, the complete test setup is depicted. Afterward, the settings of the algorithm are described. Measurement results are presented and discussed. The section is closed by a discussion.

10.4.1 Complete Test Setup with Active Cancellation System

The FFT method will be applied to the test setup depicted in Figure 10.26. The schematic can be found in Figure 10.24. Converter, injecting circuit and sensing circuit form the DUT that is depicted in Figure 10.25 in more detail. The used oscilloscope and AWG are still the HDO6104A and AFG3252, respectively. These two devices are connected via Ethernet to a PC. The measured time-domain signal of the oscilloscope is transferred to a PC and brought into the frequency domain by an FFT. The PC utilizes the FFT method according to Section 6.4 to calculate and synthesize the necessary cancellation signals. These signals are passed to the AWG and then injected into the system. The implementation is done in MATLAB and based on [108, supervisor]. The performance of the cancellation system is evaluated by an EMI test receiver at the measurement port of the artificial network.

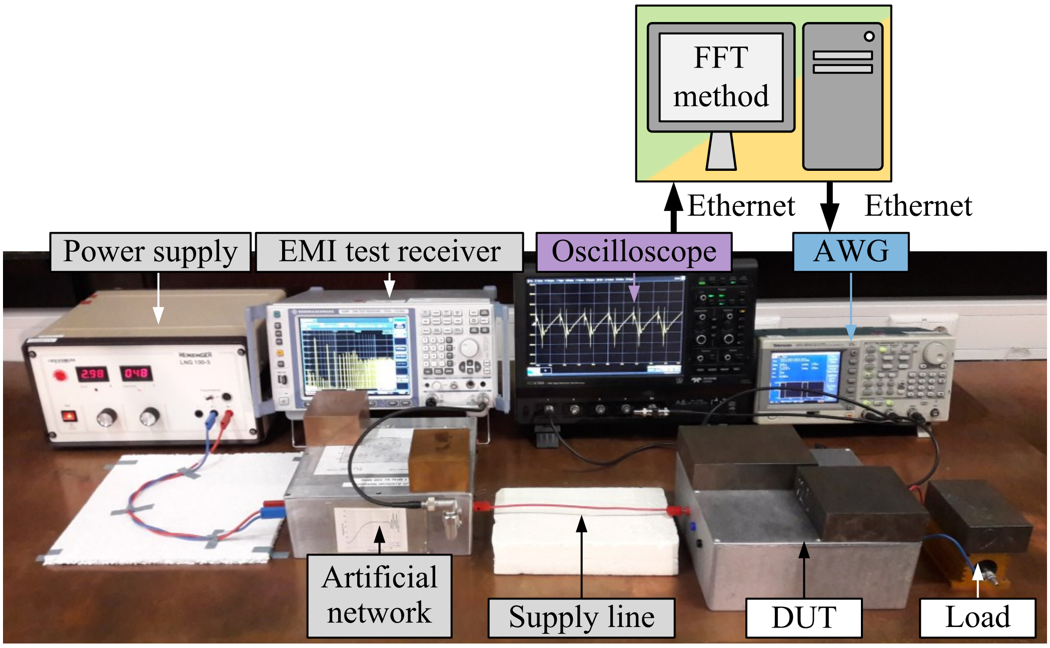

Figure 10.26: Photograph of the complete test setup with the active EMI cancellation system

10.4.2 Settings of the Algorithm

As stated before, the algorithm is based on the description in Section 6.4. To enhance the resolution of the oscilloscope measurement, 30 signal periods are used for each FFT. The algorithm is applied iteratively to optimize the results. Here, the identification of the transfer function $H_{\text{anti}}^{\rightarrow\text{sensor}}(kf_0)$ is done during nominal operation of the DC-to-DC converter. Furthermore, the transfer function is newly identified in each iteration. This is done to account for weak nonlinear effects of the overall system due to the injected cancellation signals.

10.4.3 Measurement Results

Exemplary measurement results of the EMI test receiver are depicted in Figure 10.27. Obviously, the original EMI is far above the limit of class 5 of CISPR 25 [4]. After the first iteration of the FFT method, the EMI is already significantly reduced by approximately 30 dB over the complete frequency range. The limit between 5.9 and 6.2 MHz is already fulfilled. After the eight iteration of the FFT method, the complete spectrum complies with the class 5 limit of CISPR 25 [4]. The fundamental wave is suppressed by 64 dB. There are reductions of approximately 40 dB for the highest considered harmonics.

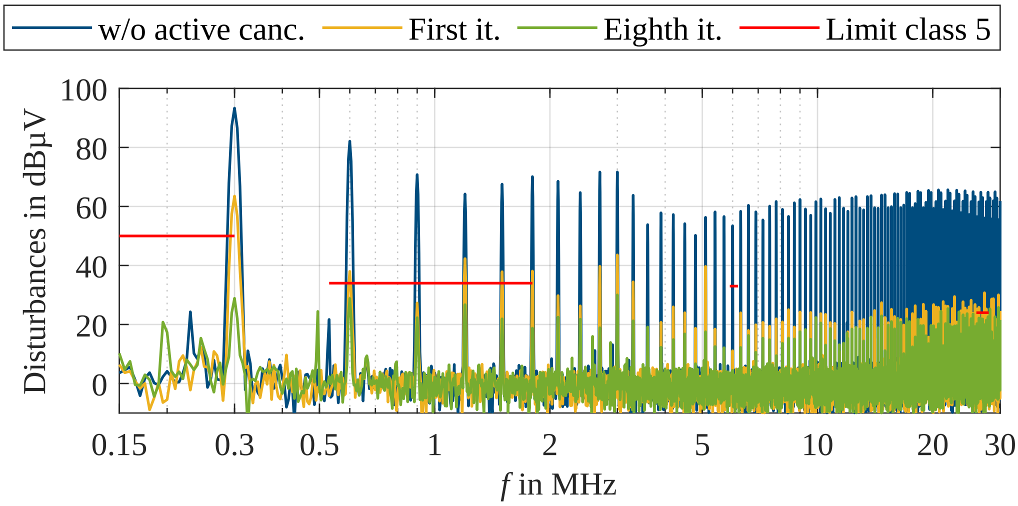

Figure 10.27: Measurement results for the EMI test receiver at the AN without active EMI cancellation, after first iteration of the algorithm, after eighth iteration of the algorithm

10.4.4 Cancellation Signal

The found cancellation signal is depicted in Figure 10.28. The signal is close to the prediction in Figure 10.20. The deviations may be due to the sensing circuit and its low-pass filter that are not respected in the analytical calculation. It would be no issue to include these elements to find more precise predictions.

10.4.5 Power Consumption of the Cancellation Signal

Last, the power consumption of the system is investigated. To do so, the RMS value of the cancellation signal is determined to $V_{\mathrm{anti,RMS}} \approx 3.05$ V. The internal impedance of the AWG is a resistance of 50 Ω. Due to the attenuators, it can be assumed that the AWG is terminated by 50 Ω. So, the power consumption of the cancellation signals can be calculated to $V^2_{\mathrm{anti,RMS}}/(50\,\Omega + 50\,\Omega) \approx 93$ mW. This additional power consumption is less than 0.07% of the transfer power of 144 W.

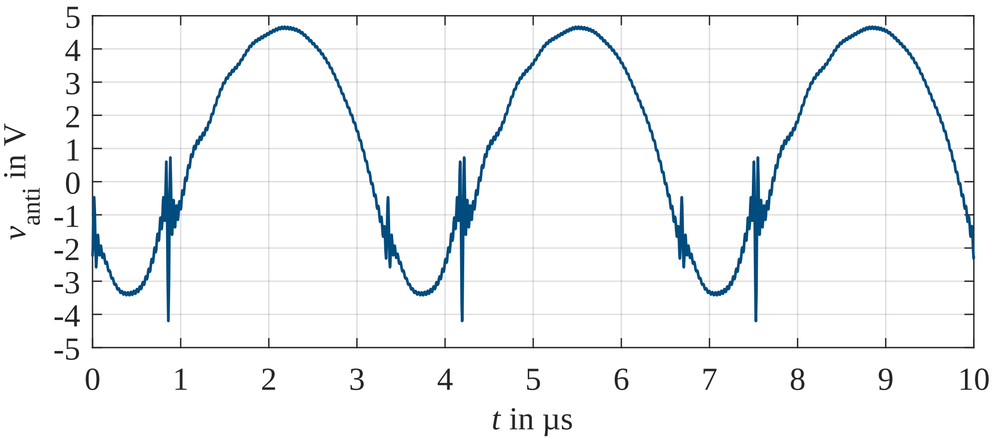

Figure 10.28: Cancellation signal found by the FFT method

10.5 Chapter Summary

In this chapter, a single-port active EMI cancellation system has been designed and demonstrated for a DC-to-DC converter in an automotive test setup. To do so, the complete system has been identified by only three measurements with standard measurement equipment. With adjustments, this method can also be applied to other single-port systems. The information on the identified system has been used to systematically design the cancellation system with all of its analog and digital components. Here, a capacitive coupling has been chosen for the injector and the sensor. The design procedure could also be applied to other injectors and sensors under consideration of the respective impedance requirements.

For demonstration, the FFT method according to Section 6.4 has been applied as optimization algorithm. The fundamental wave is suppressed by 64 dB and the frequencies up to 30 MHz are suppressed by approximately 40 dB. In comparison to the results for AEFs (Table 4.6) and DAEFs (Table 5.2), the proposed cancellation technique shows a very good performance. The power consumption of the cancellation signal is only 0.07 % of the converter's transfer power.

Here, a laboratory test setup has been used to measure, calculate and generate the necessary signals. Obviously, these components cannot be used for commercial applications. For industrialization of this method, different approaches can be pursued. It would be possible to design a cancellation system that is taught by an external trainer. In this case, the oscilloscope and PC can still be used to measure the disturbances and to calculate the cancellation signals. However, the AWG should be realized by simpler hardware consisting of, e.g., memory, microcontroller and DAC. For self-adapting systems, the signal sensing and signal generation must also be done by a cheaper hardware. In this case, a possible hardware could consist of, e.g., ADC, microcontroller and DAC. The rescaling of the oscilloscope could be replicated by programmable attenuators.

11 Systematic Design of an FFT-Based Multi-Port Active EMI Cancellation System

In this chapter, a multi-port active EMI cancellation system is designed for the four supply lines of an isolated DC-to-DC converter. This will be done in analogy to the single-port active EMI cancellation system of Chapter 10. The FFT method will be extended for the application to multi-port systems. The active EMI cancellation system will be realized by three **a**rbitrary **w**aveform **g**enerators (AWGs), a PC and an oscilloscope.

Also here, three steps are required to realize the active EMI cancellation system:

1. Definition of the application and its EMC requirement
2. Identification of the disturbing and disturbed system
3. Design of the cancellation system

11.1 Application and EMC Requirement

The application is an isolated 48 V-to-12 V DC-to-DC converter for, e.g., an automotive application. The relevant schematics and a photograph of the overall test system are depicted in Figure 11.1a and Figure 11.1b, respectively. The inside of the **d**evice **u**nder **t**est (DUT) can be found in Figure 11.2.

The DC-to-DC converter is realized by a GaN evaluation board GS61008P-EVBHF from GaN Systems. The switching frequency f_0 and the duty cycle are set to 1 MHz and 25%, respectively. The load is a 1 Ω resistor. So, the converter transfers a power of approximately 144 W. There is an auxiliary power supply for the driver of the power transistors. The control signal is generated externally by an AWG of the Tektronix AFG3000 series. Since the DC-to-DC converter is isolated from ground, this signal must be passed through a digital isolator.

The inputs and outputs are isolated two-wire systems with DM and CM disturbances (Section 2.4.2). The DM disturbances result from the galvanic coupling of the switching transistors to the input and output ports. The CM disturbances result from a capacitive coupling of the switching node (between the power transistors) to the ground plane.

This DC-to-DC converter is a four-port system due to the four wires isolated from ground. For active EMI cancellation, the DC-to-DC converter requires a combination of decoupler, injector and sensor at the input and output. The DC-to-DC converter and the active cancellation system represent the DUT and will be built into the same shielding case.

The EMI test setup is done in reference to the automotive EMC standard CISPR 25 [4]. The conducted emissions up to a frequency of 30 MHz are evaluated by placing one **a**rtificial **n**etwork (AN) at each input and output line. These ANs represent a standardized impedance

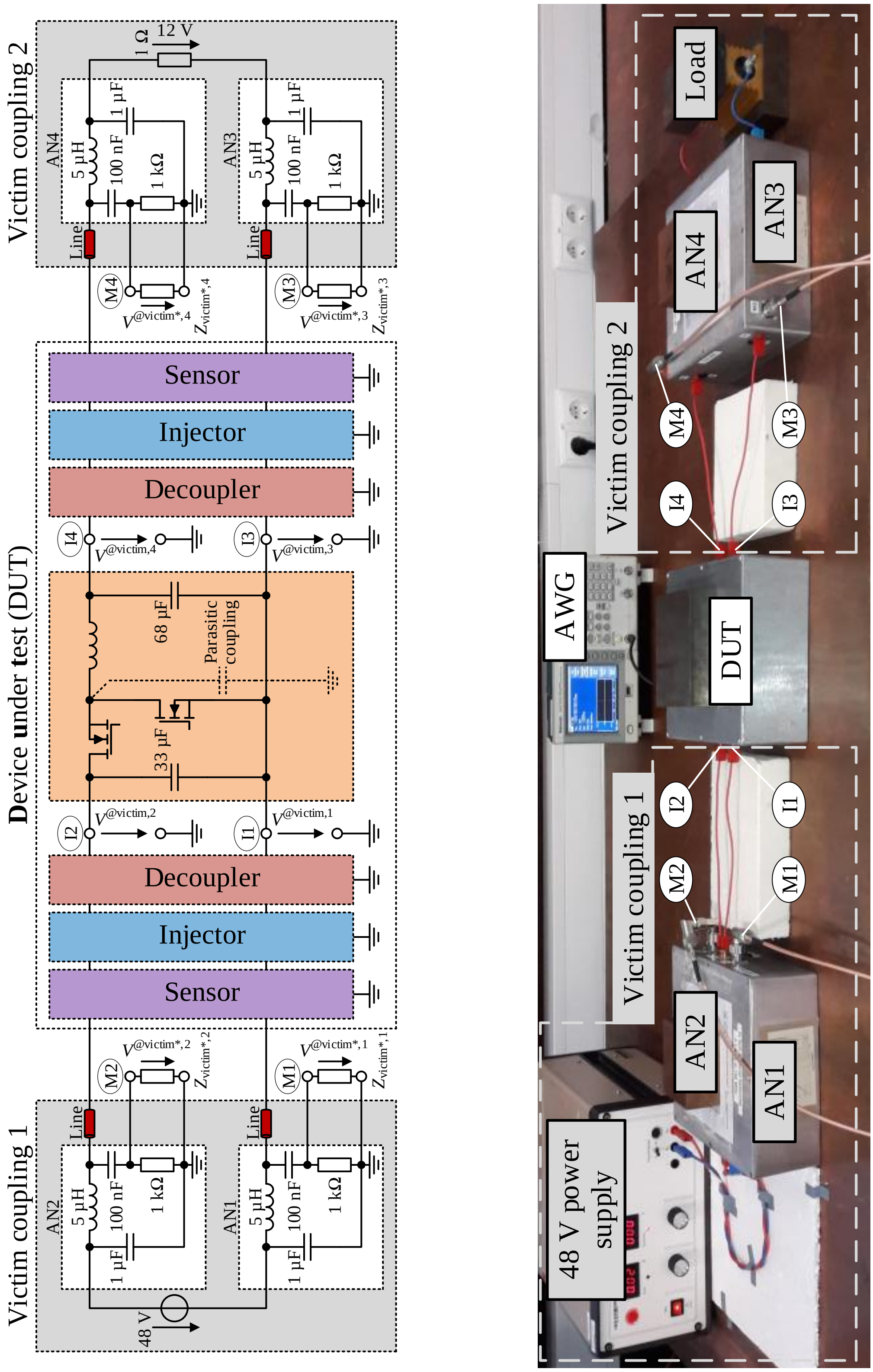

(a) Schematics

(b) Photograph

Figure 11.1: Overall test setup

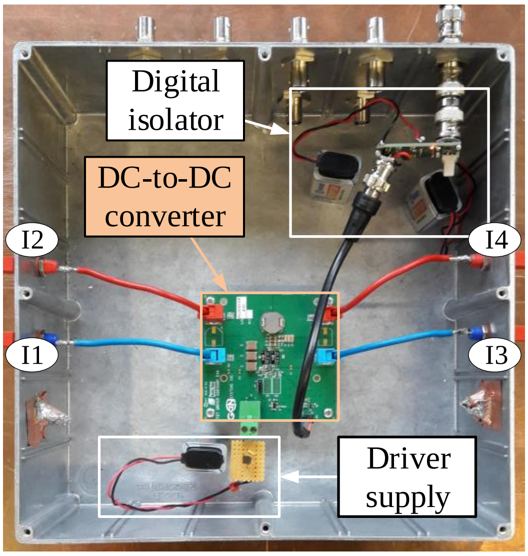

Figure 11.2: Photograph of the inside of the DUT

for the disturbances and also offer ports (denoted by I1, I2, I3 and I4) for standard measurements of $V^{@\text{victim}*,\text{p}}$. These measurements are conducted with an EMI test receiver. According to [4], the resolution bandwidth is set to 9 kHz and the measurement time for each frequency point is at least 50 ms. Its internal resistance of $Z_{\text{victim}*,\text{p}} = 50\ \Omega$ terminates the ANs. The measurements are done one by one for each AN. The ANs without EMI test receiver are terminated by a resistor according to $Z_{\text{victim}*,\text{p}} = 50\ \Omega$. There are short lines between the ANs and the DC-to-DC converter.

Here, two victim couplings are defined. The first is the one of the input comprising the 48 V power supply, the ANs 1 and 2 and the supply lines. This coupling connects the interface ports I1 and I2 with the measurement ports M1 and M2. In analogy, there is a second victim coupling for the output that consists of the ANs 3 and 4, the load and the respective lines. It connects the interface ports I3 and I4 with the measurement ports M3 and M4.

The goal is to suppress the disturbances below the limits of class 5 in the frequency range from 150 kHz to 30 MHz [4]. Due to the periodically repeating EMI, peak- and average-detector lead to basically the same results. However, the average limits are much lower than the peak limits. So, if the average limits are fulfilled, the peak limits are also fulfilled. Therefore, only the average EMI will be evaluated. Considering the frequency range and the switching frequency f_0 of 1 MHz, there will be 30 disturbing harmonics at each of the four ports.

The here used DC-to-DC converter is a rather simple power electronic system. However, the EMI problem is already complex. There are four disturbed ports that are all mutually coupled by the DC-to-DC converter. An active EMI cancellation system will require each four decoupling circuits, injecting circuits, sensing circuits, cancelling sources and sensing sinks. To purposefully design this complex cancellation system, the DC-to-DC converter and the victim couplings must be identified first.

11.2 System Identification

In this section, the overall system is identified. This is done in analogy to the single-port case of Section 10.2. However, due to the multiple ports, the descriptions must be extended. The goal of this identification approach is to find an EMI model according to Figure 11.3.

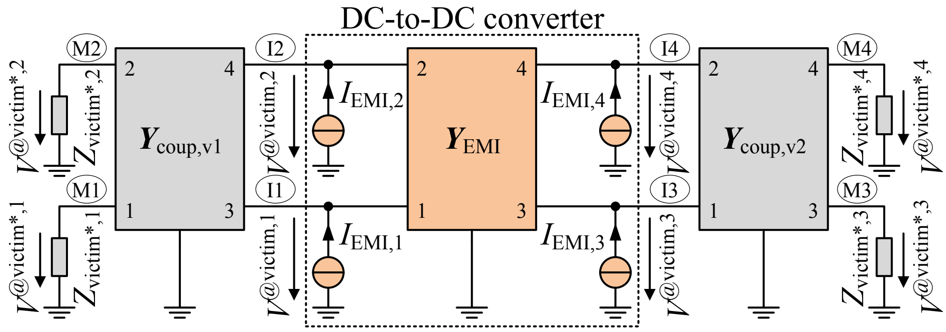

Figure 11.3: Block diagram of the system to be identified

There are fundamentally three blocks. The two 4×4 admittance matrices $\boldsymbol{Y}_{\mathrm{coup,v1}}(f)$ and $\boldsymbol{Y}_{\mathrm{coup,v2}}(f)$ represent the victim couplings. The power electronic system is modeled as a multi-port Norton equivalent with a 4×4 admittance matrix $\boldsymbol{Y}_{\mathrm{EMI}}(f)$ and four current sources $\vec{I}_{\mathrm{EMI}}(f)$. Here, a Norton equivalent is chosen since it is more convenient for the nodal analysis that is done later (same explanation as in Section 3.1.2.a)). In the following, the unknowns $\boldsymbol{Y}_{\mathrm{coup,v1}}(f)$, $\boldsymbol{Y}_{\mathrm{coup,v2}}(f)$, $\boldsymbol{Y}_{\mathrm{EMI}}(f)$ and $\vec{I}_{\mathrm{EMI}}(f)$ are identified for the laboratory system. This is basically done by the same steps as in Section 10.2:

1. Identification of the EMI victim couplings $\boldsymbol{Y}_{\mathrm{coup,v1}}(f)$ and $\boldsymbol{Y}_{\mathrm{coup,v2}}(f)$ by a VNA measurement
2. Identification of the EMI source's equivalent admittance $\boldsymbol{Y}_{\mathrm{EMI}}(f)$ by another VNA measurement and de-embedding
3. Identification of the EMI source's equivalent current sources $\vec{I}_{\mathrm{EMI}}(f)$ by an oscilloscope measurement and a short calculation

The VNA measurements are done with a ZNB 8 from Rohde & Schwarz that is calibrated by using a calibration unit ZN-Z154 from Rohde & Schwarz. The oscilloscope is an HDO6104A from Teledyne LeCroy.

11.2.1 Step 1: Identification of the EMI Victim Couplings

In the first step, $\boldsymbol{Y}_{\mathrm{coup,v1}}(f)$ and $\boldsymbol{Y}_{\mathrm{coup,v2}}(f)$ are identified by using a VNA. The setup is depicted in Figure 11.4. Since only the victim couplings are identified in this step, the DUT is removed.

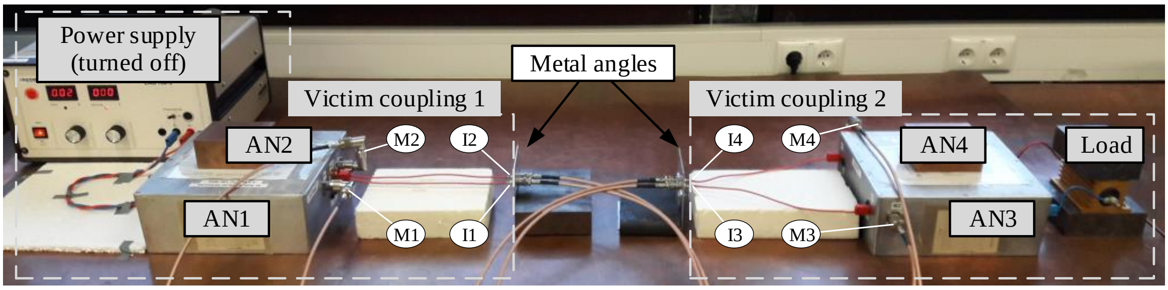

Figure 11.4: Photograph of the test setup for identification of the victim couplings $\boldsymbol{Y}_{\text{coup,v1}}(f)$ and $\boldsymbol{Y}_{\text{coup,v2}}(f)$

The first victim coupling consists of the (turned off) power supply, the first two ANs and the wires for the connection of the DUT. The second victim coupling consists of the load, the last two ANs and the wires for connection. Both of these couplings are identified by one individual four-port measurement. The measurement ports (M1, M2, M3, M4) of the ANs are well suited for the VNA measurement. The measurement at the wires for the DUT is not that easy since a clear ground reference is missing. To resolve this issue, metal angles are applied. By doing so, there are well-defined measurement ports (I1, I2, I3, I4).

The first 4×4 scattering matrix $\boldsymbol{S}_{\text{coup,v1}}(f)$ is found by applying the VNA to the ports M1, M2, I1 and I2. The second 4×4 scattering matrix $\boldsymbol{S}_{\text{coup,v2}}(f)$ is found by applying the VNA to the ports I3, I4, M3 and M4. These matrices can be transferred to the 4×4 admittance matrices $\boldsymbol{Y}_{\text{coup,v1}}(f)$ and $\boldsymbol{Y}_{\text{coup,v2}}(f)$ by, e.g., using the RF Toolbox of MATLAB.

11.2.2 Step 2: Identification of the EMI Source's Equivalent Admittance by VNA Measurement

Next, the admittance matrix $\boldsymbol{Y}_{\text{EMI}}(f)$ of the DC-to-DC converter must be identified. This is no trivial task since the DC-to-DC converter has no dedicated measurement ports. It is necessary to use some form of fixture that must be de-embedded after measurement. Since the victim couplings are already identified, they are convenient fixtures. So, the overall test setup of Figure 11.1b is used for measurement. The power supply and the control signal of the DC-to-DC converter are turned off for this measurement.

The VNA is connected to the measurement ports of the four ANs (M1, M2, M3, M4). By doing so, the 4×4 scattering matrix of the complete system $\boldsymbol{S}_{\text{total}}(f)$ can be determined. By de-embedding the scattering matrices $\boldsymbol{S}_{\text{coup,v1}}(f)$ and $\boldsymbol{S}_{\text{coup,v2}}(f)$ of the victim couplings, the scattering matrix of the converter $\boldsymbol{S}_{\text{EMI}}(f)$ can be calculated. This can be done by using, e.g., the function "deembedsparams" of the RF Toolbox of MATLAB. This scattering matrix is transferred to the admittance matrix $\boldsymbol{Y}_{\text{EMI}}(f)$.

11.2.3 Step 3: Identification of the EMI Source's Equivalent Current Sources by Oscilloscope Measurement

Last, the short-circuit currents $\vec{I}_{\text{EMI}}(f)$ must be determined. Since these sources are only virtual, they cannot be directly measured in the laboratory system. However, the effect of these current sources can be measured at the measurement ports of the ANs $\vec{V}_{\text{EMI}}^{\text{@victim*}}$ (note Figure 11.3). Since the admittance matrices $\boldsymbol{Y}_{\text{coup,v1}}(f)$, $\boldsymbol{Y}_{\text{coup,v2}}(f)$, $\boldsymbol{Y}_{\text{EMI}}(f)$ are known, the short-circuit currents $\vec{I}_{\text{EMI}}(f)$ can be calculated. This is done in reference to [114]. The complete system is described by a nodal analysis according to (11.1):

$$\begin{pmatrix} \vec{I}_{\text{EMI}} \\ \vec{0} \end{pmatrix} = \begin{bmatrix} \boldsymbol{Y}_{\text{A}} & \boldsymbol{Y}_{\text{B}} \\ \boldsymbol{Y}_{\text{C}} & \boldsymbol{Y}_{\text{D}} \end{bmatrix} \cdot \begin{pmatrix} \vec{V}_{\text{EMI}}^{\text{@victim}} \\ \vec{V}_{\text{EMI}}^{\text{@victim*}} \end{pmatrix} \tag{11.1}$$

The matrices $\boldsymbol{Y}_{\text{A}}(f)$, $\boldsymbol{Y}_{\text{B}}(f)$, $\boldsymbol{Y}_{\text{C}}(f)$ and $\boldsymbol{Y}_{\text{D}}(f)$ according to (11.2)-(11.5) are introduced for later use:

$$\boldsymbol{Y}_{\text{A}} = \begin{bmatrix} Y_{\text{EMI},1,1} + Y_{\text{coup,v1},3,3} & Y_{\text{EMI},1,2} + Y_{\text{coup,v1},3,4} & Y_{\text{EMI},1,3} & Y_{\text{EMI},1,4} \\ Y_{\text{EMI},2,1} + Y_{\text{coup,v1},4,3} & Y_{\text{EMI},2,2} + Y_{\text{coup,v1},4,4} & Y_{\text{EMI},2,3} & Y_{\text{EMI},2,4} \\ Y_{\text{EMI},3,1} & Y_{\text{EMI},3,2} & Y_{\text{EMI},3,3} + Y_{\text{coup,v2},1,1} & Y_{\text{EMI},3,4} + Y_{\text{coup,v2},1,2} \\ Y_{\text{EMI},4,1} & Y_{\text{EMI},4,2} & Y_{\text{EMI},4,3} + Y_{\text{coup,v2},2,1} & Y_{\text{EMI},4,4} + Y_{\text{coup,v2},2,2} \end{bmatrix} \tag{11.2}$$

$$\boldsymbol{Y}_{\text{B}} = \begin{bmatrix} Y_{\text{coup,v1},3,1} & Y_{\text{coup,v1},3,2} & 0 & 0 \\ Y_{\text{coup,v1},4,1} & Y_{\text{coup,v1},4,2} & 0 & 0 \\ 0 & 0 & Y_{\text{coup,v2},1,3} & Y_{\text{coup,v2},1,4} \\ 0 & 0 & Y_{\text{coup,v2},2,3} & Y_{\text{coup,v2},2,4} \end{bmatrix} \tag{11.3}$$

$$\boldsymbol{Y}_{\text{C}} = \begin{bmatrix} Y_{\text{coup,v1},1,3} & Y_{\text{coup,v1},1,4} & 0 & 0 \\ Y_{\text{coup,v1},2,3} & Y_{\text{coup,v1},2,4} & 0 & 0 \\ 0 & 0 & Y_{\text{coup,v2},3,1} & Y_{\text{coup,v2},3,2} \\ 0 & 0 & Y_{\text{coup,v2},4,1} & Y_{\text{coup,v2},4,2} \end{bmatrix} \tag{11.4}$$

$$\boldsymbol{Y}_{\text{D}} = \begin{bmatrix} Y_{\text{coup,v1},1,1} + Y_{\text{victim*},1} & Y_{\text{coup,v1},1,2} & 0 & 0 \\ Y_{\text{coup,v1},2,1} & Y_{\text{coup,v1},2,2} + Y_{\text{victim*},2} & 0 & 0 \\ 0 & 0 & Y_{\text{coup,v2},3,3} + Y_{\text{victim*},3} & Y_{\text{coup,v2},3,4} \\ 0 & 0 & Y_{\text{coup,v2},4,3} & Y_{\text{coup,v2},4,4} + Y_{\text{victim*},4} \end{bmatrix} \tag{11.5}$$

The second equation of (11.1) leads to (11.6) and (11.7):

$$\overset{(11.1)}{\Rightarrow} \vec{0} = \boldsymbol{Y}_{\text{C}} \cdot \vec{V}_{\text{EMI}}^{\text{@victim}} + \boldsymbol{Y}_{\text{D}} \cdot \vec{V}_{\text{EMI}}^{\text{@victim*}} \tag{11.6}$$

$$\Rightarrow \vec{V}_{\text{EMI}}^{\text{@victim}} = -\boldsymbol{Y}_{\text{C}}^{-1} \cdot \boldsymbol{Y}_{\text{D}} \cdot \vec{V}_{\text{EMI}}^{\text{@victim*}} \tag{11.7}$$

The first equation of (11.1) and (11.7) result in the short-circuit currents $\vec{I}_{\text{EMI}}(f)$ according to (11.8):

$$\overset{(11.1)}{\Rightarrow} \vec{I}_{\text{EMI}} = \boldsymbol{Y}_{\text{A}} \cdot \vec{V}_{\text{EMI}}^{\text{@victim}} + \boldsymbol{Y}_{\text{B}} \cdot \vec{V}_{\text{EMI}}^{\text{@victim*}} \overset{(11.7)}{=} \left(\boldsymbol{Y}_{\text{B}} - \boldsymbol{Y}_{\text{A}} \cdot \boldsymbol{Y}_{\text{C}}^{-1} \cdot \boldsymbol{Y}_{\text{D}}\right) \cdot \vec{V}_{\text{EMI}}^{\text{@victim*}} \tag{11.8}$$

Since the matrices $\boldsymbol{Y}_{\text{A}}(f)$, $\boldsymbol{Y}_{\text{B}}(f)$, $\boldsymbol{Y}_{\text{C}}(f)$ and $\boldsymbol{Y}_{\text{D}}(f)$ are already determined, only the voltages $\vec{V}_{\mathrm{EMI}}^{@\mathrm{victim}*}(f)$ must be found for the activated DC-to-DC converter. To do so, the power supply is set to 48 V and the control signal is activated. The resulting time-domain voltages $\vec{v}_{\mathrm{EMI}}^{@\mathrm{victim}*}(t)$ at the measurement ports of the ANs are measured by an oscilloscope with terminations $Z_{\mathrm{victim}*,\mathrm{p}}$ of 50 Ω. The spectra $\vec{V}_{\mathrm{EMI}}^{@\mathrm{victim}}(kf_0)$ are found by applying an FFT. These original EMI signals (in RMS values) are depicted in Figure 11.5. The disturbances are far above the class 5 limit of CISPR 25 [4] and must be reduced by up to 62 dB. The spectra of the short-circuit currents $\vec{I}_{\mathrm{EMI}}(kf_0)$ result from (11.8).

By finishing this step, the complete system according to Figure 11.3 is identified. In the following, this model is used to design the cancellation system.

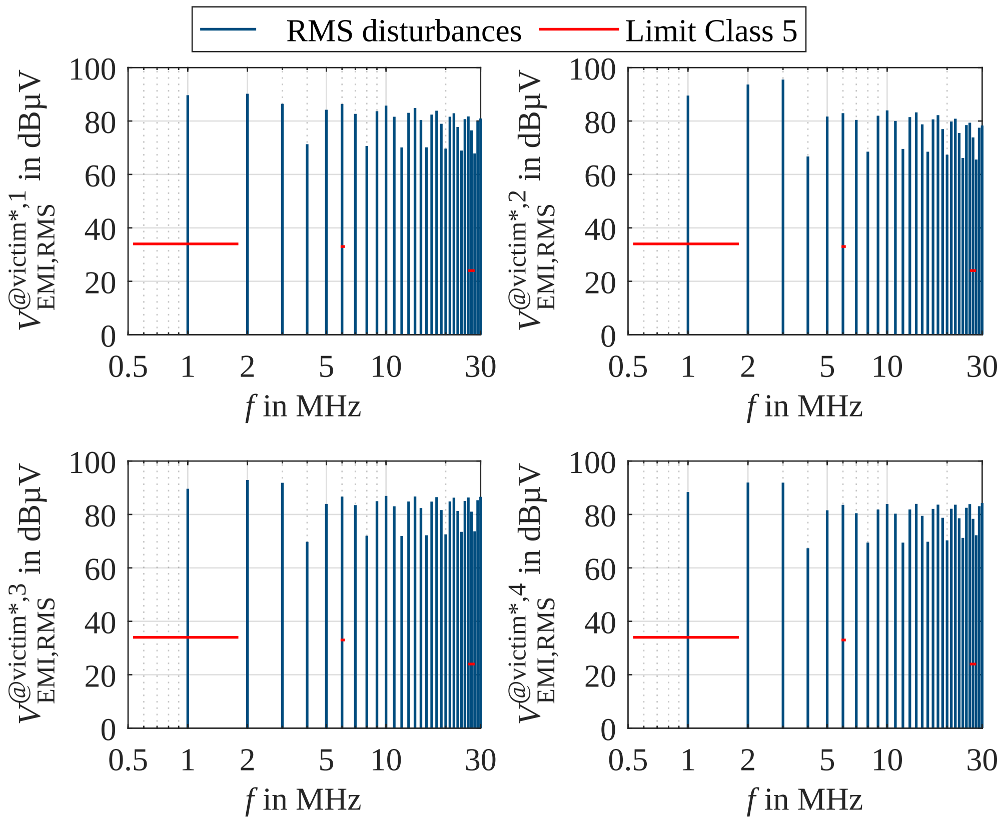

Figure 11.5: Original disturbances at the ANs $\vec{V}_{\mathrm{EMI,RMS}}^{@\mathrm{victim}*}(kf_0)$ vs. required limits (all in RMS values)

11.3 Design of the Active EMI Cancellation System

In this section, the active EMI cancellation system is designed. Like for the single-port case of Section 10.3.1, the injector is designed first.

11.3.1 Design of the Injector

In this section, the injector for a four-port cancellation system is designed. Since all cancellation sources can potentially be coupled to each other, this is a challenging task. The required steps are basically the same as in the single-port case of Section 10.3.1. However, they must be extended for the multi-port case. This is done for the given example in the following.

Here, two additional AWGs of the Tektronix AFG3000 series are used to generate the four cancellation signals. The symmetric voltage range of the internal DACs is at least ± 5 V with a resolution of 14 bits. The AWGs have an analog bandwidth of at least 100 MHz. The internal impedance is $Z_{\mathrm{anti,p}} = 50\ \Omega$.

a) Step 1: Selection of the Injecting Circuit

In this demonstration, one capacitive injector is applied to each interface port. Although voltage sources are used instead of current sources, the injector fulfills the same purpose as described in Section 4.4.2.a). According to Section 4.4.2.a) such an injector requires a decoupling inductance between the injection point and the EMI source. The resulting schematics can be found in Figure 11.6. There are the elements $C_{\mathrm{inj,p}}$, $L_{\mathrm{dec,p}}$ and $Z_{\mathrm{anti,p}}$ that must be defined for each interface port p. In this setup, each cancellation source p should be predominantly coupled to its respective interface port p. The source's equivalent admittance $\boldsymbol{Y}_{\mathrm{EMI}}(kf_0)$ may potentially couple all injectors to all interface ports. To avoid unintended couplings, the dimensioning of the decoupling elements is very important.

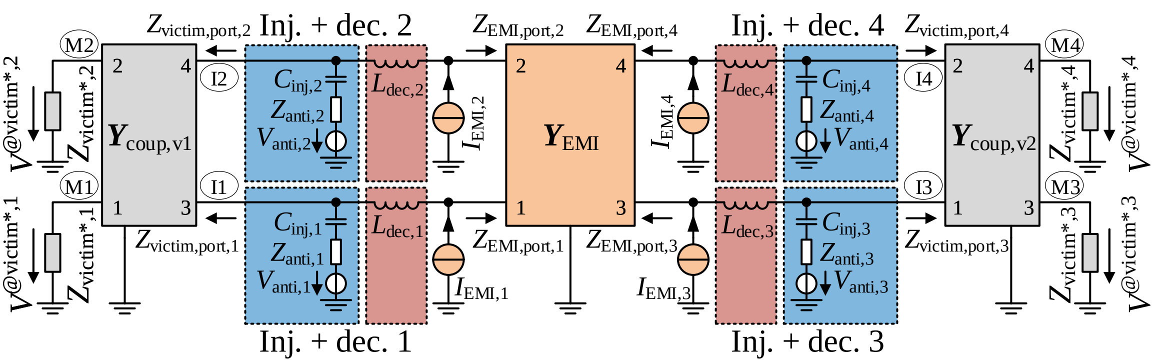

Figure 11.6: Schematic of the overall system with the injecting and decoupling circuits included

The impedances $Z_{\mathrm{EMI,port,p}}(kf_0)$ and $Z_{\mathrm{victim,port,p}}(kf_0)$ are the ones seen into the respective subsystem from the port p. These can be calculated by considering the reflexion coefficient that is represented by the diagonal elements of the scattering matrices. It must be noted that this calculation assumes that all ports are terminated by $Z_0 = 50\ \Omega$. While this is true for the measurement impedances $Z_{\mathrm{victim*}}(f)$, it does actually not apply for the ports at which the injectors are connected. Nevertheless, this simplified calculation can be done as a first approximation. So, the impedances $Z_{\mathrm{EMI,port,p}}(kf_0)$ can be calculated by (11.9). The impedances $Z_{\mathrm{EMI,port,p}}(kf_0)$ are all very similar to each other. In analogy, the impedances $Z_{\mathrm{victim,port,p}}(kf_0)$ are calculated by using (11.10)-(11.13). Also the elements $Z_{\mathrm{victim,port,p}}(kf_0)$

are very similar.

$$Z_{\mathrm{EMI,port,p}}(kf_0) = Z_0 \cdot \frac{1+S_{\mathrm{EMI,p,p}}(kf_0)}{1-S_{\mathrm{EMI,p,p}}(kf_0)} \tag{11.9}$$

$$Z_{\mathrm{victim,port,1}}(kf_0) = Z_0 \cdot \frac{1+S_{\mathrm{coup,v1,3,3}}(kf_0)}{1-S_{\mathrm{coup,v1,3,3}}(kf_0)} \tag{11.10}$$

$$Z_{\mathrm{victim,port,2}}(kf_0) = Z_0 \cdot \frac{1+S_{\mathrm{coup,v1,4,4}}(kf_0)}{1-S_{\mathrm{coup,v1,4,4}}(kf_0)} \tag{11.11}$$

$$Z_{\mathrm{victim,port,3}}(kf_0) = Z_0 \cdot \frac{1+S_{\mathrm{coup,v2,1,1}}(kf_0)}{1-S_{\mathrm{coup,v2,1,1}}(kf_0)} \tag{11.12}$$

$$Z_{\mathrm{victim,port,4}}(kf_0) = Z_0 \cdot \frac{1+S_{\mathrm{coup,v2,2,2}}(kf_0)}{1-S_{\mathrm{coup,v2,2,2}}(kf_0)} \tag{11.13}$$

b) Step 2: Dimensioning of the Decoupling Element

Since the DC-to-DC converter potentially couples all injectors to each interface port, they must be decoupled by a sufficiently large inductance. To achieve that at least 50% of the injected current acts at the intended interface port, the relationship of (11.14) must be fulfilled for each port p:

$$\left|Z_{\mathrm{EMI,port,p}}(kf_0) + j2\pi kf_0 \cdot L_{\mathrm{dec,p}}\right| \overset{!}{\geq} \left|Z_{\mathrm{victim,port,p}}(kf_0)\right| \tag{11.14}$$

Since all ports show nearly the same impedance, only the first ($p = 1$) is considered. To find the right value for the decoupling inductance $L_{\mathrm{dec,p}}$, different values are assumed. The frequency-dependent impedances can be found in Figure 11.7.

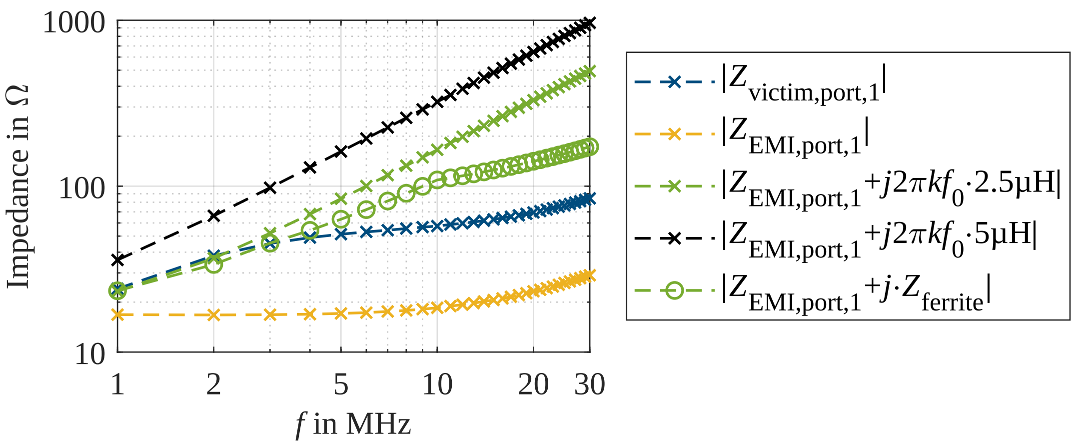

Figure 11.7: Comparison of impedances for different values $L_{\mathrm{dec,p}}$ of the decoupling inductances

Without decoupling inductor, the victim impedance is larger than the source impedance. Considering the current divider, most current would flow towards the source and not support the active EMI cancellation at the victim. For an inductance value of 2.5 µH, the impedances are basically the same for the first few harmonics. For higher harmonics, the combined source impedance becomes larger. For an inductance of 5 µH, the combined source impedance is larger than the victim impedance for the complete considered frequency range. For demonstration, a split core ferrite NiZn 74271733 from Würth Elektronik is chosen that has an inductance of approximately 2.5 µH at 1 MHz for one turn [115]. By extracting the impedance values $Z_{\text{ferrite}}(kf_0)$ from the data sheet [115], the combined source impedance can be calculated (Figure 11.7). The resulting impedance may be slightly too low for the first two harmonics, but this effect is assumed to be negligible. One of these ferrites will be used for each of the four decoupling circuits.

c) Step 3: Dimensioning of the Coupling Element

The coupling capacitor should have such a large value that it causes only a small voltage drop for the cancellation signal. For calculation, the total impedance $Z_{\text{total,port,p}}(kf_0)$ is introduced that is seen by each injector into the overall system. So, it is defined by the parallel connection of $Z_{\text{victim,port,p}}$ and $\left(Z_{\text{EMI,port,p}} + j \cdot Z_{\text{ferrite}}(kf_0)\right)$ according to (11.15):

$$Z_{\text{total,port,p}}(kf_0) = \frac{\left(Z_{\text{EMI,port,p}}(kf_0) + j \cdot Z_{\text{ferrite}}(kf_0)\right) \cdot Z_{\text{victim,port,p}}(kf_0)}{Z_{\text{EMI,port,p}}(kf_0) + j \cdot Z_{\text{ferrite}}(kf_0) + Z_{\text{victim,port,p}}(kf_0)} \tag{11.15}$$

To have only a small voltage drop over the capacitive coupling element $C_{\text{inj,p}}(kf_0)$, its impedance should be much smaller than the one of $\left|Z_{\text{total,p}}(kf_0)\right|$ according to (11.16):

$$\left|\frac{1}{j2\pi kf_0 \cdot C_{\text{inj,p}}}\right| = \frac{1}{2\pi kf_0 \cdot C_{\text{inj,p}}} \overset{!}{\ll} \left|Z_{\text{total,port,p}}(kf_0)\right| \tag{11.16}$$

In Figure 11.8, the relationship of (11.16) is investigated for different values of the coupling capacitance $C_{\text{inj,p}}$. Here, a 100 nF capacitor is chosen.

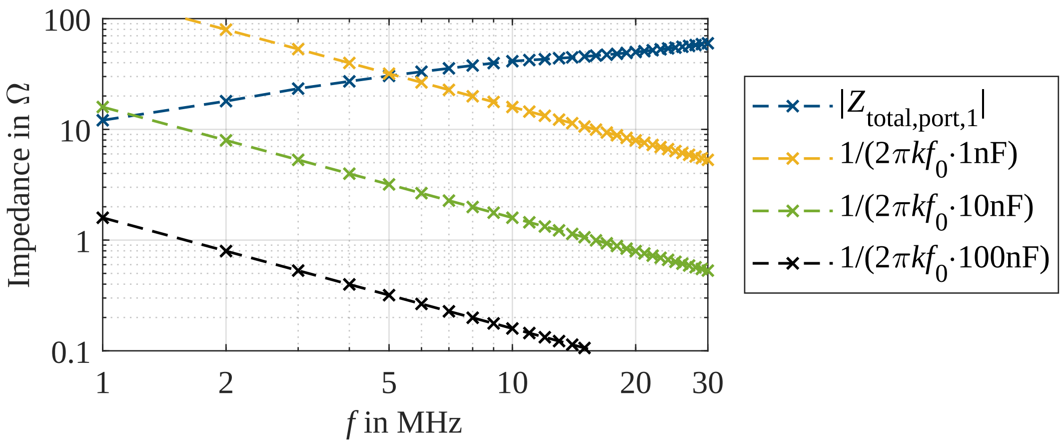

Figure 11.8: Comparison of impedances for different values $C_{\text{inj,p}}$ of the coupling capacitances

The resulting system can be found in Figure 11.9. The coupling capacitors are connected to the wires and to the inner conductor of BNC cables. These cables are connected to BNC feedthroughs in the shielding enclose. The AWGs for the generation of the cancellation signals will be connected to these ports. This connection introduces a parasitic series inductance for the coupling path. By measurements, it has been found that this value is in the range of 250 nH. In the photograph, nine BNC cables can be found. One is for the control of the DC-to-DC converter and four are for the cancellation signals. The last four will be used for the sensors. The coupling capacitors of the sensors may also be seen under very close inspection of the photograph, but they are not connected to the wires yet.

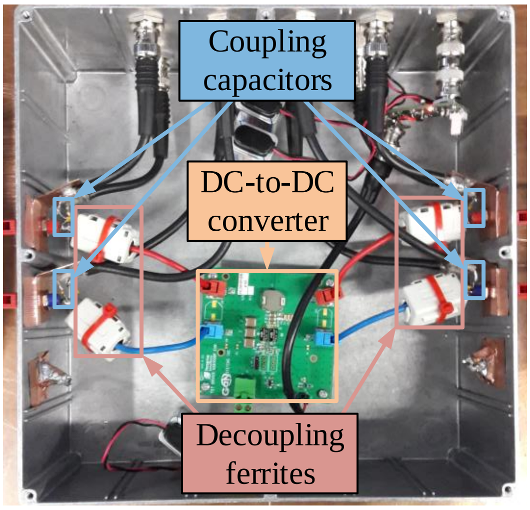

Figure 11.9: Photograph of the DUT with installed decoupling and coupling elements

d) Step 4: Calculation of the Required Cancellation Source Impedance

In general, the cancellation source impedance $|Z_{\mathrm{anti}}(kf_0)|$ should be much smaller than $|Z_{\mathrm{total}}(kf_0)|$ for a small insertion loss. Here, $Z_{\mathrm{anti}}(kf_0)$ equals 50 Ω due to the application of AWGs as cancellation sources. Considering $|Z_{\mathrm{total}}(kf_0)|$ in Figure 11.8, this value is actually too high. In the following, it will be checked if the AWGs' internal voltage range of ±5 V is still sufficient. In this case, the high cancellation source impedance is no issue.

e) Step 5: Estimation of the Required Cancellation Signal

For the next steps, the cancellation signal $V_{\mathrm{anti}}(kf_0)$ must be estimated. In general, the EMI at the interface ports must be suppressed to ensure that the DUT emits no EMI. In this demonstration, the calculation is referred to the ANs. This is viable since the ANs are closely coupled to the respective interface port. By doing so, the calculations can be verified by measurements.

In analogy to (3.27), the superposition of EMI and anti-EMI at the measurement ports of the ANs $V_{\text{res}}^{@\text{victim*}}(kf_0)$ can be calculated by (11.17):

$$\overset{(3.27)}{\Rightarrow} \vec{V}_{\text{res}}^{@\text{victim*}}(kf_0) = \underbrace{\boldsymbol{H}_{\text{EMI}}^{\rightarrow\text{victim*}}(kf_0)\cdot\vec{I}_{\text{EMI}}(kf_0)}_{=\vec{V}_{\text{EMI}}^{@\text{victim*}}(kf_0)} + \underbrace{\boldsymbol{H}_{\text{anti}}^{\rightarrow\text{victim*}}(kf_0)\cdot\vec{V}_{\text{anti}}(kf_0)}_{=\vec{V}_{\text{anti}}^{@\text{victim*}}(kf_0)} \quad (11.17)$$

With the requirement of $\vec{V}_{\text{res}}^{@\text{victim*}}(kf_0) \overset{!}{=} \vec{0}$, the necessary cancellation signals can be calculated by (11.18):

$$\overset{(11.17)}{\Rightarrow} \vec{V}_{\text{anti}}(kf_0) = -\boldsymbol{H}_{\text{anti}}^{\rightarrow\text{victim*}-1}(kf_0)\cdot\boldsymbol{H}_{\text{EMI}}^{\rightarrow\text{victim*}}(kf_0)\cdot\vec{I}_{\text{EMI}}(kf_0) \quad (11.18)$$

Since all elements are known, the transfer matrices can be found by calculations or simulations. For the sake of convenience, the transfer matrices $\boldsymbol{H}_{\text{EMI}}^{\rightarrow\text{victim*}}(kf_0)$ and $\boldsymbol{H}_{\text{anti}}^{\rightarrow\text{victim*}}(kf_0)$ are determined by an AC simulation in the **Q**uite **U**niversal **C**ircuit **S**imulator (Qucs) for the complete system of Figure 11.6. To do so, the measured 4×4 coupling matrices $\boldsymbol{Y}_{\text{EMI}}(kf_0)$ and $\boldsymbol{Y}_{\text{victim}}(kf_0)$ are converted to scattering matrices and imported. The split core ferrite has been characterized by a two-port VNA measurement and the results are also imported in Qucs. The coupling capacitor with $C_{\text{inj,p}} = 100$ nF, the internal impedance of the AWGs $Z_{\text{anti,p}} = 50\ \Omega$ and the parasitic inductance of 250 nH are respected. The EMI and anti-EMI sources are added. To identify $\boldsymbol{H}_{\text{EMI}}^{\rightarrow\text{victim*}}(kf_0)$, an arbitrary signal is injected by one EMI source at a time and the response at all victims is evaluated. The same is done for $\boldsymbol{H}_{\text{anti}}^{\rightarrow\text{victim*}}(kf_0)$ by the cancelling sources. The EMI at the AN measurement ports $\vec{V}_{\text{EMI}}^{@\text{victim*}}(kf_0)$ can be calculated by (11.19):

$$\vec{V}_{\text{EMI}}^{@\text{victim*}}(kf_0) = \boldsymbol{H}_{\text{EMI}}^{\rightarrow\text{victim*}}(kf_0)\cdot\vec{I}_{\text{EMI}}(kf_0) \quad (11.19)$$

The result can be found in Figure 11.10. To verify the calculation, the EMI is also measured at the AN measurement ports. The comparison of these spectra shows a very high conformity. The slight deviation may be due to nonlinear effects (e.g. of the decoupling inductors that may show saturation effects due to the relatively high operating currents) or an imperfect de-embedding. Comparing the measurements with and without deactivated injector in Figure 11.10, the passive attenuation can be found. There is almost no passive EMI reduction for the first harmonic. For higher harmonics, the attenuation rises up to 10 dB. So, most of the EMI reduction must be achieved by the active system. The time-domain signals for the first 30 harmonics are calculated by (2.8). These can be found in Figure 11.11. Also the time-domain signals show a very high conformity between measurement and calculation. It can be seen that the deactivated injectors mostly attenuate the higher harmonics since only the spikes are significantly reduced.

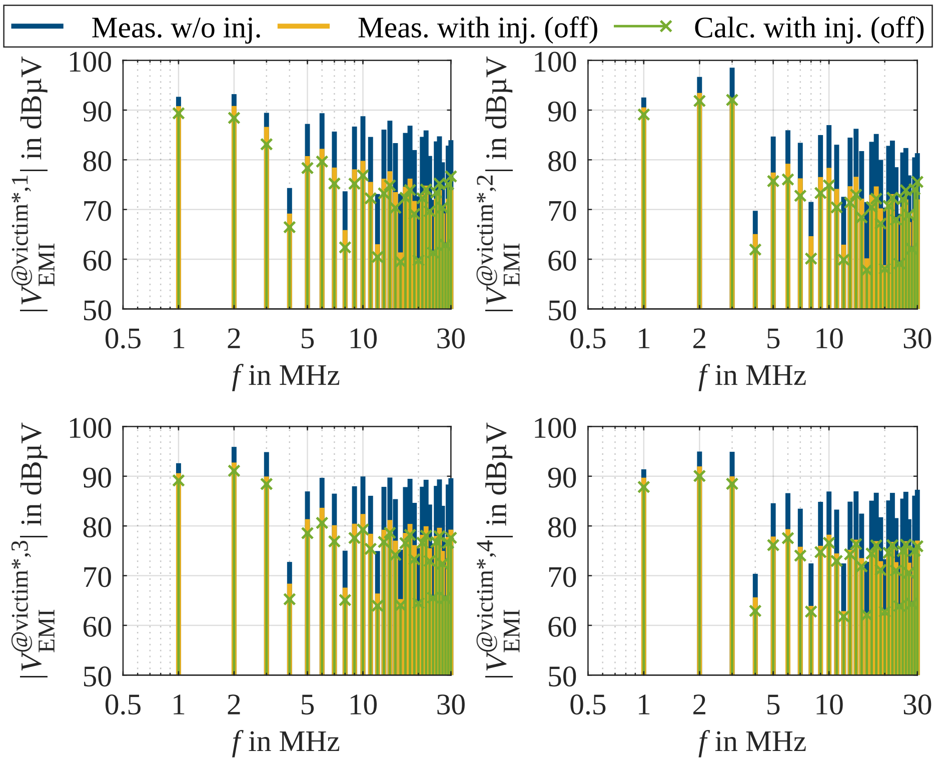

Figure 11.10: EMI spectra at the measurement ports of the ANs without and with deactivated injector, also: comparison of measurement and calculation

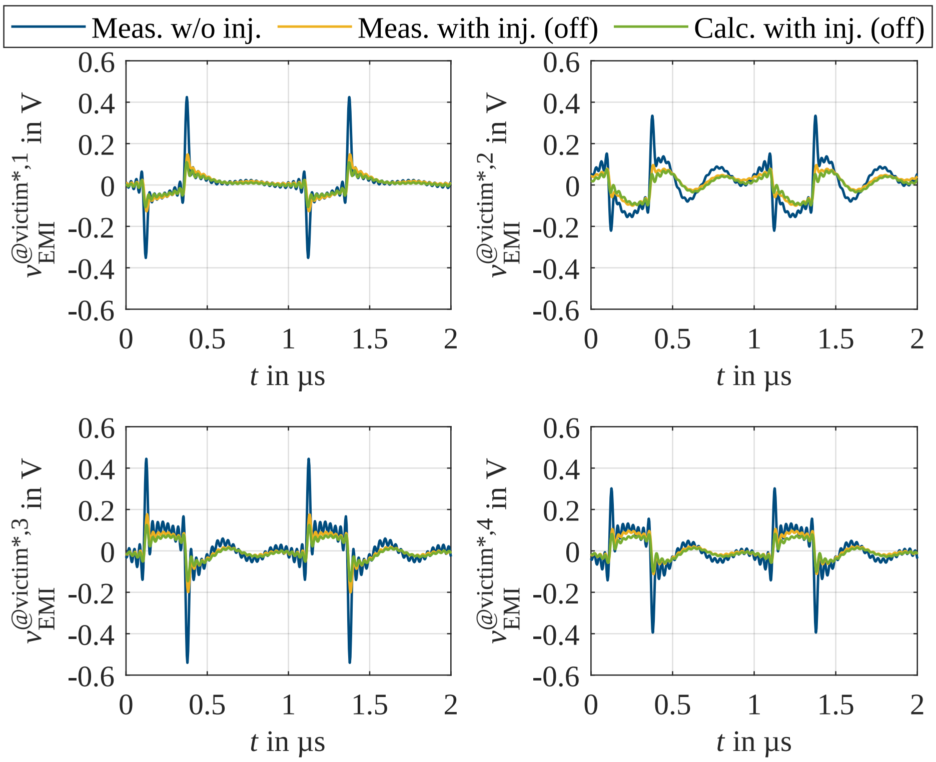

Figure 11.11: EMI signals at the measurement ports of the ANs without and with deactivated injector, also: comparison of measurement and calculation

Before calculating the necessary cancellation signals, the calculated transfer matrix $\boldsymbol{H}_{\text{anti}}^{\rightarrow\text{victim*}}(kf_0)$ is verified by measurements. To do so, the first column of the transfer matrix is measured by four individual two-port measurements with a VNA (with deactivated DC-to-DC converter). A comparison between the measured and calculated transfer functions can be found in Figure 11.12. The calculation is verified by the very high conformity between the magnitudes. Furthermore, it can be found that there is a successful decoupling between the ports since there is a difference of at least 10 dB between the intended coupling path $H_{\text{anti},1}^{\rightarrow\text{victim*},1}(kf_0)$ and the other ones.

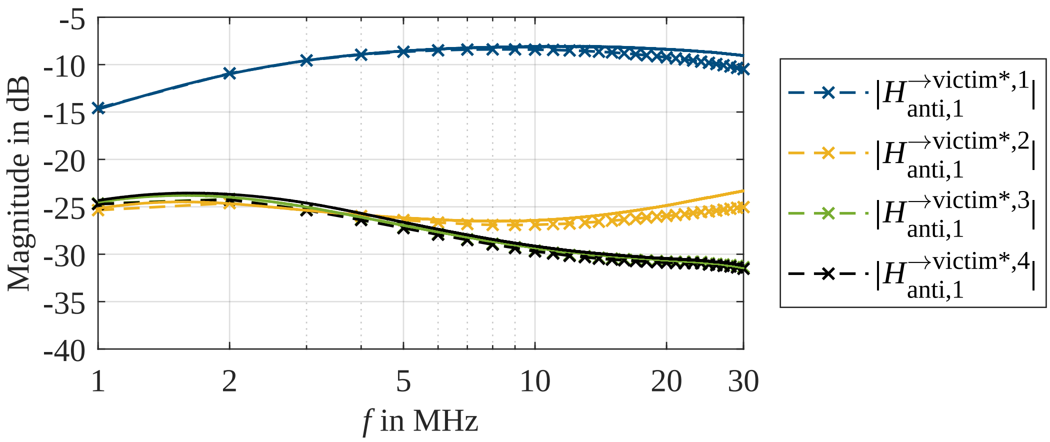

Figure 11.12: Transfer functions from the first injector to all four measurement ports of the ANs (with marker: calculation, without marker: measurement)

Since $\vec{V}_{\text{EMI}}^{@\text{victim*}}(kf_0)$ and $\boldsymbol{H}_{\text{anti}}^{\rightarrow\text{victim*}}(kf_0)$ have been found very precisely, it can be expected that the cancellation signals $\vec{V}_{\text{anti}}(kf_0)$ calculated by (11.20) will be close to the ones actually necessary:

$$\vec{V}_{\text{anti}}(kf_0) = -\boldsymbol{H}_{\text{anti}}^{\rightarrow\text{victim*}-1}(kf_0) \cdot \vec{V}_{\text{EMI}}^{@\text{victim*}}(kf_0) \tag{11.20}$$

These harmonics are transferred into time domain by (2.8). The result is presented in Figure 11.13. These are the signals that must be injected to eliminate the EMI of Figure 11.11. Since the signals are between the ±5 V voltage ranges of the AWGs, the internal impedances $Z_{\text{anti,p}}$ of 50 Ω are no issue.

f) Step 6: Adjustment of the DAC Voltage Range

In this step, the voltage ranges of the injectors are adjusted. To do so, the cancellation signals are symmetrized around 0 V by applying (10.23). The symmetric signals can be found in Figure 11.14. The maximum values of the signals are determined to 0.38 V, 0.56 V, 0.52 V and 0.47 V, respectively. Considering the ±5 V voltage ranges of the here used AWGs, they will only be used by 7.6%, 11.2%, 10.4% and 9.4%, respectively. Without any further measures, most of the available voltage range (and a significant portion of the resolution) would remain unused. To resolve this issue, the transfer matrix $\boldsymbol{H}_{\text{anti}}^{\rightarrow\text{victim*}}(kf_0)$ must be attenuated. This is done by introducing 50 Ω attenuators between the AWGs and the coupling capacitors. The goal is to utilize the DACs of the AWGs by 50%. Furthermore, it is chosen to use the same attenuation value for all injectors. Considering the highest signal of 0.56 V, the transfer matrix must be weakened by a factor of 4.5. So, an attenuation of approximately 13 dB is necessary.

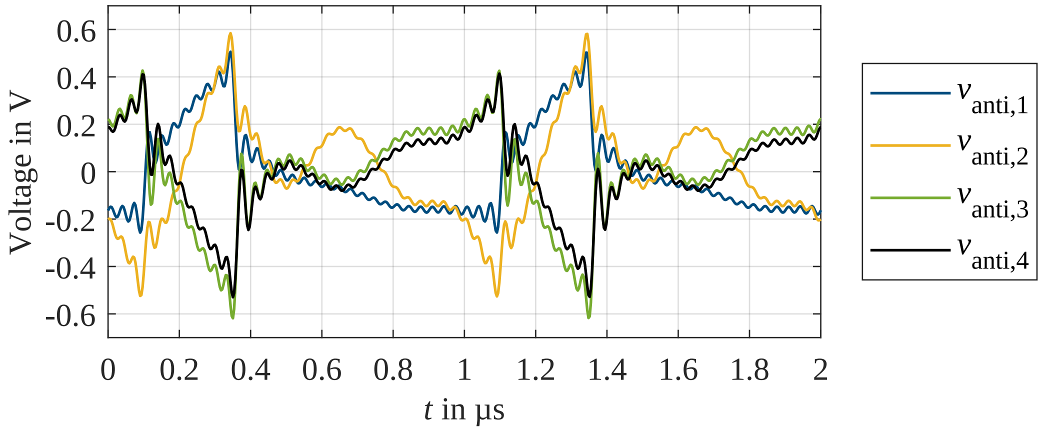

Figure 11.13: Calculated cancellation signals $\vec{v}_{\text{anti}}(t)$

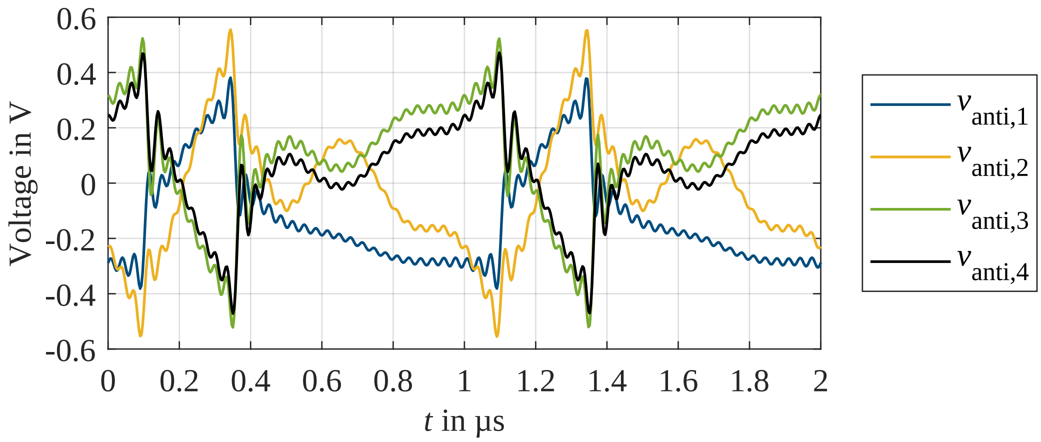

Figure 11.14: Symmetric calculated cancellation signals $\vec{v}_{\text{anti}}(t)$

g) Step 7: Determination of the Required DAC Resolution

Next, the required DAC resolution must be determined to comply with the class 5 limit of CISPR 25 [4]. The limit of the measurement ports $V_{\text{limit,RMS}}^{@\text{victim*,p}}(kf_0)$ must be transferred to the cancellation sources. This is no trivial task due to the complex coupling. However, since the cancellation sources are partially decoupled (note Figure 11.12), it is sufficient to use the individual transfer functions $H_{\text{anti,p}}^{\rightarrow\text{victim*,p}}(kf_0)$ from the cancellation source p to the respective measurement port p. So, The limit is transferred to the DACs by using (11.21) (note that the transfer matrix is reduced by 13 dB due to the previously introduced attenuators).

$$V^{@\text{anti,p}}_{\text{limit,RMS}}(kf_0) = \frac{V^{@\text{victim*,p}}_{\text{limit,RMS}}(kf_0)}{\left|H^{\rightarrow\text{victim*,p}}_{\text{anti,p}}(kf_0)\right|} \tag{11.21}$$

Since the description is very similar for all ports, it is described only for the first ($p = 1$) in detail. The limit at the victim $V^{@\text{anti,1}}_{\text{limit,RMS}}(kf_0)$ can be found in Figure 11.15. Since only the limits for the relevant harmonics kf_0 have been transferred, there are discrete limit points instead of limit lines. The RMS spectrum of the first cancellation signal $V_{\text{anti,RMS,1}}(kf_0)$ is also depicted in Figure 11.15.

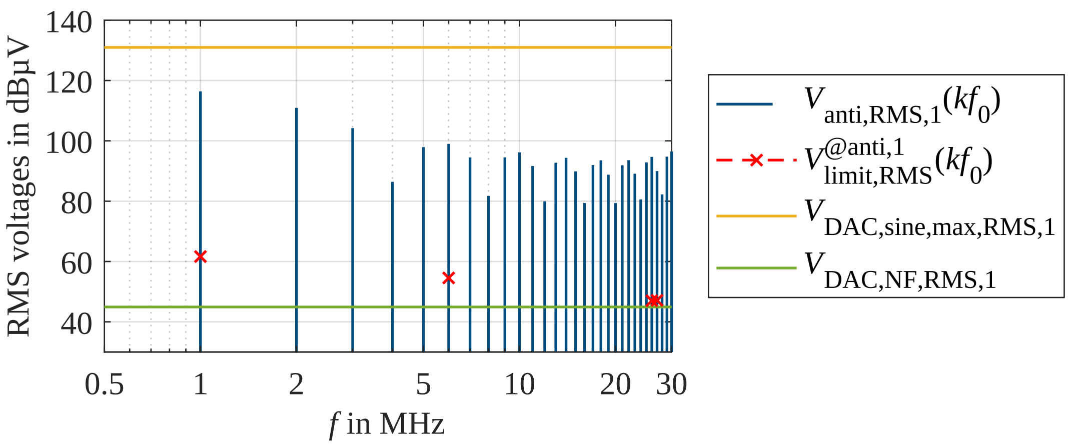

Figure 11.15: RMS voltages of the cancellation signal (at the first DAC), the limit (transferred to the first DAC) and the range (of the first DAC)

The quantization noise floor of the DACs $V_{\text{DAC,NF,RMS,p}}$ must be below the lowest limit. Since the lowest limit to be reached by the first DAC is approximately 200 µV $\widehat{=}$ 46 dBµV (the same value is true for the other DACs), the quantization noise floor must be below this value. The RMS value of the maximum generable sine wave $V_{\text{DAC,sine,max,RMS,p}}$ is calculated to approximately $5/\sqrt{2}$ V $\approx$ 3.54 V $\widehat{=}$ 131 dBµV. The required SNR is calculated to 131 dBµV $-$ 46 dBµV $=$ 85 dB. The necessary amount of bits can be calculated to 14 by (5.1). Since the DACs of the used AWGs (Tektronix AFG3000 series) have a vertical resolution of 14 bits, they are capable of suppressing the EMI below the limits of class 5. The actual SNR for 14 bits can be calculated to 86 dB by (5.1). So, the actual noise floors of the DACs have a value of 131 dBµV $-$ 86 dB $=$ 45 dBµV. This noise floor is below the given limit, but there is only 1 dB leeway.

h) Step 8: Determination of the Required DAC Sampling Rate

Last, the required DAC sampling rate must be determined. Since the highest considered harmonic is 30 MHz, a sampling rate of 60 MHz would theoretically be sufficient (Nyquist-

Shannon theorem). The here used AWGs of the Tektronix AFG3000 series have a sampling rate of at least 250 MS/s and an analog bandwidth (-3 dB) of at least 100 MHz. So, they are well applicable for the considered frequency range.

11.3.2 Design of the Sensor

Like for the single-port cancellation system of Section 10.3.2, a capacitive voltage sensor according to Section 4.4.3.a) has been chosen due to its simplicity (one sensor for each line against ground). Like for the single-port demonstration of Chapter 10, an oscilloscope HDO6104A from Teledyne LeCroy will be used with a termination Z_{meas} of 50 Ω. Due to the decoupling, the sensors can be designed individually. Since the design can be done like in the single-port case of Section 10.3.2, it will not be described again. Also here, 100 nF capacitors have been chosen and low-pass filters with a cutoff frequency of 32 MHz are applied between the sensing capacitors and the oscilloscope. The resulting cancellation system is basically the same as in Figure 11.9. The only difference is the connection of the sensing capacitors to the lines.

11.4 Application of the FFT Method

In this section, the FFT method is applied to the previously designed cancellation system. At first, the complete test setup is depicted and the algorithm is explained. The cancellation results are presented and critically discussed. The necessary cancellation signals are depicted and the power consumption of the cancelling DACs is estimated. The implementation of the algorithm and the measurement results go back to [108, supervisor].

11.4.1 Complete Test Setup with Active Cancellation System

The complete test setup with the active cancellation system can be found in Figure 11.16. The time-domain signals of the oscilloscope are transferred to a PC via Ethernet. The PC runs MATLAB with a multi-port implementation of the FFT method. The calculated and synthesized time-domain cancellation signals are passed to the AWGs via Ethernet. The performance of the cancellation system is evaluated by an EMI test receiver at the measurement ports of the ANs.

11.4.2 Algorithm

As stated before, the FFT method is applied in this demonstration (Section 6.4). The FFT method can be extended to be applicable to multi-port systems that have a weak but significant coupling between the injectors [17, author]. To do so, the mathematical descriptions of Section 3.2.2 are transferred to (11.22)-(11.24) with the same adjustments explained in Section 6.4.2. In the solution of $\vec{X}_{\mathrm{anti}}(kf_0)$, the couplings of all injectors to all sensors are

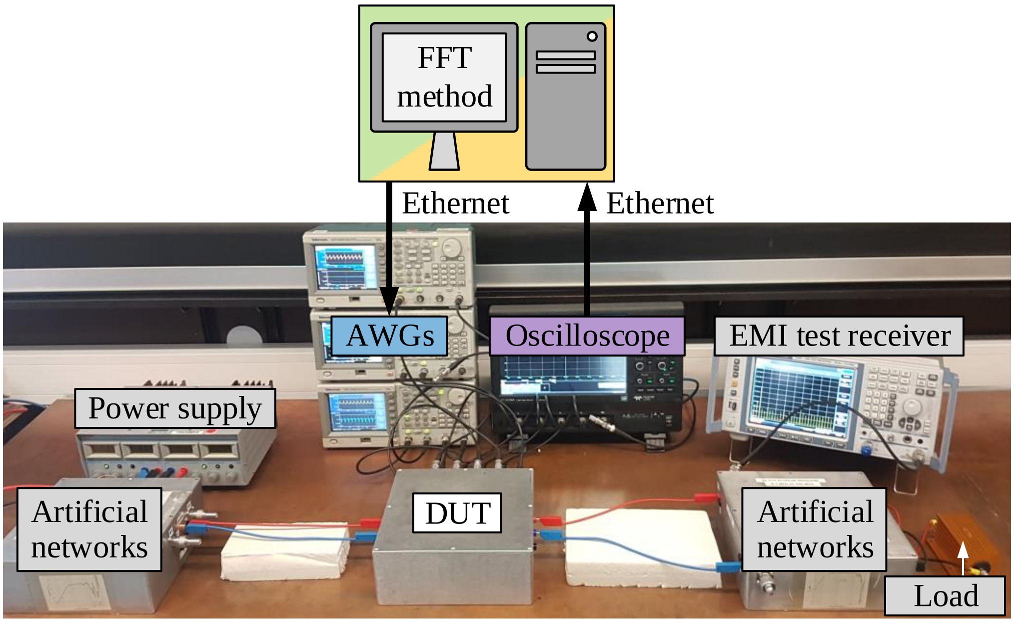

Figure 11.16: Photograph of the complete test setup with the active EMI cancellation system

respected due to the inversion of the transfer matrix $\boldsymbol{H}_{\text{anti}}^{\rightarrow\text{sensor}-1}(kf_0)$.

$$\vec{X}_{\text{res}}^{@\text{sensor}}(kf_0) = \vec{X}_{\text{EMI}}^{@\text{sensor}}(kf_0) + \boldsymbol{H}_{\text{anti}}^{\rightarrow\text{sensor}}(kf_0) \cdot \vec{X}_{\text{anti}}(kf_0) \tag{11.22}$$

$$\stackrel{!}{=} 0 \tag{11.23}$$

$$\Rightarrow \vec{X}_{\text{anti}}(kf_0) = -\boldsymbol{H}_{\text{anti}}^{\rightarrow\text{sensor}-1}(kf_0) \cdot \vec{X}_{\text{EMI}}^{@\text{sensor}}(kf_0) \tag{11.24}$$

The identification of $\vec{X}_{\text{EMI}}^{@\text{sensor}}(kf_0)$ can easily be done by measuring $\vec{x}_{\text{EMI}}^{@\text{sensor}}(t)$ with the cancellation system deactivated. To find $\boldsymbol{H}_{\text{anti}}^{\rightarrow\text{sensor}}(kf_0)$, test signals can be applied one by one to each injector. By evaluating the response at each sensor, the columns of the matrix are successively determined.

To enhance the resolution of the oscilloscope measurement by the FFT processing gain, 30 signal periods are used for each FFT. The algorithm is applied iteratively to optimize the results. The identification of the transfer function $H_{\text{anti}}^{\rightarrow\text{sensor}}(kf_0)$ is done during nominal operation of the DC-to-DC converter. The transfer function is newly identified in each iteration to account for weak nonlinear effects due to the injected cancellation signals.

11.4.3 Measurement Results

The measurement results of the EMI test receiver at the ANs are depicted in Figure 11.17. In the first measurement, the active cancellation system is installed but deactivated. In the second measurement, the active cancellation system is activated. So, the difference between both measurements is the performance of the active cancellation. The passive attenuation of the injectors and sensors comes on top.

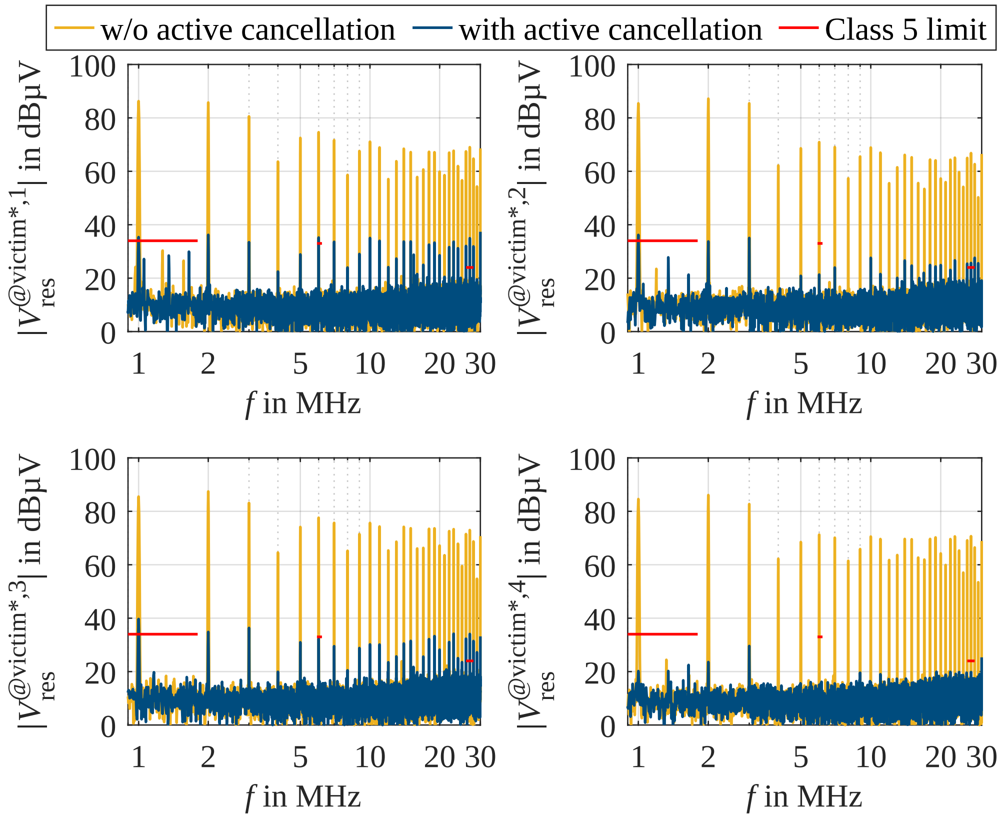

Figure 11.17: Measurement results for the EMI test receiver at the ANs with and without active EMI cancellation

First of all, the FFT method proves to be very effective in cancelling the EMI of the DC-to-DC converter. The fundamental waves are suppressed by up to 64 dB. Even the higher harmonics of up to 30 MHz are reduced by up to 47 dB. The class 5 limit of CISPR 25 is fulfilled for the AN 4. For the AN 2, the limit line is only slightly exceeded. Unfortunately, the limit line is significantly exceeded for the higher harmonics at the ANs 1 and 3. Nevertheless, these results surpass the performance of AEFs (Section 4.5.1) and DAEFs (Section 5.2).

There are numerous possible reasons why the theoretical performance could not be achieved in this setup. Some of them are discussed in the following:

- It could be expected that the higher harmonics are an issue since the noise floors of the DACs were already very close to the transferred limits (Figure 11.15).
- The introduction of the sensors may have changed the transfer functions in regard to the DACs. This could be investigated by repeating the design procedure for the injectors with the sensors included.
- The operating currents may have caused saturation effects in the decoupling ferrites leading to smaller decoupling inductances than intended. A worsened decoupling can degrade the performance of the cancellation system.

- As analyzed in Section 6.4.7 and 6.4.8, the FFT method is robust against deviations in the identified transfer functions and the (residual) EMI measurement. However, measurement noise and nonlinear effects can still degrade the performance of the algorithm. Especially in this multi-port case, it can be expected that not all cancellation signals will convergence in each iteration of the algorithm.
- Numerical issues in, e.g., the matrix inversion are also a possible source for deviations.
- The hardware setup of this system is already very complex. There are many cables connecting various devices to another. It is possible that, e.g., ground loops deteriorated the performance of the system. In practical systems, the cancellation system would be integrated and miniaturized. Such a design may lead to less unintended couplings.
- The sensors and injectors have been installed by very simple means. It is possible that some of the internal EMI of the DC-to-DC converter has coupled over the sensors and injectors to the output wires. Internal EMI may have also coupled through the non-ideal shielding enclosure to the external wires of the ANs. In practical systems, such coupling paths must be avoided.
- During measurements, it has been found that the DC-to-DC converter changes its characteristics with the temperature. To avoid problems due to this effect, all measurements are done in thermal equilibrium. However, it is possible that slight temperature drifts during measurement have degraded the fit between EMI and anti-EMI.
- Fluctuations of, e.g., the power supply can also cause slight changes that can affect the performance.

11.4.4 Cancellation Signals

The signals required for cancellation are presented in Figure 11.18. In step 5 of Section 11.3.1.f), the cancellation signals are designed to use a voltage range of 2.5 V. Here, higher signals are necessary. This is no further issue because enough leeway has been provided by the used AWGs. However, it hints to possible changes in the system. These may be due to saturation effects of the decoupling ferrites or due to the introduced sensors as discussed in the previous section. However, the shape of the signals is very similar to the ones of Figure 11.14. Note that these signals were intentionally increased by a factor of 4.5 by introducing attenuators of 13 dB.

11.4.5 Power Consumption of the Cancellation Signals

The power consumption of the cancellation signals can be approximated by considering the internal AWG impedances Z_{anti} of 50 Ω and the 13 dB attenuators that lead to a termination of basically 50 Ω for the AWGs. The RMS voltages are calculated to

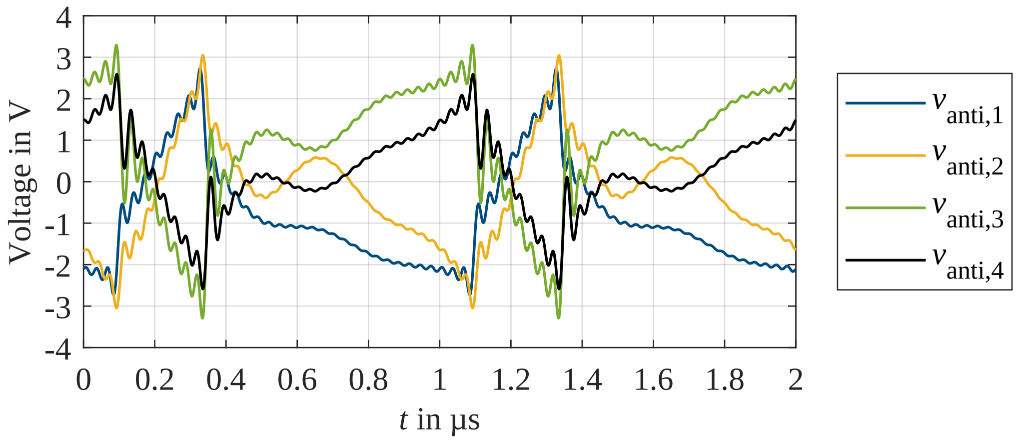

Figure 11.18: Cancellation signals found by the FFT method

$\vec{V}_{\mathrm{anti,RMS}} \approx [1.48\ \mathrm{V},\ 1.21\ \mathrm{V},\ 1.65\ \mathrm{V},\ 1.00\ \mathrm{V}]^{\mathrm{T}}$. So, the total power consumption $P_{\mathrm{anti,total}}$ of the cancellation signals can be calculated by (11.25) to approximately 74 mW. This is only about 0.05% of the DC-to-DC converter's transfer power of 144 W.

$$P_{\mathrm{anti,total}} = \frac{\vec{V}^{\mathrm{T}}_{\mathrm{anti,RMS}} \cdot \vec{V}_{\mathrm{anti,RMS}}}{50\ \Omega + 50\ \Omega} \tag{11.25}$$

11.5 Chapter Summary

In this chapter, a four-port active EMI cancellation system has been designed for an isolated DC-to-DC converter in an automotive test setup. The complete system has been identified by measurements and the cancellation system has been designed. With small adjustments, the respective procedures may also be applied to other multi-port systems. The FFT method according to Section 6.4 has been extended for the application to this multi-port system.

The fundamental switching harmonic at 1 MHz has been suppressed by up to 64 dB. The higher harmonics of up to 30 MHz have also been suppressed by up to 47 dB. These results widely surpass the performance of AEFs (Section 4.5.1) and DAEFs (Section 5.2). The power consumption of the cancellation signals is only about 0.05% of the DC-to-DC converter's transfer power.

12 Conclusion

In this work, a new method has been developed and demonstrated for the active cancellation of predictable EMI by injecting synthesized and synchronized signals.

At first, a generic description for active EMI cancellation in arbitrary single- and multi-port systems has been elaborated. This description has been used to identify the ideally necessary cancellation signals and fundamental requirements. To achieve convincing results, extremely precise cancellation signals are necessary. E.g., for an EMI reduction of 60 dB, the amplitude and phase of the cancellation signal may only deviate by 0.1% and 0.05°, respectively.

One established method for the generation of cancellation signals are active EMI filters. These use analog amplifiers in feedback or feedforward structures to directly generate the cancellation signal from a measured quantity. For this method, there are two effects that limit the precision of the cancellation signals: The first is the gain-bandwidth product of the analog amplifiers. This can be interpreted as a time constant that limits the high-frequency response. The second limitation results from the finite propagation speed of electric signals.

To overcome the restrictions due to limited gain-bandwidth products, digital active EMI filters have been developed. These use digital hardware with ADCs and DACs instead of an analog amplifier. The signal generation still uses a feedback or feedforward approach, but the amplification is done by the digital hardware. While the ADCs and DACs are only limited by the sampling rate and the vertical resolution, there are unavoidable delay times for signal processing that limit the performance of the feedback and feedforward loops.

To find other ways for the generation of the cancellation signals, methods of active power filters (power quality) and active noise cancellation (acoustics) have been reviewed. The FFT method of active power filters and the single-frequency adaptive notch filter of active noise cancellation have been identified as promising approaches to suppress quasi-periodic EMI. These methods use synthesized cancellation signals that are injected in synchronicity with the EMI. Due to the quasi-periodicity of the EMI, these methods can use the knowledge of the past to predict the upcoming EMI. Time constants and complex transfer functions can be compensated by shaping the cancellation signals. Delay times are compensated by injecting the cancellation signal before the EMI occurs.

These identified methods are further abstracted to a new active cancellation technique that uses synthesized and synchronized cancellation signals. The signal generation can be done by, e.g., the FFT method or the single-frequency adaptive notch filter, but other strategies are applicable as well. The proposed technique requires the EMI to be predictable so that the cancellation signals can be synthesized and injected at the right time. The predictability is intrinsically given for quasi-periodic signals (since the past signals allow for an extrapolation into the future), but may also be given for non-periodic signals if there is sufficient knowledge on the upcoming events. For implementation, self-adapting and externally trained systems have been proposed and discussed.

A self-adapting realization using an FPGA system with the single-frequency adaptive notch filter has been developed and investigated. It has been shown that this method is capable of fully utilizing the frequency range and vertical resolution of the ADCs and DACs. For the given system, a single sine wave could be suppressed by 80 dB for frequencies of up to 50 MHz. The digital system may cause some harmonic distortion for higher frequencies, but this effect can be actively suppressed as well. In the demonstrations for a DC-to-DC converter, this effect has been no further issue. In the best results, the EMI of a DC-to-DC converter has been suppressed by approximately 60 dB for the fundamental wave of 300 kHz and by 40 dB for up to 30 MHz. The necessary power for the cancellation signals has shown to be negligibly small (3 mW) in comparison to the transfer power of 144 W. The method has also been applied to the "slowly" changing EMI of, e.g., PFCs. Here, the fundamental wave of 100 kHz has been suppressed by approximately 46 dB. By previous investigations, it has been found that similar EMI reductions may also be achievable for harmonics of up to 1 MHz.

Afterward, the FFT method has been applied to one port of a DC-to-DC converter in a typical automotive test setup according to the EMC standard CISPR 25 [4]. The analog components of the cancellation system have been systematically designed after a characterization of the EMI source and EMI victim. With small adjustments, this methodology may also be applied to other single-port systems. An arbitrary waveform generator, an oscilloscope and a PC have been used as prototype hardware. In practical realizations, the required functionalities may be realized by using specialized mixed-signal integrated circuits. As intended by the design, the EMI could be suppressed below the strictest limit of the standard CISPR 25 [4]. The EMI is suppressed by 64 dB for the fundamental wave of 300 kHz and by 40 dB for the higher harmonics of up to 30 MHz.

In the last demonstration, the FFT method is extended for multi-port systems and applied to the four supply lines of an isolated DC-to-DC converter in a similar test setup according to the standard CISPR 25 [4]. The multi-port EMI source and EMI victims are characterized by measurements. Using this information, the analog components of the active EMI cancellation system have been designed by using the previously developed methodology. Special aspects due to the multiple ports are discussed and respected in the design. The signal processing of the cancellation system has been realized by multiple arbitrary waveform generations, an oscilloscope and a PC. While the EMI has been suppressed by up to 64 dB for the fundamental wave of 1 MHz and by up to 47 dB for the higher harmonics of up to 30 MHz, the actual goal of the design could not be reached. There are many potential reasons due to the practical setup that have been transparently discussed. These aspects and hints can be used to improve future designs and realizations.

The high potential of the proposed method has also been confirmed by numerous further demonstration results that have been briefly summarized and discussed.

All in all, the active EMI cancellation using synthesized and synchronized signals has proven to be a very promising approach in the suppression of predictable EMI. The achieved results significantly surpass the performance of analog and digital active EMI filters (with their feedback and feedforward topologies) in the literature. The predictability is a fundamental requirement that must be fulfilled for this new method. Until now, only quasi-periodic EMI has been considered that is intrinsically predictable. In future works, the method could be extended by developing methods for a prediction of non-periodic EMI. In power electronic systems, the control parameters could be used to predict the EMI of, e.g., the next switching period. Such an addition could significantly widen the applicability of the proposed method.

References

[1] S. Feng, W. Sander, and T. Wilson, "Small-capacitance nondissipative ripple filters for DC supplies," *IEEE Trans. Magn.*, vol. 6, no. 1, pp. 137–142, Mar. 1970.

[2] Y.-C. Son and S.-K. Sul, "Generalization of active filters for EMI reduction and harmonics compensation," *IEEE Trans. Ind. Appl.*, vol. 42, no. 2, pp. 545–551, Mar./Apr. 2006.

[3] S. M. Kuo and D. R. Morgan, "Active noise control: a tutorial review," *Proc. IEEE*, vol. 87, no. 6, pp. 943–975, Jun. 1999.

[4] CISPR 25, *Vehicles, boats and internal combustion engines - Radio disturbance characteristics - Limits and methods of measurement for the protection of on-board receivers*, 4th ed., Feb. 2015.

[5] P. Lueg, "Process of silencing sound oscillations: U.S. patent," Patent 2 043 416, 9 Jun. 1936.

[6] J. Walker, "Designing practical and effective active EMI filters," in *Proc. Powercon 11 Conf.*, Dallas, TX, USA, 10-12 April 1984, pp. Paper I–3.

[7] L. E. LaWhite and M. F. Schlecht, "Active filters for 1-MHz power circuits with strict input/output ripple requirements," *IEEE Trans. Power Electron.*, vol. PE-2, no. 4, pp. 282–290, Oct. 1987.

[8] L. LaWhite and M. F. Schlecht, "Design of active ripple filters for power circuits operating in the 1-10 MHz range," *IEEE Trans. Power Electron.*, vol. 3, no. 3, pp. 310–317, Jul. 1988.

[9] D. Hamza, M. Pahlevaninezhad, and P. K. Jain, "Implementation of a novel digital active EMI technique in a DSP-based DC-DC digital controller used in electric vehicle (EV)," *IEEE Trans. Power. Electron.*, vol. 28, no. 7, pp. 3126–3137, Jul. 2013.

[10] D. Hamza and M. Qiu, "Digital active EMI control technique for switch mode power converters," *IEEE Trans. Electromagn. Compat.*, vol. 55, no. 1, pp. 81–88, Feb. 2013.

[11] D. Hamza, M. Qiu, and P. K. Jain, "Application and stability analysis of a novel digital active EMI filter used in a grid-tied PV microinverter module," *IEEE Trans. Power. Electron.*, vol. 28, no. 6, pp. 2867–2874, Jun. 2013.

[12] H. Sasaki and T. Machida, "A new method to eliminate AC harmonic currents by magnetic flux compensation-considerations on basic design," *IEEE Trans. Power App. Syst.*, vol. PAS-90, no. 5, pp. 2009–2019, Sep. 1971.

[13] B. Singh, K. Al-Haddad, and A. Chandra, "A review of active filters for power quality improvement," *IEEE Trans. Ind. Electron.*, vol. 46, no. 5, pp. 960–971, Oct. 1999.

[14] S. M. Kuo and C. Chen, "Implementation of adaptive filters with the TMS320C25 or the TM320C30," *Digital Signal Processing Applications with the TMS320 Family*, vol. 3, P. Papamichalis, Ed. Englewood Cliffs, NJ: Prentice-Hall, 1990, ch. 7, pp. 191-271.

[15] A. Bendicks, T. Dörlemann, S. Frei, N. Hees, and M. Wiegand, "Active EMI reduction of stationary clocked systems by adapted harmonics cancellation," *IEEE Trans. Electromagn. Compat.*, vol. 61, no. 4, pp. 998–1006, Aug. 2019.

[16] A. Bendicks and S. Frei, "Broadband noise suppression of stationary clocked DC/DC converters by injecting synthesized and synchronized cancellation signals," *IEEE Trans. Power Electron.*, vol. 34, no. 11, pp. 10 665–10 674, Nov. 2019.

[17] A. Bendicks, M. Rübartsch, and S. Frei, "Simultaneous EMI suppression of the input and output terminals of a DC/DC converter by injecting multiple synthesized cancellation signals," in *Proc. Int. Symp. Electromagn. Compat. Eur.*, Barcelona, Spain, 2-6 Sep. 2019, pp. 842–847.

[18] N. Mohan, T. M. Undeland, and W. P. Robbins, *Power Electronics*, 3rd ed., New York, NY, USA: John Wiley & Sons Inc, 2002.

[19] C. R. Paul, *Introduction to Electromagnetic Compatibility*, 2nd ed., Hoboken, NJ, USA: Wiley, 2006.

[20] S. Frei and A. Mushtaq, "Active Shielding/Filtering for Noise Reduction on HV Cable Systems," in *Proc. Int. Symp. Electromagn. Compat. Eur.*, Wroclaw, Poland, 5-9 Sep. 2016.

[21] T. Dörlemann, A. Bendicks, and S. Frei, "Zeit- und frequenzbereichsbasierte Bestimmung der Grundfrequenz von Störsignalen zur Anwendung in der aktiven Störunterdrückung mithilfe von synthetisierten Signalen," in *Proc. Conf. Electromagn. Compat.*, Cologne, Germany, 12-13 May 2020, pp. 151–159.

[22] N. K. Poon, J. Liu, C. K. Tse, and M. H. Pong, "Techniques for input ripple current cancellation: classification and implementation [in SMPS]," *IEEE Trans. Power. Electron.*, vol. 15, no. 6, pp. 1144–1152, Nov. 2000.

[23] B. Narayanasamy and F. Luo, "A survey of active EMI filters for conducted EMI noise reduction in power electronic converters," *IEEE Trans. Electromagn. Compat.*, vol. 61, no. 6, pp. 2040–2049, Dec. 2019.

[24] R. Goswami and S. Wang, "Modeling and stability analysis of active differential-mode EMI filters for AC/DC power converters," *IEEE Trans. Power. Electron.*, vol. 33, no. 12, pp. 10 277–10 291, Dec. 2018.

[25] T. Farkas and M. F. Schlecht, "Viability of active EMI filters for utility applications," *IEEE Trans. Power. Electron.*, vol. 9, no. 3, pp. 328–337, May 1994.

[26] A. C. Chow and D. J. Perreault, "Design and evaluation of a hybrid passive/active ripple filter with voltage injection," *IEEE Trans. Aerosp. Electron. Syst.*, vol. 39, no. 2, pp. 471–480, Apr. 2003.

[27] U. Tietze, C. Schenk, and E. Gamm, *Halbleiter-Schaltungstechnik*, 13th ed., Berlin Heidelberg, Germany: Springer-Verlag, 2009.

[28] "uA741 data sheet," Texas Instruments Incorporated, Dallas, Texas, USA, 2018, Rev. G.

[29] D. C. Hamill, "An efficient active ripple filter for use in DC-DC conversion," *IEEE Trans. Aerosp. Electron. Syst.*, vol. 32, no. 3, Jul. 1996.

[30] "LM6172 data sheet," Texas Instruments Incorporated, Dallas, Texas, USA, 2013, Rev. D.

[31] M. C. Di Piazza, A. Ragusa, and G. Vitale, "An optimized feedback common mode active filter for vehicular induction motor drives," *IEEE Trans. Power. Electron.*, vol. 26, no. 11, pp. 3153–3162, Nov. 2011.

[32] M. C. Di Piazza, M. Luna, and G. Vitale, "EMI reduction in DC-fed electric drives by active common-mode compensator," *IEEE Trans. Electromagn. Compat.*, vol. 56, no. 5, pp. 1067–1076, Oct. 2014.

[33] "AD829 data sheet," Analog Devices Inc., Norwood, MA, USA, 2011, Rev. I.

[34] R. Goswami, S. Wang, E. Solodovnik, and K. J. Karimi, "Differential mode active EMI filter design for a boost power factor correction AC/DC converter," *IEEE Trans. Emerg. Sel. Topics Circuits Syst.*, vol. 7, no. 1, pp. 576–590, Mar. 2019.

[35] R. Goswami and S. Wang, "Investigation and modeling of combined feedforward and feedback control schemes to improve the performance of differential mode active EMI filters in AC-DC power converters," *IEEE Trans. Ind. Electron.*, vol. 66, no. 8, pp. 6538–6548, Aug. 2019.

[36] "OPA847 data sheet," Texas Instruments Incorporated, Dallas, Texas, USA, 2008, Rev. E.

[37] D. Shin, S. Kim, G. Jeong, J. Park, J. Park, K. J. Han, and J. Kim, "Analysis and design guide of active EMI filter in a compact package for reduction of common-mode conducted emissions," *IEEE Trans. Electromagn. Compat.*, vol. 57, no. 4, pp. 660–671, Aug. 2015.

[38] J. Lunze, *Regelungstechnik 1*, 11th ed., Berlin, Germany: Springer Vieweg, 2016.

[39] M. Zhu, D. J. Perreault, V. Caliskan, T. C. Neugebauer, S. Guttowski, and J. G. Kassakian, "Design and evaluation of feedforward active ripple filters," *IEEE Trans. Power. Electron.*, vol. 20, no. 2, pp. 276–285, Mar. 2005.

[40] J. Biela, A. Wirthmueller, R. Waespe, M. L. Heldwein, K. Raggl, and J. W. Kolar, "Passive and active hybrid integrated EMI filters," *IEEE Trans. Power. Electron.*, vol. 24, no. 5, pp. 1340–1349, May 2009.

[41] S. Ogasawara, H. Ayano, and H. Akagi, "An active circuit for cancellation of common-mode voltage generated by a PWM inverter," *IEEE Trans. Power. Electron.*, vol. 13, no. 5, pp. 835–841, Sep. 1998.

[42] S. Ogasawara, S. Zhang, and H. Akagi, "Configurations and characteristics of active canceling and compensating circuits for reducing common-mode voltage generated by voltage-source PWM inverters," *ELECTR ENG JPN*, vol. 137, no. 1, pp. 658–665, Oct. 2001.

[43] S. Ogasawara and H. Akagi, "A PWM rectifier/inverter system capable of suppressing both harmonics and EMI," *ELECTR ENG JPN*, vol. 141, no. 4, pp. 59–68, Dec. 2002.

[44] Y.-C. Son and S.-K. Sul, "A new active common-mode EMI filter for PWM inverter," *IEEE Trans. Power. Electron.*, vol. 18, no. 6, pp. 1309–1314, Nov. 2003.

[45] C. Mei, J. C. Balda, and W. P. Waite, "Cancellation of common-mode voltages for induction motor drives using active method," *IEEE Trans. Energy Convers*, vol. 21, no. 2, pp. 380–386, Jun. 2006.

[46] M. C. Di Piazza, G. Tine, and G. Vitale, "An improved active common-mode voltage compensation device for induction motor drives," *IEEE Trans. Ind. Electron.*, vol. 55, no. 4, pp. 1823–1834, Apr. 2008.

[47] M. C. Di Piazza, A. Ragusa, and G. Vitale, "Design of grid-side electromagnetic interference filters in AC motor drives with motor-side common mode active compensation," *IEEE Trans. Electromagn. Compat.*, vol. 51, no. 3, pp. 673–682, Aug. 2009.

[48] ——, “Power-loss evaluation in cm active EMI filters for bearing current suppression,” *IEEE Trans. Ind. Electron.*, vol. 58, no. 11, pp. 5142–5153, Nov. 2011.

[49] M. S. Moon and B. H. Cho, “Novel active ripple filter for the solar array shunt switching unit,” *J. Propul. Power*, vol. 12, no. 1, pp. 78–82, Jan. 1996.

[50] S. Wang, Y. Y. Maillet, F. Wang, D. Boroyevich, and R. Burgos, “Investigation of hybrid EMI filters for common-mode EMI suppression in a motor drive system,” *IEEE Trans. Power. Electron.*, vol. 25, no. 4, pp. 1034–1045, Apr. 2010.

[51] D. Shin, S. Jeong, and J. Kim, “Quantified design guidelines of a compact transformerless active EMI filter for performance, stability, and high voltage immunity,” *IEEE Trans. Power. Electron.*, vol. 33, no. 8, pp. 6723–6737, Aug. 2018.

[52] P. Midya and P. T. Krein, “Feed-forward active filter for output ripple cancellation,” *Int. J. Electron.*, vol. 77, no. 5, pp. 805–818, Nov. 1994.

[53] V. Vlatkovic, D. Borojevic, and F. C. Lee, “Input filter design for power factor correction circuits,” *IEEE Trans. Power Electron.*, vol. 11, no. 1, pp. 199–205, Jan. 1996.

[54] P. Cantillon-Murphy, T. C. Neugebauer, C. Brasca, and D. J. Perreault, “An active ripple filtering technique for improving common-mode inductor performance,” *IEEE Power Electron. Lett.*, vol. 2, no. 2, pp. 45–50, Jun. 2004.

[55] W. Chen, X. Yang, and Z. Wang, “An active EMI filtering technique for improving passive filter low-frequency performance,” *IEEE Trans. Electromagn. Compat.*, vol. 48, no. 1, pp. 172–177, Feb. 2006.

[56] W. Chen, W. Zhang, X. Yang, Z. Sheng, and Z. Wang, “An experimental study of common- and differential-mode active EMI filter compensation characteristics,” *IEEE Trans. Electromagn. Compat.*, vol. 51, no. 3, pp. 683–691, Aug. 2009.

[57] W. Chen, X. Yang, and Z. Wang, “A novel hybrid common-mode EMI filter with active impedance multiplication,” *IEEE Trans. Ind. Electron.*, vol. 58, no. 5, pp. 1826–1834, May 2011.

[58] M. Ali, E. Laboure, and F. Costa, “Integrated active filter for differential-mode noise suppression,” *IEEE Trans. Power Electron.*, vol. 29, no. 3, pp. 1053–1057, Mar. 2014.

[59] C. Zhu and T. H. Hubing, “An active cancellation circuit for reducing electrical noise from three-phase AC motor drivers,” *IEEE Trans. Electromagn. Compat.*, vol. 56, no. 1, pp. 60–66, Feb. 2014.

[60] Y. Chu, S. Wang, and Q. Wang, "Modeling and stability analysis of active/hybrid common-mode EMI filters for DC/DC power converters," *IEEE Trans. Power. Electron.*, vol. 31, no. 9, pp. 6254–6263, Sep. 2016.

[61] L. Dai, W. Chen, X. Yang, M. Zheng, Y. Yang, and R. Wang, "A multi-function common mode choke based on active cm EMI filters for AC/DC power converters," *IEEE Access*, vol. 7, pp. 43 534–43 546, Mar. 2019.

[62] S. Jeong, D. Shin, and J. Kim, "A transformer-isolated common-mode active EMI filter without additional components on power lines," *IEEE Trans. Power Electron.*, vol. 34, no. 3, pp. 2244–2257, Mar. 2019.

[63] J. Ji, W. Chen, X. Yang, and J. Lu, "Delay and decoupling analysis of a digital active EMI filter used in arc welding inverter," *IEEE Trans. Power. Electron.*, vol. 33, no. 8, pp. 6710–6722, Aug. 2018.

[64] M. C. Di Piazza, A. Ragusa, and G. Vitale, "Effects of common-mode active filtering in induction motor drives for electric vehicles," *IEEE Trans. Veh. Technol.*, vol. 59, no. 6, pp. 2664–2673, Jul. 2010.

[65] S. Takahashi, S. Ogasawara, M. Takemoto, K. Orikawa, and M. Tamate, "Common-mode voltage attenuation of an active common-mode filter in a motor drive system fed by a PWM inverter," *IEEE Trans. Ind. Appl.*, vol. 55, no. 3, pp. 2721–2730, May/Jun. 2019.

[66] M. L. Heldwein, H. Ertl, J. Biela, and J. W. Kolar, "Implementation of a transformer-less common-mode active filter for offline converter systems," *IEEE Trans. Ind. Electron.*, vol. 57, no. 5, pp. 1772–1786, May 2010.

[67] "TMS320F28335 data sheet," Texas Instruments Incorporated, Dallas, Texas, USA, 2019, Rev. O.

[68] "XC2C64A data sheet," Xilinx Inc., San Jose, California, USA, 2008, Rev. 2.3.

[69] "KAD5514P data sheet," Renesas Electronics Corporation, Koto City, Tokyo, Japan, 2019, Rev. 4.00.

[70] "ADS4229 data sheet," Texas Instruments Incorporated, Dallas, Texas, USA, 2015, Rev. C.

[71] "ISL5957 data sheet," Renesas Electronics Corporation, Koto City, Tokyo, Japan, 2015, Rev. 2.00.

[72] "DAC5662A data sheet," Texas Instruments Incorporated, Dallas, Texas, USA, 2010, Rev. B.

[73] J. Ji, W. Chen, Z. Gu, X. Yang, and X. Zhang, "A control method of digital active EMI filter," in *Proc. IEEE Appl. Power Electron. Conf. Expo.*, Tampa, FL, USA, 26-30 Mar. 2017, pp. 1141–1145.

[74] M. El-Habrouk, M. K. Darwish, and P. Mehta, "Active power filters: a review," *IEE Proceedings - Electric Power Applications*, vol. 147, no. 5, pp. 403–413, Sep. 2000.

[75] D. Chen and S. Xie, "Review of the control strategies applied to active power filters," in *Proc. IEEE International Conference on Electric Utility Deregulation, Restructuring and Power Technologies*, Hong Kong, China, 5-8 Apr. 2004, pp. 666–670.

[76] T. Demirdelen, M. Inci, K. C. Bayindir, and M. Tumay, "Review of hybrid active power filter topologies and controllers," in *Proc. 4th International Conference on Power Engineering, Energy and Electrical Drives*, Istanbul, Turkey, 13-17 May 2013, pp. 587–592.

[77] S. Mariethoz and A. C. Rufer, "Open loop and closed loop spectral frequency active filtering," *IEEE Trans. Power Electron.*, vol. 17, no. 4, pp. 564–573, Jul. 2002.

[78] W. M. Grady, M. J. Samotyj, and A. H. Noyola, "Survey of active power line conditioning methodologies," *IEEE Trans. Power Del.*, vol. 5, no. 3, pp. 1536–1542, Jul. 1990.

[79] C. A. Quinn and N. Mohan, "Active filtering of harmonic currents in three-phase, four-wire systems with three-phase and single-phase nonlinear loads," in *Proc. IEEE Appl. Power Electron. Conf. Expo.*, Boston, MA, USA, 23-27 Feb. 1992, pp. 829–836.

[80] C. A. Quinn, N. Mohan, and H. Mehta, "A four-wire, current-controlled converter provides harmonic neutralization in three-phase, four-wire systems," in *Proc. IEEE Appl. Power Electron. Conf. Expo.*, San Diego, CA, USA, 7-11 Mar. 1993, pp. 841–846.

[81] M. Gerten, "Realisierung eines 48 V-Antriebsprüfstands zur Untersuchung der aktiven Unterdrückung der elektromagnetischen Störungen mithilfe von synthetisierten Gegenstörsignalen," M.Sc. thesis, TU Dortmund University, On-board Systems Lab, Dortmund, Germany, Sep. 2019.

[82] S. J. Elliott and P. A. Nelson, "The active control of sound," *Electronics Communication Engineering Journal*, vol. 2, no. 4, pp. 127–136, Aug. 1990.

[83] J. C. Burgess, “Active adaptive sound control in a duct: A computer simulation,” *J. Acoust. Soc. Am.*, vol. 70, no. 3, pp. 715–726, Sep. 1981.

[84] G. E. Warnaka, L. Tichy, and L. A. Poole, “Improvements in adaptive active attenuators,” in *Proc. Inter-noise*, Amsterdam, the Netherlands, 6-8 Oct. 1981, pp. 307–310.

[85] K. Kido, “Reduction of noise by use of additional sound sources,” in *Proc. Inter-noise*, Amsterdam, the Netherlands, 6-8 Oct. 1981, pp. 647–650.

[86] C. F. Ross, “A demonstration of active control of broadband sound,” *J. Sound Vib.*, vol. 74, no. 3, pp. 411–417, Feb. 1981.

[87] L. J. Eriksson, “Computer-aided silencing — an emerging technology,” *Sound Vib.*, vol. 24, pp. 42–45, Jul. 1990.

[88] M. G. Jozwiak, “Aktive Unterdrückung der elektromagnetischen Störungen eines Antriebswechselrichters mithilfe von synthetisierten Gegenstörsignalen,” M.Sc. thesis, TU Dortmund University, On-board Systems Lab, Dortmund, Germany, Jul. 2019.

[89] W. B. Conover, “Fighting noise with noise,” *Noise Control*, vol. 2, no. 2, pp. 78–92, 1956.

[90] B. Widrow, J. R. Glover, J. M. McCool, J. Kaunitz, C. S. Williams, R. H. Hearn, J. R. Zeidler, Jr. Eugene Dong, and R. C. Goodlin, “Adaptive noise cancelling: Principles and applications,” *Proc. IEEE*, vol. 63, no. 12, pp. 1692–1716, Dec. 1975.

[91] J. E. Ziegler, “Selective active cancellation system for repetitive phenomena: U.S. patent,” Patent 4 878 188, 31 Oct. 1989.

[92] E. W. Weisstein. “Harmonic Addition Theorem”. From Mathworld - A Wolfram Web Resource. Accessed on 25 Sep. 2019. [Online]. Available: http://mathworld.wolfram.com/HarmonicAdditionTheorem.html

[93] B. Widrow and S. D. Stearns, *Adaptive signal processing*, ser. Prentice-Hall signal processing series., Englewood Cliffs, NJ: Prentice-Hall, 1985.

[94] B. Widrow, D. Shur, and S. Shaffer, “On adaptive inverse control,” in *Proc. 15th Asilomar Conf.*, 1981, pp. 185–189.

[95] S. J. Elliott and P. A. Nelson, “The application of adaptive filtering to the active control of sound and vibration,” ISVR, Univ. Southampton, U.K., Tech. Rep. 136, 1985.

[96] D. Morgan, “An analysis of multiple correlation cancellation loops with a filter in the auxiliary path,” *IEEE Trans. Acoust., Speech, Signal Process.*, vol. 28, no. 4, pp. 454–467, Aug. 1980.

[97] C. C. Boucher, S. J. Elliot, and P. A. Nelson, "The effects of modeling errors on the performance and stability of active noise control systems," in *Proc. Recent Advances in Active Control of Sound Vibration*, 1991, pp. 290–301.

[98] ——, "Effect of errors in the plant model on the performance of algorithms for adaptive feedforward control," in *IEE PROC-F*, vol. 138, Aug. 1991, pp. 313–319.

[99] G. Long, F. Ling, and J. G. Proakis, "The LMS algorithm with delayed coefficient adaptation," *IEEE Trans. Acoust., Speech, Signal Process.*, vol. 37, no. 9, pp. 1397–1405, Sep. 1989.

[100] ——, "Corrections to 'the LMS algorithm with delayed coefficient adaptation'," *IEEE Trans. Signal Process.*, vol. 40, pp. 230–232, Jan. 1992.

[101] A. Bendicks, T. Dörlemann, S. Frei, N. Hees, and M. Wiegand, "FPGA-basierte aktive Gegenkopplung der Schaltharmonischen von leistungselektronischen Systemen," in *Proc. Conf. Electromagn. Compat.*, Düsseldorf, Germany, 20-22 Feb. 2018, pp. 652–661.

[102] ——, "Development of an adaptive EMI cancellation strategy for stationary clocked systems," in *Proc. Int. Symp. Electromagn. Compat. Eur.*, Amsterdam, Netherlands, 27-30 Aug. 2018, pp. 78–83.

[103] J. Glover, "Adaptive noise canceling applied to sinusoidal interferences," *IEEE Trans. Acoust., Speech, Signal Process.*, vol. 25, no. 6, pp. 484–491, Dec. 1977.

[104] A. Bendicks, T. Osterburg, S. Frei, M. Wiegand, and N. Hees, "Wide-frequency EMI suppression of stationary clocked systems by injecting successively adapted cancellation signals," in *Proc. Int. Symp. Electromagn. Compat. Eur.*, Barcelona, Spain, 2-6 Sep. 2019, pp. 36–41.

[105] A. S. Brush, "Measurement of microwave power - a review of techniques used for measurement of high-frequency RF power," *IEEE Instrumentation & Measurement Magazine*, vol. 10, no. 2, pp. 20–25, May 2007.

[106] A. Bendicks, A. Peters, S. Frei, M. Wiegand, and N. Hees, "FPGA-basierte aktive Unterdrückung der elektromagnetischen Störungen einer aktiven Leistungsfaktorkorrektur (PFC) durch die Injektion von modulierten Sinussignalen," in *Proc. Conf. Electromagn. Compat.*, Cologne, Germany, 12-13 May 2020, pp. 433–442.

[107] A. Peters, "Aktive Unterdrückung der elektromagnetischen Störungen einer Leistungsfaktorkorrektur (PFC) mithilfe von synthetisierten Gegenstörsignalen," M.Sc.

thesis, TU Dortmund University, On-board Systems Lab, Dortmund, Germany, May 2019.

[108] M. Rübartsch, "Aktive Unterdrückung der elektromagnetischen Störungen von DC/DC-Wandlern mithilfe mehrerer synthetisierter Gegenstörsignale," M.Sc. thesis, TU Dortmund University, On-board Systems Lab, Dortmund, Germany, May 2019.

[109] M. Rübartsch, A. Bendicks, and S. Frei, "Injektorkonzepte zur aktiven Unterdrückung der elektromagnetischen Störungen aller Klemmen eines stationär betriebenen DC/DC-Wandlers," in *Proc. Conf. Electromagn. Compat.*, Cologne, Germany, 12-13 May 2020, pp. 327–336.

[110] A. Bendicks, M. Gerten, and S. Frei, "Aktive Unterdrückung der elektromagnetischen Störungen eines stationär betriebenen Antriebswechselrichters mithilfe von synthetisierten und synchronisierten Gegenstörsignalen," in *Proc. Conf. Electromagn. Compat.*, Cologne, Germany, 12-13 May 2020, pp. 423–432.

[111] ——, "Active Cancellation of Periodic DM EMI at the Input of a GaN Motor Inverter by Injecting Synthesized and Synchronized Signals," in *Proc. Int. Symp. Electromagn. Compat. Eur.*, Rome, Italy, 7-11 Sep. 2020, accepted to be published.

[112] T. Dörlemann, "Entwicklung und Analyse einer FPGA-basierten Gegenkopplung elektromagnetischer Störungen von leistungselektronischen Konvertern," M.Sc. thesis, TU Dortmund University, On-board Systems Lab, Dortmund, Germany, Dec. 2017.

[113] "74272733 data sheet," Würth Elektronik eiSos GmbH & Co. KG, Waldenburg, Germany, 2018, 002.009.

[114] P. Hillenbrand, H. Aichele, C. Keller, and P. Kralicek, "Generation of terminal equivalent circuits applied to a DC brush motor," in *Proc. Int. Symp. Electromagn. Compat. Eur.*, Barcelona, Spain, 2-6 Sep. 2019, pp. 48–53.

[115] "74271733 data sheet," Würth Elektronik eiSos GmbH & Co. KG, Waldenburg, Germany, 2018, 002.008.

List of Publications of the Author

1. A. Bendicks, M. Wiegand, D. Heberling, and D. Hölscher, "EMI, losses and cooling of low-inductance GaN-HEMTs in a CCM PFC of an on-board charger," in *Proc. AmE 2017 - Automotive meets Electronics; 8th GMM-Symposium*, Dortmund, Germany, 7-8 Mar. 2017, pp. 149-154.

2. A. Bendicks, H. Haverland, S. Frei, N. Hees, and M. Wiegand, "Application of spread spectrum techniques for the reduction of disturbances of automotive power electronic converters," in *Proc. Int. Conf. Elect. Electron. Syst. Hybrid Elect. Veh. Elect. Energy Manage. (EEHE)*, Bamberg, Germany, 17-18 May 2017, pp. 1-6.

3. A. Bendicks, S. Frei, N. Hees, and M. Wiegand, "Channel selective adaption of PWM frequencies for undisturbed AM and FM reception in automobiles," in *Proc. Int. Symp. Electromagn. Compat. Eur.*, Angers, France, 4-7 Sep. 2017, pp. 1-6.

4. A. Bendicks, S. Frei, N. Hees, and M. Wiegand, "Systematic reduction of peak and average emissions of power electronic converters by the application of spread spectrum," *IEEE Trans. Electromagn. Compat.*, vol. 60, no. 5, pp. 1571-1580, Oct. 2018.

5. A. Bendicks, T. Dörlemann, S. Frei, N. Hees, and M. Wiegand, "FPGA-basierte aktive Gegenkopplung der Schaltharmonischen von leistungselektronischen Systemen," in *Proc. Conf. Electromagn. Compat.*, Düsseldorf, Germany, 20-22 Feb. 2018, pp. 652–661.

6. N. Hees and A. Bendicks, "Laderegler - aktueller Stand und Ansätze zur Erhöhung der Leistungsdichte," in *Proc. AmE 2018 - Automotive meets Electronics; 9th GMM-Symposium*, Dortmund, Germany, 7-8 Mar. 2018, pp. 126-131.

7. A. Bendicks, T. Dörlemann, S. Frei, N. Hees, and M. Wiegand, "Development of an adaptive EMI cancellation strategy for stationary clocked systems," in *Proc. Int. Symp. Electromagn. Compat. Eur.*, Amsterdam, Netherlands, 27-30 Aug. 2018, pp. 78-83.

8. A. Bendicks, T. Dörlemann, S. Frei, N. Hees, and M. Wiegand, "Possibilities and potentials of active EMI cancellation for the volume reduction of DC/DC converters in automobiles," in *Proc. Int. Conf. Elect. Electron. Syst. Hybrid Elect. Veh. Elect. Energy Manage. (EEHE)*, Bad Nauheim, Germany, 22–23 May 2019, pp. 168-174.

9. A. Bendicks, T. Dörlemann, S. Frei, N. Hees, and M. Wiegand, "Active EMI reduction of stationary clocked systems by adapted harmonics cancellation," *IEEE Trans. Electromagn. Compat.*, vol. 61, no. 4, pp. 998-1006, Aug. 2019.

10. A. Bendicks, T. Osterburg, S. Frei, M. Wiegand, and N. Hees, “Wide-frequency EMI suppression of stationary clocked systems by injecting successively adapted cancellation signals,” in *Proc. Int. Symp. Electromagn. Compat. Eur.*, Barcelona, Spain, 2-6 Sep. 2019, pp. 36-41.
11. A. Bendicks, M. Rübartsch, and S. Frei, “Simultaneous EMI suppression of the input and output terminals of a DC/DC converter by injecting multiple synthesized cancellation signals,” in *Proc. Int. Symp. Electromagn. Compat. Eur.*, Barcelona, Spain, 2-6 Sep. 2019, pp. 842-847.
12. T. Dörlemann, A. Bendicks, C. Krause, and S. Frei, “Noise reduction in periodically switching MOSFET circuits using iteratively found synthesized control signals,” in *Proc. Int. Symp. Electromagn. Compat. Eur.*, Barcelona, Spain, 2-6 Sep. 2019, pp. 848-853.
13. C. Krause, A. Bendicks, T. Dörlemann, and S. Frei, “Synthesis of an optimized control signal for an improved EMC switching behavior of MOSFETs Using a System Characterization Approach,” in *Proc. Int. Symp. Electromagn. Compat. Eur.*, Barcelona, Spain, 2-6 Sep. 2019, pp. 345-350.
14. A. Bendicks and S. Frei, “Broadband noise suppression of stationary clocked DC/DC converters by injecting synthesized and synchronized cancellation signals,” *IEEE Trans. Power Electron.*, vol. 34, no. 11, pp. 10665-10674, Nov. 2019.
15. A. Bendicks, T. Dörlemann, T. Osterburg, S. Frei, N. Hees, and M. Wiegand, “Active cancellation of periodic electromagnetic disturbances for passive filter reduction in automotive DC-to-DC converters,” in *Proc. AmE 2020 - Automotive meets Electronics; 11th GMM-Symposium*, Dortmund, Germany, 10-11 Mar. 2020, 149-153.
16. A. Bendicks, A. Peters, S. Frei, M. Wiegand, and N. Hees, “FPGA-basierte aktive Unterdrückung der elektromagnetischen Störungen einer aktiven Leistungsfaktorkorrektur (PFC) durch die Injektion von modulierten Sinussignalen,” in *Proc. Conf. Electromagn. Compat.*, Cologne, Germany, 12-13 May 2020, pp. 433-442.
17. A. Bendicks, M. Gerten, and S. Frei, “Aktive Unterdrückung der elektromagnetischen Störungen eines stationär betriebenen Antriebswechselrichters mithilfe von synthetisierten und synchronisierten Gegenstörsignalen,” in *Proc. Conf. Electromagn. Compat.*, Cologne, Germany, 12-13 May 2020, pp. 423-432.
18. M. Rübartsch, A. Bendicks, and S. Frei, “Injektorkonzepte zur aktiven Unterdrückung der elektromagnetischen Störungen aller Klemmen eines stationär betriebenen DC/DC-Wandlers,” in *Proc. Conf. Electromagn. Compat.*, Cologne, Germany, 12-13 May 2020, pp. 327-336.

19. C. Krause, A. Bendicks, and S. Frei, “Verbesserung des EMV-Verhaltens getakteter MOSFETs mithilfe synthetisierter Ansteuerungssignale auf Grundlage einer Netzwerkanalyse und des EKV-Modells,” in *Proc. Conf. Electromagn. Compat.*, Cologne, Germany, 12-13 May 2020, pp. 131-138.

20. T. Dörlemann, A. Bendicks, and S. Frei, “Zeit- und frequenzbereichsbasierte Bestimmung der Grundfrequenz von Störsignalen zur Anwendung in der aktiven Störunterdrückung mithilfe von synthetisierten Signalen,” in *Proc. Conf. Electromagn. Compat.*, Cologne, Germany, 12-13 May 2020, pp. 151-159.

21. A. Bendicks, T. Dörlemann, T. Osterburg, and S. Frei, “Active Cancellation of Periodic EMI of Power Electronic Systems by Injecting Artificially Synthesized Signals,” *IEEE Electromagn. Compat. Magazine*, accepted to be published.

22. A. Bendicks, M. Rübartsch, and S. Frei, “Active Cancellation of Periodic EMI at All Terminals of a DC-to-DC Converter by Injecting Multiple Artificially Synthesized Signals,” *IEEE Electromagn. Compat. Magazine*, accepted to be published.

23. A. Bendicks, M. Gerten, and S. Frei, “Active Cancellation of Periodic DM EMI at the Input of a GaN Motor Inverter by Injecting Synthesized and Synchronized Signals,” in *Proc. Int. Symp. Electromagn. Compat. Eur.*, Rome, Italy, 7-11 Sep. 2020, accepted to be published.

List of Bachelor and Master Theses Supervised by the Author

1. H. Haverland, “Untersuchung von Frequenzspreizungsverfahren zur Reduktion elektromagnetischer Störungen in der Leistungselektronik,” B.Sc. thesis, TU Dortmund University, On-board Systems Lab, Dortmund, Germany, Jan. 2017.

2. Z. El Amri, “Realisierung einer leistungselektronischen Universaltopologie für Laboranwendungen,” B.Sc. thesis, TU Dortmund University, On-board Systems Lab, Dortmund, Germany, Mar. 2017.

3. T. Dörlemann, “Entwicklung und Analyse einer FPGA-basierten Gegenkopplung elektromagnetischer Störungen von leistungselektronischen Konvertern,” M.Sc. thesis, TU Dortmund University, On-board Systems Lab, Dortmund, Germany, Dec. 2017.

4. O. Niewerth, “Analyse von Sensoren und Injektoren zur aktiven Gegenkopplung elektromagnetischer Störungen von DC/DC-Wandlern,” M.Sc. thesis, TU Dortmund University, On-board Systems Lab, Dortmund, Germany, Jun. 2018.

5. H. Wang, “Automatisierte Signalsynthese zur adaptiven Gegenkopplung von elektromagnetischen Störungen,” M.Sc. thesis, TU Dortmund University, On-board Systems Lab, Dortmund, Germany, Jul. 2018.

6. C. Eramba Uthayakanthan, “Integration der adaptiven Gegenkopplung in die passive Filterstruktur eines Ladereglers zur Bauraumreduktion,” M.Sc. thesis, TU Dortmund University, On-board Systems Lab, Dortmund, Germany, Dec. 2018.

7. C. Krause, “Entwicklung und Realisierung einer adaptiven Gatemodulation mit Harmonischen zur Verbesserung des EMV-Verhaltens getakteter Leistungselektronik,” M.Sc. thesis, TU Dortmund University, On-board Systems Lab, Dortmund, Germany, Mar. 2019.

8. A. Peters, “Aktive Unterdrückung der elektromagnetischen Störungen einer Leistungsfaktorkorrektur (PFC) mithilfe von synthetisierten Gegenstörsignalen,” M.Sc. thesis, TU Dortmund University, On-board Systems Lab, Dortmund, Germany, May 2019.

9. M. Rübartsch, “Aktive Unterdrückung der elektromagnetischen Störungen von DC/DC-Wandlern mithilfe mehrerer synthetisierter Gegenstörsignale,” M.Sc. thesis, TU Dortmund University, On-board Systems Lab, Dortmund, Germany, May 2019.

10. H. Haverland, “Entwicklung einer EMV-optimierten Schaltstrategie von mehrphasigen Ladereglern anhand einer Analyse der leitungsgeführten Störaussendungen,” M.Sc. thesis, TU Dortmund University, On-board Systems Lab, Dortmund, Germany, Jul. 2019.

11. M. G. Jozwiak, “Aktive Unterdrückung der elektromagnetischen Störungen eines Antriebswechselrichters mithilfe von synthetisierten Gegenstörsignalen,” M.Sc. thesis, TU Dortmund University, On-board Systems Lab, Dortmund, Germany, Jul. 2019.

12. M. Gerten, “Realisierung eines 48 V-Antriebsprüfstands zur Untersuchung der aktiven Unterdrückung der elektromagnetischen Störungen mithilfe von synthetisierten Gegenstörsignalen,” M.Sc. thesis, TU Dortmund University, On-board Systems Lab, Dortmund, Germany, Sep. 2019.

13. S. Windhövel, “Entwicklung eines 48 V-Antriebsprüfstands mit Wide-Bandgap-Leistungshalbleitern zur Untersuchung der aktiven Unterdrückung der Gleich- und Gegentaktstörungen mithilfe von synthetisierten Gegenstörsignalen,” M.Sc. thesis, TU Dortmund University, On-board Systems Lab, Dortmund, Germany, ongoing.

14. J. Aigner, “Untersuchung der aktiven Unterdrückung von Gleichtaktstörungen auf den Motorleitungen eines Antriebswechselrichters mithilfe synthetisierter Gegenstörsignale,” B.Sc. thesis, TU Dortmund University, On-board Systems Lab, Dortmund, Germany, ongoing.

List of Awards and Nominations of the Author

1. Nomination for the Best Student Paper Award for the contribution “Channel selective adaption of PWM frequencies for undisturbed AM and FM reception in automobiles” to the EMC Europe, Angers, France, 4-7 Sep. 2017.

2. **Receipt** of the Young Engineer Award for the contribution “FPGA-basierte aktive Gegenkopplung der Schaltharmonischen von leistungselektronischen Systemen” to the EMV Düsseldorf, Düsseldorf, Germany, 20-22 Feb. 2018.

3. Nomination for the Best Student Paper Award for the contribution “Development of an adaptive EMI cancellation strategy for stationary clocked systems” to the EMC Europe, Amsterdam, Netherlands, 27-30 Aug. 2018.

4. **Receipt** of the SEMIKRON Young Engineer Award 2019 for the proposal “Active EMI Reduction in Power Electronic Systems by Injecting Synthesized and Synchronized Cancellation Signals”

5. Nomination for the Best Student Paper Award for the contribution “Wide-frequency EMI suppression of stationary clocked systems by injecting successively adapted cancellation signals” to the EMC Europe, Barcelona, Spain, 2-6 Sep. 2019.

6. **Receipt** of the Best Student Paper Award for the contribution “Simultaneous EMI suppression of the input and output terminals of a DC/DC converter by injecting multiple synthesized cancellation signals” to the EMC Europe, Barcelona, Spain, 2-6 Sep. 2019.

7. **Receipt** of the Young Engineer Award for the contribution “FPGA-basierte aktive Unterdrückung der elektromagnetischen Störungen einer aktiven Leistungsfaktorkorrektur (PFC) durch die Injektion von modulierten Sinussignalen” to the EMV Cologne, Cologne, Germany, 17-19 Mar. 2020.

8. Nomination for the Best Paper Award for the contribution “FPGA-basierte aktive Unterdrückung der elektromagnetischen Störungen einer aktiven Leistungsfaktorkorrektur (PFC) durch die Injektion von modulierten Sinussignalen” to the EMV Cologne, Cologne, Germany, 17-19 Mar. 2020.

9. Nomination (as co-author) for the Best Paper Award and Young Engineer Award for the contribution “Injektorkonzepte zur aktiven Unterdrückung der elektromagnetischen Störungen aller Klemmen eines stationär betriebenen DC/DC-Wandlers” to the EMV Cologne, Cologne, Germany, 17-19 Mar. 2020.

List of Patents of the Author

1. DE102017001788A1 - “Verfahren zur Steuerung eines elektrischen Verbrauchers mittels Pulsweitenmodulation,” A. Bendicks, S. Frei, N. Hees, M. Wiegand, DE, 30 Aug. 2018.

2. WO002018153749A1 - “Method for controlling an electrical load by means of pulse width modulation,” A. Bendicks, S. Frei, N. Hees, M. Wiegand, EP, 30 Aug. 2018.

3. DE102018001051A1 - “Verfahren zur Reduktion eines elektromagnetischen Störsignals eines getaktet angesteuerten elektronischen Systems,” A. Bendicks, S. Frei, N. Hees, M. Wiegand, DE, 14 Aug. 2019.

4. US020190372683A1 - “Method for controlling an electrical load by means of pulse width modulation,” A. Bendicks, S. Frei, N. Hees, M. Wiegand, US, 05 Dec. 2019.

5. EP000003586455A1 - “Method for controlling an electrical load by means of pulse width modulation,” A. Bendicks, S. Frei, N. Hees, M. Wiegand, EP, 1 Jan. 2020.